Focused-Ion-Beam Growth of Nanomechanical Resonators

Huan Wang

Department of Electronic and Electrical Engineering

University College London

A dissertation submitted for

the degree of Doctor of Philosophy

September 2013

I, Huan Wang, confirm that the result presented in this thesis is my own work. Where information has been derived from other sources, I confirm that this has been indicated in the thesis.

To my parents

Abstract

Nanoscale mechanical resonators exhibit excellent sensitivity and therefore potential advantages for application as ultrasensitive mass sensors by comparison with micromachined cantilevers. We fabricated three dimensional vertical C-W-nanorods on silicon substrates by focussed ion beam induced deposition (FIB-CVD) and investigated the factors which affected the growth rate and smoothness of the nanorod sidewall, including the heating temperature of precursor gas and the ion beam current. We also discussed the effects on reducing the thickness of the nanorod with FIB milling, including the ion beam current, ion beam energy and ion incident angle. We fabricated a doubly-clamped beam and a singly-clamped beam by felling a vertical nanorod over a trench with FIB milling. We investigated the static mechanical properties (i.e. Young's modulus) of doubly-clamped and singly-clamped nanorods by atomic force microscopy (AFM) with force displacement measurement.

Since the optical signal reflected from a cantilever whose dimensions are sub-wavelength is very weak, it is difficult to measure the absolute nanoscale displacement of such cantilevers with an optical technique. We describe an electron microscope technique for measuring the absolute oscillation amplitude and resonance of nanomechanical resonators with a model-independent method. A piezo-actuator mounted in a field-emission scanning-electron microscope (SEM) is used to excite the nanomechanical resonator to vibrate. The secondary electron signal is recorded as the primary electron beam is scanned linearly over the resonator. An absolute oscillation amplitude as low as 5 nm can be resolved, this being comparable to the size (~1.5 nm) of the primary electron beam. The *Q*-factor of nanomechanical resonators was measured ranging 300 to 600. The mass resolution of the resonators was also estimated to the level of 10^{-15} g.

Acknowledgement

First and foremost I would like to thank Dr. Paul Warburton, my supervisor, for his kind training, guiding and helping me throughout the whole PhD studies in the past four years. I would also like to thank Dr. Jon Fenton and Dr. Olivio Chiatti, both of whom assisted me in the analysis and presentation of experimental data. In particular, Dr. Jon Fenton helped me start with the Matlab code for my data analysis, and Dr. Olivio Chiatti advised me on the set-up designing for the resonant frequency detection of nanorods in the Scanning Electron Microscope (SEM). I am also very grateful for the help from Dr. Ed Romans and Dr. Sajid Saleem because they have given me lots of advice on PhD studies and life in London.

A big thanks to Dr. Suguo Huo, who is in charge of SEM/FIB. Every time my experiment was affected by SEM/FIB, he always either solved the problem quickly or contacted with engineers from Carl Zeiss immediately. I also show thanks to Dr Bart Hoogenboom, who helped me with the AFM at the beginning of my PhD.

Finally, I would like to express thanks to all of my colleagues, especially Mr Ed Osley and Mr Paul Thompson who have patiently assisted me in the improvement of my English. I also would like to say thanks to my friends who offered support and encouragement when needed. I must thank my parents, to whom I dedicate this dissertation with all my love.

Contents

List of Figures

Chapter 1 Introduction

1.1The need for nanomechanical resonators

Nanometre scale cantilevers are resonators which use physical principles similar to those found in atomic force microscopy. They have been proposed for a variety of applications including metal deposition monitors, mechanical reaction monitors, biomedical sensors, mass detectors, etc. (1-4). The mass sensor is generally operated in the resonant mode, where binding on the cantilever increases mass and thus decreases the resonant frequencies. These mass sensors (5, 6) create opportunities for novel, label-free detectors with high sensitivity and very high levels of multiplexing.

The detection sensitivity is proportional to both the resonant frequency and the reciprocal of the effective mass of the resonator (7). Therefore, fabrication of devices with a higher resonant frequency and lower mass is very important. The high frequency is achieved by scaling down the size of the resonator because the resonant frequency is proportional to L^{-2}, where L is the length of the device. It has been reported that the detectable mass can be made as small as several femtograms by using microsized silicon, silicon nitride cantilevers, or diamond-like carbon cantilevers (8-12). An even higher mass resolution (attogram) has been achieved by using nanosized resonators such as silicon, silicon nitride, SiC, carbon nanotube (11, 13-16). Nanoscale resonators have traditionally been fabricated using “top-down” lithography techniques using silicon nitride, single-crystal silicon and so on (17, 18). In the past few years, “bottom-up” techniques have been used to fabricate nanomechanical

resonators, such as single wall carbon nanotube resonators (19), platinum nanorods (20), and carbon nanofibre resonators (21). Focused-ion-beam induced deposition techniques are powerful for fabricating three-dimensional nanoscale structures. Diamondlike-carbon (DLC) pillars have been grown by FIB-CVD (12). This method enables fabrication of 3D nanostructures on the order of several tens of nanometers. A highly sensitive miniature cantilever can be produced using FIB-CVD. Furthermore, it is possible to fabricate 3D nanostructures on any position of the sample on demand. This should enable applications never achieved by conventional lithography techniques.

A wide variety of techniques have been used to excite and detect resonance in the devices. Optical detection is the most popular with micromechanical cantilevers, where transduction is achieved by detecting light from a laser beam. The laser is reflected off the surface of the cantilever. For larger cantilevers, optical detection is an option, but as devices become smaller the reflected signal diminishes. Alternative techniques are therefore being actively pursued for detecting the resonant frequency. One technique involves placing an electrode just within the range of motion of a cantilever resonating in-plane so that the cantilever will physically hit the electrode once every cycle. This sends an electrical signal which is used to determine the resonant frequency (22). Poncharal *et al* (23) demonstrated femtogram-order mass detection using a nanotube cantilever in a transmission electron microscope (TEM). However, it was difficult to track the resonant frequency because resonant oscillation was measured using transmission electron microscope images. Recently, the resonant frequency for a nanoscale pillar excited by a piezo actuator in a scanning electron microscope (SEM) was estimated from the spectrum of secondary electrons (SE), measured using a spectrum analyzer. Nishio *et al* (11) proposed a quantitative method to measure the oscillation amplitude and the resonant frequency of a nanotube cantilever using SEM. However, none of those techniques can measure the absolute oscillation amplitude.

In this thesis we present the results of experimental work on fabrication and characterisation of tungsten nanomechanical resonators. We have used focussed ion beam (FIB-CVD) to deposit free-standing C-W-nanorods as nanomechanical resonators. We took advantage of FIB-CVD to grow C-W-nanorods with differing lengths and arbitrary cross-section with a resonant frequency up to 1 MHz. To make in-situ resonance detection, we used a piece of piezo as an electrical actuator inside a field-emission scanning-electron microscope (SEM) chamber as our measurement setup. Then we use SEM linescan technique to characterise the absolute oscillation amplitude and the resonant frequency of the nanorod. This technique enables us to measure oscillation amplitude as low as 5 nm. In addition, the Q-factor of the tungsten nanomechanical resonators was measured to be 300-600 and their mass resolution was also estimated to be 10^{-15} g.

1.2 Form of the thesis

We first demonstrate the experimental development of nanomechanical resonators (Chapter 2). In chapter 3 we discuss the background theory required to understand the project by describing the classic static and dynamic mechanical properties of cantilever-based resonators. Chapter 4 describes our experimental details. Chapter 5 presents the results obtained and their analysis. Finally chapter 6 presents the conclusions and future work to be undertaken.

Chapter 2 Experimental Development of Nanomechanical Sensors

2.1 Introduction

Micrometre-sized cantilevers have great potential as label-free, sensitive, portable, cheap, highly parallel and fast sensors for field use and have thus attracted considerable interest from applications such as point of care (POC) diagnostics, homeland security and environmental monitoring. Moreover, the sensors offer the possibility of measuring quantities and phenomena such as weak changes in surface stress, temperature and mass, which are very difficult to achieve by other methods and they are therefore also very interesting fundamental research tools. For example, the current trend in mass detection of nanomechanical resonators in ultra high vacuum environments is pushing past femtogram sensitivity toward zeptogram mass sensing for single molecule detection and eventually towards mass spectroscopy (24). Thus nano/micromechanical resonators show the promising ability to provide the detailed mechanisms of biochemical reactions (25-28). Current biosensing tools are unable to accurately detect marker proteins (relevant to specific cancers) in a concentration of ~ 1ng/ml in blood serum. Micro/nanomechanical resonators are able to overcome this diagnostic grey zone because of their unprecedented detection sensitivity even at single-molecule resolution (29-31). This shows that nanomechanical resonators can be used as lab-on-a-chip biosensors enabling the early diagnosis of important diseases like

cancer. Furthermore, the sensors can be operated in different modes which yield different information and which when combined can be used to obtain a unique set of coupled data.

In order to fully understand the versatility of micro/nanomechanical resonators, four main aspects of the micro/nanomechanical resonators will be demonstrated in the following: the history of their development, resonator materials and fabrication, the resonator readout principle and applications of resonators.

2.2 History of development

In 1986 the invention of the atomic force microscope (AFM) demonstrated a cantilever with sharp tip mechanically probing a surface. This tip was scanned either in contact with the sample surface, using cantilever deflection to map sample topography by the tip-sample interaction force, or it is resonantly excited slightly above the sample, monitoring changes in the resonant properties of the cantilever to probe the surface (32). Higher resonant frequency of the cantilever makes the probe less sensitive to external vibrations and the lower spring constant improves the force sensitivity of the probe. Therefore the dimensions of AFM probe needs to be manufactured in microscale to achieve a high resonant frequency. The technique made the micro-sized cantilevers available (33). Since then, the versatility of this technique has been fully explored by the development of various sensors for different applications. The following is the development path of microsized cantilevers and their applications in the past two decades.

The first micromachined cantilevers with integrated tips were realized in 1990 by Tom Albrecht and co-workers at Stanford University (34) and by the group of Wolter at IBM (35). The field of cantilever-based sensing emerged in the mid-1990s. Thomas Thundat and co-workers at Oakridge National Laboratory started to explore the potential of the cantilevers as a physical and chemical sensor in 1994 (36). The group around Mark Welland in Cambridge

and the group around Jim Gimzewski and Christoph Gerber at IBM, Zurich, both used the bimorph effect to perform sensitive photothermal spectroscopy (37, 38). Roberto Raiteri and Hans-Jurgen Butt from the Max-Planck-institute for Biophysics in Frankfurt reported on studies of surface stress changes induced electrochemically (39). Butt (40) reported unspecific binding of proteins to a hydrophobic surface in 1996. Berger *et al* (41) demonstrated a gold-coated cantilever exposed to alkanethiols, which made the cantilever sensors used for online measurements of surface stress changes. In 2000, cantilever-based sensing in the field of diagnostics became popular. Fritz *et al* (42) (42) demonstrated that a pair of cantilevers coated with two short strands of DNA-oligos that only differ by a single base can be used for single-nucleotide polymorphism detection. These experiment results were the source of many studies related to specific recognition of DNA, proteins and macromolecules.

Followed by the emergence of nanotechnology in the last decade, the development of nanoscale functional resonators designed for specific aims such as nanoscale actuation, sensing, and detection (5, 6) has been improved significantly. Micro/nanoelectro-mechanical system (MEMS/NEMS) sensing devices have been extended to detect physical quantities such as spin (43, 44), molecular mass (30, 45-47), quantum state (48), thermal fluctuation (49-51), coupled resonance(52, 53), and biochemical reactions (25-28). Among MEMS/NEMS devices, nanomechanical resonators have been recently highlighted for their unprecedented dynamic characteristics as they can easily reach ultrahigh frequency (UHF) and/or very high frequency (VHF) dynamic behaviour up to the Giga Hertz regime (54). Reaching this frequency range is critical as it implies that nanoresonators can be directly utilized as an ultrasensitive sensor.

This high frequency dynamic behaviour is achieved by scaling down the dimension of the resonator because the resonant frequency is proportional to L^{-2}, where L is the length of a device. Therefore, if the resonator length is decreased by an order of magnitude, then its

resonant frequency is increased by two orders of magnitude. Furthermore, the ability of the resonator to sense or detect physical quantities (i.e. mass, force or pressure) is closely related to its resonant frequency. For example, for sensing mass that is added onto a resonator, the detection sensitivity is given by the relation $\Delta f_n/\Delta m = (1/2m)f_n$ (16), where f_n and m represent the resonant frequency and the effective mass of a device, respectively, while f_n and Δm indicate the resonant frequency shift and the added mass. Clearly, this relationship suggests that as the frequency of the resonator increases, so does its ability to sense or detect ever smaller masses, which implies that UHF/VHF resonators are suitable for ultra-sensitive detection, where the eventual limit of a single atom or molecule is experimentally within reach.

An example of the incredible potential of NEMS resonators can be found in recent works by Roukes and co-workers (30, 45, 46), who first showed the possibility of nanoscale mass spectrometers that enable the measurement of the molecular weight of specific molecules. This implies not only that nanomechanical resonators could be a viable alternative to conventional mass spectrometry techniques such as matrix-assisted laser desorption/ionization time-of-flight, but also that mass spectrometry could be realized in a lab-on-a-chip (55).

2.3 Resonator materials and fabrication

In general the method of resonator fabrication is related to its readout system. For example, if an external optical read-out system is used to measure the cantilever deflection, the focus of the fabrication will be simple free-standing beams for optical read-out. Additional requirements to the final resonator structure are necessary, in addition to the material choice:

(1) For higher surface stress sensitivity, the resonator needs to be as thin and long as possible. Processing of suspended fragile structures is necessary;

(2) For higher mass sensitivity, the clamping of the resonator should minimize clamping losses. Moreover, it requires the material have internal damping as low as possible and the resonator geometry should allow for a high *Q* factor;

(3) For all purposes, the geometries of the cantilevers should be controlled with a high accuracy because the dimensions and the uniformity of the sensors have a huge influence on the sensitivity. For instance, accurate geometries of reference and measurement resonators is crucial to avoid measurement errors.

(4) For optical read-out, the surface of the resonator should be reflecting and of high optical quality instead of scattering the light in all directions.

(5) The resonators should ideally have no initial bending because the bending complicates the optical alignment and makes the resonators more prone to spurious signals.

The main materials for cantilevers can be divided into three categories. In general, cantilevers are fabricated in either silicon- or polymer-based materials. Cantilevers with alternative materials have emerged in recent years, including carbon nanotube (13, 16), diamond-like carbon (56) and ZnO (57). These materials offer unique chemical and mechanical properties.

2.3.1 Silicon-based cantilevers

Silicon-based materials are widely used to fabricate cantilever sensors. Since 1960s silicon microfabrication has been developed by the IC industry. Now its fabrication, integration of wiring for actuation and readout is well established. Silicon, silicon nitride and silicon oxide are well characterised and stable over time. Therefore, cantilevers fabricated with these classical materials can be operated in a large range of temperatures and environmental conditions. The typical length and thickness of microcantilevers is 450-950 μm and 1 μm, respectively. Commercially available ultrasensitive cantilevers have a thickness of 500 nm and a length of 500 μm (58). Ultrathin cantilevers with a thickness less than 200 nm have

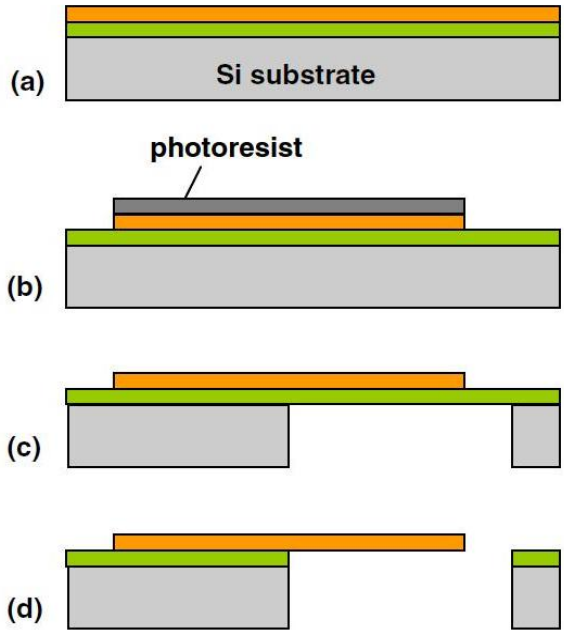

Figure 2. 1: Fabrication of silicon-based cantilevers (*a*) substrate preparation by thin film deposition;(*b*) patterning by photolithography and etching; (*c*) cantilever release by etching from the backside and (*d*) removal of the etch stop layer. Image taken from Ref. (58)

been fabricated (59, 60). The most useful and general micromachining strategy for fabrication of cantilevers with silicon-based materials is bulk micromachining. To fabricate microsized cantilever device, cleanroom process, photolithography, is used where the cantilevers are fabricated by etching three dimensionally in a silicon wafer. A typical recipe for silicon-based cantilevers consists of three main steps as shown in figure 2.1: (a) substrate preparation, (b) cantilever patterning and ((c), (d)) device release. With this method, i.e. bulk micromachining, the suspended structures are defined by etching from the backside all the way through the wafer (61). The fabrication is based on singly crystal silicon wafers of thickness ranges from 350 to 500 μm. In the process of substrate preparation, silicon nitride, silicon oxide or polysilicon is deposited. The thickness of these deposited films decides the final thickness of the cantilevers. In the first step, a three-layered substrate is prepared as shown in figure 2.1 (a).

The intermediate material is called the etch stop layer, which protects the actual device layer during the release. It can secure the cantilever with a well-defined thickness and a highly reflecting surface. For example, silicon-on-insulator (SOI) is fabricated with a single crystal silicon wafer (100) coated by a built-in silicon oxide film. The cantilevers can be defined by UV patterning of photoresist on the front side of the wafer. To fabricate a nanosized cantilever, clean room process, electron beam lithography, needs to be used (58). In Figure 2.1(b), the resist pattern is transferred to the device layer by wet etching or reactive ion etching. In the final step, the etch stop layer is removed to release the cantilever as seen in Figure 2.1(d).

The advantage of bulk micromachining is that the process is useful to fabricate free-standing cantilevers, both sides of the cantilever can be easily inspected and the cantilever can be placed in a liquid or gas flow perpendicular to the cantilever (58). However, the disadvantage is the process cannot protect the fragile cantilever and it is time consuming to etch through the whole silicon wafer.

2.3.2 Polymer-based cantilevers

In late 1990s, the fabrication of polymer-based cantilever emerged because its Young's modulus typically is two orders of magnitude lower than traditional silicon-based materials, which results in a reducing stiffness and an increasing sensitivity of the cantilever. Another reason for its popularity is that the raw materials and fabrication method cost less than silicon-based cantilever.

The first polymer microcantilevers with a standard Novolak-based photoresist material were fabricated by Pechmann and co-workers (62). In 1999, Genolet defined an AFM cantilever by using the negative epoxy photo-resist SU-8 (63). It has a Young's modulus only 4 GPa, which is much lower than silicon and silicon nitride cantilevers (180 and 290 GPa,

respectively). The smaller Young's modulus makes it suitable to measure the surface stress of micromechanical structures. At the same time, various well-known polymer have been used to fabricate micromechanical sensors, which included polyimide (64, 65), polystyrene (66-68), polypropylene (68), polyethylene therephtalate (PET) (69) and fluoropolymer (70). Most recently, new thermoplasts specifically developed as cantilever materials, such as parylene (71, 72) and TOPAS (73) have been used.

Instead of bulk micromachining, surface micromachining is employed to fabricate micro-cantilevers. With this method, the free-standing structures are fabricated by depositing layers on the surface of a substrate (74). Figure 2.2 shows the schematic process for the fabrication of polymer cantilevers. As shown in Figure 2.2 (a), first a sacrificial layer is built up, then a thin cantilever material is deposited, which, in general, is achieved by spin-coating or an organic solution of a polymer. In figure 2.2 (b), UV-photolithgraphy is used to pattern the polymer cantilever and in the case where the polymer is a photoresist (64, 75). Then the thin polymer film needs to be baked and exposed. Alternatively, the cantilever can be patterned by a combination of traditional photolithography and polymer etching. For been used to pattern cantilevers (76, 77). For example, Greve *et al* (73) fabricated cantilevers with a thickness of 4.5 μm.

After definition of the cantilevers, a polymer chip body can be added to facilitate handling of the cantilevers as shown in figure 2.2 (c). At the end, the cantilevers are released from the front side of the wafer. A selective etch is used to remove the sacrificial layer below the cantilever. The suspended cantilever is fabricated as shown figure 2.2 (d). In this process, both wet etching and dry etching in a plasma is possible (53, 78). Due to the small space between the cantilever and substrate, the adhesion of the cantilever to the substrate may increase. In order to reduce the risk, dry etching is helpful for cantilever release (79).

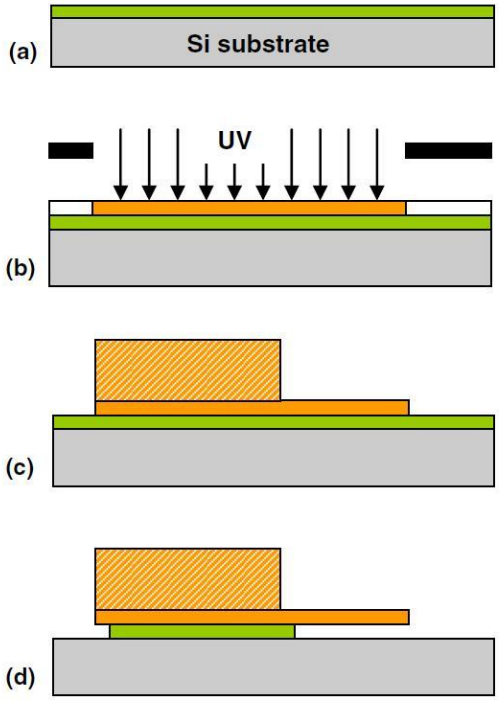

Figure 2. 2: Fabrication of polymer cantilevers (*a*) deposition of sacrificial layer; (*b*) patterning by direct UV lithography; (*c*) definition of chip body; (*d*) cantilever release by partial or complete etching of the sacrificial layer. Images taken from Ref. (58).

However, fabrication of polymer-based micromechanical cantilevers is still in at early age (58). Technique challenges exist, such as the instability of the polymer cantilever sensor during measurements. Moisture absorption in liquids or degassing in vacuum causes drift of the output signal (80). Creep deformation, ageing or bleaching also affect the long-term stability of polymer cantilever sensors. Although the process has been optimized by Martin *et al* (81) and Keller *et al* (82) to reduce drift and improve the stability, still more improvement needs to be done to fabricate robust and stable cantilevers. Another disadvantage is that thin polymer cantilevers are unsuitable for optical read-out. Usually, a metal coating for the polymer cantilever could solve this problem, but the elevated temperature heavily affects the stress gradients in polymer cantilevers during the process of metal coating (83). In future, it will be necessary to improve fabrication methods of polymer cantilevers to lessen the influence of measurement conditions.

2.3.3 Nanorods fabricated with "bottom-up" techniques

Nanoscale resonators have traditionally been fabricated using "top-down" lithography techniques as described in the above two sections. In the past few years, "bottom-up" techniques have been used to fabricate nanomechanical resonators, such as single/multi wall carbon nanotube resonators (18), ZnO resonators (19), and carbon nanofibre resonators (20).

Carbon nanotubes have been paid considerable attention for nanomechanical systems. Compared with conventional silicon-based nanomechanical resonators, carbon nanotubes have several advantages. For example, carbon nanotubes have much higher strength and stiffness and thermal and electrical conductivity. Nanosized silicon-based resonators do not have high-*Q* mechanical resonances due to dominant surface effects and thermoelastic damping. One of the most popular ways to synthesise multiwall carbon nanotube is by using a short-period arc-discharge method (2, 5). Basically, a voltage is applied between graphite electrodes in a vacuum chamber filled with He or Ar gas. Then the electric discharge heats the graphite. Individual carbon atoms break away and migrate onto the negative electrode to create the multiwall carbon nanotube. The diameter of the carbon nanotubes ranges from 8 to 32 nm. Nishio *et al* (11) aligned the nanotube on a Pt-coated knife edge using an alternating current electrophoresis technique to produce a nanotube cartridge, which can be fixed on a piece of electrical actuator as a resonator. Another common method to fabrication carbon nanotube is chemical vapour deposition (CVD). In 1998, the group of Hongjie Dai (84) synthesised single wall carbon nanotubes using chemical vapour deposition. Here, carbon nanotubes grow in a steam of gases blown across catalysts on silicon wafers. The silicon wafers are dipped into a solution of ferric nitrate nonanhydrate in 2-propanol, rinsed in hexane and dried. The process continues with the silicon wafter placed in a tube furnace, which is heated up to 900^{o}C in flowing argon gas. The sample needs to be annealed for 15 mins in flowing hydrogen. Then the argon and hydrogen are replaced by methane to flow through the tube for 5 mins. In the end, the furnace is cooled under argon. This technique

yields single wall carbon nanotubes with diameters ranging from 0.8 to 3 nm. The group of Akita (85) used this method to study the mechanical properties of the carbon nanotube resonators. However, the disadvantages of this technology for sensor applications are that it is hard to grow the nanotubes to a useful length and assemble them for systematic nanoelectromechanical measurements.

Focused-ion-beam and focused-electron-beam induced deposition are a newly emerged techniques for fabricating three-dimensional nanoscale structures. A highly sensitive miniature resonator can be produced using FIB-CVD. The material of the resonators can be changed by choosing different gas precursor of FIB/FEB. Furthermore, it is possible to fabricate 3D nanostructures on any position of the sample on demand. This method enables fabrication of 3D nanostructures on the order of several tens of nanometers. This should enable applications never achieved by conventional lithography techniques. The fabrication process with focused-ion-beam induced deposition is demonstrated with detailed information in chapter 3.

Nanomechanical resonator of diamond-like-carbon (DLC) pillars was fabricated with Ga^+ focused ion beam-induced chemical vapour deposition by Fujita *et al* (21). The length is time-dependent and ranges from 5 μm to 28 μm. The thickness of the resonators ranges from 80 nm to 480 nm. The Young's modulus was measured to be 65-130 GPa by testing the resonant frequency of the pillars. The group of Utke (86) took advantage of FIB to modify an AFM cantilever by growing a vertical nanorod with a precursor gas of $Co_2(CO)_8$ on the tip of it to study mass sensing. The vertical nanorod on the tip of the cantilever has a diameter of 600 nm and a length of 5 to 8 μm. Utke *et al* (87, 88) also deposited resonators with precursor gases of $Cu(C_5HF_6O_2)_2$ and resonators of cobalt to measure their mechanical properties. However, the disadvantage is that the diameter of the resonator is limited by the ion beam diameter and the surface of the sidewall is not smooth, which may cause more energy dissipation resulting in a low *Q*-factor.

It is well known that the focused ion beam induced tungsten deposition is not crystalline, but is amorphous and always includes certain percentage of carbon, gallium and even oxygen elements. The variation of compositions in FIB induced tungsten deposition depends on the deposition parameters. This variation results in changes in their physical and structural characteristics as shown in literatures.

Sadki *et al*.(89) used FIB induced tungsten deposition to fabricate nanowires and thin films. The operating Ga^+ ion beam energy is 30 keV and beam current is 98 pA. Deposition gas pressure is 2.6×10^{-5} Torr and the FIB ion dose is 1 $nC/\mu m^2$. With these parameters, the atomic concentration in their tungsten film is 40%, 40% and 20% for W, C and Ga, respectively with the test of electron probe microanalysis (EPMA).

Li *et al*. (90) also used FIB induced tungsten deposition to fabricate thin films and investigate its superconductivity. Their thin films were deposited with a Ga^+ ion beam energy of 30 keV and beam current of 20 pA. Gas pressure is between $1.1\text{-}1.3\times10^{-5}$ mbar and the FIB ion dose is 0.05 nC/um^2. Their Energy dispersive X-ray spectroscopy (EDS) test showed that the atomic concentration in tungsten film is 34%, 53%, 11% and 2% for W, C, Ga and O, respectively. Li *et al*. (91)also investigated the composition and superconductivity of tungsten nanowires fabricated by FIB induced deposition with 1pA ion beam current at 30kV with a gas pressure of $7.4\text{-}8.3\times10^{-6}$ mbar. However, the composition of tungsten nanowires characterized by EDS is tungsten rich instead of carbon rich, which is 49%, 29%, 10% and 6% for W, C, Ga and O, respectively.

Ross *et al*.(92) paid more attention on the morphology and composition of a serious of tungsten nanowires fabricated by both ion and electron beam induced deposition. The FIB induced deposition parameter included a Ga^+ ion beam energy of 30 keV, beam current of 20 pA and gas deposition pressure of $1\text{-}2\times10^{-5}$ mbar. TEM image shows the microstructure of both of the nanowires are amorphous, but a nano-polycrystalline structure appears in the

electron beam induced tungsten nanowires due to the localized annealing caused by exposing to 200 kV of TEM. The composition of ion beam induced deposition tungsten nanowires characterized by EDS and EELS is around 40, 40 and 20 atomic % for W, C and Ga, respectively. In contrast, the composition of electron beam induced deposition tungsten nanowires is 24, 40 and 36 atomic % for W, C and O, respectively.

X-ray photoelectron spectroscopy (XPS) was also used to characterize the focused ion beam induced tungsten deposition by Guillamon *et al*. (93). Their deposition parameters are the same as Sadki *et al*.(89). XPS and an argon etching process shows that the tungsten deposition is very homogeneous with an average concentration of 40±7%, 43±4%, 10±3% and 7±2% for W, C, Ga and O, respectively. They also found that the tungsten deposition remains clean after exposure to ambient conditions.

In addition, new materials with new fabrication techniques are still being on. For example, ZnO nanorods attracted the interest of several groups (57, 94). They fabricated ZnO nanorods by a vapour-solid growth process and investigated their stiffness and Q-factor through the resonance techniques to make useful nanomechanical resonators. GaN nanorods as nanomechanical resonators with a diameter of 30-50 nm and a length of 5-30 μm were synthesised via the vapour-liquid-solid mechanism using Au/Pd as catalyst (95, 96).

2.3.4 Comparison of materials and fabrication methods

It is important to consider the advantage and disadvantage of different materials and fabrication methods for a specific application of sensors.

For mass sensing in dynamic mode, usually silicon-based cantilever sensors are preferred. One of the main reasons is that its lower internal damping results in a higher quality factor of the sensors. Second, the higher Young's modulus and nanoscaled cantilevers fabricated with e-beam lithography enable high resonant frequencies and mass sensitivity. Compared with

silicon-based cantilevers, polymer cantilevers have significant damping affected by temperature and humidity during the measurement.

For sensors operated at elevated temperatures, silicon-based cantilevers are more popular than polymer-based cantilevers due to the increased temperature stability. However, fabrication of silicon-based cantilevers generally is more expensive than using polymers.

For measurement of surface stress in liquids, silicon-based cantilevers are superior to polymer cantilevers because drift caused by moisture absorption can be neglected. However, polymer cantilevers are a good alternative because they can achieve higher beam thickness for higher surface stress sensitivity. The group of Boisen (58) reported that polymer cantilevers and silicon cantilevers are comparable for surface stress measurements.

For the mass sensing in dynamic mode with resonators of newly developed materials, carbon nanotubes exhibit its nanosized dimensions and promising mechanical properties due to its low mass and high stiffness. Resonators fabricated with FIB-CVD show its fabrication flexibility and precise controlling of location and materials options and nanosize thickness. However, their Q-factor is much lower compared with cantilever sensors. Therefore is still a large space to improve their properties for better sensing applications by optimising its fabrication process.

2.4 Resonator read-out principles

Real-time measurements of cantilever deflections with its accuracy of nanometer are very critical for the operation of any cantilever sensor. Therefore, an important part of any cantilever sensor is a readout system capable of monitoring changes in one of the parameters directly related to the cantilever deflection. Such parameters include cantilever tip position, spatial orientation, radius of curvature, and intrinsic stress. Specific requirements for the readout of cantilever sensors can be dictated by the operation mode (either static or dynamic),

cantilever design, and materials used as well as the magnitude of expected responses. In this section, we discuss methods for cantilever sensor readout that can be broadly classified as either optical or electrical. Using optical, piezoresistive, piezoelectric, capacitance, or electron tunneling methods, deformations and resonance frequency shifts of cantilever transducers can be measured with sufficient precision.

2.4.1 Optical methods

Optical lever readout scheme is one of popular read out system for cantilever sensing. The optical method is similar to the operation principle of AFM instrument and its probe. The optical read out system includes optical beam deflection (also referred to the optical level method) (97) and optical interferometry (98). The optical beam deflection technique was used initially in AFM by Meyer and Amer (97), and it is as sensitive as the complex interferometric scheme. In the optical beam deflection technique, a laser diode is focused at the free end of the cantilever. A small mirror is attached to the cantilever so that the position of a laser beam reflected off this mirror can be monitored by a position sensitive photodetector (PSD). This optical detection scheme is shown in figure 2.3. Small cantilever bending can be detected with this technique. According to (99), a cantilever displacement of 10^{-14} m was measured.

A typical PSD is based on a quadrant photodiode, which consists of four cells A, B, C and D. Each of the cells is coupled to the input of a separate transimpedance amplifier the output voltages of which, V_A, V_B, V_C and V_D, are proportional to the illumination of the respective quadrant. The normalized differential output, $V_{out}=[(V_A+V_C)-(V_B+ V_D)/(V_A+V_B+V_C+V_D)]$, depends linearly on the vertical displacement of the weighted centre of the light spot projected by the cantilever. The absence of electrical connections to the cantilever, linear response, simplicity, and reliability are important advantages of the optical lever method. Although this method is popular to the majority of cantilever sensor work, its limitations are

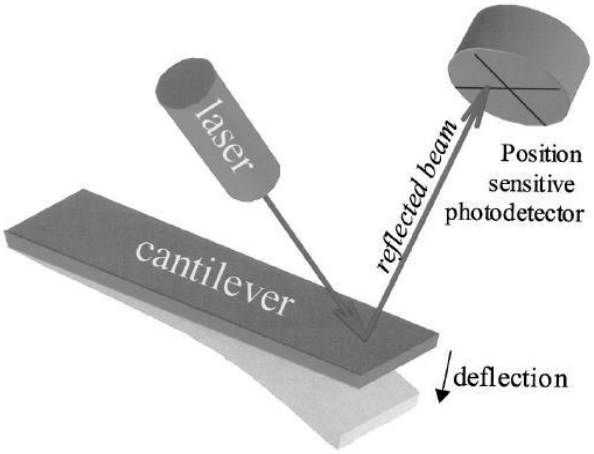

Figure 2. 3: The ‘‘optical lever’’ readout commonly used to measure deflections of microfabricated cantilever probes in AFM. Image taken from ref. (99).

well known. Changes in the optical properties of the medium surrounding the cantilever may interfere with the output signal. Tippl *et al.* (100) reported that the interference can be avoided largely by using a proper orientation of the cantilever relative to the optical components. The effect of the refractive index change and other interfering factors can be further suppressed by using differential pairs or arrays of cantilevers. However, this technique has limitations of analysing in low opacity and low turbidity media. Another limitation is related to the bandwidth of PSDs, which is typically on the order of several hundred kilohertz.

In order to operate the cantilever sensors at higher resonant frequency or higher resonant mode in the case of cantilevers with smaller dimension or larger stiffness, the bandwidth becomes critical. A new technique is developed. The motion of a cantilever illuminated with a tightly focused laser beam produces a change in the spatial distribution of the reflected and/or scattered light. A knife-edge obstacle combined with a simple spot photodetector can be used to monitor these intensity fluctuations (101). The readout bandwidth of this technique can achieve gigahertz range by using a small area, high-speed avalanche photodiode. However, the light scattering of this approach interferes with ambient light,

resulting in a less controllable optical gain. The interferometry technique enables measurement of the cantilever deflection with more accurately and with high bandwidth. AFM uses the interferometry as an optical technique for the measurements of cantilever deflections.

In order to carry more accurate high-bandwidth optical measurement of cantilever deflections, interferometry is helpful. For example, it is used by AFM for measurements of cantilever deflection. It is also used for MEMs readout and characterization. The reason is that this optical technique gives a high resolution mapping of nanoscale deflections of cantilevers (102). Rugar (103) *et al*. detected the subnanometer deflection of ultrasensitive cantilevers with this technique for ultrasensitive force measurement.

More recently, optical detection techniques was further developed by several research groups (104) (105) for the readout system of larger arrays of cantilevers. In their works the cantilever array was illuminated by a single laser source and the reflected light is interferometrically coupled with a reference beam and measured by a charge-coupled device (CCD) imager.

In order to ensure the best possible performance of cantilever sensors, inherent advantages and disadvantages of different readout techniques were analyzed in recent studies. The optical beam deflection method was shown to have excellent readout efficiency in the case of cantilevers with a reflecting area of at least a 10×10 mm^2. Optical readout techniques may, however, be inefficient when applied to nanocantilevers. The shortcomings of some optical techniques, in particular the optical deflection method, are related to loss of intensity and directionality of optical beams reflected (scattered) by nanosize cantilevers.

2.4.2 Piezoresistance method

Piezoresistance method is also largely used for readout system of cantilever sensors. Piezoresistivity is the phenomenon of changes in the bulk resistivity with applied stress. For example, if a silicon cantilever with an appropriately shaped doped region is deformed, the change in resistance of the doped region reflects the degree of deformation. Doped single crystal silicon is one of the most common materials to exhibit a strong piezoresistive effect (106-108). The piezoresistance technique is a DC-based Wheat stone bridge, which the resistance variation of the cantilever can be measured with. The typical resistance of a silicon microsized cantilever with a boron doped channel is a few kiloohms (99). If the voltage V is applied to the Wheat stone bridge with resistors of identical initial resistance R, the differential voltage across the bridge can be expressed as $\delta V=V(\delta R/4R)$. It is necessary that the piezoresistive cantilevers are designed with two identical 'legs' because the resistance of the boron channel can be measured by connecting two conductive paths to the cantilever base next to the legs as shown in figure 2.4. However, the disadvantage of the piezoresistive technique is that it requires current to flow through the cantilever. As a result, additional dissipation of heat and associated thermal drifts will appear. If the cantilever is heated above the room temperature, changes in the thermal conductivity of the environment will result in fluctuations of the cantilever temperature. Then parasitic cantilever deflection and piezoresistance may occur.

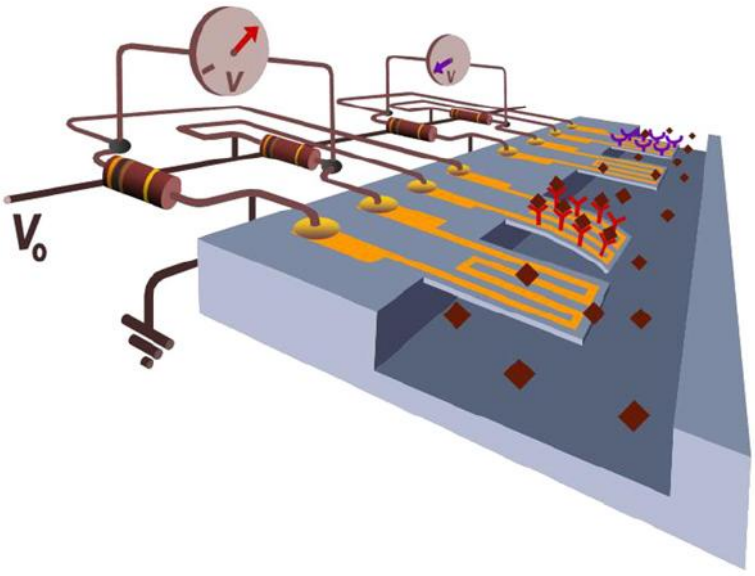

Figure 2. 4: Schematic diagram of the cantilever measuring principle. When molecules attach to the cantilever, the cantilever bends, which is detected as a change in the resistance of the resistor placed inside the cantilever. Images taken from Ref. (58).

2.4.3 Piezoelectric method

The piezoelectric readout technique requires deposition of a piezoelectric material, such as ZnO, on the cantilever. Transient charges are induced in the piezoelectric layer because of the piezoelectric effects, when a cantilever is deformed (109-111).

Lee *et al.* (112) successfully worked on self-excited piezoelectric cantilevers with resonance in the acoustic frequency range. In their work, the piezoelectric cantilever contained a zinc oxide piezoelectric thin film sandwiched between two aluminium layers on a piece of silicon nitride. Then Lee *et al.* (112) developed piezoelectric cantilevers using PZT films. Recently, Adam *et al.* (113) showed a microsized cantilever chemical detection platform based on an array of piezoelectric microcantilevers with power consumption in the range of nanowatts. Lee *et al.* (114) demonstrated that micromachined piezoelectric cantilevers with a width of 100 μm, a length of 200 μm and a thickness of 2.1 μm had a gravimetric sensitivity of 300 cm^2/g. Then the mass detection reached the level of 5 ng. The gravimetric sensitivity in their

work was characterised by depositing a known amount of gold on the backside of the cantilevers.

However, the requirement of electrical connections to the cantilever is the main limitation for both of the piezoelectric and piezoresistive readout. The second disadvantage is that the thickness of the piezoelectric film must be well above certain values, which is related to the optimal mechanical characteristics. Otherwise, the output signal is not large to be obtained.

2.4.4 Capacitance method

The principle of the capacitance readout is based on measuring the capacitance between a conductor on the cantilever and another fixed conductor on the substrate, which is separated from the cantilever by a small gap (115, 116). The cantilever deformation decides the changes in the gap, which results in the capacitance between two conductor plates. The capacitance of a planar capacitor is inversely proportional to the separation distance. Therefore the sensitivity of the capacitance method is decided by the small gap between the cantilever and the substrate. The disadvantage is that variations in the dielectric constant of the medium can interfere the capacitance readout. One of the main advantages of the capacitance readout is that it can be used in integrated MEMS devices that are fully compliant with standard CMOS technology. One interesting development of the capacitance readout is the 'electron shutting' regime, which is promising for nanosized electro-mechanical systems. As an example, Erbe *et al*. demonstrated 'quantum bell' (117), which consists of five metal coated cantilever structures and operates in the radio frequency range.

2.4.5 Electron tunnelling

Electron tunnelling has been used to detect the cantilever deflection in AFM (33). Electron tunnelling occurs between a conducting tip and the cantilever separated by a subnanometer

gap. The bias voltage applied between the tunnelling tip and cantilever causes a flow of electrons between the tip and the cantilever. The tunnelling current is very sensitive to the gap, which is related to the position changes of the cantilever. It increases by one order of magnitude for each 0.1 nm change in second (118). Therefore, the electron tunnelling readout is very highly sensitive to the position change of the cantilever. It has a nonlinear response and a limited dynamic range. According to Kenny (118), the cantilever displacement with this technique can be measure as small as 10^{-4} nm. The disadvantage of the electron tunnelling readout is that the tunnelling processes are sensitive to the materials between which the tunnelling process occurs, which often translates into challenging requirements to device implementation. However electron tunnelling readout was successful with accelerometers, infrared sensors (118) and magnetic field sensors (119).

2.4.6 Actuation

A lot of techniques have been employed to actuate the cantilevers. The method of actuation has to be coordinated with the read-out principle. It is common that the cantilever is excited to vibrate by using an external piezoelectric platform on which the cantilever chip is fixed and vibrated at a driven frequency. As an alternative option, the actuation can be miniaturized and integrated with the sensor. In general, actuation principles include electrostatic actuation, thermal actuation and magnetomotive actuation. For electrostatic actuation, an electrode close to the cantilever is biased with an alternating voltage with respect to the cantilever. Then a periodic electrostatic force is created on the cantilever. Forsen E *et al.* (13) have used the electrostatic actuation in combination with capacitive readout and they also have used it in combination with hard contact read-out (120). Electrostatic actuation can be used with dielectric materials such as silicon nitride or polymers where an inhomogeneous electric field produces a net force acting on a dielectric mirco- or nano-beam (121-124). In thermal actuation, a bimorph cantilever is heated in pulsed manner using an integrated resistive heater (125) or an external laser (126). In

magnetomotive actuation a static magnetic field is applied perpendicular to a cantilever through which an alternating current flows. The Lorentz forces cause the cantilever to deflect. This technique requires large magnetic fields and low temperature and has recently been used in mass detection using nanometre-sized cantilevers (127).

2.5 Applications of micro/nanomechanical resonators

2.5.1 Material characterization

Material characterization is one of the important applications of the cantilever sensors. It is necessary to know the material properties first in order to seek a successful design. One of the standard mechanical material tests is uniaxial tension test to measure properties such as Young's modulus and fracture strength of the cantilever. However, the fracture strength test is not suitable for the characterization of thin film materials because they are very fragile and difficult to handle and align. Designing integrated micromechanical test structures such as membranes and cantilevers is one solution. The Young's modulus of the material can be extracted from resonant frequency measurements, if the dimensions (length and width) of the cantilever are known by referring to the equations (3.22 b). Resonant microcantilevers have been used to determine Young's modulus of thin films since 1979 (128). In addition, a variety of other micromechanical material tests were demonstrated in review papers (129, 130).

The cantilever sensors enable characterising the material at small length scales. Materials show a different behaviour if scaled down and bulk property values are no longer valid. From an engineering point view, it is important to investigate the mechanical properties of micromechanically fabricated cantilevers to design robust nanomechanical devices.

In 2003, Li *et al.* (15) fabricated ultrathin single-crystalline-silicon cantilevers by photolithography and measured their Young's modulus with resonant detection. Their results

show that when the thickness of the cantilever was reduced from 300 nm to 12 nm, the Young's modulus steadily decreased by 30%. At 300 nm, the Young's modulus is the same as the bulk value of 170 GPa. They concluded that for ultrathin single-crystalline silicon, surface effects play an important role by comparison with bulk effects. Nilsson *et al*. (126) fabricated thin chromium cantilevers of various thickness by electron beam lithography, metal lift off and subsequent reactive ion etching. The Young's modulus was measured by static deflection. They found when the thickness of the cantilever decreases from 100 nm to 50 nm, its Young's modulus decreases from 70 GPa to 40 GPa.

By contrast with the above work, which showed a decrease in Young's modulus on the dimension reduces, some work found the opposite trend. In Chen's work (131), they found that the Young's modulus increasing dramatically from 150 GPa to 220 GPa with the diameter of ZnO nanowires ([0001] oriented) decreasing from 120 nm to 17 nm and the Young's modulus increased slowly from 140 GPa to 150GPa when the diameter of the nanowire decrease from 550 nm to 120 nm. It is very important to notice that the experimental value of the Young's modulus of bulk ZnO is only 140 GPa. They concluded the size dependence of Young's modulus is caused by surface effect due to the high surface-to-volume ratio. Cuenot *et al*. (132) also found that the Young's modulus of silver and lead nanowires increase dramatically with the decreasing diameter from 250 nm to 30 nm. The reason is attributed to surface tension effects.

Other measurements report mechanical properties, which are independent of dimensions. According to Wong's (133)static bending measurement with AFM, the Young's modulus of SiC nanorods is about 610 GPa, which agree with the 600 GPa value theoretically predicted. Similarly, Wu *et al*. (134)also used the static bending measurement with AFM to investigate the Young's modulus, yield strength and plastic deformation of gold nanowires. They found that the Young's modulus of gold nanowires is independent of its diameter, but its yield strength increases dramatically with a decreasing diameter and the yield strength are up to

100 times larger than the bulk nanocrystalline metals. According to their analysis, there is a significant reduction in defects and hence a strengthening of the materials happens.

Cantilevers have also been used to characterise polymer thin films. Nagy *et al*. (135) have estimated the Young's modulus of a phenyl substituted polymer spin-coated onto silicon cantilevers. In their work, they have observed changes of secondary transitions and Young's modulus during the conversion of the polymer by means of the resonance method.

With varying temperature, silicon cantilevers with a polymer film coating were measured. Changes of resonant frequency and deflection were observed. The mechanical properties in the vicinity of the glass transition were determined. The temperature dependence of Young's modulus and the volume change of polystyrene and poly were demonstrated. According to Haramina (136), size effects for thin polystyrene layers below 100 nm can be observed and the glass transition temperature was lowered by 10 K as the film thickness was decreased from 100 nm to 7.5 nm. The group of Hierod has fabricated and characterised all-polymer microcantilevers (137). By measuring the quality factor and resonant frequency of cantilevers with different lengths at varying temperatures, first and second phase transition has been observed. In addition, they also determined the temperature dependence of Young's modulus and material ageing by monitoring the resonant frequency over more than 30 days (138).

In terms of material characterisation of nanomechanical resonators, another important application is to measure the density of a deposited mass on the cantilever by measuring the resonant frequency drift. This material of this deposited mass could be different from the cantilever. Nishio *et al*. (11) demonstrated the application of a carbon nanotube resonator to detect mass at the zeptogram-level range, which was deposited by FIB-CVD. By analyzing the Secondary electron intensities induced by an SEM in terms of the oscillation amplitude, the density of the FIB-CVD deposited tungsten was obtained.

Furthermore, the group of Utke (86) took the advantages of this technique by using a silicon cantilever-based mass sensor for in situ monitoring of deposition and milling with focused ion beam and electron beam using the precursor TRIMethly (methycyclopentadienyl) platinum $(CH_3)_3PtCpCH_3$. The resolution of their mass measurement reached the *fg* level by tracking the resonance frequency shift of a temperature stabilized piezoresistive cantilever using phase locking. For FIB/FEB-induced deposition, by measuring the resonant frequency drift as a function of deposition time, the deposition rate and irradiation dose can be obtained. This mass sensing based technique enables to detect for the density evolution of FIB/FEB-induced deposition. For FIB milling, a silicon milling rate of two atoms per ion was measured. Together with the corresponding frequency shift, the mass response and the spring constant of the cantilever can be determined. Utke *et al.* (87) also demonstrated that the dose and energy of the electron beam determined the Young's modulus, density and quality factor of FEB deposited nanopillar using gas precursor of $Cu(C_5HF_6O_2)_2$ by force-deflection measurement and resonant frequency detecting measurement.

In 2001 Fujita *et al.* (21) fabricated diamond-like carbon pillars as resonators with Ga^+ focused ion beam-induced chemical vapour deposition and measured their resonant frequencies using SEM. The Young's modulus of the carbon pillar was extracted from this mechanical measurement and formed to range from 65 to 130 GPa. Furthermore, they also found that the Young's modulus depended on the growth conditions of the ion beam current and gas pressure. With this application of nanomechanical resonators, they can have a better control of the stiffness of the carbon deposition by changing deposition parameters.

2.5.2 Biosensors

In order to enable a cantilever-based sensor to detect specific molecules, it is necessary to coat the cantilever with specific 'detector' molecules first. It is important that only one side of the cantilever is coated because a uniform generation of surface stress on both cantilever

sides will not result in a cantilever deflection. In order to selectively coat cantilevers, different technologies have been developed. A common technology is to first coat the cantilevers with a thin gold layer on one side and then later use thiol-based chemistry to bind the probe molecules strongly to the gold surface. It is well known that the quality of the evaporated gold has a high influence on the size and signature of the generated signals. For the silicon surface, silane coupling chemistry is often used and for polymer cantilevers, epoxy groups are used (139).

Both whole bacteria and segments of bacteria can be caught directly on a cantilever sensor. For instance, a cantilever coated with antibodies against E.coli will specifically bind to E.coli. In 2001, Craighead *et al*. (2), one of the first groups, reported the bacteria detection and showed the mass detection of E.coli bacteria. In 2003, bacteria of Salmonella enteric were detected by monitoring the change in surface stress upon binding of bacteria on the cantilever. If the sensor is expanded to contain several cantilevers and each coated with a specific antibody, it is possible to detect multiple bacteria simultaneously. Fundamental researches showed that the position of bacteria on the cantilever affects the mass signal generated (140, 141). The fundamental research included analysing the resonant frequency shift for bacteria positioned on different positions along the cantilever sensor and operating the cantilever at its different resonance mode. The results showed that both the added mass and the resulting change in stiffness of the cantilever determined the mass signal. If a bacterium adsorbs on regions of high vibration amplitude, the added mass will be the main reason for the resonant frequency shift. If the bacterium is positioned at a nodal point or a clamped end of the cantilever, the change in stiffness will dominated the resonant frequency change. Therefore either the stiffness effect or the mass change can be employed for biosensors. The general problem for the resonators operated in liquid is damping, which reduce the sensitivity significantly. A well-developed sophisticated system for single cell detection has been designed by Manalis *et al.* (142).

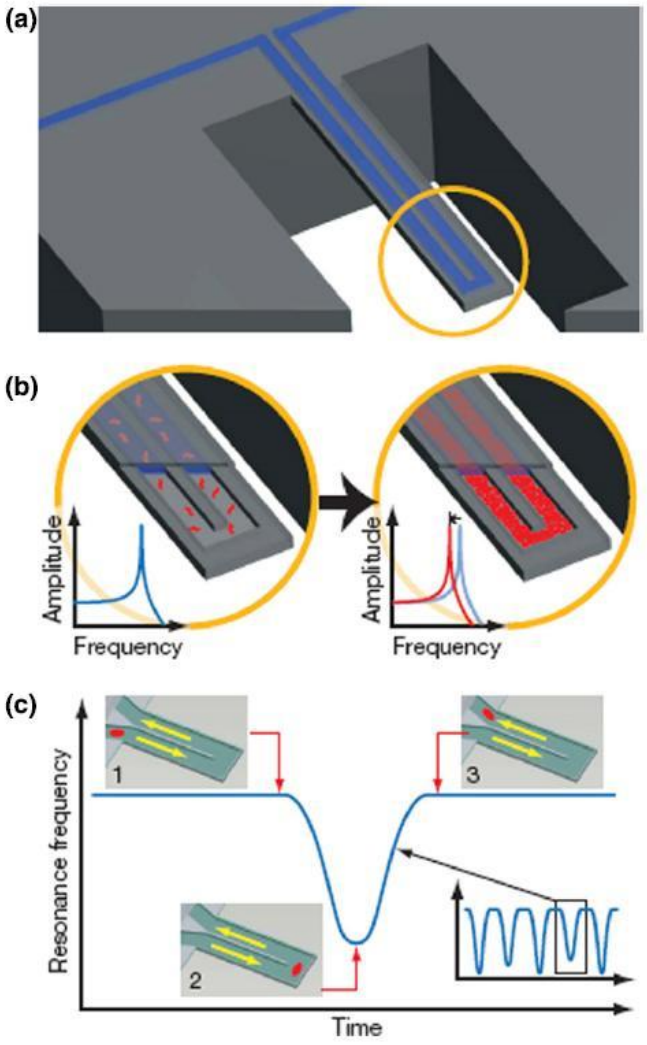

Figure 2. 5: Schematic diagram of a hollow cantilever (*a*) A hollow cantilever detects mass changes by detecting its resonance frequency shifting. Fluid continuously flows to deliver biomolecules. Sub-femtogram mass resolution is attained under high vacuum. (*b*) Specific detection was obtained by way of immobilized receptors of the cantilever channel. (*c*) The observed signal depends on the position of particles along the channel (insets 1-3). The exact mass of a particle can be quantified by detecting the frequency shifting. Images taken from Ref. (58).

This system removed the damping problem by flowing liquid inside the cantilever. Therefore, the cantilever sensor can work in vacuum and the liquids can be analysed at the same time. In order to detect the avidin binding in the beginning, they flushed the inner channel walls with biotinylated bovine serum albumin. They monitored the resonant frequency shift when the avidin is flushed through the system and binds to the functionalized walls. Manalis'

group demonstrated single E.coli cell detection in 2007 (27). Figure 2.5 is the schematic diagram to show their device and its operation. When a buffer solution with E.coli runs through the cantilever sensor, the resonant frequency shift is measured continuously. The mass of an E.coli cell was found to be 110±30 *fg* by plotting the resonant frequency change in a histogram.

2.5.3 Additional applications

Drug discovery, as one of the applications of cantilever sensors, is new and interesting. About drug discovery, it is essential to study membrane proteins, which are important targets for new medicine. In 2009, the group of Hegner *et al.* (143) demonstrated cantilever sensor can work for the binding interaction between specific membrane proteins and the bacteriphage T5. They found that even if the cantilevers are subsequently exposed to a buffer, the resonant frequency remains unchanged. This means an irreversible nature of the binding of the phages happened. It is the first to discover that the cantilever could be a useful tool for drug screening and also measuring cell's mechanical response to drug treatment. The cantilever sensor can also be used to study the interaction between antibiotics and bacterial cell wall precursor analogues (144).

As a detector of explosives, cantilever sensors are highly suitable for use in anti-terror efforts, boarder control, environmental monitoring and demining (145) (146, 147). The cantilever sensors rely on specific receptors for binding of explosives or on specific properties of the explosives such as phase transitions. Due specific receptors for explosives detection are difficult to achieve, different types of receptor need to be explored. The cantilever can be highly sensitive to temperature changes and can thus be used for photothermal deflection spectroscopy (148-150). The principle is when the material absorbs a photon, a fraction of the energy may be transformed into heat. Then a measurement of photothermal heating as a function of wavelength can provide an absorption spectrum of the material. Basically, they

detected heat changes of the order of picojoules in the investigation of fluorecein molecules by using a silicon cantilever with a thin layer of aluminium coating.

Chapter 3 Classical Theory of Mechanical Resonators

This chapter presents theory details, including determining the static mechanical properties of both singly- and doubly-clamped beams, determining the dynamic mechanical properties of cantilever-based resonators, including the natural resonant frequencies, *Q*-factor *etc*.

3.1 Theory of static mechanical properties

The fundamental theory of static mechanical properties of both singly- and doubly-clamped beams is commonly found in many textbooks. Here we will follow the text book from Warren Young (151). To review the beam theory, the simple beam is defined as a single component of a machine or structure. Its length of beam is assumed to be much longer than its width or thickness. Additional assumptions include:

(1) The beam is of homogeneous material, which has the same modulus of elasticity in tension and compression.

(2) The beam is straight or nearly so; if it is slightly curved, the curvature is in the plane of bending and the radius of curvature is at least 10 times the depth.

(3) The cross section of the beam is uniform.

(4) The beam has at least one longitudinal plane of symmetry.

(5) All loads and reactions are perpendicular to the axis of the beam and lie in the same plane, which is a longitudinal plane of symmetry.

(6) The beam is long in proportion to its depth, the span/depth ratio being 8 or more for metal beams of compact section.

(7) The quantify statement about beam is not disproportionately wide.

(8) The maximum stress does not exceed the proportional limit.

It is necessary to follow the above assumptions to make sure the formulas are valid.

3.1.1 Beam bending behaviour

The bending of the beam makes its convex side lengthened and its concave side shortened. The neutral surface is normal to the plane of the loads and contains the centroids of all sections, therefore the neutral axis of any section is the horizontal central axis. Plane sections remain plane, and hence the strains and stresses of each beam unit are proportional to its distance from the neutral surface. It is supposed that longitudinal displacements of points on the neutral surface are negligible. Due to beam bending, its vertical deflection is large. Here the shearing is negligible.

At any point a longitudinal fibre stress σ occurs. This stress can be tensile if the point lies between the neutral and convex surfaces of the beam. This stress turns to be compressive if the point lies between the neutral and concave surfaces of the beam. This fibre stress σ usually is assumed uniform across the width of the beam.

At any point a longitudinal shear stress τ on the horizontal plane and an equal vertical shear stress on the transverse plane occur. Due to the transverse beam forces, these shear stresses usually are assumed uniform as well across the width of the beam.

3.1.2 Beam bending formulas

Figure 3.1 represents a beam under loading and shows the various dimensions that appear in the formulas; Figure 3.1(c) shows a small stress element at a point *q* acted on due to the stresses σ and τ. The moment of inertia of the section of the beam with respect to the neutral axis is *I* and the modulus of elasticity of the material is *E*.

Hence the fibre stress σ at any point *q* is

$$\sigma = -\frac{My}{I} \tag{3.1},$$

where *M* is the bending moment at the point *q*, and *y* is the vertical distance from the neutral axis to *q*.

The shear stress τ at any point *q* is

$$\tau = \frac{VA'\bar{y}}{Ib} \tag{3.2},$$

where *V* is the vertical shear at at the point *q*, *A'* is the area of that part of the section above (or below) *q*; $\bar{y}$ is the distance from the neutral axis to the centroid of *A'*, and *b* is the net breadth of the section measured through *q*.

The radius of curvature *r* of the elastic curve at any section is

$$\rho = \frac{EI}{M} \tag{3.4},$$

where *M* is the bending moment at the section in question.

The differential equation of the elastic curve is

$$EI\frac{d^2y_c}{dx^2} = M \tag{3.5},$$

where y_c is the vertical deflection of the centroidal axis of the beam. Solution of this equation for the vertical deflection y_c is affected by the bending moment *M* and the boundary

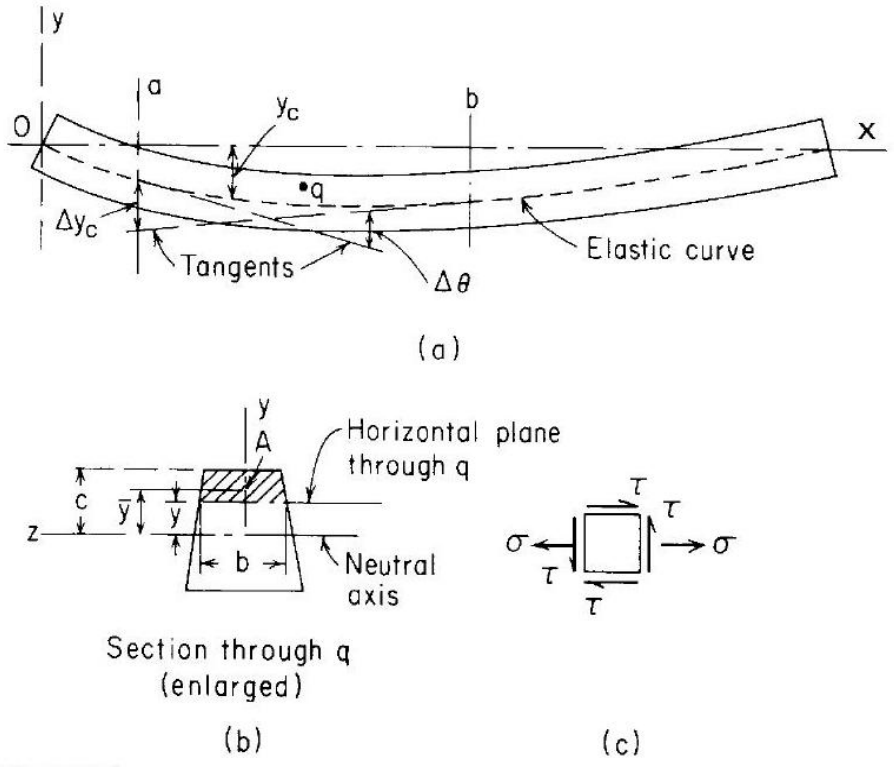

Figure 3. 1: A beam under load. Image taken from ref.(151)

conditions. Therefore the vertical deflection y_c at any point is found to be

$$y_c = \int \frac{Mm}{EI} dx \qquad (3.6),$$

where m is the equation of the bending moment due to a unit load acting vertically at the section where y_c is to be found.

A Positive results for y_c means that the deflection is in the direction of the assumed unit load; a negative result means it is in the opposite direction.

The change in slope of elastic curve $\Delta\theta$ (radians) between any two sections a and b is

$$\Delta\theta = \int_a^b \frac{M}{EI} dx \qquad (3.7).$$

The deflection Δy_c at any section a, measured vertically from a tangent drawn to the elastic curve at any section b, is

$$\Delta y_c = \int_a^b \frac{M}{EI} x dx \tag{3.8},$$

where x is the distance from a to any section dx between a and b.

The relationship between the bending moment and shear equations is

$$V = \frac{dM}{dx} \tag{3.9}.$$

$$M = \int V dx \tag{3.10}.$$

These relations are useful in constructing shear and moment diagrams and locating the section or sections of maximum bending moment since Eq. (3.9) shows that the maximum moment occurs when V, its first derivative, passes through zero and Eq. (3.10) shows that the increment in bending moment that occurs between any two sections is equal to the area under the shear diagram between those sections.

3.1.3 Determining the mechanical properties of doubly-clamped beams

Based on equation (3.8), the vertical deflection y_c of the doubly-clamped beam applied by a point load, as seen in Figure 3.2, can be calculated as the equation (3.11).

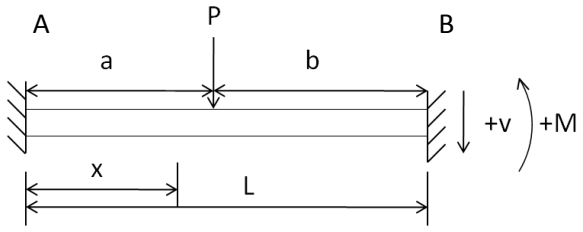

Figure 3. 2: Schematic diagram of doubly-clamped beam

Boundary conditions for the doubly-clamped beam are:

$$\theta_A = 0, y_A = 0, \theta_B = 0, y_B = 0$$

According to equation (3.8), the deflection at the point loading is

$$y_c = \frac{P}{6EI}\left[\frac{b^2x^3}{L^3}(L+2a) - \frac{3ab^2x^2}{L^2} - 3(x-a)^3\right] \quad (3.11).$$

By considering the deflection at the point where the load is applied, $P = -ky_c$ and $x = a$. So we can obtain the Young's modulus by simplifying the equation 3.11:

$$E = \frac{k(L-a)^3a^3}{3IL^3} \quad (3.12),$$

where I is the moment of inertia, which depends on the shape of cross section of the beam. For a beam with a circular cross section, its moment of inertia is $I = \frac{1}{4}\pi r^4$; For a beam with a rectangular cross section, its moment of inertia is $I = \frac{ab^3}{12}$, where a is the length and b is the width of the rectangle.

3.1.4 Determining the mechanical properties of singly-clamped beams

Based on equation (3.8), the vertical deflection y_c of the singly-clamped beam, as seen in Figure 3.3, can be calculated as the equation (3.13).

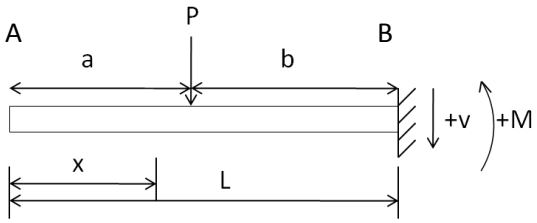

Figure 3. 3: Schematic diagram of singly-clamped beam

Boundary conditions for the singly-clamped beam are :

$$\theta_B = 0, y_B = 0$$

So the deflection at the point loading is

$$y_c = \frac{P}{6EI}\left[3b^2x - 2L^3 + 2L^2a - a^3 - (x-a)^3\right] \quad (3.13).$$

Considering the elastic properties at the loading point, $x = a$ and $P = -ky_c$, and we can obtain the Young's modulus:

$$E = \frac{x^3k}{3I} \quad (3.14).$$

3.2 Theory of dynamic mechanical properties

3.2.1 Natural frequencies of finite beams

The governing equation for transverse beam motion will be developed and the frequency spectrum will be presented. Consider a thin beam undergoing transverse motion, as shown in Figure 3.1. Consider a differential element of the beam as isolated in Figure 3.1 (b). Bending moment *M*, shear force *V*, and variations of these quantities act on the beam element, as well as a distributed force *q*. The basic hypothesis of the Bernoulli-Euler theory of beams was employed. In this theory, the plane cross-section initially perpendicular to the axis of the beam remains plane and perpendicular to the neutral axis during bending. This assumption implies that the longitudinal strains vary linearly across the depth of the beam and that, for elastic behaviour, the neutral axis of the beam passes through the centroid of the cross-section. The relationship between the bending moment and curvature is given by (3.5). The result Eq. (3.5) carries the assumption that slopes and deflections of the beam are small.

Writing the equation of motion in the vertical direction for the element of Figure 3.1 (b), we have

$$-V + \left(V + \frac{\partial V}{\partial x}dx\right) + qdx = \rho A dx \frac{\partial^2 y}{\partial t^2} \quad (3.15),$$

where A is the cross-sectional area of the beam and ρ is the mass density per unit volume. This reduces to

$$\frac{\partial V}{\partial x} + q = \rho A \frac{\partial^2 y}{\partial t^2} \tag{3.16}.$$

Summation of moments is the second equation to be written. If we neglect the rotational-inertia effects of the element, the moment equation is, effectively, that of statics and gives

$$V = \frac{\partial M}{\partial x} \tag{3.17},$$

where the high-order contributions of the loading q to the moment are neglected. Substituting (3.16) and (3.17) gives

$$\frac{\partial^2 M}{\partial x^2} + q = \rho A \frac{\partial^2 y}{\partial t^2} \tag{3.18}.$$

Finally, substituting (3.5) in (3.18) gives

$$\frac{\partial^2}{\partial x^2}(EI \frac{\partial^2 y}{\partial x^2}) + \rho A \frac{\partial^2 y}{\partial t^2} = q(x,t) \tag{3.19},$$

where y denotes the transverse displacement of the beam, x is position on the beam, ρ is the mass density of the nanorod and A is the cross-sectional area. If the loading on the rod is absent (q=0), and the material of the beam is homogeneous, so that the Young's modulus E is constant and, furthermore, the cross-section is constant so that moment of inertia I is constant, then equation (3.19) reduces to the following form:

$$\frac{\partial^4 y}{\partial x^4} + \frac{1}{a^2}\frac{\partial^2 y}{\partial t^2} = 0,$$

$$a^2 = \frac{EI}{\rho A} \tag{3.20}.$$

3.2.2 Solution for special boundary conditions

First let $y = Y(x)T(t)$, and substituting in the equation (3.20), then the solution for *Y*, the vibration amplitude at the free cantilever end, may be expressed as the following form, where *Y*(*x*) is the inverse Laplace transform of function and *T*(*t*) is the translational kinetic energy of the beam,

$Y = D_1(\cos\beta x + \cosh\beta x) + D_2(\cos\beta x - \cosh\beta x) + D_3(\sin\beta x + \sinh\beta x) + D_4(\sin\beta x - \sinh\beta x)$ (3.21).

For clamped-free beams, the boundary conditions imposed are zero displacement and slope at the clamped end, and vanishing external torque and shear forces at the free end.

$$Y(0) = \frac{dY(0)}{dx} = 0, \quad \frac{d^2Y(l)}{dx^2} = \frac{d^3Y(l)}{dx^3} = 0$$

where *l* is the length.

It is found that D_1=D_3=0 with the frequency equation being given by $cos\beta l cosh\beta l = -1$. The dimensionless eigenvalue $\beta_n l$ of the nth flexural resonance mode can be calculated numerically (152).

The first few roots are

$$\beta_1 l = 1.875, \beta_2 l = 4.694, \beta_3 l = 7.855, \beta_4 l = 10.96, \beta_5 l = 14.137, \beta_6 l = 17.278$$

As $\beta_n^4 = \frac{\omega_n^2}{a^2}$, $\omega_n = \beta_n^2 a$,

$$f_n = \frac{\beta_n^2 a}{2\pi} = \frac{\beta_n^2}{2\pi}\sqrt{\frac{EI}{\rho A}} \qquad \text{(3.22 a),}$$

Hence, for the fundamental resonant frequency f_1 is:

$$f_1 = \frac{1.875^2}{2\pi l^2}\sqrt{\frac{EI}{\rho A}} \qquad (3.22\ b).$$

3.2.3 Beams with elliptical cross-section

For beams with an irregular cross-section, there exist nearly orthogonal modes with distinct natural frequencies. A finite beam with an elliptical cross section, as shown in Figure 3.4, has two orthogonal modes (152).

In this case, a pair of eigenfrequencies $f_{n,x}$ and $f_{n,y}$ is predicted from equation (3.22 a):

$$f_{n,x} = \frac{\beta_n^2}{2\pi}\sqrt{\frac{EI_x}{\rho A}} \qquad (3.23\ a),$$

$$f_{n,y} = \frac{\beta_n^2}{2\pi}\sqrt{\frac{EI_y}{\rho A}} \qquad (3.23\ b),$$

where

$$A = \pi ab,$$

$$I_x = \frac{\pi ab^3}{4},$$

$$I_y = \frac{\pi a^3 b}{4}.$$

Therefore, a pair of eigenfrequencies $f_{n,x}$ and $f_{n,y}$ is defined as following:

$$f_{n,x} = \frac{\beta_n^2 b}{4\pi}\sqrt{\frac{E}{\rho}} \qquad (3.24\ a),$$

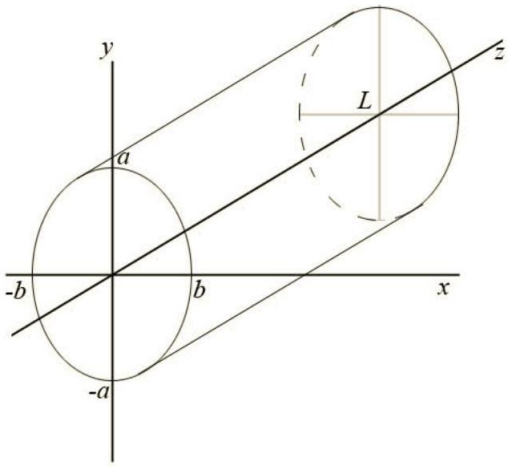

Figure 3. 4: An elliptical cross section of a beam (The elliptical beam has a length *l* along the z-axis, a semi-major axis of length *a* along the y-axis, and semi-minor axis of length *b* along the x-axis)

$$f_{n,y} = \frac{\beta_n^2 a}{4\pi}\sqrt{\frac{E}{\rho}} \qquad (3.24\ b).$$

From Eq.(3.24a) and Eq.(3.24b), the ratio of frequency peaks for a finite beam with elliptical cross section is

$$\frac{f_{n,x}}{f_{n,y}} = \frac{b}{a} \qquad (3.25).$$

Hence, the ratio of the resonant frequencies is proportional to the ratio of the length of the axes.

3.2.4 Fundamentals of cantilever-based mass sensor

3.2.4.1 The Point-Mass Model

In order to simplify the cantilever dynamic vibrations, the point-mass model (also called the first mode approximation) was used, as shown in Figure 3.5.

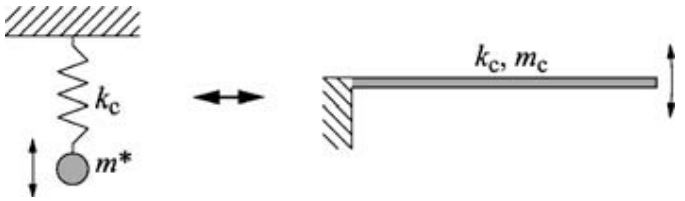

Figure 3. 5: The point mass model for the singly-clamped cantilever with distributed mass (The damping is ignored.) Image taken from (154).

In the point-mass model the cantilever is approximated by a one-degree-of-freedom mass-spring model and the higher-order flexural modes are neglected. The distributed cantilever mass is replaced by an effective point mass $m*$ attached to a massless spring with stiffness k_c.

Therefore the fundamental resonance frequency f_1 of the free cantilever equals the point-mass resonance frequency (153):

$$f = 2\pi\sqrt{\frac{k_c}{m^*}} \tag{3.26}$$

The spring constant k_c of a rectangular cantilever is

$$k_c = \frac{Eb^3a}{4L^3} \tag{3.27}$$

The fundamental flexural vibration frequency is obtained from Eqs (3.24 b) by setting n=1:

Now $m*$ can be calculated directly from Eqs (3.26) and (3.27):

$$m^* = \frac{k_c}{\omega_1^2} = \frac{3LA\rho}{1.875^4} \approx \frac{1}{4}m_c \tag{3.28}$$

The effective mass $m*$ of a cantilever with a rectangular cross section is about one quarter of its real mass m_c. This also means that the fundamental resonant frequency of a beam with a mass m_{tip} attached to its end is

$$\omega_{tip} \approx \sqrt{\frac{k_c}{\frac{m}{4} + m_{tip}}} \quad (3.29).$$

3.2.4.2 Dissipation and Quality Factor

In the model of the harmonic oscillator, dissipation can be included in the system by introducing the dimensionless quality factor Q of the resonator which is a description of the total damping. The quality factor of a resonator is inversely proportional to the damping coefficient (155) and is defined as

$$Q = 2\pi \frac{W_0}{\Delta W} \quad (3.30),$$

$$\Delta W = \sum_i \Delta W_i \quad (3.31),$$

where W_0 is the stored vibration energy and ΔW is the total energy lost per oscillation cycle. ΔW_i is the energy lost due to various dissipation mechanisms. The energy loss can be divided into internal damping, external damping and internal friction. The internal damping is caused by the dissipation via coupling to the support structure (i.e. clamping loss). The external damping is due to the molecular, viscous, and turbulent flow of the surrounding media or acoustic radiation. The internal friction results from a variety of physical mechanisms such as motion of lattice defects, thermoelastic dissipation, phonon-phonon scattering etc. Traditionally, internal friction is considered as a bulk (volume) effect, but surface effects can dominate for sub-micron-thick cantilevers or for resonators with very high Q. In high and ultrahigh vacuum conditions external damping is negligible.

We also can write the inverse Q as the sum

$$\frac{1}{Q} = \sum_i \frac{1}{Q_i}$$

$$= \frac{1}{Q_{clamping}} + \frac{1}{Q_{TED}} + \frac{1}{Q_{volume}} + \frac{1}{Q_{surface}} + \frac{1}{Q_{other}} \quad (3.32).$$

Due to low damping, in a vacuum condition, the modal shape solutions *Y(x)* are the same as zero damping (see (3.23)), but the dispersion relation giving the damped eigenfrequencies f_0' in terms of the undamped frequencies f_0 is

$$f_0' = f_0\sqrt{1-\frac{1}{2Q^2}} \tag{3.33}$$

In high and ultrahigh vacuum conditions damping induced shifts are negligible because the quality factors are typically larger than 10000. The steady-state solution of the equation of motion for the forced damped harmonic oscillator leads to the following expressions:

$$A_c = \frac{A_d\omega_0^2}{\sqrt{\left(\frac{\omega_0\omega_d}{Q}\right)^2+\left(\omega_0^2-\omega_d^2\right)^2}} \tag{3.34}$$

$$\varphi = \arctan\left(\frac{\omega_0\omega_d}{Q\left(\omega_0^2-\omega_d^2\right)}\right) \tag{3.35}$$

where A_c is the oscillation amplitude, φ is the oscillation phase, A_d is the driving amplitude and ω_d is the driving frequency.

It is clear from (3.34) and (3.35) that if $Q \gg 1$, the amplitude goes up to the maximum value at the frequency where the oscillation has a 90^o phase lag relative to the excitation. However, this does not generally occur at higher damping conditions (such as in air and water). In practice the quality factor can be determined either from the full width at half maximum (FWHM) of the squared amplitude peak or from the phase variation dφ/df at its resonance (see (3.35)) according to

$$Q \approx \frac{f_0}{FWHM} = \frac{f_0}{2}\frac{d\varphi}{df} \tag{3.36}$$

3.2.4.3 Mass Loading

The resonant mass sensor is operated by providing a shift in its resonance frequency Δf due to the added mass Δm as shown in Eq (3.37). Here two extreme cases shown in figure 3.6 will be discussed: homogeneous surface coverage loading and point-mass loading:

$$\Delta m = \frac{k}{4\pi^2}\left(\frac{1}{f_1^2} - \frac{1}{f_0^2}\right) \tag{3.37},$$

where Δm is the change in mass, f_0 is the initial resonant frequency, and f_1 is the resonant frequency after mass adhesion.

Homogeneous Mass Loading

Assuming that the added mass Δm is a small fraction of the cantilever mass m_c and the loading mass is distributed homogeneously upon the surface of the cantilever as shown in Figure 3.6 (a), the resonant frequency response can be written as

$$R = \frac{\Delta f}{\Delta m} = -2\pi^2 n_e \frac{f_0^3}{k_c} = -\frac{1}{2}\frac{f_0}{m_c} \tag{3.38}.$$

This expression is under the conditions that the cantilever stiffness EI, surface stress, and damping are not significantly affected by the added homogeneous mass. This equation also works if the added species forms a film without significant intra cross-linking and bonding to the cantilever surface rigidly. Hence, the frequency response given by Eq (3.38) for a homogeneously loaded mass depends on the active sensor area.

Point-Mass Loading

Instead of distributing the added mass evenly on the surface of the cantilever, the added small mass can be located on a precise position of the cantilever as shown in figure 3.6 (b). Here, we only think the simplest situation, which is the point-mass loaded at the free end of

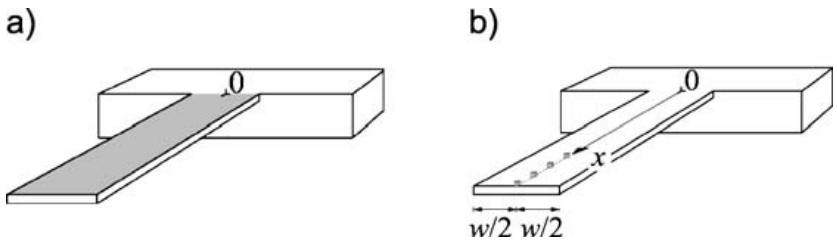

Figure 3.6: Cantilevers with mass loading (a) homogeneous surface loading (b) Point-mass loading. Image taken from (154)

the cantilever. For the point-mass loading, the mass response of the cantilever resonant sensor can be considered as constant. Therefore the response of the cantilever at its resonant frequency, after loading a point mass at the free end, is defined as:

$$R = \frac{\Delta f}{\Delta m} = -2\pi^2 \frac{f_0^3}{k_c} = -\frac{1}{2n_e}\frac{f_0}{m_c} \qquad (3.39).$$

In this situation, SEM imaging readout system has advantage of determining the volume of the point-mass at microscaled with a very high resolution.

3.2.4.4 Detection limits

The limitations of microscale cantilever sensors are determined by the ratio of their sensitivity to the level of intrinsic noise. The minimum detectable frequency shift $\delta f_{\min}$ of the measuring system determines the minimum detectable mass changes as $\delta m_{\min} = \delta f_{\min} R^{-1}$. The reason is that noise and drift sources from the environment and measuring systems are involved, such as temperature instability. From an engineering point of view, these noise and drift can be minimized in a carefully designed measurement setup. The problems of the intrinsic noise mechanisms which determine the ultimate fundamental limits set by the thermomechanical noise, will not be discussed here. By referring to (99), the minimal detectable relative frequency shift is:

$$\frac{\delta f}{f_0} = \frac{1}{A_c}\sqrt{\frac{2\pi k_B TB}{f_0 k_c Q}} \quad (3.42),$$

where $k_B T$ is the thermal energy and B the measurement bandwidth. Eq (3.42) shows that thermomechanical noise is dependent on the dissipation Q^{-1}, which contributes the high-resolution operation in a vacuum. The measurement bandwidth is determined by the minimum noise level and the maximum measurement response. Eq (3.42) also shows that increasing the vibration amplitude of the cantilever sensor is helpful to reduce the thermomechanical noise.

3.2.4.5 Sensor scaling

The limitation of mass sensing detection can be reduced by scaling down the dimension or choosing different materials of the mass sensor. The relationship between dimensions and material properties, resonance frequency, sensitivities, and the mass resolution at the thermomechanical noise limit are shown in Table 3.1.

It can be seen in table 3.1 that if the size of a cantilever is reduced proportionally by a scaling factor of a ($a < 1$), the sensitivity will increase by a factor of a^{-4} and the mass resolution at the thermomechanical noise limit will decrease by a factor of a^{-3}. If a reduction of the cantilever length is bl ($b < 1$) and an increase of its height to cl ($c > 1$), the sensitivity will increase by a factor of b^{-3} and the mass resolution at the thermomechanical noise limit will decrease by a factor of $(b^7 c^{-2})^{1/2}$. Therefore reducing both the size of the cantilever and the l/h ratio can improve the sensing ability through increasing of its resonance frequency by a factor a^{-1} and $b^{-2}c$, respectively.

In addition, the materials of the cantilever affect its sensing ability as well. From Table 3.1, it can be seen that a high stiffness-to-density ratio contributes to a high resolution sensitivity of the mass sensor.

Table 3.1 Scaling laws of rectangular cantilever mass sensors for point-mass loading. (For homogeneous loading, the responsivity *R* must be divided by the active area)

Spring constant	$kc \propto l^{-3} w h^3 E$
Resonant frequency	$f_0 \propto l^{-2} h \sqrt{E \rho^{-1}}$
Sensitivity	$R \propto f_0 m_c^{-1} \propto l^{-3} w^{-1} \sqrt{E \rho^{-3}}$
Mass resolution	$\delta f R^{-1} \propto \sqrt{l^7 w h^{-2}} \sqrt{E^{-3/2} \rho^{5/2}}$
at the thermomechanical noise limit	

Chapter 4 Experimental Procedures

This chapter presents experimental details, including background of experimental techniques, sample preparation and measurement of physical properties. First the fabrication of doubly- and singly- clamped beams with FIB, including free standing nanorod growth and trench milling, is presented. Static mechanical measurement of the Young's modulus of C-W-nanorods with AFM is then discussed. Finally in this chapter the dynamic mechanical measurement of the resonant frequency of C-W-nanorods with SEM is described.

4.1 Focused Ion Beam operating principles

A focused ion beam system may combine three parts: Scanning Electron Microscope (SEM), Focused Ion Beam (FIB) and Gas Injection System (GIS). The system has been produced commercially since the 1980s as a tool mainly geared toward the semiconductor growth industry (156). FIB is powerful for modifying a surface locally at micron and submicron dimensions or fabricating nanoscale structures in three dimensions. Applications include photomask repair, circuit restructuring, and transmission electron microscopy (TEM) sample preparation. The focused gallium ions in the FIB system are used to remove material with a very high spatial precision and the cross sections can be designed in various shapes and made at a specific location. The most popular ion source used today is the liquid-metal ion source. This consists of a reservoir of liquid metal. The liquid-metal is fed from here to a sharpened needle, usually tungsten. The ion species used almost exclusively in the

applications we are considering here is Ga^+. The ions are accelerated and focused into a beam by an electric field. They are subsequently passed through apertures and scanned over the sample surface. In addition, Helium ion beam was developed in the past few years. With this ion source, its imaging resolution can go up to subnanometer, while focused gallium beam only has an imaging resolution of 5 nm. A neon gas field ion source was recently pursued as the source of positive ions for FIB due to its small energy spreads (~1 eV) and a virtual source size of ~2 nm and less contamination.

The FIB system has four basic functions: milling, deposition, implantation, and imaging. Milling is a process that digs into the sample surface as a result of the use of relatively heavy ions in the beam. The FIB system can be converted into a deposition system simply by adding a gas delivery device that allows the application of certain materials, usually metals, to the surface of the material where the beam strikes. The combined process of milling and deposition of FIB can be used to fabricate many nanostructures. More details about the milling and deposition of FIB are discussed in the following.

Imaging: As illustrated in figure 4.1 (a), during FIB imaging the finely focused ion beam is raster scanned over a substrate, and secondary particles (neutral atoms, ions and electrons) are generated in the sample. As they leave the sample, the electrons or ions are collected with a biased detector. The detector bias is a positive or a negative voltage, for collecting secondary electrons or secondary ions, respectively. The secondary ions that are emitted can be used for secondary ion mass spectroscopy (SIMS) of the target material in a mass spectrometer attached to the system.

Milling or sputtering: In focused ion beam milling, physical sputtering of sample material is achieved by using a high-current gallium ion beam, as illustrated schematically in figure 4.1 (b). By scanning the beam over the substrate, an arbitrary shape can be milled. Sputtering occurs when the energy transfer E_{max} is greater than wE_s, where E_s is the surface binding

energy often inferred from the sublimation energy per atom. Based on other people's experiments, the pre-factor was found to vary between w=1 and 6.7 according to the mass

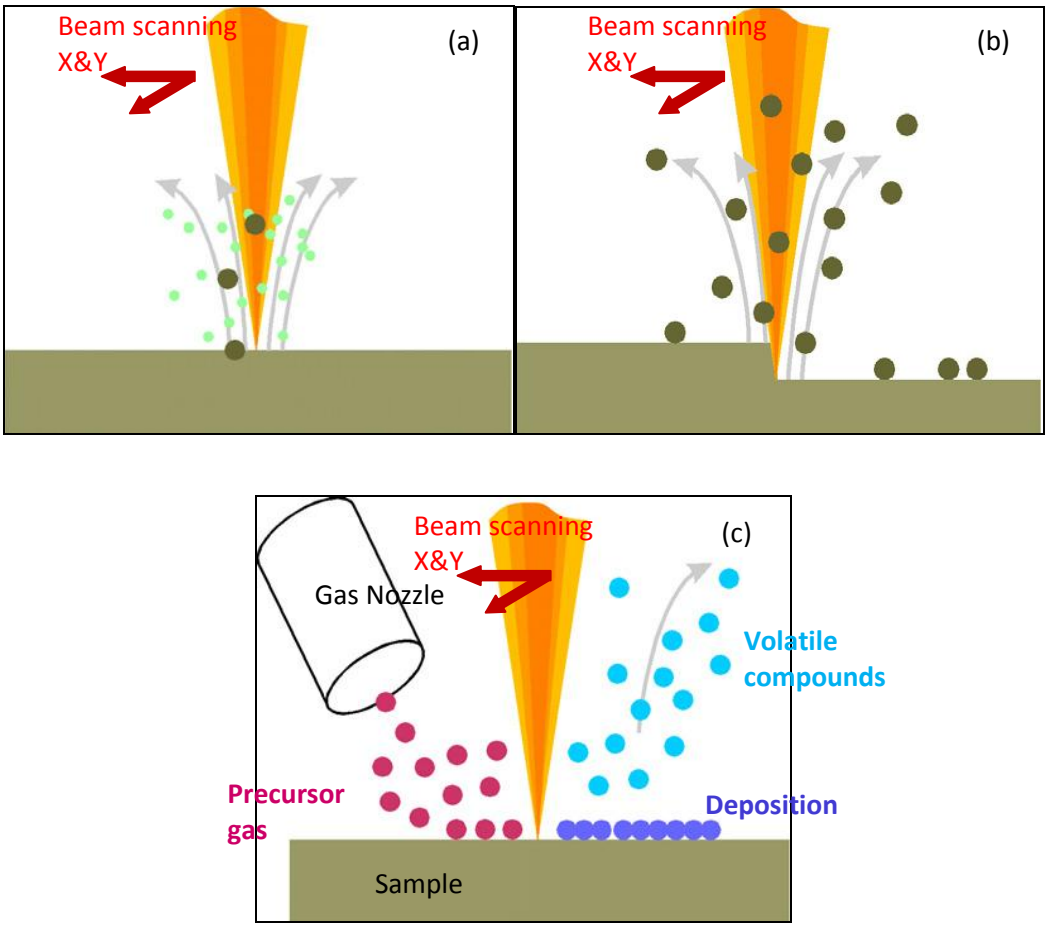

Figure 4. 1: Schematic program of FIB operating principle ((a) Schematic representation of FIB imaging (b) Schematic representation of FIB milling (c)Schematic representation of FIB induced deposition) Image taken form (158)

ratio of ion and target atom (157). The fundamental quantity that describes the milling rate at a given ion current is sputter yield, i.e., the average number of substrate atoms or molecules removed from the surface by each incident ion. The relation of the sputter yield Y_s in units of removed volume per unit charge (often given in $\mu m^3/nC$) is $R_s=Y_sM/(\rho N_A e_0)$, where R_s is the sputtering rate, N_A is the Avogadro's constant, e_0 is the elementary charge, and M and ρ are the molar mass and density of the sputtered material. However, the sputtering yield or rate can not always be easily measured because of complications including the angle of ion

incidence on the surface, re-deposition of sputtered material and the temperature dependent ion-surface interaction. The sputtering yield depends on various parameters of the incident ions (mass, energy, dose rate, angle of incidence, and clustering), target materials (masses and fractions of atoms, crystallinity, crystal orientation, surface binding energies, conductivity, surface curvature), and so on. In order to speed up the milling process, or to increase the selectivity towards different materials, an etching gas can be introduced into the work chamber during milling. This will increase the etching rate and the selectivity towards different materials by chemically facilitating the removal of reaction products. This technique is called gas-assisted etching (GAE). The choice of etching gas depends on the target materials (159).

Deposition: Gas assisted deposition is direct deposition by the focused ion beam in the presence of a gas and takes place in a very localised area where the controlled ion beam is scanning. The gas-assisted FIB-induced deposition process can be finished in three steps: first, a gas precursor is heated and introduced through the gas nozzle located close to the surface and adsorbs on the surface of the sample; second, the gas molecules adsorbed on the surface are decomposed into non-volatile products and volatile products by the incident energetic ion beam where the focused ion beam is scanning. Simultaneously, the ion beam's energy results in sputtering of the sample surface. Third, the non-volatile products remain on the surface, producing deposition layers, while the volatile components, such as oxygen and hydrogen, leave the surface.

The 2nd step mentioned above shows the mechanism of precursor breakdown. The secondary electrons also have effect on the structure fabricated by focused ion beam induced deposition. After the precursor gas is injected to a local surface by a tube-based injection system, energetic gallium ions will interact with the gas molecules adsorbed on sample surface via desorption, dissociation and reaction of the molecules with the substrate materials. The gallium ions also crack the substrate surface, which generate secondary electrons and excited

surface atoms from the substrate surface. According to (160, 161), the excited surface atoms dominate focused ion beam induced deposition. If the gas molecule is [$W(CO)_6$], the conducting deposition of a mixture of tungsten, carbon and gallium will be generated. The distribution of focused ion beam on a plane surface is well described by a Gaussian (162). Its FWHM is only 7 nm, which enables the deposited structure in nanosize. However, the minimum size of the structure extends to 70 nm (162). The reason is that the flux distributions of the emitted secondary and the excited surface atoms determine the minimum dimensions of the structures (163). The focused ion beam induced deposition fabricated freestanding nanowire is popular with its application as mass sensors. However, it is common to see needle-like pins along the sidewall of the nanowire (164, 165). Scattered gas molecules, ionized gas molecules generated during collisions between incident ions and molecules and also secondary electrons possibly attach on the side wall as nuclear seeds and lead to the growth of needle-like pins.

Although focused ion beam induced deposition has advantages to fabricate nanostructures, the atomic proportion of the deposited structure is not well controlled. The ion beam energy spectrum and its radial distribution dominate the purity of focused ion beam induced depositions (163). Besides, ion dose also affect the purity of the deposition. Holye *et al*. (166) found a higher irradiation dose can form a tungsten-rich product and a lower irradiation dose forms a carbon-rich product by focused electron induced tungsten deposition. Chiang *et al*.(167) used a model to describe the composition of product fabricated by Ar^+ beam induced deposition. They realised a higher ion flux contribute to a higher carbon impurity fraction. This reason is that in the case of high dose, each molecule collides with a larger number of electrons or ions, which leads to more CO ligands.

For the calculation of the FIB-induced deposition rate R in the steady state, an additional physical sputter term Y_S must also be taken into account:

$$Y_{net} = Y_D - Y_S \tag{4.1},$$

$$Y_D = n \cdot \sigma \tag{4.2},$$

$$Y_{net} = R/(f \cdot V) \tag{4.3},$$

$$R = (n \cdot \sigma - Y_S) \cdot f \cdot V \tag{4.4},$$

where Y_{net} is the net deposition yield, Y_D is the chemical deposition, Y_S is the physical sputter yield, n is the number of adsorbed molecules per unit surface area, σ is the energy dependent ion impact dissociation cross section (ion impact dissociation leads to deposition of non-volatile fragments), V is the volume of molecules deposited, and f is the ion flux distribution which can be measured independently.

Since deposition can be measured straightforwardly, we can attempt to solve the above equations for the unknown parameter (n) by using the steady state model without diffusion as follows:

From equation (4.4) the chemical deposition rate R' is developed:

$$R' = n \cdot \sigma \cdot f \cdot V \tag{4.5}.$$

For steady state, dn/dt=0, and the adsorption rate equation is

$$\frac{dn}{dt} = sJ\left(1 - \frac{n}{n_0}\right) - \frac{n}{\tau} - n\sigma f + D\Delta n \tag{4.6},$$

$sJ(1-\frac{n}{n_0})$ is the rate of adsorption (J is precursor molecule flux, and s is the sticking probability), $\frac{n}{\tau}$ is the rate of desorption (τ is the residence time), $n\sigma f$ is the rate of dissociation, and $D\Delta n$ is the rate of diffusion (D is the surface diffusion coefficient).

If we neglect surface diffusion for simplicity, the molecule density in the irradiated area is

$$n = \frac{sJ}{\frac{sJ}{n_0} + \frac{1}{\tau} + \sigma f} \tag{4.7},$$

then the chemical deposition rate is

$$R' = \frac{sJ}{\frac{sJ}{n_0} + \frac{1}{\tau} + \sigma f} \cdot \sigma f V \tag{4.8}.$$

Therefore, the FIB-induced deposition rate is

$$R = \left(\frac{sJ}{\frac{sJ}{n_0} + \frac{1}{\tau} + \sigma f} \cdot \sigma - Y_S \right) f V \tag{4.9}.$$

In order to improve the chemical deposition rate, the precursor is required to have sufficient sticking probability to remain on the surface long enough before it is decomposed. It is also required to be decomposed easily by the incident energetic ion beam. Also, the precursor molecule flux (gas pressure) needs to be high enough. Therefore, the deposition conditions can be optimized using controllable system parameters such as the properties of precursor gases, gas flux (needle location, the heating temperature of the gas), ion beam current, dwell time, beam overlap, and beam scanning area (168).

4.2 AFM operating principle

The atomic force microscope (AFM) is a member of the scanning probe microscope (SPM) family. SPM was founded with the invention of the scanning tunnelling microscope (STM) in 1982 (169). Four years later, Binning *et al*. (33) announced the birth of the AFM, which

then became commercially available in the early 1990's. Scanning probe microscopes form images of surfaces using a physical probe that scans the specimen. An image of the surface is

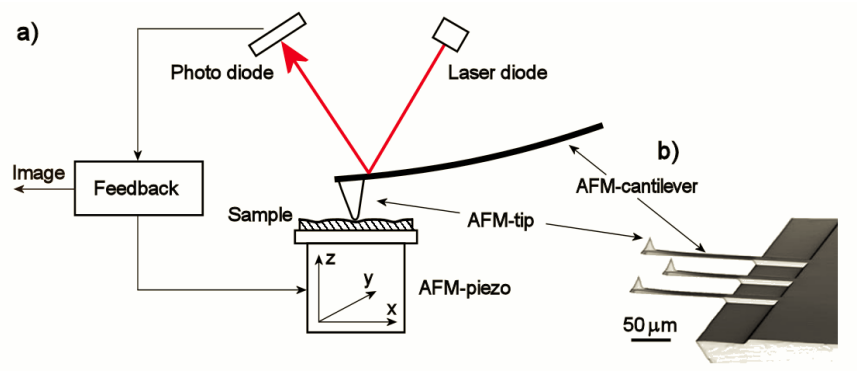

Figure 4. 2: Schematic diagram of AFM operation principle from (170)

obtained by mechanically moving the probe in a raster scan of the specimen, line by line, and recording the probe-surface interaction as a function of position. The maximum resolution depends on the sharpness of the probe tip and the accuracy with which the sample can be positioned relatively to the probe. SPM's are able to achieve atomic resolution. The principles of how an AFM works are very simple. An atomically sharp tip is scanned over a surface with feedback mechanisms that enable the piezo-electric scanners to maintain the tip at a constant force (to obtain height information), or height (to obtain force information) above the sample surface (Figure 4.2). The AFM head employs an optical detection system in which the tip is attached to the underside of a reflective cantilever. A diode laser is focused onto the back of the reflective cantilever. As the tip scans the surface of the sample, moving up and down with the contour of the surface, the laser beam is reflected off the cantilever into a photodiode. The photo-detector measures the difference in light intensities between the upper and lower parts of the photo-detector, and then converts this to voltage. Feedback from the photodiode difference signal, through software control from the computer, enables the tip to maintain either a constant force or constant height above the sample.

4.2.1 AFM operational modes

Many AFM operational modes have been developed to extend the microscope's field of application, such as contact mode, non-contact mode, tapping mode. Here, the two most common modes are illustrated, which both work in air and an aqueous medium (171).

Contact mode: The tip is in constant contact with the sample. It is attached to the end of a cantilever with a spring constant. As the scanner gently traces the tip across the sample (or moves the sample under the tip) the contact force causes the cantilever to bend and the z-feedback loop works to maintain a constant cantilever deflection. Topographical information with lateral resolution of <1 nm and height resolution of <0.1 nm is possible.

Intermittent contact (tapping) mode: This mode maps topography by lightly tapping the surface with an oscillating probe tip. The cantilever of choice for this mode is one with a high spring constant (>5 N/m) so that it does not stick to the sample surface at small amplitudes. Furthermore, a high spring constant increases the resonant frequency, and thus makes the motion of the lever generally faster and less noisy. The cantilever's oscillation amplitude changes with sample surface topography, and the topographic image is obtained by monitoring these changes and closing the z-feedback loop to minimize them. This mode guarantees accurate topographical information even for very fragile surfaces; 5 nm lateral and <0.1 nm height resolution are achievable.

4.2.2 Force-displacement curve

The cantilever deflection as a function of z-piezo displacement, shown in figure 4.3, is obtained when the cantilever cyclically approaches and is retracted from the surface of the sample. It typically shows the deflection of the free end of the AFM-cantilever as its fixed end is brought vertically towards and then away from the sample surface.

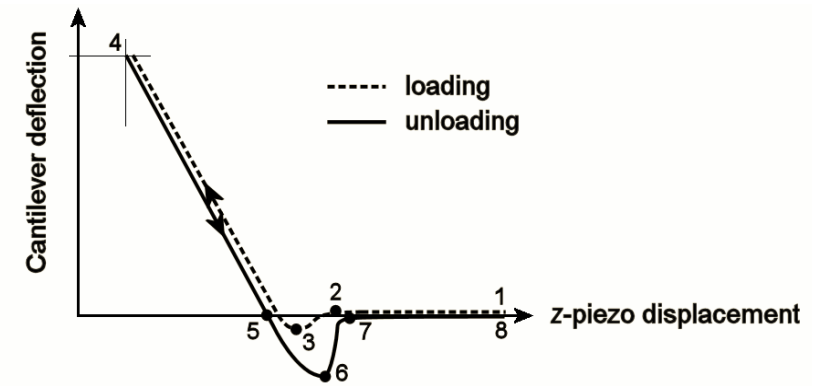

Figure 4. 3: Cantilever deflection as a function of z-piezo displacement from (170)

1-2: The piezo extends in z-direction; the tip descends. No contact with the sample surface yet.

2-3: Attractive Van der Waals forces near the surface pull the tip down.

3-4: As the tip presses into the surface, the cantilever bends upward.

4-5: The piezo retracts and tip ascends until repulsive and attractive forces are in equilibrium (zero cantilever deflection).

5-6: The piezo continues retraction; the tip ascends further. The cantilever bends downward as surface attraction (adhesion force) holds onto the tip.

6-7: The tip finally breaks free of surface attraction. The cantilever rebounds sharply upward.

7-8: As the piezo continues retracting, the tip continues its ascent. No further contact with the surface.

4.2.2.1 Determination of the spring constant of a beam

The spring constant of a beam (see Figure 4.4) can be determined from the so-called cantilever deflection versus piezo displacement curve as seen in the following demonstration:

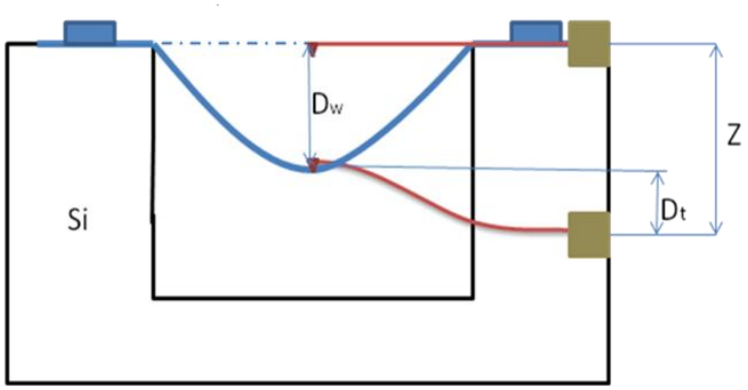

Figure 4. 4: Schematic diagram of beam-bending measurement

The total displacement of the piezo is the sum of the cantilever deflection and the deflection of the beam as it bends. For small deformations (i.e. nanometric deformations), the behaviour of both the cantilever and the beam belongs to the elastic domain, and can be described by Hooke's law, where the spring constant of the cantilever and beam system is simply the result of the combination of two springs in series, according to

$$\frac{1}{K_0} = \frac{1}{K_w} + \frac{1}{K_t} \qquad (4.10),$$

where K_0, K_w and K_t are the spring constants of the system, the beam and the cantilever, respectively.

Without any torsion component, Hooke's law for this system under a loading force F gives:

$$F = K_0 Z = K_t D_t \qquad (4.11),$$

where Z and D_t are the displacement of piezo and the deflection of the cantilever, respectively.

The slope in Figure 4.3 is therefore $D_t / Z = K_0/K_t$. K_t can be measured as shown in the following section. Therefore K_0 can be obtained from the slope. K_w can then be calculated from equation (4.10).

The cantilever deflection as a function of z-piezo displacement curve can be converted into the typical force-displacement curves since the cantilever deflection is proportional to the force applied to the sample. The system spring constant k_0 can then also be determined directly from its slope and the spring constant of the beam can be calculated from equation (4.10).

4.2.3 Calibration of the spring constant of the cantilever

The calibration of a force measurement involves two steps: first, the calibration of the displacement sensitivity of the cantilever; second, the calibration of the normal spring constants of the cantilever. The vertical displacement sensitivity of an AFM tip can be accurately determined by applying known displacements to the tip. The procedure includes the determination of the probe's inclination to the sample surface and the calibration of the vertical scanner. For the determination of the spring constant, there are four methods including estimation from representative geometry, comparison with and without added mass, by hydrodynamic model and thermal tuning. The first method is quick, but suffers from uncertainty because typically the specific cantilever geometry is not measured and may vary in production. The second method requires careful work that is rewarded with a more accurate value. The fourth method is often preferred as it is neither as demanding and time-consuming as attaching a particle (method two) nor has as large an associated uncertainty as relying on a representative model (method one).

Hutter and Bechhoefer (172) proposed that the spring constant of an AFM cantilever was related to its thermal energy using the equipartition theorem. The measurement data consist of a time interval of the deflection signal in contact mode (i.e. with no driving oscillation applied electronically) at thermal equilibrium, while the cantilever is suspended. Brownian motion of surrounding molecules imparts random impulses to the cantilever during the sampling. The resulting function of time is Fourier transformed to obtain its Power Spectral

Density (PSD) in the frequency domain. Integrating the area under the resonant peak in the spectrum yields the power associated with the resonance.

Expressing the dynamics of the cantilever as a harmonic oscillator, the average value of the kinetic and potential energy terms are both $\frac{1}{2}k_BT$, where T is the temperature in Kelvin and k_B is Boltzmann's constant = 1.3805×10^{-23} Joules/Kelvin. In particular, for the potential energy, $\left\langle \frac{1}{2}m\omega_0^2 z^2 \right\rangle = \frac{1}{2}k_BT$, where ω_0 is the resonant angular frequency, m is the effective mass, z is the displacement of the free end of the cantilever and the "angle" brackets indicate an average value over time (171). Simplifying, the temperature and average displacement determine the cantilever spring constant $k = \frac{k_BT}{\left\langle z^2 \right\rangle} = \frac{k_BT}{P}$.

Hence k can be determined from the power spectral density of the cantilever.

4.3 Fabrication of doubly and singly clamped beams with FIB

The present experimental set up is a commercially available cross beam system (Carl Zeiss XB 1540), which couples a scanning electron microscope and a focused ion beam. Figure 4.5 is an image of this cross beam system. This dual beam system enables the localized maskless deposition of both metal and insulator materials on the surface of substrates at room temperature. The two beam systems are focused on the same point of the sample by adjusting the distance between SEM column and sample surface (work distance) to 5 mm and the distance between FIB column and sample surface to 12 mm, which allows real-time simultaneous FIB machining and non-destructive, non-contaminating SEM imaging. The FIB column usually operates at an accelerating voltage of Ga^+ ions of 30 keV. The beam current can be varied from 1 pA for the lowest current to a few nanoamperes. The precursor vapour is delivered via a gas injection system composed of five temperature-controlled

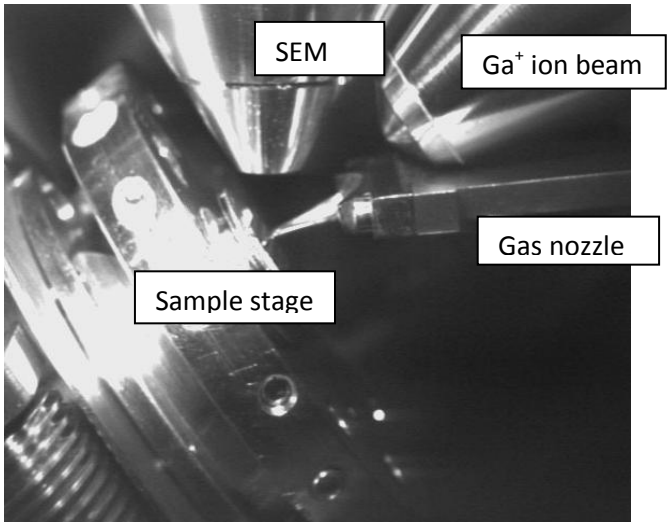

Figure 4. 5: Focused ion beam system

reservoirs coupled to the injection lines. This system is driven by a three axis microstage. The FIB is scanned with certain frequencies in the *x* and *y* directions to write the desired pattern by computer control. Focused Ga ions are utilized to decompose organo-metallic molecules of the precursor gas for depositing a uniform amorphous film of the desired thickness of metallic element on those sample surfaces. The growth conditions in the *x* and *y* directions are controlled by both beam-deflectors. The growth in the *z*-direction is determined by the deposition rate, that is, the height of structure is proportional to the irradiation-time when the deposition rate is constant. Here three-dimensional vertical C-W-nanorods as were fabricated. As a result of the requirement mentioned in chapter 2, we also need to fabricate both doubly and singly clamped beams by felling down the vertical C-W-nanorods using SEM/FIB (Carl Zeiss XB 1540) system.

4.3.1 Nanorod deposition

The operating principle for fabricating vertical C-W-nanorods is similar to the deposition of film mentioned above. In this work, we tried to deposit vertical nanorods on phosphorus doped silicon substrates with different cross sections by setting target areas ranging from 20×20 to 100×100 nm^2. Tungsten hexacarbonyl [$W(CO)_6$] was used as the precursor gas for

all depositions. Since tungsten hexacarbonyl is in the solid phase at room temperature, the reservoir was heated to a temperature in the range of 63 ℃ to 72 ℃ to obtain an appropriate vapour pressure. The evaporated gas was injected into the growth area on a substrate through a gas nozzle, which was pointed approximately at the centre of the deposition area at an angle of 30 °. The distance between the bottom of the precursor injection nozzle and the sample surface was in the range of 100 to 500 μm. 30 keV Ga^+ ions at currents varying from 1 pA to 10 pA were used with scanning mode. The scanning frequencies of the gallium ion beam in the X and Y directions were 20000 Hz and 0.02 Hz, respectively. The base pressure of the specimen chamber was about 2.0×10^{-6} mbar, and the average gas pressure was increased to 1.5×10^{-5} mbar during deposition. However, the local gas pressure at the specific area was presumably much higher than the average. With these conditions, the length of nanorod was proportional to the growth time. The deposition was monitored by in-situ SEM through raster scanning. The diameter and length of the nanorod were measured by SEM. Figure 4.6 (a) is an SEM image of vertical C-W-nanorods viewed at an angle of 36 °. Figure 4.6 (b) is an FIB image of a vertical nanorod, which was perpendicular to the FIB.

We also tried to grow nanorods with electron beam deposition instead of gallium ion beam deposition. The beam current is 1 pA and the voltage is 30 kV. The electron beam was focused and kept at a constant spot. The nanorod was deposited on the silicon substrate using the same gas precursor tungsten hexacarbonyl [$W(CO)_6$]. The chamber pressure was about 1.5×10^{-5} mbar during deposition, which was at room temperature. The upward growth caused by the deposition created a free standing nanorod, which was around 80 nm in diameter. The length of the nanorod was proportional to the growth time.

4.3.2 Trench milling

In this experiment, micro-trenches were milled into the phosphorus-doped silicon substrate by the dual-beam FIB system. The gallium ion beam was operated at 30 keV with a beam

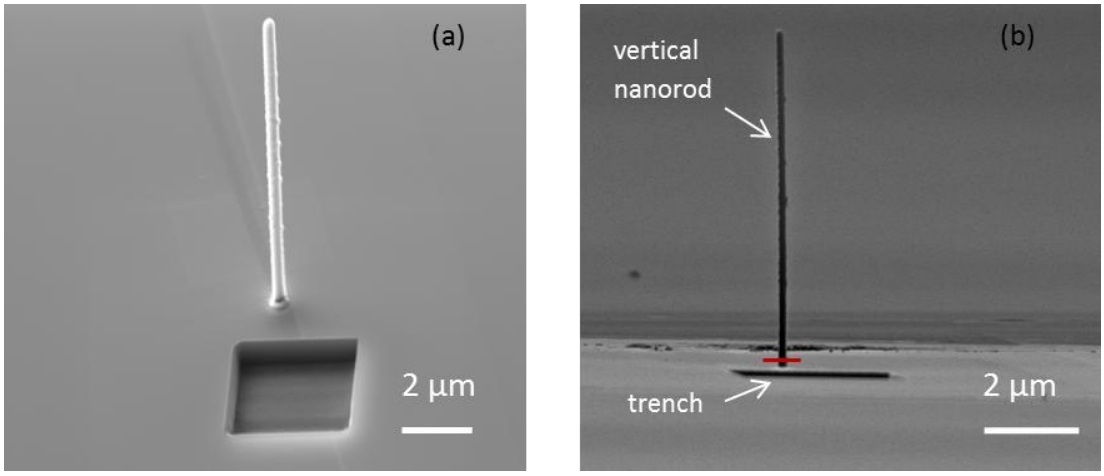

Figure 4. 6: SEM and FIB image of vertical C-W-nanorod (a) SEM image of a vertical C-W-nanorod looking at an angle of 36 °to the surface normal (b) FIB image of a vertical C-W-nanorodscanning)

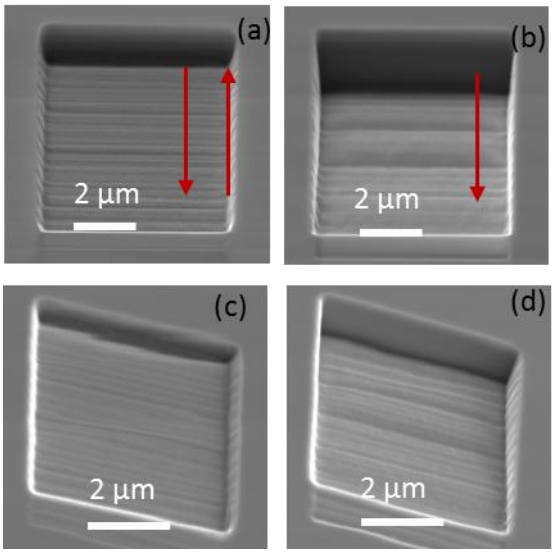

Figure 4. 7: SEM images of trenches milled by FIB on silicon substrate (a) SEM image of trench milling started from one side of the target area and then restarted from the other side as the red arrows show (b) SEM image of trench milling just started from one side of the target area as the red arrow shows (c) SEM image of the same trench as in (a) with a stage tilt of 45 °(d) SEM image of the same trench as in (b) with a stage tilt of 45 °(All the above SEM images were viewed at an angle of 36 °to the surface normal)

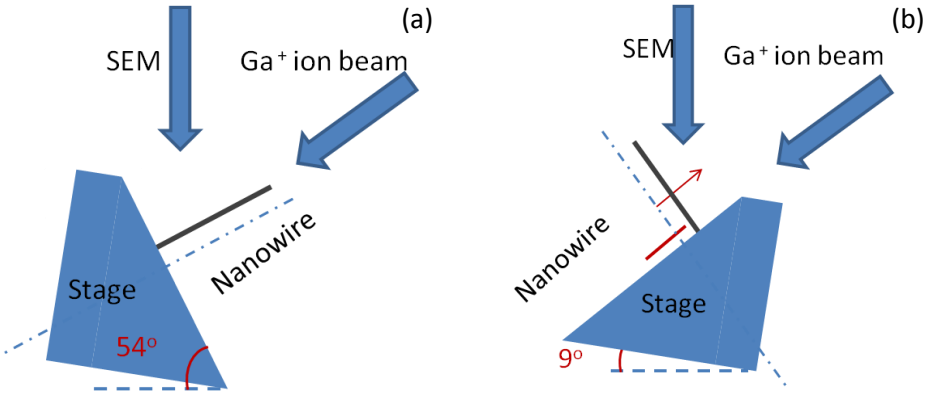

Figure 4. 8: Schematic diagram of sample stage positions (a) stage position for depositing the nanorod (b) stage position for milling the nanorod after the stage was rotated 180 °(The red arrow is the felling direction of the nanorod and the red line is the position where the nanorod was milled by Ga^+ ion beam)

current of 500 pA. The stage can be tilted to allow the sample surface to become perpendicular to the gallium ion beam. After a target area was defined, the gallium ion beam was digitally steered in a repeating raster scan over it. To form the raster, the digitally steered focused ion beam is stepped in a serpentine pattern over the area to be micromachined. When the farthest extreme of the raster scan is reached, the FIB is quickly stepped back to the beginning of the pattern and the pattern is repeated. Generally, the raster scan is repeated many times and more material is removed away. Target areas ranging from6 ×6 μm^2 to 12 ×12 μm^2 were milled using the raster scanning mode with a beam current ranging from 300 pA to 1 nA. The raster-scan time and milling time were dependent on the desired depth for the trenches, which was around 1.5 to 2 μm in this work. The milling rate was about 0.16 μm^3 s^{-1} at 500 pA.

We fabricated the trenches as demonstrated in figure 4.7 (a). As shown by the first red arrow, the raster scan started from one side of the trench and kept milling for a certain time. We then restarted milling from the other side of the trench in the direction of the second red arrow. Using this method, we can obtain a trench with a constant depth of 2 μm as shown in figure 4.7 (c). If we mill only from one side, we cannot obtain a trench with a constant depth

as shown in figure 4.7 (d) due to the redeposition which accompanies milling the trench from one side as seen in figure 4.7 (b).

In order to make doubly or singly clamped beams for the force-displacement measurement as seen in section 4.4, a trench with a depth of 1.5 to 2 μm on the silicon substrate is needed to sputtered by FIB next to the vertical C-W-nanorod as shown in figure 4.6. Effects on the FIB milling were discussed. These include scan rate, ion beam current and milling time.

4.3.2.1 Effect of scan rate on milling

Figure 4.9 shows SEM images of four sets of trenches milled by FIB with the ion beam current ranging from 50 pA to 500 pA for 3 mins. The target area is 6×6 μm^2. The SEM images show that in each set of trenches, increasing the scan rate meant the depth of the trenches became larger. The scan rate is given by the time needed for a single milling pass. The figure also shows that a larger ion beam current can make a contribution to fabricating a deeper trench. The sputtering rate was affected by both the scan rate and the ion beam current. Figure 4.10 shows that the sputtering rate of trenches can be increased by increasing the scan rate from 0.06 to 0.17 pass per second, under the same ion beam current and milling time. A possible reason for this is that the increased number of milling passes under the same total milling time (i.e. scan rate) significantly decreases the dwell time of the ion beam. Therefore the increased scan rate can reduce re-deposition significantly, which results in a sputtering rate increases. For an ion beam current of 500, 200, 100 and 50 pA, respectively, the sputtered volume of each pass is calculated to be 1.02, 0.76, 0.2 and 0.4 μm^3/pass.

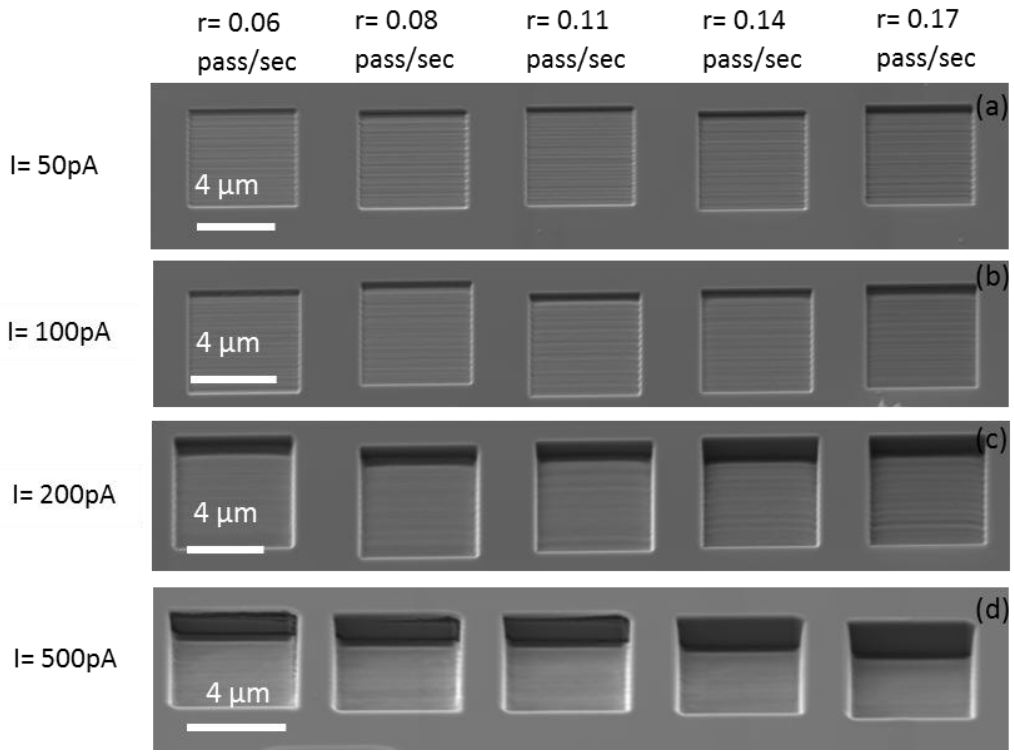

Figure 4. 9: SEM images (with a viewing angle of 36o) of trenches on a silicon substrate milled at different ion beam currents and raster scan milling passes. The corresponding scan rates from left to right were 0.06, 0.08, 0.11, 0.14 and 0.17 pass/sec, respectively, and the target area was 6 6 μm^2.

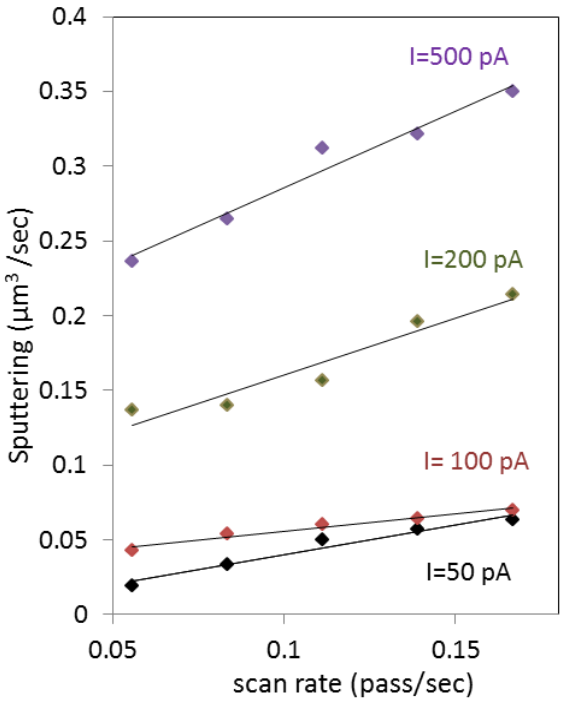

Figure 4. 10: The sputtering rate as a function of scan rate. (The target area is 6 6 μm^2, the milling time is 3 mins and the ion beam current varied from 50 pA to 500 pA)

4.3.2.2 Effect of ion beam current on sputtering rate

The influence of ion beam current on the sputtering rate is presented in Figure 4.11. Each trench with a target area of $6 \times 6\ \mu m^2$ was milled with a time period of 3 mins under various beam currents, namely, 50, 100, 200, 500 pA. A slight increase of the sputtering rate was observed when a higher ion beam current of 100 pA was applied. By increasing further ion beam current, the sputtering rate reached a maximum value of $0.35\ \mu m^3\ s^{-1}$.

4.3.2.3 Effect of milling time on the milling

In another experiment, trenches were fabricated for various milling times, namely, 1, 1.5, 2, 2.5 and 3 mins with an ion beam current of 500 pA and 5 raster scan milling passes. The results are presented in Figure 4.12. The sputtering rate was $0.27 \mu m^3 sec^{-1}$.

In this part, trenches with a depth of 1.5 to 2 μm on the silicon subtrate can be sputtered with focused ion beam. The sputtering rate can reach $0.27 \mu m^3$/sec with a scan rate of milling of 0.17 pass per second and a high gallium ion beam current up to 500 pA at an accelerating voltage of Ga^+ ions of 30 keV.

4.3.3 Felling and clamping

Doubly- and singly- clamped beams were prepared in the SEM/FIB system as well, because the FIB has the advantages of precise milling on the nanoscale. After rotating the 45 ° SEM sample holder to 180 °, as can be seen in figure 4.8 the gallium ion beam was scanned along a line drawn at the bottom of nanorod (as shown in figure 4.6 (b)) with a beam current of 50 pA for 1 min's single raster scan milling. As a result the nanorod was milled, felled down in the direction of gallium ion beam, and is thereby suspended over the trench. After rotating the sample holder back to 0 °, both free ends of the nanorod were fixed to the substrate by depositing tungsten pads with an area of ($1 \times 2\ \mu m^2$) and a thickness of 300 nm, which can.

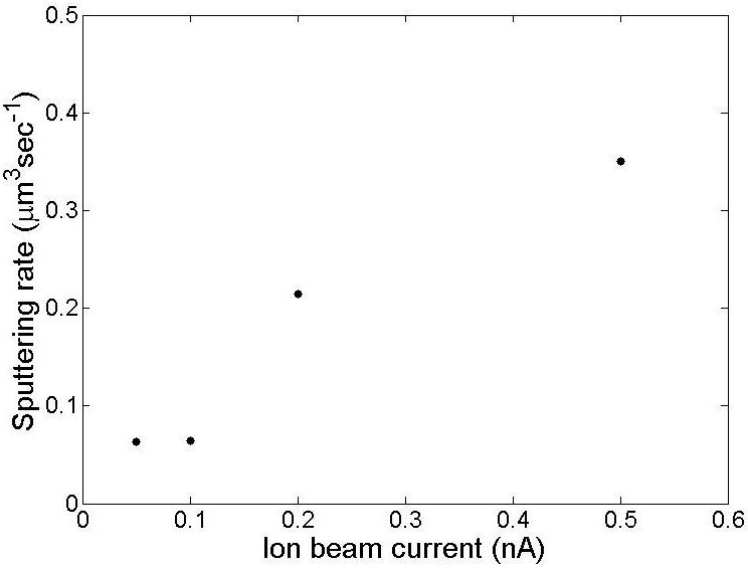

Figure 4. 11: Ion beam current dependent sputtering rate of trenches with target area size of 6 6 μm^2 fabricated by FIB with various ion beam currents

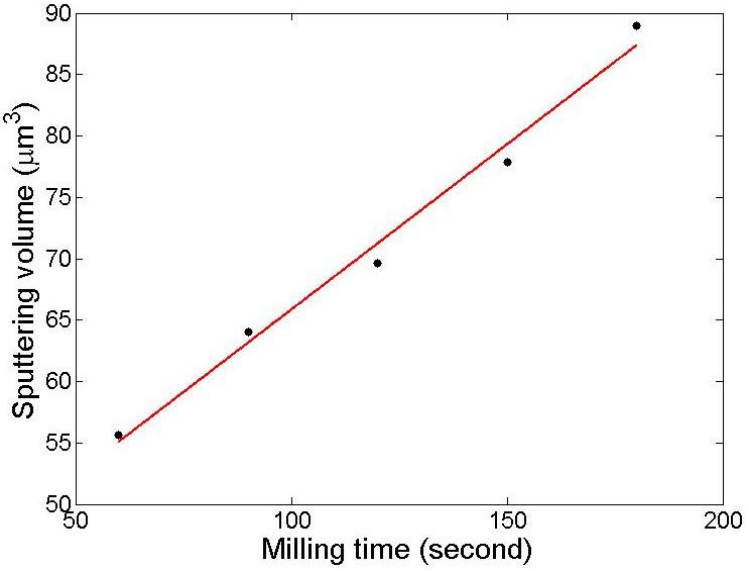

Figure 4. 12: The sputtering rate as a function of milling time. The target area was 6 6 μm^2. Ion beam current was 500 pA

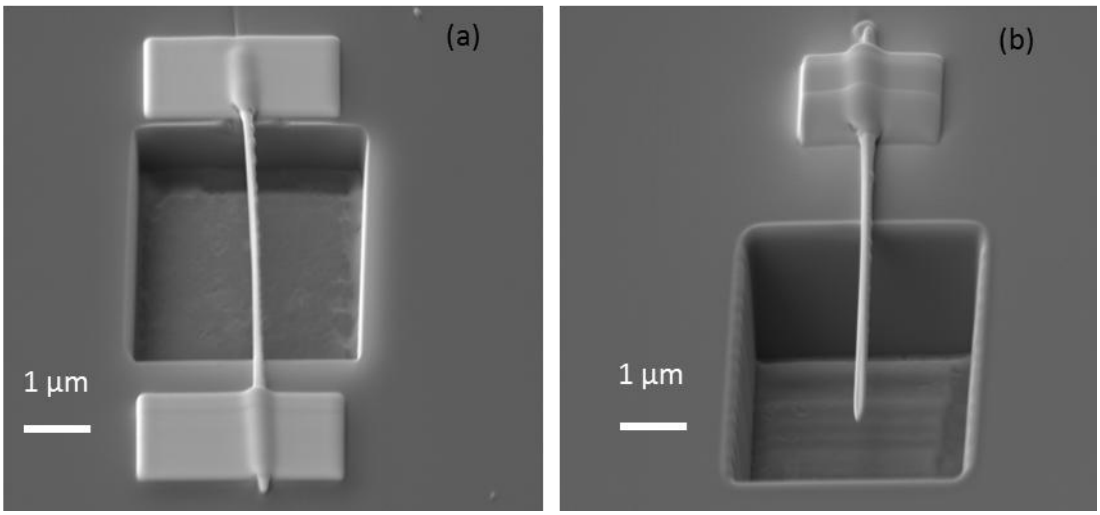

Figure 4. 13: SEM images of doubly- and singly- clamped beams (a) SEM image of a doubly clamped beam (b) SEM image of a singly clamped beam

be seen in figure 4.13. In the case of the singly clamped beams, it is necessary that half of the nanorod was suspended freely over the trench and the other half was clamped to the silicon surface.

4.4 Diameter reduction with FIB

The diameter of the freestanding C-W-nanorod deposited by FIB-induced deposition was mainly determined by the diameter of the gallium ion beam (the detailed explanation can be seen in section 4.1). The smallest diameter of the nanorod grown by FIB-induced deposition with the current tungsten source is about 130 nm. FIB milling is the most commonly used application, especially FIB annular milling, which was used to sharpened the AFM tip to enable measurement of high-aspect-ratio structures. However, after FIB annular milling, the nanostructure has a needles shape. In our case, the uniformity is more important to fabricate an ultrasensitive sensor. In order to fabricate a nanorod with smaller diameter, the technique of lathing with FIB was employed. Figure 4.14 (a) is a schematic diagram of the set-up for lathing the nanorod with FIB. In order to use the FIB as a lathe, it was necessary to accurately find the rotation centre of the sample substrate on the stage in the FIB image,

shown in figure 4.14 (b). First, the crosshair of the SEM can be used as a reference, then the silicon substrate was rotated 360 ^{o} under the maximum magnification around *z*-axis. A rough rotation centre was found and marked on the substrate by milling a cross with FIB. Again the substrate was rotated 90 ^{o} by referring to this cross, and marked by milling a second cross. The substrate was rotated 180 ^{o} and 270 ^{o} by referring the first cross respectively, then the third and fourth cross was milled correspondingly. The centre of the four crosses is the real rotation centre of this substrate, where the vertical nanorod was grown here by FIB-induced deposition. The typical nanorod was fabricated by focused ion beam, with a constant beam current of 1 pA at an accelerating voltage of Ga^{+} ions of 30 keV. This vertical nanorod has a length of 10 μm and a diameter of 130 nm. In the FIB mode, a reduced area with a length of 12 μm and a width of 3 μm was chosen, which is larger than the nanorod. The gallium ion beam energy was 30 keV and the beam current was 50 pA. At the same time, the sample stage was kept rotating with a speed of 180 ^{o} per second. In order to reduce the e-beam caused carbon deposition, the maximum SEM magnification was used. As shown in figure 4.15, after 120 sec's lathing, the diameter of the nanorod was reduced from 130 nm to 60 nm. However, with this lathe method, the minimum diameter can be achieve is about 60nm. Under this value, the nanorod lathed by FIB started bending.

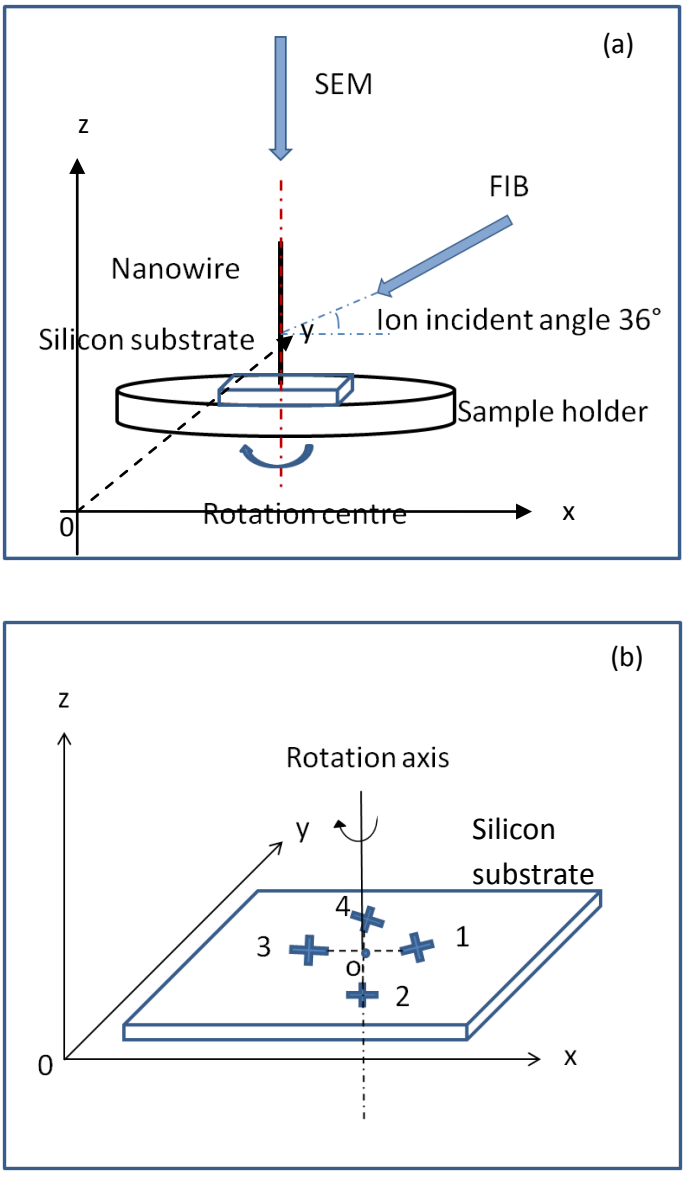

Figure 4. 14: Schematic diagram of set up for lathing the nanorod with FIB. (a) The geometry of FIB as a lathe for the nanorod (b) Marked crosses as references to find out the rotation centre *o* on the silicon substrate

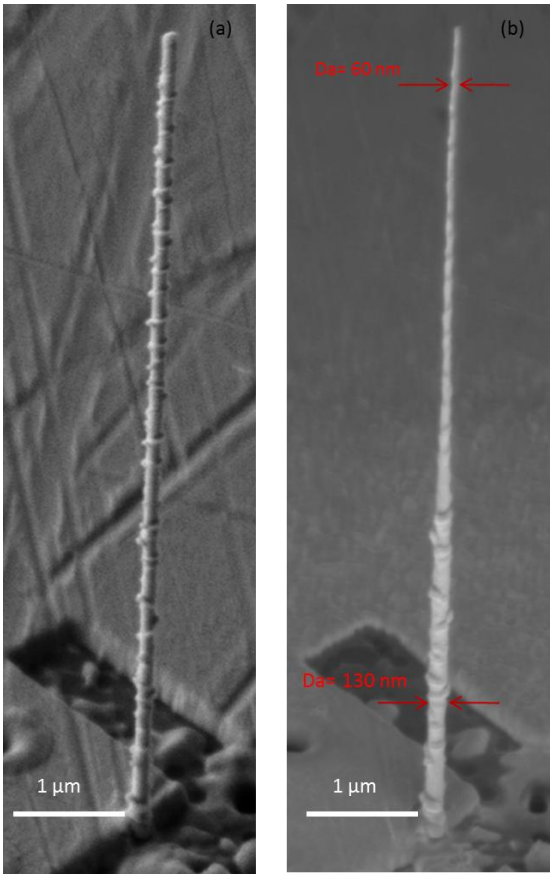

Figure 4. 15: SEM image of nanorod (a) before and (b) after lathing by FIB

4.5 Static measurements of C-W-nanorods

The mechanical properties (in particular, the Young's modulus) of doubly clamped C-W-nanorods were characterized by a commercially available Atomic Force Microscope (Veeco Dimension 3100 with nanoscope software version 5). Elastic nanometric deflections were applied by a tapping mode AFM cantilever at a constant force in scanning mode. The probe was a micromachined [100] Silicon tip, supplied by Mikromasch. Its estimated spring constant is given by the manufacturer as about 40 N/m. For quantitative force measurements,

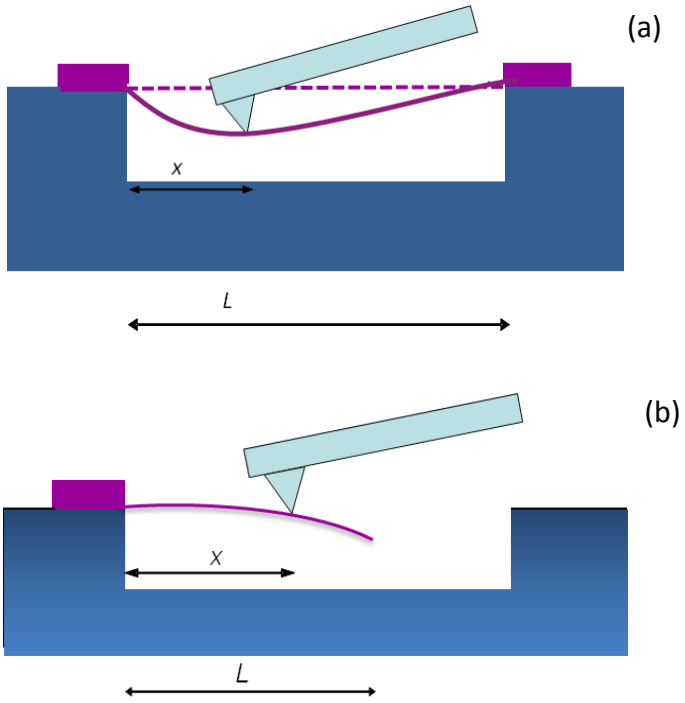

Figure 4. 16: Schematic diagram of Young's modulus measurement for doubly-clamped and singly-clamped beams with AFM (a) Schematic diagram of Young's modulus measurement for the doubly-clamped beam (b) Schematic diagram of Young's modulus measurement for the singly-clamped beam

we measured the spring constant accurately by using the thermal noise method as mentioned in section 4.2, and the resulting spring constant was 57 N/m. The sensitivity of the AFM system, i.e. the photodiode voltage versus the distance travelled by the piezo, or the photodiode voltage versus the voltage applied to the piezo, was calibrated by a force-displacement curve measured on the silicon surface.

For successful micromechanical bending of the nanorod above a trench, it is necessary first to image the surface to determine the position of the nanorod. The scanning direction needs to be parallel to the nanorod to avoid breaking it, and the scanning area was typically slightly larger than the trench size. Nanorod bending was achieved by moving the cantilever perpendicular to the surface as shown in figure 4.16 (a). The cantilever was driven by the piezo movement in the *z*-direction. A typical piezo movement of 3.0 μm with a frequency of

1.3 Hz in the z-direction was applied. The tip then touched and pushed the surface of the sample and was deflected as the piezo moved down. The maximum deflection of the tip was determined by setting the trigger threshold. According to Hooke's law, the maximum applied force was 2850 nN. Each step included one cycle of extension and retraction of the cantilever. After every step, the tip was moved one step further along the nanorod. The distance moved each step depended on the number of scanning pixels, which can be set in the range from 32×32 to 512×512, and depended on the data scale of the image. In this experiment, a complete scan consisted of 32 steps and the distance moved each step is 137 nm.

In the case of the singly clamped nanorod, the Young's modulus was measured by AFM in the point and shoot mode (available in the software of nanoscope version 6). In this mode, the operating principle is the same as in software version 5 and the schematic diagram is shown in figure 4.16 (b). After the precise position of the singly-clamped beams was determined, we needed to switch into the point and shoot mode. A line was then drawn along the nanorod, and this can be converted into a number of points. There was one cycle of extension and retraction of the cantilever per step on each point. The tip was then moved to the next point automatically at a constant force. The trigger threshold was set at 50 nm. The velocity of the tip both towards to the sample and away from the sample was 10 nm s^{-1}.

4.6 Set up for resonant frequency dynamic measurement with spot mode

Another way of detecting the resonant frequencies of FIB-deposited C-W-nanorods is using a systematic set-up for monitoring and detecting mechanical harmonic oscillations with spot mode of an SEM. This system set-up shown in figure 4.17 is similar to the set-up mentioned above, but the experiment was carried out at EMPA in Switzerland. A ceramic piezo was used as the electric actuator in the SEM chamber. The piezo has a thickness of 0.5 mm and

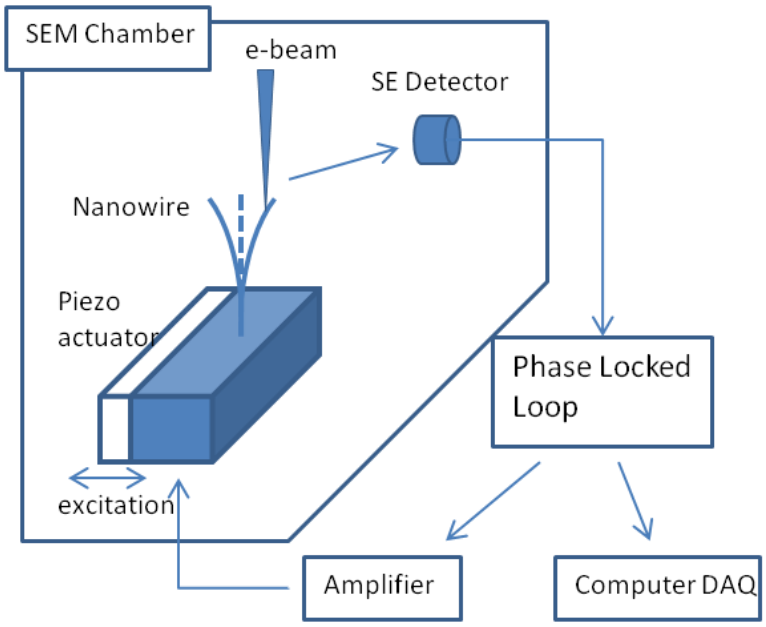

Figure 4. 17: schematic diagram of set up for resonant frequency measurement

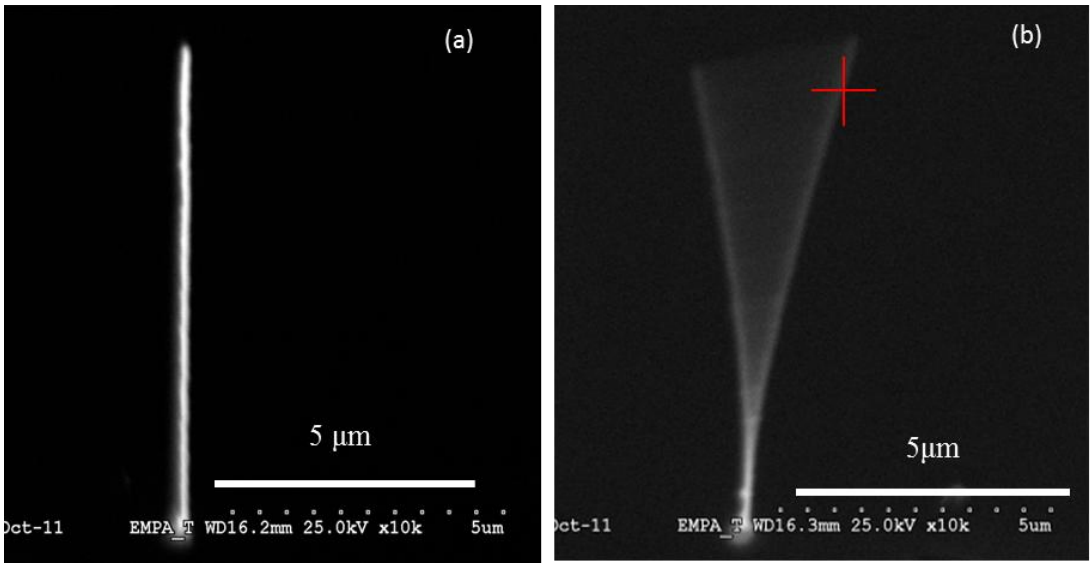

Figure 4. 18: SEM image of (a) without and (b) with vibration of the C-W-nanorod (both of the images were viewed at angle of 45^{o} to the surface normal. The red cross is the position of the stationary beam position).

an area of 5×5 mm^2 and was glued onto a printed circuit board. A lock-in amplifier was used as a power source to apply an ac voltage to the piezoelectric actuator. The sample, a piece of silicon substrate, was fixed to an intermediate stainless steel angled piece using silver paste.

A homemade 10×-amplifier with a bandwidth of 1.2 MHz was used to drive the 1 nC capacitive load of the piezo at ±10 V using a digital Phase-lock-loop (PLL). The SE detector had a bandwidth exceeding 15.36 MHz since it is used for the acquisition of 640 × 480 pixel images at TV mode scan rate (50 Hz). Therefore the available overall bandwidth of the setup was sufficient to measure the fundamental resonance mode of the nanorod up to 1 MHz. Actually the highest resonant frequency detectable with this system is up to 850 kHz only. Since the excitation power is not enough to drive the piezo.

In all the resonance detecting experiments, the excitation power applied to the piezo was adjusted to limit the peak deflection amplitude to be less than 10% of the pillar length. The relative position of both the stationary e-beam and the vibrating nanorod are shown in figure 4.18. The distance between the stationary e-beam and the nanorod, and the nanorod peak vibration amplitude crucially determines the amount of "spatial" truncation of small deflection amplitudes. At the maximum tolerable distance, the PLL locks the deflection and excitation signals for a minimum number of data points while sweeping through resonance, which enables determination of the amplitude peak value and the slope of the phase curve at its resonant frequency. If, on the other hand, the stationary electron beam is positioned very close to the beam static position, the non-linearity in the amplitude response becomes very strong. Good measurement results were achieved by slightly defocusing the stationary electron beam, which increased the dynamic range of the technique due to a spatially increased interaction between the beam and the vibrating nanorod.

A typical resonant frequency measurement result can be seen in figure 4.19. This C-W-nanorod was grown on a silicon substrate by FIB-induced deposition with a constant beam current of 1 pA at an accelerating voltage of Ga^+ ions of 30 keV. The length is 13.07 μm and the diameter is about 103 nm. Firstly, an overview spectrum was acquired with the stationary beam technique to roughly decide the resonant frequency by sweeping the excitation

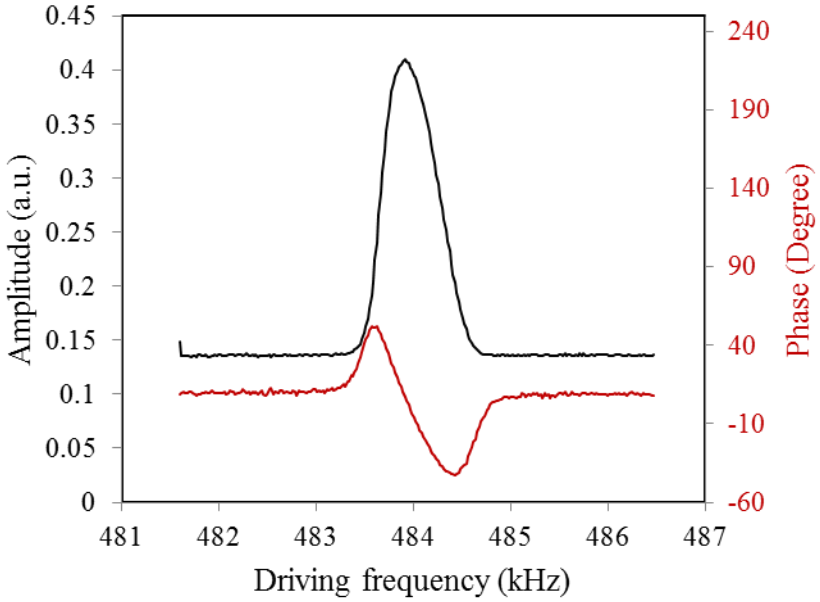

Figure 4. 19: Electron beam intensity (black curve) and variation of the phase (red curve) as a function of driving frequency

frequency through certain frequency range based on theoretical calculations. By measuring the amplitude and phase response, the excitation power and stationary beam position was adjusted. Secondly, close up spectra were acquired at the frequencies of interest. SEM imaging of the nanorod at resonance revealed the modal shape and the absolute maximum deflection amplitude at a given excitation amplitude. From the amplitude response, the resonance peak position was determined to be f_0 = 484 kHz and from the phase response, the slope at resonance is $\varphi/\Delta f$ = 143.3 ° kHz^{-1}, which implies that Q = 629. The way of Q-factor calculation method is decided by the theory shown in section 3.2.

In some of the experiments we observed orthogonal resonance modes vibrating along the orthogonal principal axes (Figure 4.20). This behavior is attributed to a non-circular cross-section. From the theory (as shown in section 3.2), a nanorod with an elliptical cross section has two fundamental resonance modes, which is proportional to the ratio of the two principle diameters respectively. To detect all resonance modes, first the orthogonal directions of the resonance were required to identify at a top-view incidence. Then the stationary electron

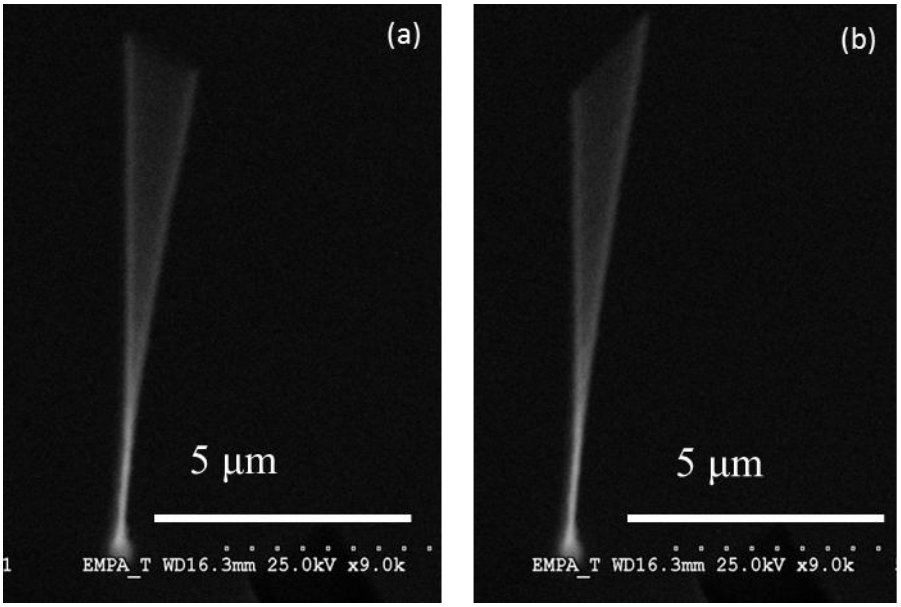

Figure 4. 20: SEM images of a single nanorod with two different resonant frequencies in orthogonal directions (a) f_0=484 kHz (b) f_0=501 kHz

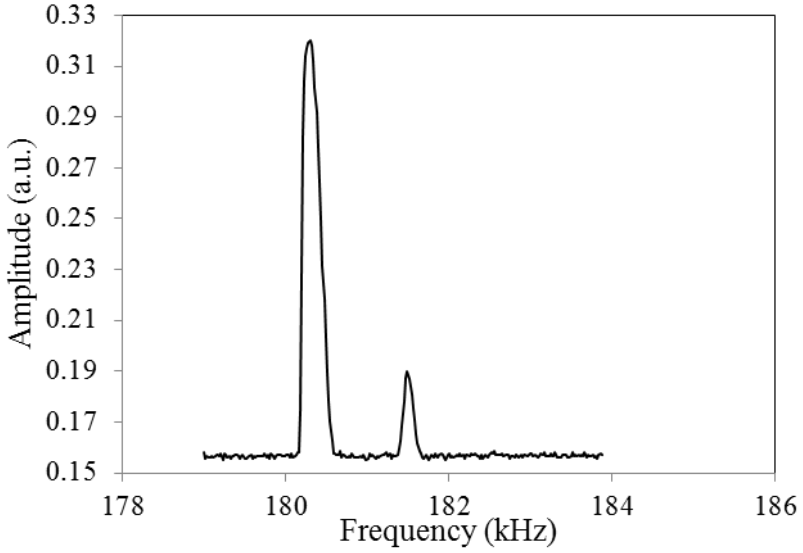

Figure 4. 21: Amplitude as a function of sweep frequency for an orthogonal resonant frequency mode

beam was required to locate at 45 °between the two perpendicular directions. This stationary beam position enabled the observation of all resonance peaks in a single excitation frequency sweep, which can be seen in figure 4.20. Another option is that the stationary beam can point

at the centre of the nanorod. This assures that no ‘spatial’ filtering happens. However, serious carbon contamination will occur due to the irradiation from the electron beam.

The detection of vibration amplitude of the nanorod is possible by SEM imaging. The overall harmonic oscillation of the nanorod is visualized by scanning a normal image. The frequency response spectrum is taken via the secondary electron (SE) detector with the stationary beam technique as shown in figure 4.21. If the electron beam irradiates the maximum amplitude position, in the integrated SE signal a peak is detected at resonance while sweeping the excitation frequency due to the increasing dwell time of the vibrating sample inside the beam. If the electron beam irradiates the zero amplitude position the resonance manifests as a negative SE-peak due to a decreasing dwell time. Employing phase locking of the time-resolved SE and excitation signal enables the extraction of the response of both amplitude and phase at resonance from the noisy SE signal. Integrated and time-resolved measurements can be performed simultaneously. The deflection signal acquired by the stationary beam technique is in general not linear with vibration amplitude, whereas the phase does not suffer from this non-linearity.

Chapter 5 Results and Discussion

Results in this chapter are divided into three parts: discussing the factors of C-W-nanorod growth and trench milling, the static measurement of the Young's modulus of C-W-nanorods and the dynamic measurement of the resonance frequency of tungsten nanomechanical resonators.

5.1 Factors influencing nanorod growth

C-W-nanorods with a diameter up to 250 nm, different lengths in micro-scale and a smooth sidewall were attempted to fabricate with gas-assisted focused ion beam. Deposition of C-W-nanorods can be optimized by varying the system parameters of FIB-induced deposition. These parameters include local gas pressure, needle position, the heating temperature of the precursor gas, ion beam current, dwell time, beam overlap, *etc*. Here, we will mainly discuss the effects of the local pressure of the precursor gas and the ion beam current on the growth of nanorods.

5.1.1 Effects of heating temperature of precursor

Vertical C-W-nanorods were grown on a silicon substrate by FIB-induced deposition with a constant gallium ion beam current of 1 pA at an accelerating voltage of Ga^+ ions of 30 keV. The target area was defined to be 60×60 nm^2 and the growth time was 10 mins. The heating

temperature of the gas precursor reservoir was increased from 63°C to 71°C resulting in the local gas pressure increasing from 1.19×10^{-5} to 2.9×10^{-5} mbar as shown in figure 5.1.

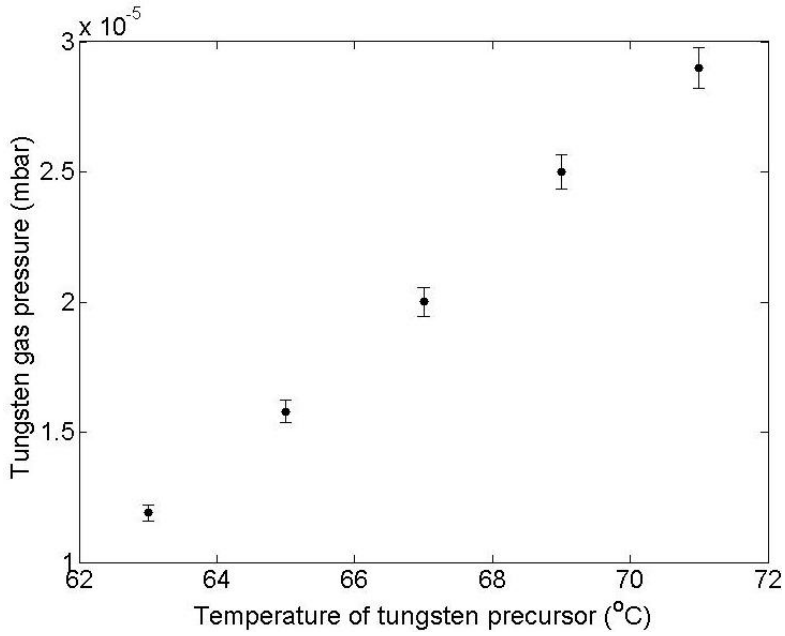

Figure 5. 1: Tungsten precursor gas pressure as a function of temperature of its reservoir

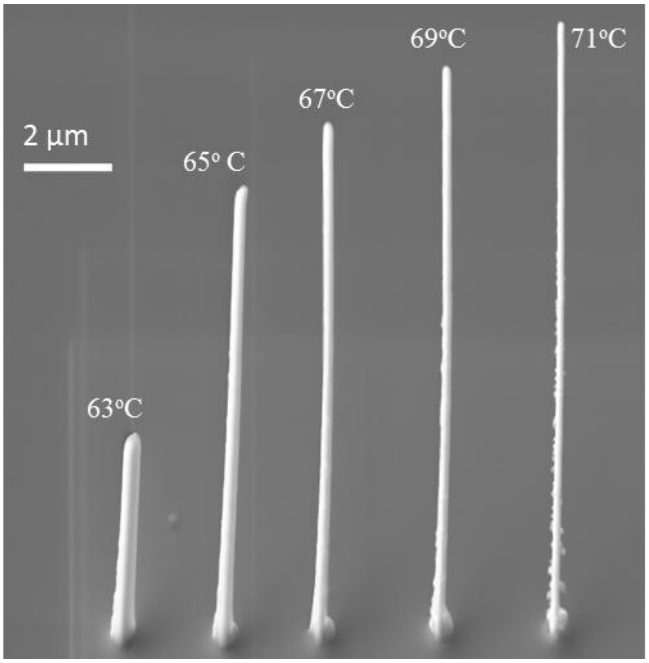

Figure 5. 2: An SEM image of C-W-nanorods grown by FIB-induced deposition at different heating temperatures of the precursor gas of 63°C, 65°C, 67°C, 69°C and 71°C (viewing at an

angle of 36°)

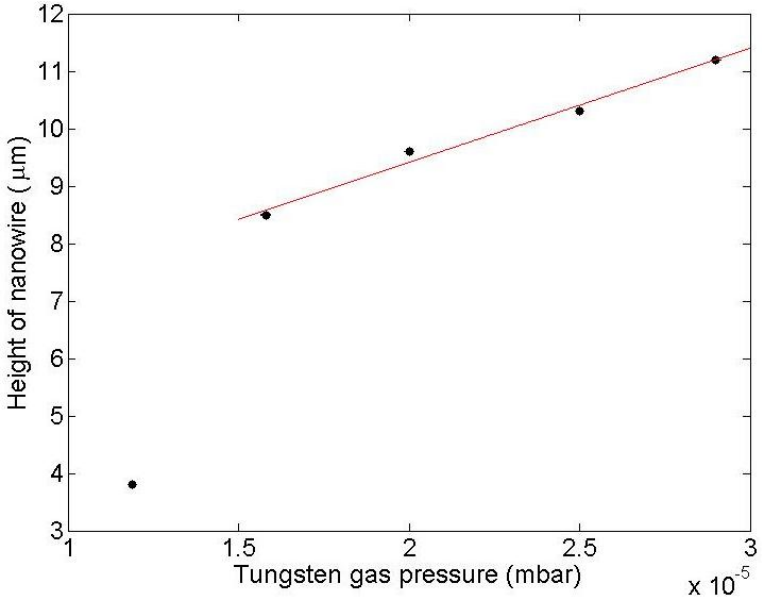

Figure 5. 3: The height of the nanorods shown in figure 5.1 as a function of the local pressure of the tungsten precursor gas

Figure 5.2 is an SEM image of nanorods grown at reservoir temperatures ranging from 63°C to 71°C. The nanorod grown at 63°C has a bigger diameter than that grown at 71°C. It can be seen that the volume of the grown nanorods was increasing at a rate of 0.75 um $^{o}C^{-1}$ when the local gas pressure increased from 1.58×10^{-5} to 2.9×10^{-5} mbar in figure 5.3. The heating temperature of precursor gas crucible affects the gas flux by controlling the precursor gas's pressure. A higher precursor gas flux can enhance the growth of the nanorod. The growth rate of the nanorod at 63°C was much slower as the lower temperature of the gas crucible resulted in a lower precursor gas flux. This is due to the sputtering rate of gallium ions is larger than the deposition rate.

The heating temperature of precursor gas not only has a significantly effect on the growth rate of C-W-nanorods by changing the local gas pressure, but also affected the topography of its sidewall. From figure 5.4, we can see that the nanorod grown at 63 ℃ has a smoother sidewall surface. More and more pinpoints on the sidewall appeared on the nanorods with an

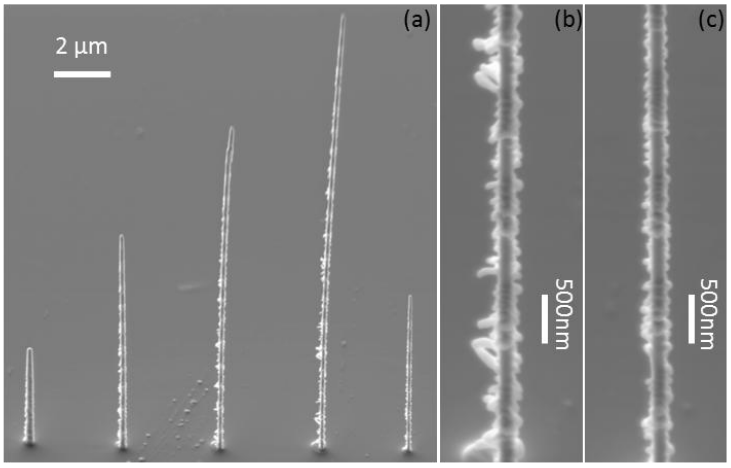

Figure 5. 4: SEM images of nanorods grown for different times (a) SEM image of nanorods from left to right grown for 3mins, 8 mins, 12 mins, 15 mins, 5 mins (b) SEM image of the sidewall surface of the nanorod grown for 15 mins (c) SEM image of the sidewall surface of the nanorod grown for 5 mins. (SEM viewing was at an angle of 36^{o}.)

increasing local gas pressure as a result of the higher heating temperature of the precursor gas. In addition, we investigated the relationship between the sidewall surface topography and the growth time of the nanorods. Figure 5.4 shows SEM images of nanorods grown for different times with a constant ion beam current of 1 pA. It also shows us the shape and sidewall surface topography of the nanorods. Comparing Figure 5.4 (b) with Figure 5.4 (c), it can be seen that the length of protrusions on the sidewall of nanorod was significantly increased with the increase in the growth time of the nanorods. The maximum length of the prutrosions on the nanorod grown for 5 mins was about 80 nm, and it increased in 288 nm if the nanorod were grown for 15 mins. The growth rate of protrusions calculated from figure 5.4 was about 23 nm min^{-1}.

Tripathi *et al.* (173) think that there are three important conditions to promote the growth of the whisker-like structures on the sidewall of the nanorod, including crystalline seed formation on the surface for growth, the temperature of the surface and the availability of the materials in vapour form in the ambient. The ions impinge on the surface and deposit

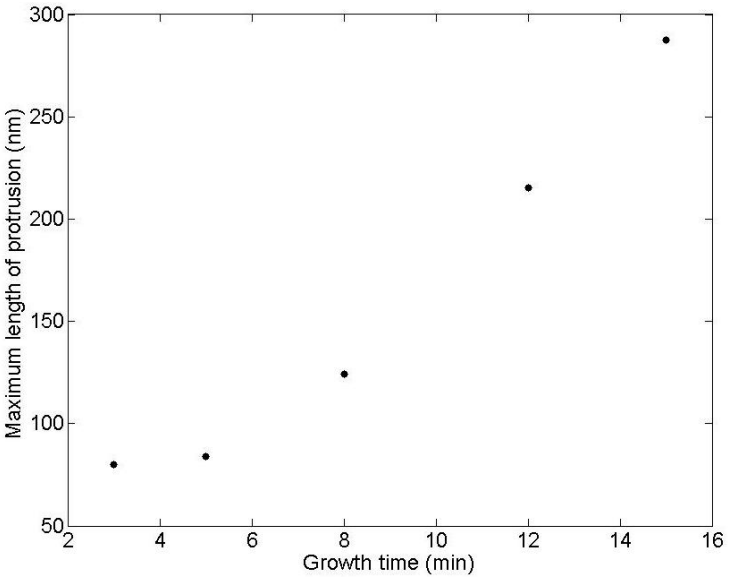

Figure 5. 5: Length of protrusions on the sidewall of nanorods as a function of growth time

their energy by electronic and nuclear energy loss processes, leading to a rise in the local temperature. The cracking of the precusor gas provides available material in elemental vapor form. Under such a mechanism the length of the whiskers or protrusions would be time dependent. Ishida *et al*. (4) explained it as a combination of sidewall roughening and dispersed beam-induced depsition. The roughness near the growth-point was formed by the redeposition of low-energy sputtered particles, surface diffusion of reactive species, or a collision casade process. The protrusion growth on the sidewall was induced by dispersed ion/electrons even at distant points.

The largest length of protrusions at the base of the nanorods in figure 5.4(a) was measured as a function of the growth time as shown in figure 5.5. It shows the length of the protrusions is linearly increased after depositing for 5 mins. Therefore the growth of protrusions is time dependent and the protrusions at the bottom get a longer time for growth. This also explains the length of the protrusions is larger at the base of the nanorod and is smaller at the tip of the nanorod in figure 5.4.

5.1.2 Effect of ion beam current

The height and sidewall surface morphology of C-W-nanorods is shown in the SEM image in figure 5.6. These nanorods have been fabricated using 30 keV Ga ions for 10 mins with beam current 1, 2, 5, 10, and 20 pA, respectively. All of the target area of deposition was defined to be 20×20 nm^2. The diameters of the nanorods was measured and is shown in figure 5.7. The diameter increased from 150 nm to 240 nm when the beam current increased from 1 pA to 20 pA. The reason is the aperture size of gallium ion beam increases with increasing of ion beam current. Thus larger gallium ion beam current results in larger diameter C-W-nanorods. All the nanorods show horizontal protusions on their sidewall. These became longer with higher ion beam currents. The variation in the length of the protrusions as a function of ion beam current of is plotted in figure 5.8. The length of the protrusions increased from around 80 nm at 1 pA to 220 nm at 20 pA. In all cases, it has been observed that the length of the protrusion is larger at the base and reduces as one moves upwards. It may be noted that the sidewall surface of the top part of C-W-nanorod is much smoother. The growth of the protrusions is still time dependent.

To conclude, we investigated the factors influencing the growth of C-W-nanorods with FIB-induced deposition. We can grow nanorods with the desired length and a diameter up to 250 nm at a rate of 0.053 $\mu m^3\ s^{-1}$. It is difficult to avoid the protrusions on the sidewall of the nanorod; the reason for this is still not well known. The optimal conditions for fabricating nanorods are, ion beam current of 1 pA with an accelerating voltage of Ga^+ of 30 keV, heating temperature of tungsten precursor gas of 69^oC with a gas pressure of 2.5×10^{-5} mbar. FIB induced tungsten vertical deposition was dependent on the growth time. It can be seen in figure 5.9 (a) and figure 5.9 (b).

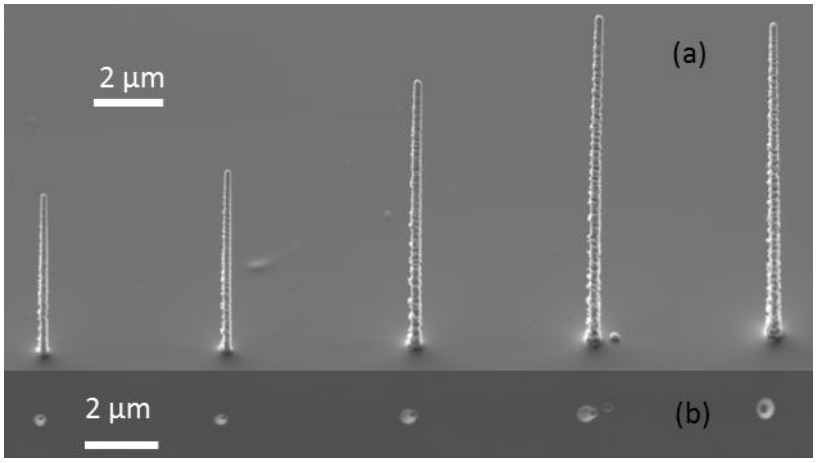

Figure 5. 6: SEM and FIB images of nanorods grown at different ion beam current (a) SEM images of nanorods grown at different ion beam current (viewing at an angle of 36^{o} to the vertical) (b) SEM images of nanorods grown at different ion beam current (top view of nanorods)

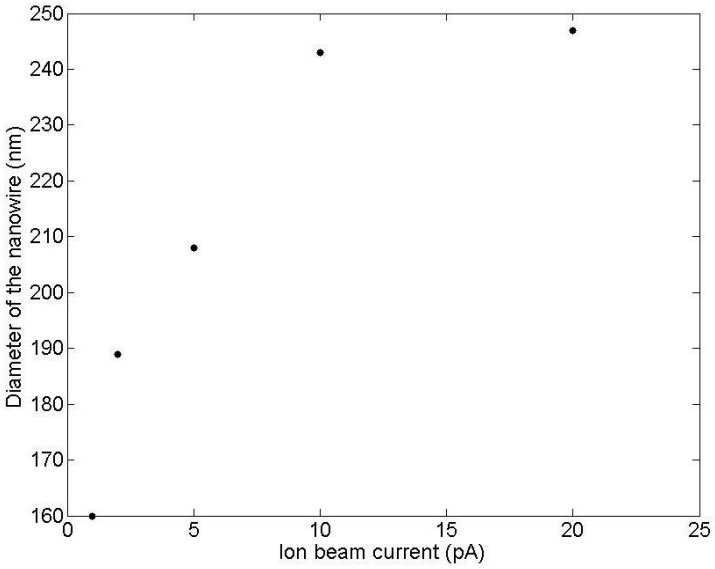

Figure 5. 7: Diameters of nanorods as a function of ion beam current (Nanorod was grown at a 30 keV Gallium ions for 10 mins with beam current 1, 2, 5, 10, and 20 pA, respectively. The target area was defined to be (20 nm)^{2})

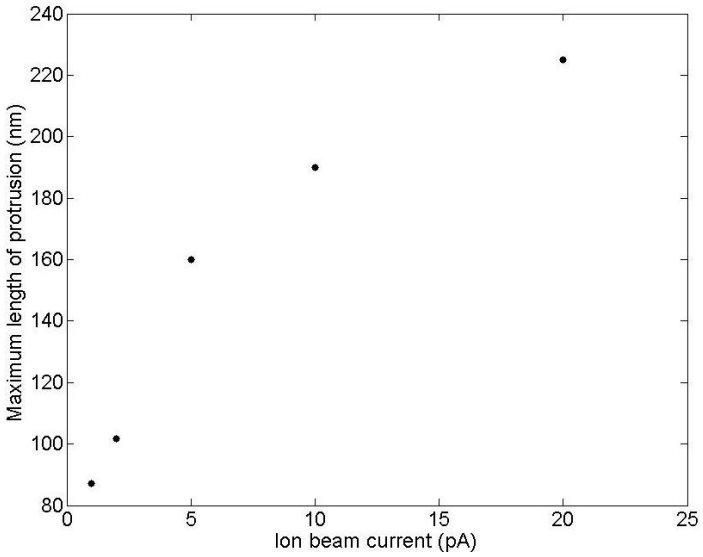

Figure 5. 8: Length of protrusion of nanorods as a function of ion beam current

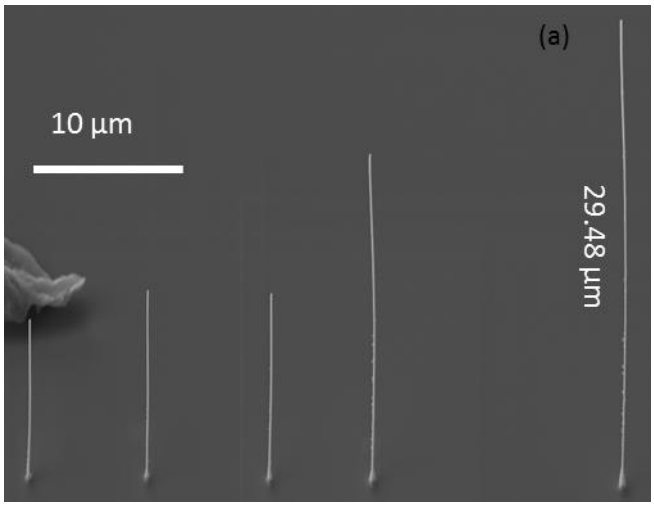

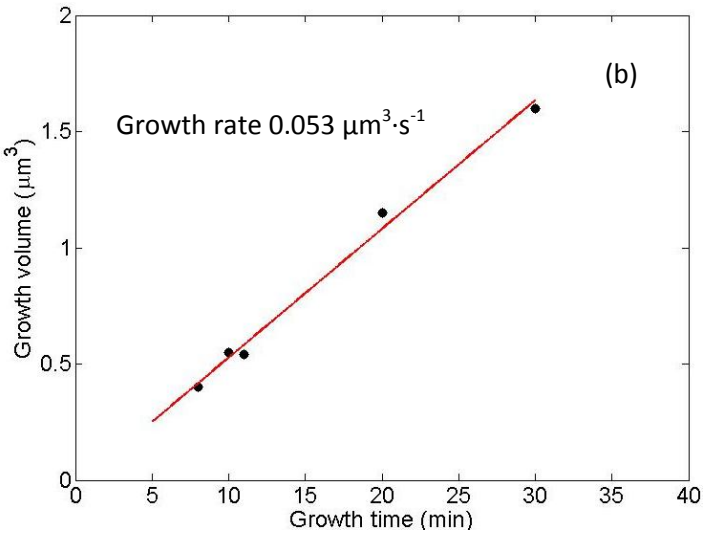

Figure 5. 9: (a) SEM images of nanorod grown for different time (nanorod grown with an accelerating voltage of Ga^+ of 30 keV, ion beam current of 1 pA, heating temperature of reservoir of 69^{o}C. The growth time of the nanorods from left to right is 8, 10, 11, 20, 30 mins, respectively) (b) Growth volume of nanorod as a function of growth time.

5.2 Nanorod diameter reducing with FIB

In order to make ultrasensitive resonator from FIB deposited C-W-nanorod, it is important to scale down its dimension including both length and diameter to gain higher resonant frequencies. The length of the nanorod is decided by the deposition time. The diameter of the nanorod is decided by the focus, the current of gallium ion beam and gallium ion sources. The well focused gallium ion beam with a current of 1 pA and energy of 30 kV has a diameter of 7 nm. However, in reality the smallest diameter of a FIB-induced deposition deposited vertical C-W-nanorod is 90 nm instead of 7 nm so far. This is due to the scatted gallium ions near the focused region also caused deposition. The reason for the effect of gallium ion source on the size of nanorod diameter is not well-known yet. Therefore, FIB milling with different process parameters was studied to reduce the thickness of vertical C-W-nanorods grown by FIB-induced deposition.

5.2.1 Different gallium ion beam current and energy

A vertical C-W-nanorod with a diameter of 155 nm and a length of 14 μm was grown in the rotation centre of the silicon substrate by FIB-induced deposition with a beam current of 1 pA at 30 kV. Then the gallium ion beam with a beam current of 10 pA at 30 kV scanned over the vertical nanorod with a defined area of 1μm×5μm to mill its sidewall while the silicon substrate was being rotated at a speed of 180^{o} per second. The detailed milling process can be seen in chapter 4. In order to investigate the effect of gallium ion beam current on diameter reducing by FIB milling, another two vertical C-W-nanorods with diameter of 168 nm and 183 nm, respectively, were milled by FIB with beam current of 20 pA and 50 pA, respectively, at 30kV. It shows in figure 5.10 (a) that the smallest diameter

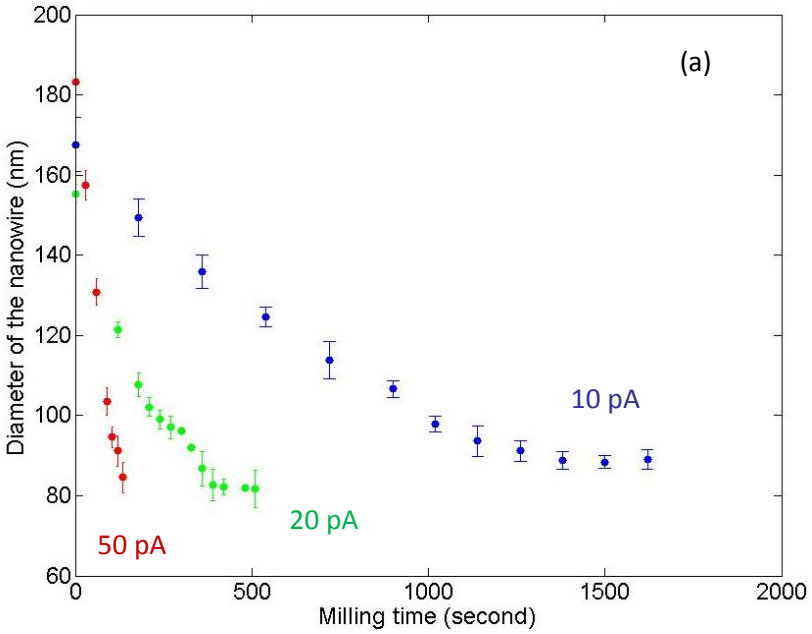

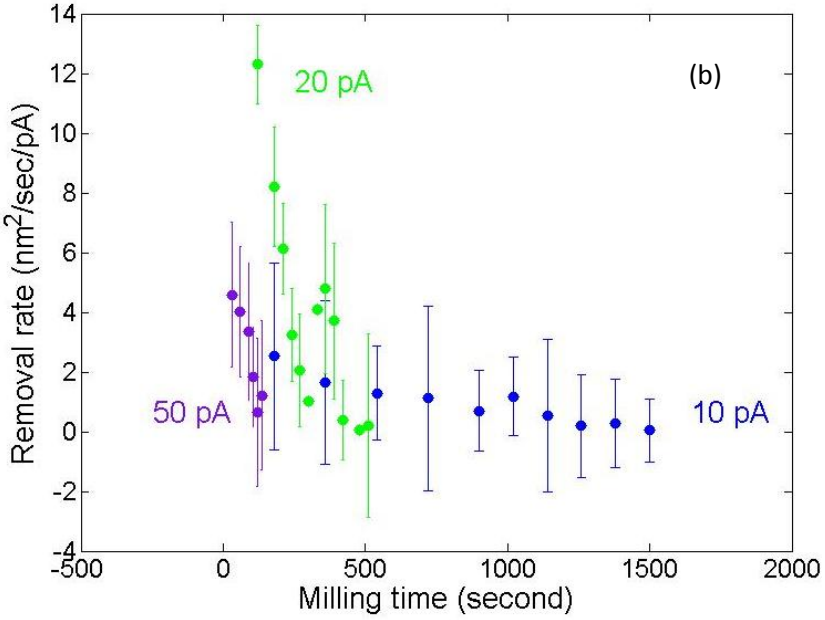

Figure 5. 10: Diameter reducing with different gallium ion beam current (a) Diameter of nanorod as a function of milling time with different beam current (b) Removal rate as a function of milling time with different beam current

achieved is about 80 nm through FIB milling with a beam current of 20 pA and 50 pA at 30 kV. However, the nanorod is easily bent after its diameter is reduced to 80 nm if FIB milling continues at 50 pA. For the FIB milling at 10 pA and 30 kV, it seems hard to reduce the diameter of C-W-nanorod after its diameter reached 88 nm. In order to fully understand the effect of gallium ion beam current on diameter reducing, data in figure 5.10 (a) was plotted as figure 5.10 (b).

It shows the corresponding removal rate of FIB milling with beam current 10 pA, 20 pA and 50 pA at 30 kV as a function of milling time. With increasing milling time, the removal rate of FIB milling with all beam current reduced. This reason is the received dose is reduced with the decreasing diameter. However, the removal rate at 50 pA, 30 kV reduces significantly and the removal rate at 10 pA, 30 kV reduces slowly. Thus considering of FIB milling time, we chose the beam current of 50 pA for milling.

In addition, the effect of FIB milling at a lower energy of 10 kV with different gallium ion beam current on diameter reducing of C-W-nanorod was also studied. Vertical C-W-nanorods fabricated by FIB-induced deposition with a diameter of 95 nm, 114 nm and 140 nm, respectively were milling by FIB through its side wall to reduce its diameter as shown in figure 5.11 (a).

After the diameters of C-W-nanorods were reduced by FIB with a beam current of 10 pA and 20 pA at 10 kV, the diameters reaches its saturation of 89 nm and 75 nm, respectively. For the milling with beam current of 50 pA at 10 kV, the diameter continue to reduce with increasing milling time until the vertical nanorod gets bent. The critical value of diameter is about 50 nm before it bends (the last point in the graph is where the nanorod became bent). Data in figure 5.11 (a) was re-plotted as shown in figure 5.11 (b). It shows the corresponding removal rate with FIB milling of vertical C-W-nanorods with a beam current of 10 pA, 20 pA and 50 pA at 10 kV. It can be seen the removal rate reduces after 90 seconds' milling for milling with all three beam currents at 10 kV.

5.2.2 Different gallium ion incident angle

Figure 5.12 is the schematic diagram of gallium ion beam incident angle. In order to investigate the effect of the incident angle of the gallium ion beam at 10 kV, 50 pA on reducing the diameter of vertical C-W-nanorods, a FIB-induced deposition deposited vertical C-W-nanorod in the rotation centre of the stage was milled with FIB at an incident ion angle of 45^{o} through tilting the sample stage of 9^{o}. In the meantime, the sample stage was rotated at a speed of 180^{o} per second. The detailed milling process is demonstrated in chapter 4 section 4.4. Figure 5.13 (a) shows the diameter of nanorods was reduced by milling its side wall through FIB with a rotation speed of its sample stage of 180^{o}/sec at an incident angle of gallium ion of 36^{o}, 45^{o}, 54^{o} and 63^{o}, respectively. It can be seen that the smallest diameter goes down to about 50 nm at an incident angle of 63^{o} and 54^{o} before the nanorod gets bend.

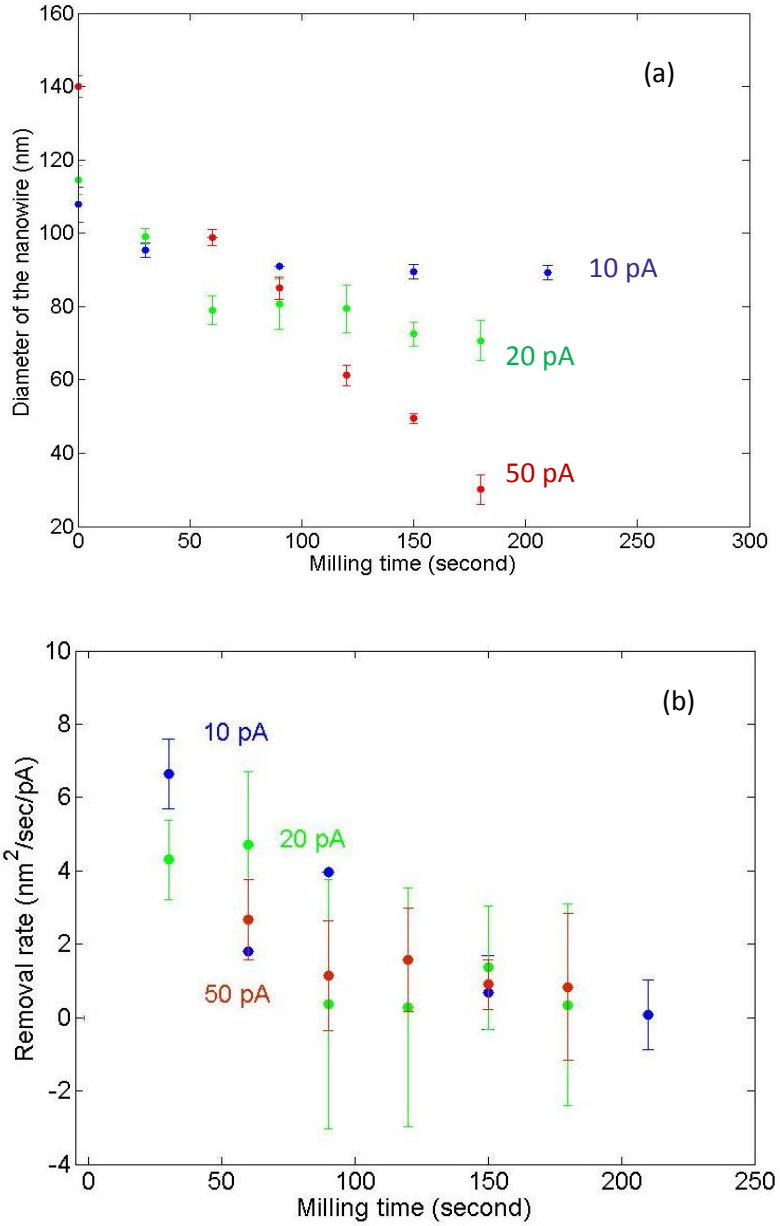

Figure 5. 11: Diameter reducing with different gallium ion beam current and energy (a) Diameter of nanorod as a function of milling time with different beam current and energy (b) Removal rate as a function of milling time with different beam current and energy

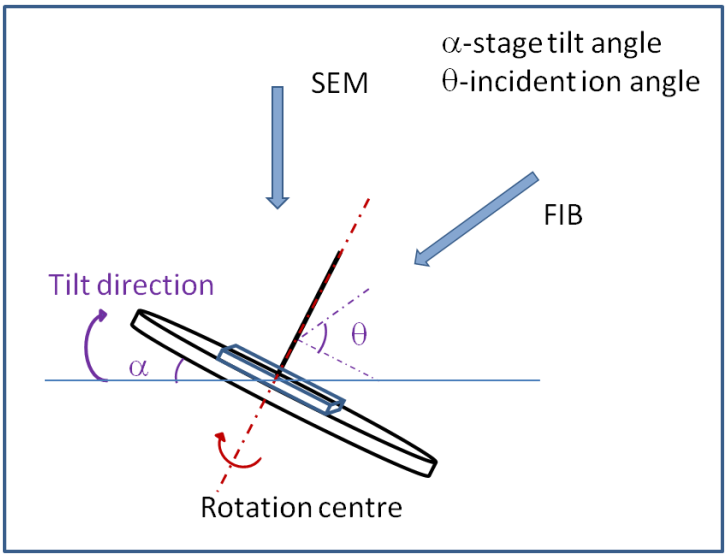

Figure 5. 12: Diagram of gallium ion beam incident angle. (α is the stage tilt angle. θ is the incident ion angle. θ= α+36°. Here we titled the stage from 0°, 9°, 18°, to 27°, respectively.)

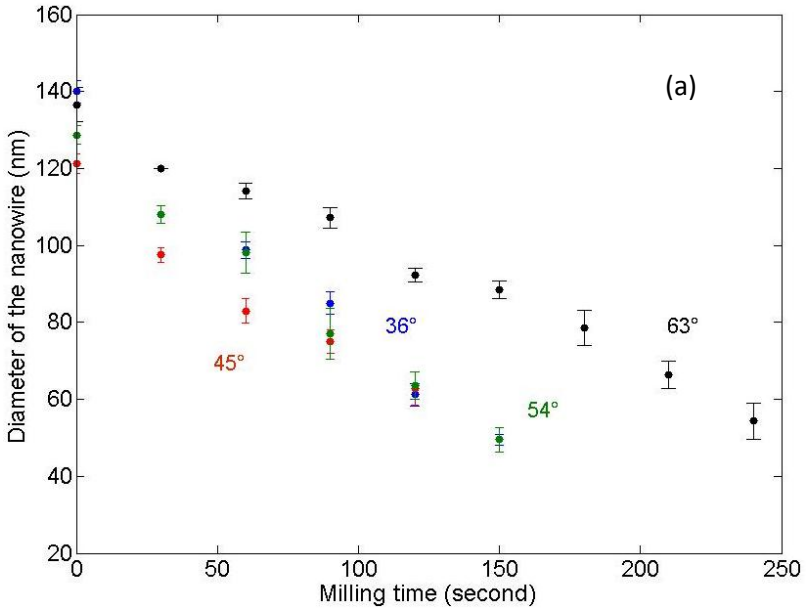

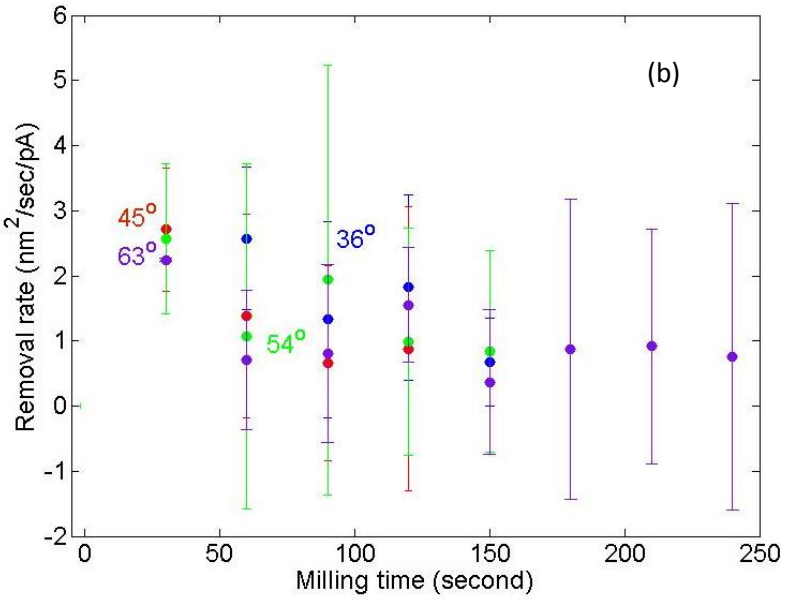

Figure 5. 13: Diameter reducing with different incident angel of gallium ion beam (a) Diameter of nanorod as a function of milling time with different incident angel of gallium ion beam (b) Removal rate as a function of milling time with different incident angel of gallium ion beam

For the incident angle of gallium ion of 45° and 36°, the nanorod gets bend at about 60 nm. In figure 5.13 (b), the same data was re-plotted to illustrate the removal rate with FIB milling of vertical C-W-nanorods at an incident angle of gallium ion of 36°, 45°, 54° and 63° with a beam current of 50 pA and a beam energy of 10 kV. It is clear that there is no obvious difference between the gallium ion incident angle of 36°, 45° and 54° to the removal rate with increasing milling time, but the removal rate at an ion incident angle of 63° is slower.

Therefore, the good incident angle of gallium ion is 63° at 10 kV, 50 pA to reduce the diameter of FIB-induced deposition deposited tungsten vertical nanorod.

In this section, the process parameter of reducing vertical C-W-nanorod's thickness by FIB milling was studied. The experiment results show that the minimum diameter of C-W-nanorod can be reduced to about 60 nm with a gallium ion current of 50 pA and energy of 10 kV at an incident ion angle of 63°.

5.3 Young's modulus measurement

In order to obtain the Young's modulus of C-W-nanorods fabricated with focused ion beam, force-displacement measurements with AFM on samples of doubly and singly clamped nanorods were carried out.

5.3.1 Young's modulus measurement of doubly-clamped nanorods

A doubly-clamped nanorod over a trench was fabricated with FIB and is shown figure in 5.14. The effective length of the nanorod, i.e. the part suspended over the trench, was about 6 μm. The diameter of the nanorod is 250 nm. Both free ends of the nanorod were fixed by FIB-induced tungsten deposition. The thickness of the deposition is 300 nm, the length and the width are 2 μm and 1 μm, respectively. The trench was milled by FIB with a depth of 1.5 μm. Both the length and the width of the trench were 6 μm. A force-displacement measurement was carried out with the AFM as demonstrated as section 4.2 in Chapter 4. Figure 5.15 is a standard tip deflection as a function of the piezo z-displacement, which can be directly obtained from the AFM (force-displacement) measurement. The piezo actuator moves down to 0 nm and the tip touches the surface, then the piezo actuator keeps moving further until the deflection of the tip reaches 50 nm as the target trigger threshold. The tip deflection as shown in figure 5.16 is slightly less than 50 nm, which is probably caused by the error of the AFM equipment. The tip deflection can be converted into the forced applied

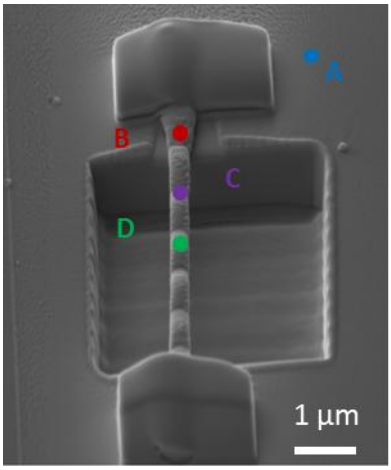

Figure 5. 14: SEM image of doubly-clamped beam over a trench on silicon substrate (Viewing at an angle of 54^{o}. A means a point on the silicon surface, B is a point on the edge of the nanorod, C is a point between the edge and middle points on the nanorod, D is a point on the middle of the nanorod)

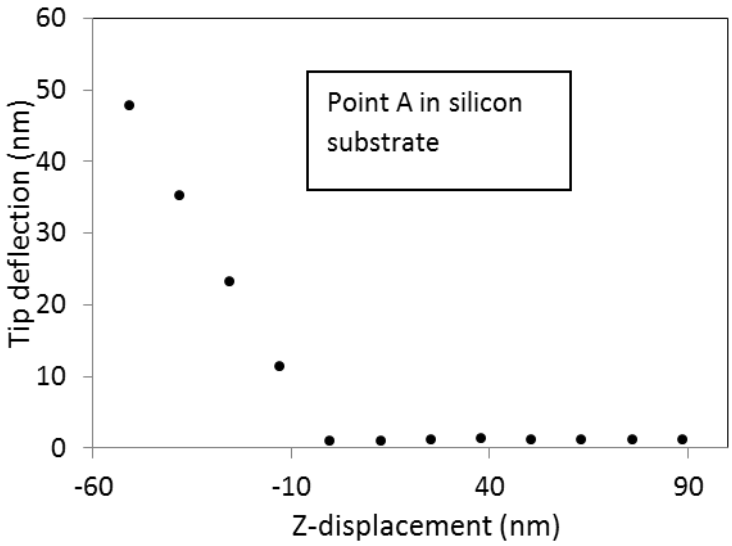

Figure 5. 15: Tip deflection of the cantilever as a function of piezo z-displacement. (This was obtained when the tip was pushing on the silicon surface)

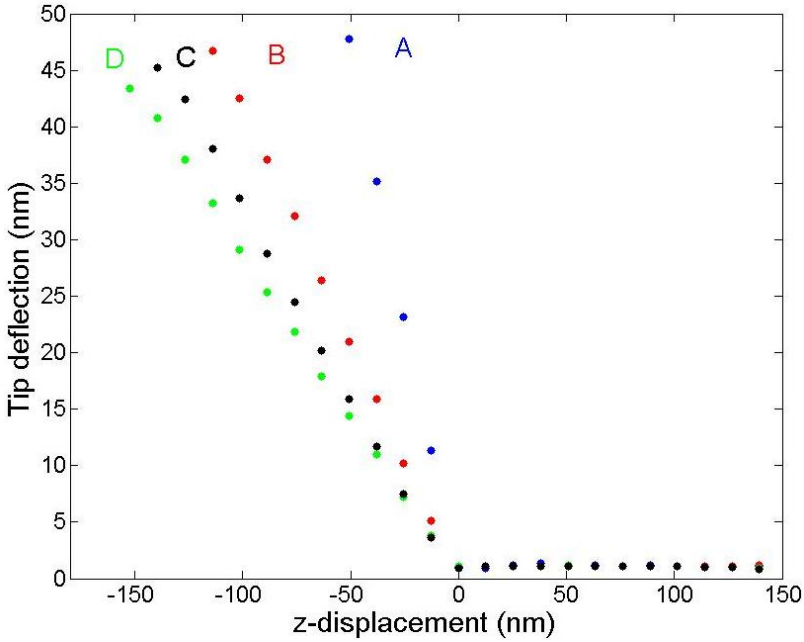

Figure 5. 16: Tip deflection as a function of piezo z displacement measurement on different positions along nanorods (The position of A, B, C, and D can be seen in figure 5.23)

on the surface (more details can be seen in the following). Figure 5.16 shows tip deflection measurements on a double clamped nanorod as a function of piezo z-displacement at different positions along its length. When the tip of cantilever was applied with a trigger threshold of 50 nm to the rigid surface of silicon (point A in figure 5.14), the slope of the curve was 1 as expected. When the tip moved along the suspended nanorod from one end to the other, the tip deflection slope decreased and reached a minimum value of 0.29.

Based on the following equations and Hooke's law, the as-obtained deflection-displacement curves can be converted into a typical force-displacement curve.

$$D_w = Z - D_t \quad (5.1),$$

$$F = D_t \times k \quad (5.2),$$

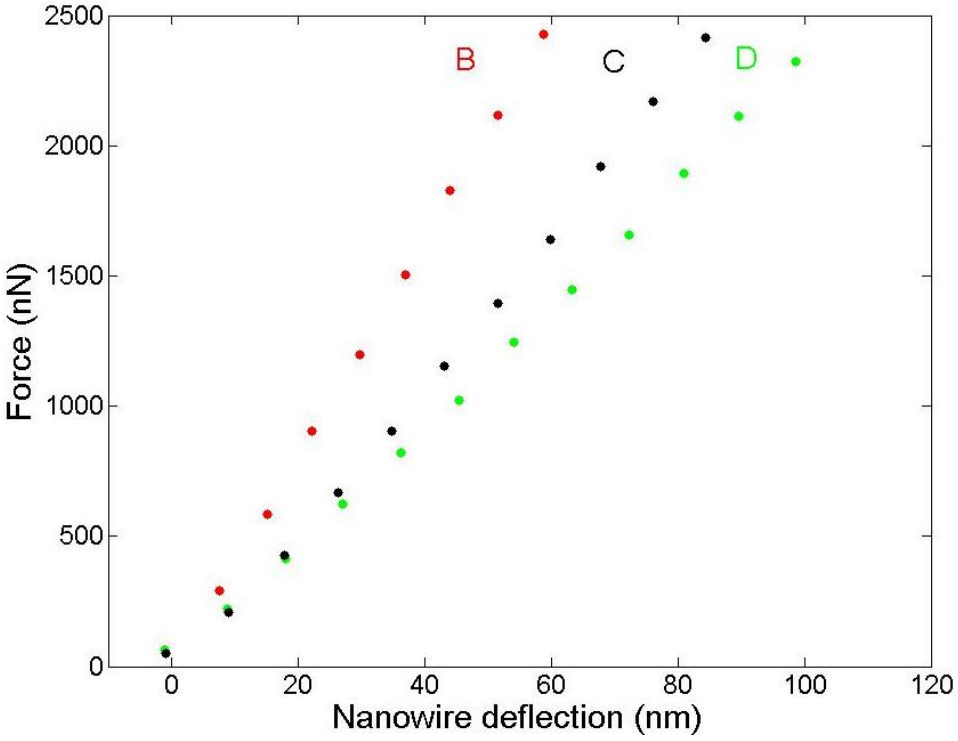

Figure 5. 17: Force as a function of the nanorod deflections measured on different positions along nanorods

in which D_w is the displacement of the nanorod during bending measurements, Z is z-displacement of the AFM piezo actuator, and D_t is the cantilever tip deflection. F is the force applied to the nanorod, and k is the calibrated spring constant of the cantilever. The slope of the curve in figure 5.15 and curve A in Figure 5.16 was -1 as expected, which showed that $Z=D_t$ due to the rigid surface. The magnitudes of the slope of curve B, C and D in figure 5.16 were less than 1, which means the nanorod deflection existed. According to equation (5.1), the nanorod deflection can be calculated and then the tip deflection can be converted into a force.

Figure 5.17 illustrates the force as a function of the nanorod vertical displacement studied on the same sample as for figure 5.15 and figure 5.16. It can be seen that with an applied force of 2500 nN the deflection of this doubly-clamped nanorod increased from 68 nm to 121 nm when the tip moves from the edge towards to the middle position of the nanorod. The slopes

of all the curves were linear, which showed that the deflection of the nanorod is elastic. The slope (dF/dD_w), i.e. the nanorod spring constant, was determined by linear fitting.

The force volume measurement was carried out with AFM by scanning an area of 8×8 μm^2 and the pixel was 32×32. The gap between pixels was 250 nm, which is same as the diameter of the nanorod. Therefore there is only one single set of force-displacement data points along the nanorod. However, in our measurement, five sets of data points along the nanorod were found. The possible reason is that part of the tip was broken and the diameter of the tip became larger than before (about 25 nm). At the same x position along the nanorod, the spring constant seemed to keep constant as seen in figure 5.18 (a). The distribution of the spring constant in both along and across the nanorod (as shown in figure 5.18 (b)) is corresponding to figure 5.18 (a).

Therefore, we then obtained the average spring constant of the nanorod and obtained its standard error as shown in figure 5.19. Figure 5.19 shows the spring constant of the doubly clamped nanorod as a function of the tip position along the nanorod. A decrease in spring constant was found during scanning from the edge up to the middle of the trench, which clearly proves that the nanorod was freely suspending in the trench and no plastic deformation of the nanorod happened. It must be noted that, two data points (outside of the two vertical dot line in figure 5.18 (a)) was excluded from each end of the nanorod to obtain a fitting with the theory. The reason for this is that in the measurements near the edges of the trench, the cantilever can touch the silicon surface when the nanorod is bent, and those data cannot fit the theory because of edge effects.

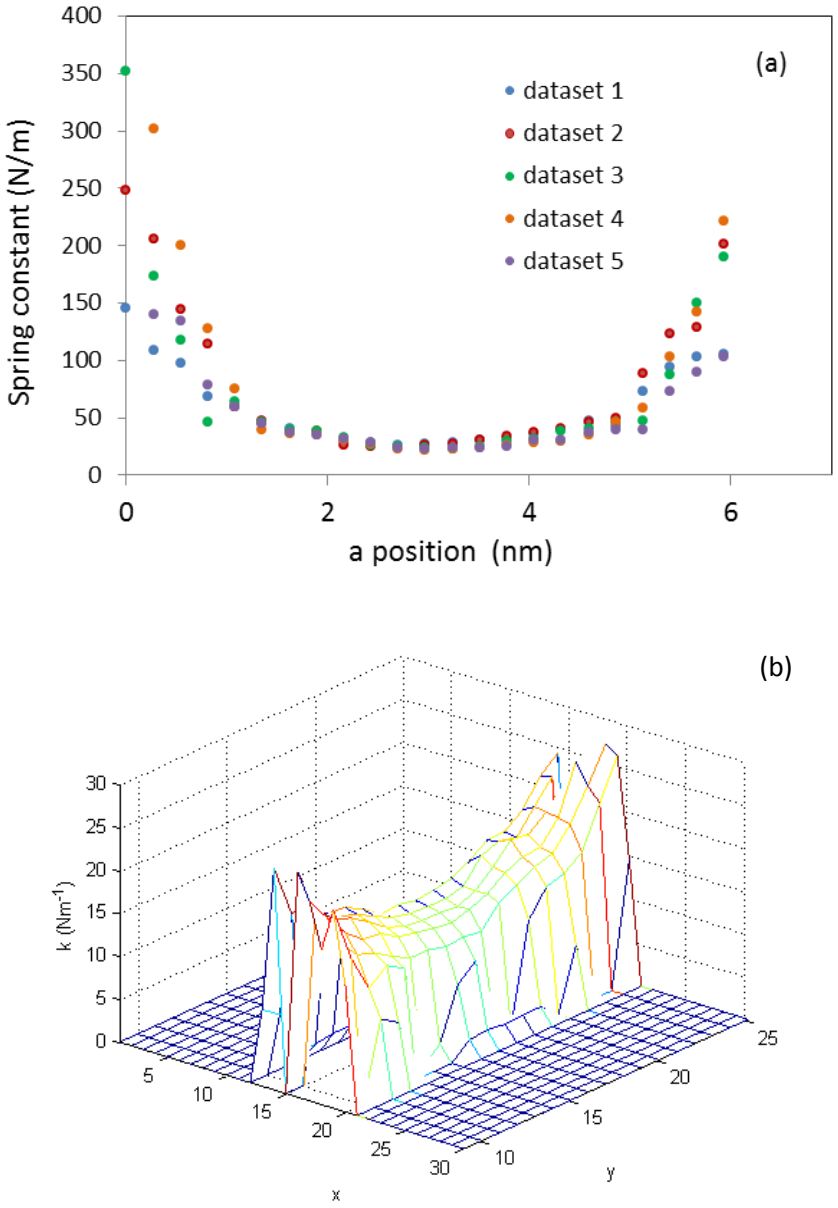

Figure 5. 18: (a) Spring constant of nanorods as a function of x position along the nanorod. (b) Distribution of the spring constant of the nanorod in 3D graph.

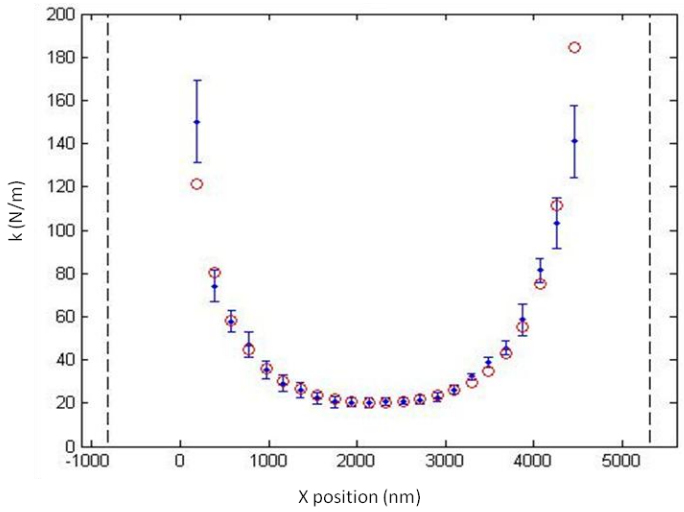

Figure 5. 19: Spring constant of nanorods as a function of x position along the nanorod (The red line is the theoritical fitting and the blue dot is the experimental data. The two vertical dot lines are the limitation of the experimental data on the two clamped ends).

The experimental data was fitted with the following equation (5.3), which is derived from the equation (3.12) mentioned in chapter 3.

$$k = \frac{3EIL^3}{(L-x)^3 x^3} \qquad (5.3),$$

where x is the AFM tip position. It has the same meaning as a in equation (3.12)

The effective length and Young's modulus of this nanorod as fitting parameters, the experiment data as shown in figure 5.19 is fitted. The radius of the nanorods was measured with SEM and repeated measurement gave its standard deviation, which is 400 ± 10 nm. The fitting result shows the effective length is 6.08± 0.072 μm and a Young's modulus of 19 ± 9 GPa. In this experiment, the determination of Young's modulus with different force applied on the same doubly clamped nanorod was presented in table 5.1. It can be seen that the Young's modulus was kept constant within small ranges of forces for three samples. The reason for this is the nanorod was deflected linearly according to the applied forces without touching the bottom of the trench. There is a variation of the Youngs' modulus from sample

to sample. It is probably caused by the fabrication conditions of the nanorod with FIB-induced deposition. The local pressure may affect the growth rate and the density of the nanorod. The Ga^+ ion beam might cause some damage of the nanorod, when it was fell down over the trench. When both the free ends of the nanorod were fixed by tungsten deposition, the extra deposition occurred on the nanorod might result in a larger diameter.

Table5.1 Young's modulus determination with different applied force by AFM

Sample	Length (μm)	Force (nN)	E (GPa)
1	6	2850	31± 9
		3420	32 ±4
2	5.6	2850	32± 4
		3420	28 ± 2
3	6.1	2280	17 ± 1
		2850	19±1

With a different tungsten gas precursor sources, another ten doubly clamped C-W nanorods were fabricated with FIB induced tungsten deposition. With the same AFM force displacement measurement and analysis method, the Young's modulus of the newly made samples was characterised. The Young's modulus as a function of the diameter of C-W nanorods was plotted as shown in figure 5.20. It is clear that the Young's modulus decreases from 87 GPa to 20 GPa with an increasing diameter of C-W nanorods from 110 nm to 330 nm.

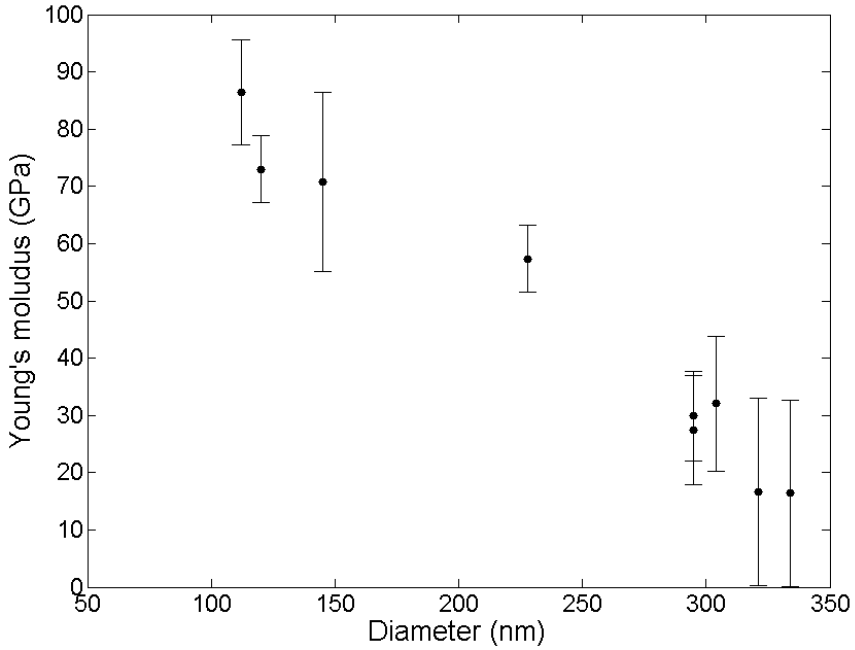

Figure 5. 20: Young's modulus as a function of diameter of the doubly clamped C-W nanorods fabricated with FIB induced tungsten deposition

5.3.2 Young's modulus measurement of singly-clamped nanorods

The singly clamped nanorod is scanned at different points in a line along the nanorod (as shown in figure 5.21) and force-deflection as a function of z piezo displacement curve was recorded as shown in figure 5.22. However, the baseline of the force-deflection curve was tilted, whereas it should be horizontal. The tilted baseline shows that there is an apparent deflection of the cantilever without touching the sample surface. This apparent deflection is likely due to a systematic problem of the AFM microscope. The laser light (which is used to measure the deflection of the cantilever) and the movement of the piezo have to be oriented in parallel to ensure a straight baseline. The tilted baseline here shows this wasn't the case. Therefore the deflection point of the laser on the cantilever beam changes laterally, while the piezo extends or is retracted. A correction was made by assuming that the offset in the tip deflection changed linearly with the piezo position once the tip contact with the surface After the correction of the slope of the force-displacement curves, and similar analysis to the doubly clamped nanorods, the stiffness (spring constant) of the system can be determined

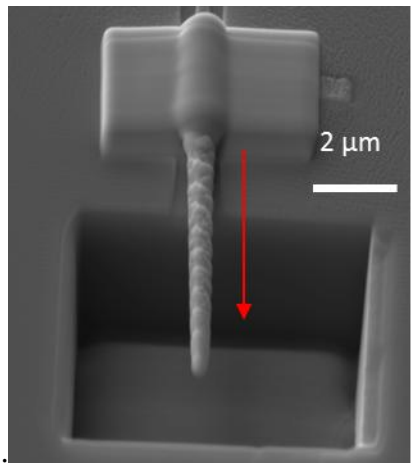

Figure 5. 21: SEM image of singly-clamped beam over a trench on silicon substrate (Viewing at an angle of 54^{o}. The red arrow on the nanorod is the position and direction the AFM tip scanned at)

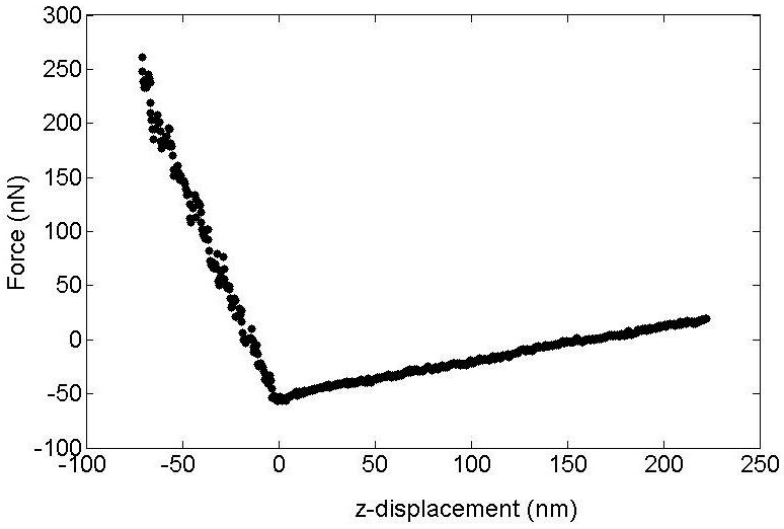

Figure 5. 22: Force as a function of z-displacement

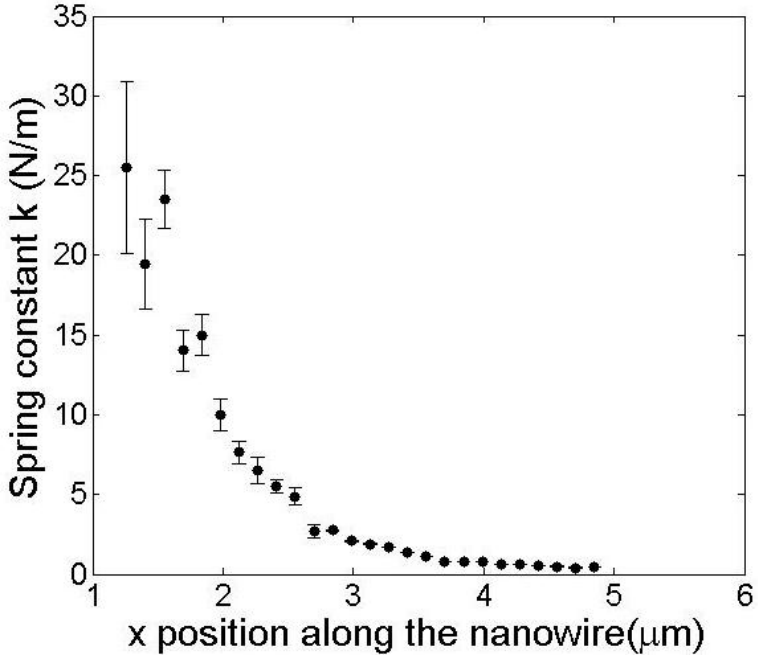

Figure 5. 23: Spring constant as a function of tip position along nanorod

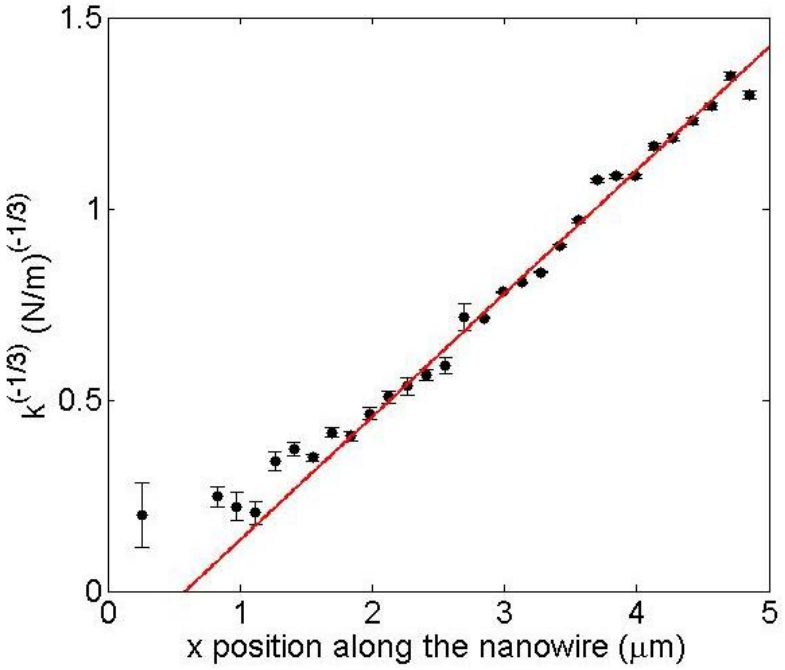

Figure 5. 24: Spring constant of the singly clamped nanorod as a function of x position (The red line is the linear fitting, which gives y=0.316x-0.162)

from the slope of the force-deflection curves and then the spring constant of the nanorod can be calculated. Figure 5.23 is the spring constant of the singly clamped nanorod as a function of the tip position along the nanorod. As expected the spring constant of the nanorod decreases with increased distance from the free end, which clearly proves that the nanorod was freely suspending in the trench and no plastic deformation of the nanorod happened. In order to determine Young's modulus of the nanorod, the typical equation (3.14) was written as follows:

$$k = \frac{3EI}{\left(x - x_0\right)^3}$$

then $$k^{-1/3} = ax - b$$

where x_0 is the offset of the x position on the nanorod the tip pushed,

$$a = (3EI)^{-1/3},$$

$$b = (3EI)^{-1/3} x_0$$

Figure 5.24 shows a graph relating $k^{-1/3}$ to x. The Young's modulus can be extracted from the slope. The linear fitting gave the uncertainty of the slope, which is ±0.0105. The radius of the nanorod is 160±4 nm. Therefore, the Young's modulus is 21±4 GPa, which is slightly bigger than that of the doubly clamped beams. This is probably affected by the fabrication conditions of the nanorod with FIB-induced deposition. The density and the stiffness are affected by the growth rate or the local gas pressure.

In this section, the Young's modulus was obtained from the measurement of both doubly and singly clamped C-W-nanorods with AFM force-displacement measurement. The Young's modulus of C-W-nanorods shows a size-effect, which ranges from 87 to 20 GPa with a diameter increasing from 110 nm to 400 nm.

5.4 Set up for resonant frequency dynamic measurement with SEM linescan

In order to observe harmonic oscillations of a C-W-nanorod at its natural frequency, a system set-up for monitoring mechanical vibration was developed by installing a piece of electronic piezo actuator in the SEM/FIB system. This set-up is shown in figure 5.25. A piece of thin PVDF piezo film was used as an electrical actuator to excite the nanorod vibrates. The piezoelectric film is polyvinylidene fluoride (PVDF) with thin-film gold as electrodes on both sides. Compared with the PZT ceramic piezo, the PVDF piezo has a much wider range of frequencies from 0.001 Hz to 10^9 Hz. Besides, it is suitable to work in high vacuum. This piezo film has a thickness of 28 μm and an area of about 3×2 cm^2. The thickness of the piezo film and the applied voltage on it determine the displacement of the piezoactuator. The piezoactuator was set on the top of the SEM's sample holder by silver paint. Silver paint exhibits a more physically stable connection between the piezo film and sample holder by comparison with general glue. Due to the exposure of the electrodes of the piezo film, an extra piece of copper as shielding was used to prevent electrostatic deflection of the electrons from the SEM.

An ac voltage provided by a function generator (Keithly 3390) was applied to the piezo actuator. The drive frequency and the amplitude of the piezo actuator were controlled in the range of kHz and up to 20 V_{pp} by adjusting the function generator. The function generator was connected to the feedthrough of the SEM chamber through by a standard BNC cable with a D-connector. This was also connected to the piezo actuator by coaxial cabling. The piezo actuator was grounded by connecting the negative electrode of the piezo film to the ground. This can prevent the electrons and secondary electrons from being deflected because of extra potentials. The grounding also stops the SEM imaging drifting effectively. Figure 5.26 shows the schematic program of the electrical circuits of the piezo-actuator.

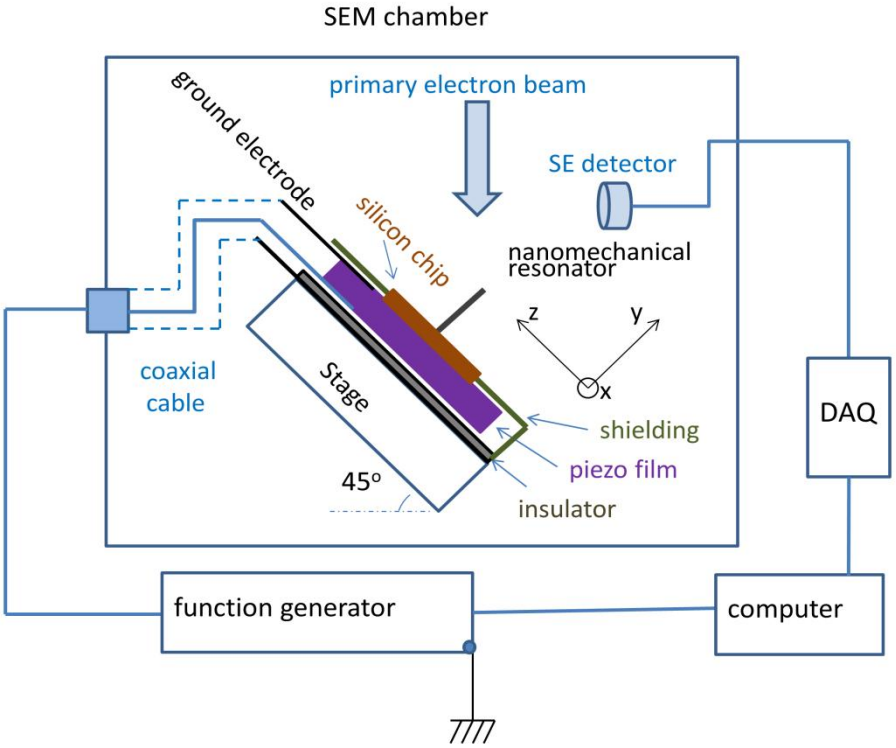

Figure 5. 25: Schematic diagram of the experimental set-up. (SE: secondary-electron; DAQ: data acquisition card.)

In order to achieve maximum displacement of the piezo, an appropriate drive is the first consideration. Here we chose a commercial function generator (Keithley 3390) as our piezo-actuator drive. The output voltage range of this function generator is 20 V_{pp}. According to the information on the data sheet of the PVDF piezo, this output voltage gave an ideal displacement of piezo-actuator of 4 nm.

The maximum output current of the piezo-actuator drive is also very important. The required drive current is proportional to the rate-of-change in voltage

$$I = C\frac{dV}{dt} \tag{5.4},$$

where C is the capacitance of the piezo, dV/dt is the rate-of-change in voltage

For a sinusoidal voltage, the maximum required current is

$$I_{\max} = \pm V_{pp} \pi C f \tag{5.5}$$

In my experiment the capacitance of the piezoactuator is 1.36×10^{-9} F, and the maximum frequency 1MHz. Therefore the maximum current needed from the drive is 85.4 mA. The Keithley 3390 has the max output current is 200 mA, which meets our request.

The bandwidth of the piezoactuator drive is also very important. If the operation frequency exceeds the bandwidth, the output power will drop quickly. From the technical data sheet of the function generator (Keithley 3390), we notice that the drive bandwidth is 50 MHz, which is much larger than we need (1MHz).

We must also check the actual power from the driver is applied to the piezoactuator. The whole electrical system is simplified to the circuit shown in figure 5.26. R_0 is the output impedance from the power source (i.e. function generator), which is about 110 Ω based on the data sheet of the function generator. R_1 is the impedance of the feed through of SEM chamber, which is about 50 Ω based on its data sheet. R_2 is the impedance of the cables between the piezoactuator and power source, which is about 50 Ω. If we assume the piezoactuator works at a maximum frequency of 1MHz, its impedance will be 170 Ω. From the impedance ratio, we can see 55% of the power from the drive is reflected. However, there is still enough power to excite the piezo to vibrate according to our observation in the experiment. In future, if the piezo vibrates in higher frequencies (larger than 1 MHz), it is very important to work on the selection of impedance-matched cables and feed-through. A data acquisition system was designed to control the measurement automatically. This data acquisition system reduced the measurement time significantly, thereby minimizing carbon deposition on the nanorod. The data acquisition system includes a data acquisition card (PCI6035E) with a maximum sample rate of 390 kS/second and a LabVIEW program as shown in Appendix II.

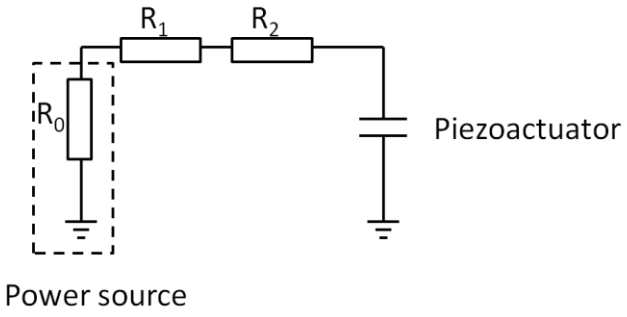

Figure 5. 26: Electrical circuit of the piezoactuator system

The experiment is carried out with our homemade electrical piezoactuator inside a commercial SEM with standard linescan techniques. The setup design itself is similar to that reported by Utke (87), Nishio (11) and Nonacha (174). However, in the work of Utke *et al*.(87), rather than linescan, an electron beam is fixed (i.e. spot mode). Using lock-in detection at the drive frequency, the phase and amplitude of the SE signal is measured. This technique allows detecting resonant frequency and Q-factor of nanomechanical resonators. In the work of Nishio *et al*. (11), spot mode is used to detect the vibration amplitude, resonant frequency and Q-factor. However, the vibration amplitude can't be detected when it is much smaller than the radius of the resonator. In the work of Nonaka *et al*. (174), thermal noise excitation was used to drive the resonator vibrating. Similar to my work, linescan was used to detect vibration amplitude, resonant frequency and Q-factor. With his method, the small vibration amplitude, which is smaller than the radius of the resonator also can be detected by fitting a model. This model took consideration of the cross-sectional geometry by assuming a cylindrical resonator with uniform material properties. However, with my technique, the model is not required. My technique can be straightforwardly applied to resonators with arbitrary cross-sectional geometry, and to resonators whose materials properties are not radically homogeneous.

5.4.1 Testing of system measurement set-up by using an AFM cantilever

An AFM cantilever was used as a resonator instead of a C-W-nanorod so as to test the reliability of the home-made resonant frequency measurement system, as shown in figure 5.27 (a).

Cantilever vibrations in the SEM chamber were induced by a thin piezo-electric actuator. The applied voltage through the function generator is 20 V_{pp} and the driving frequency was swept from 15.06 kHz to 15.26 kHz. During the vibration of the cantilever, by frame-integrating the signal with a scan speed with a cycle time of 2.6 seconds, an SEM image of AFM cantilever vibration can be observed. In order to record the vibration information of the cantilever, a single static electron beam was focused on its edge, and the time averaged secondary electron voltage as a function of the driving frequency was quantitatively obtained. Figure 5.27 (a) is an SEM image of the cantilever when it is not vibrating and (b) is an image of the vibration of the cantilever. Figure 5.27 (c) shows the driving frequency as a function of secondary electron voltage. From the Lorentz function fit, it can be seen that the vibration frequency of the cantilever is around 15.17 kHz in vacuum.

At the same time, the resonant frequency of this rectangular AFM cantilever (with a spring constant of 0.02 N/m, a length of 200 μm, a width of 20 μm and a thickness of 0.6 μm) was also tested with an AFM system by auto-tuning in air. The AFM software executed a routine resulting in the identification of a resonant peak, which is the primary resonant frequency of the cantilever. Its resonant frequency is found to be 14.9 kHz. Therefore testing result from the AFM confirmed that the homemade system setup for resonant frequency detection is reliable.

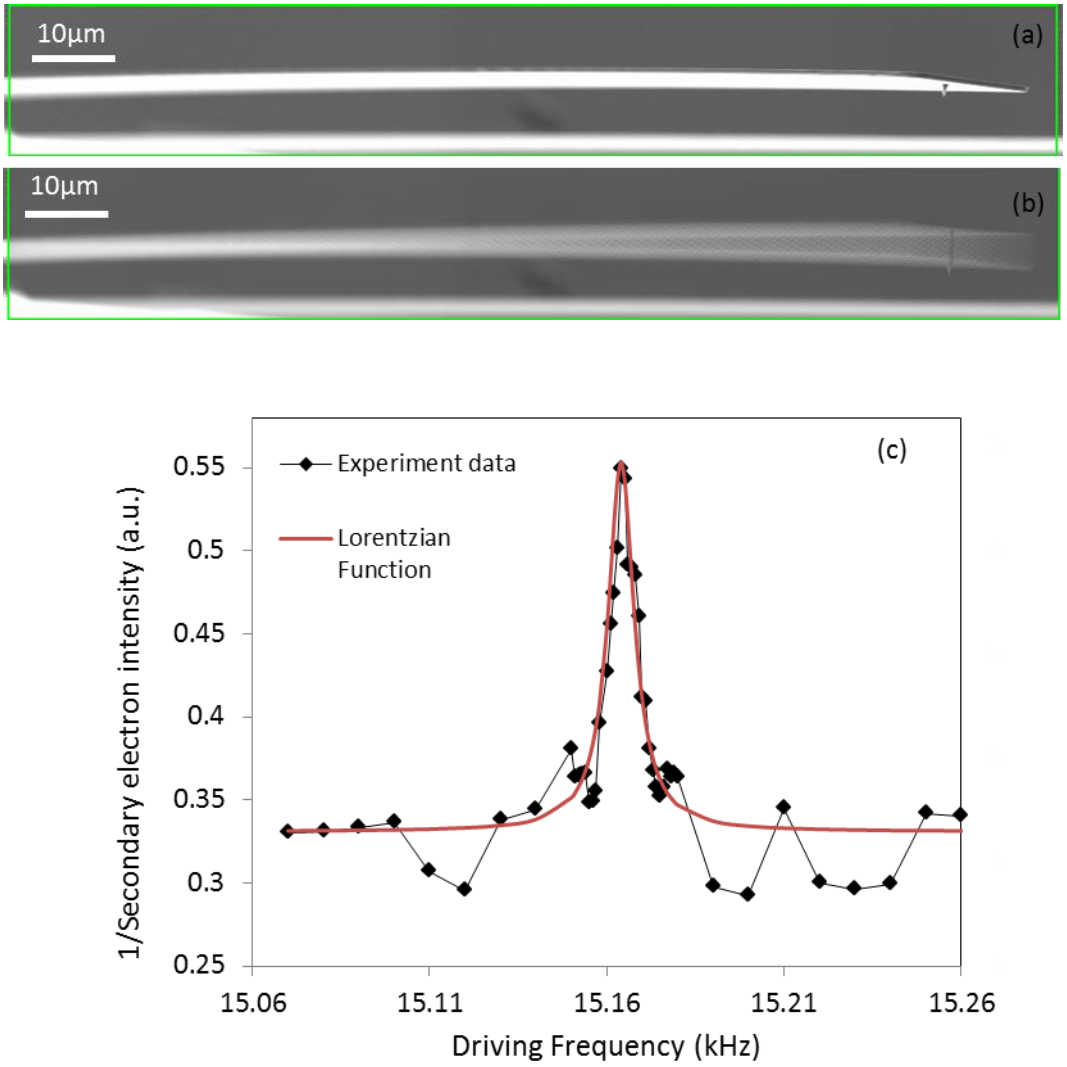

Figure 5. 27: SEM image of (a) without and (b) with vibration of the AFM cantilever, (c) is SE signal as a function of driving frequency (The black dot is the experiment data and the red line is the Lorentz function fitting)

5.4.2 Detection of resonant frequency of C-W-nanorods

Vibration of a C-W-nanorod was observed with this experimental set-up, and shown in figure 5.28. This nanorod was fabricated by focused ion beam, with a constant beam current of 1 pA at an accelerating voltage of Ga^+ ions of 30 kV. The nanorod has a length of 68 µm and a diameter of 150 nm. When the function generator applied a voltage of 20 V_{pp} to the piezo film and swept the excitation frequency in certain range, the resonant frequency of the nanorod was found to be 25.6 kHz.

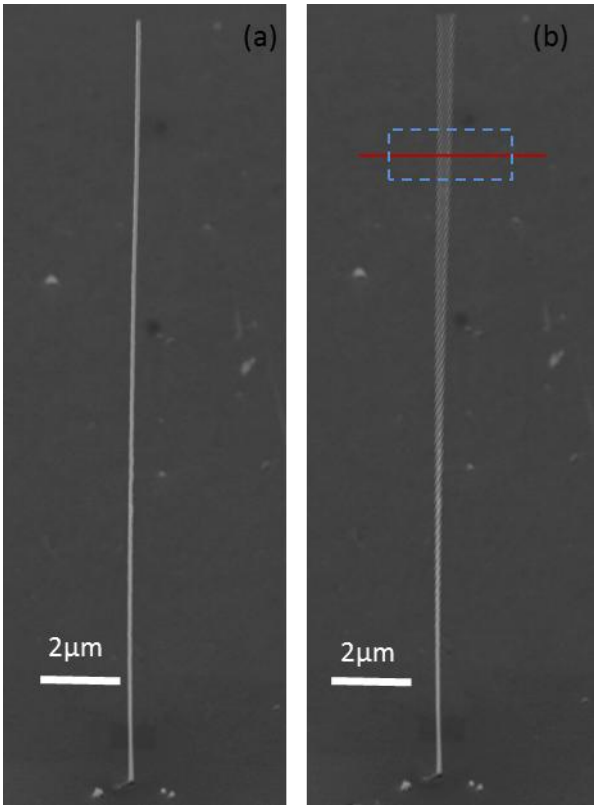

Figure 5. 28: SEM image of (a) without and (b) with vibration of the C-W-nanorod (both of the images were viewed at angle of 45^{o} to the surface normal. The red line is the track of the line scan as shown in Figure 5.29 (b). The rectangle area was zoomed in as shown in Figure 5.29 (a))

In order to read out the harmonic oscillation signal of the tungsten mechanical resonator qualitatively, a scanning single electron beam (linescan) of the SEM was also employed as shown in figure 5.29 (b). Linescan of SEM means the single electron beam was scanned along a single line instead of full screen as the typical raster scan. Measurements were made with the nanorod oriented in the *y*-direction. The nanorod was excited so that it performed sinusoidal transverse oscillations in the *x*-direction. Figure 5.33 shows the detailed schematic diagram of the geometry. The electron beam was scanned in the *x*-direction at some fixed value of *y* as shown in figure 5.28 (b) and figure 5.29 (a). The average secondary voltage signal intensity as a function of the *x* position was then obtained. This is shown in figure 5.29 (b). In order to obtain the absolute vibration amplitude of the nanorod, both the stationary linescan and vibrating linescan are necessary. Based on the theory shown in the following

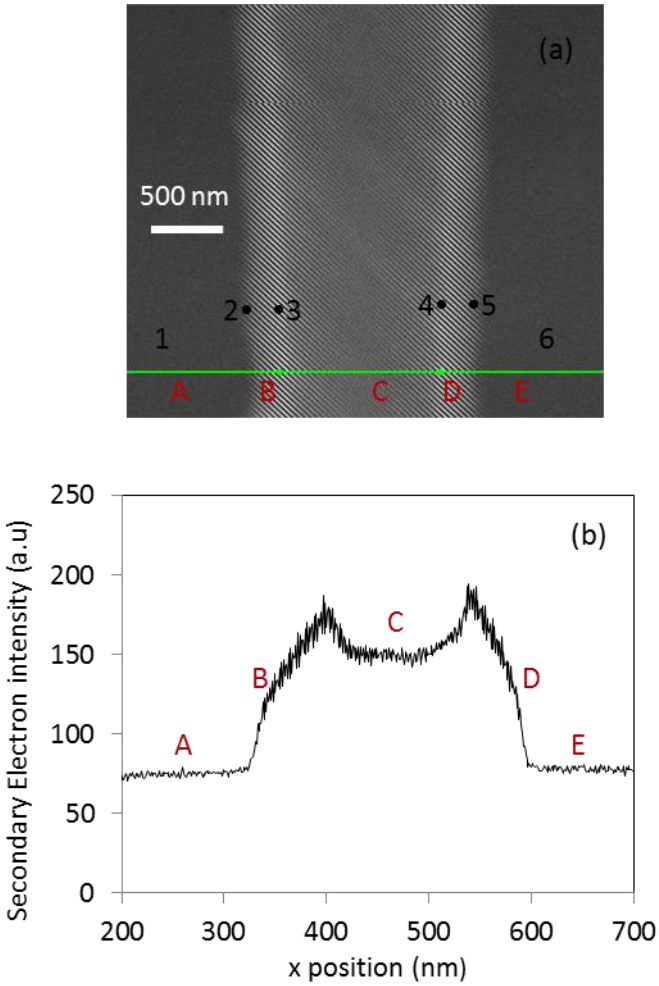

Figure 5. 29: (a) Line scan across the vibrating nanorod (b) Electron beam intensity as a function of x position (extracted from line scan along the vibrating nanorod as the red line shown in Figure 4.15 (b)) (area A and E is corresponding to 1 and 6, respectively; area B and is corresponding to 2-3 and 4-5, respectively; area C is corresponding to 3-4)

section 5.4.4, the vibration amplitude can be calculated. During the sweeping of the driving frequency, both stationary and vibrating linescans are collected automatically at each frequency step, then a driving frequency as a function of vibration amplitude can be plotted. Through forced Lorentz fitting, the resonant frequency and *Q*-factor of the nanorod can be found. The details about the measurement and data analysis will be shown in section 5.5.4.

5.4.3 Dimension scaling

The dimension scaling of cantilever resonators with a rectangular cross-section was demonstrated in chapter 3. Here, we calculated the dimension scaling of resonators with a circle cross-section for the resonant frequency characterisation with the above setup.

Suppose a nanorod has a length L and a circular cross section with a radius r. Its resonant frequency is

$$f_0 = \frac{ar}{L^2} \tag{5.6},$$

where

$$a = \frac{3.52}{2\pi}\left(\frac{E}{4\rho}\right)^{1/2} \tag{5.7},$$

E is the Young's modulus and ρ is the mass density. From the measurement of several nanorods we obtained $a \sim 900$ ms^{-1}.

The stiffness at the free end of the nanorod (see equation (3.14)) is given by

$$k = \frac{\beta r^4}{L^3} \tag{5.8},$$

where

$$\beta = \frac{3E\pi}{4} \tag{5.9}.$$

From static bending measurements, we obtained the Young's modulus (E=100 GPa), β = 2×10^{11} Nm^{-2}.

Combining (5.6) and (5.8) we find that the radius needed to give a nanorod with resonant frequency f_0 and stiffness k is given by

$$r = \left(\frac{k}{\beta}\right)^{2/5} \left(\frac{a}{f_0}\right)^{3/5} \tag{5.10}$$

The amplitude of the oscillation at the free end of the nanorod at resonance is given by

$$a = \frac{FQ}{k} \tag{5.12}$$

where F is the driving force from the piezo actuator and Q is the quality factor. From the measurement of a nanorod of length about 68 μm we obtained an amplitude of 5 μm and Q of 440, so F is 3×10^{-13} N. On the assumption that both the driving force F and the Q do not change as the frequency increases, then

$$r = \left(\frac{FQ}{\beta a}\right)^{2/5} \left(\frac{a}{f_0}\right)^{3/5} \tag{5.13}$$

Equation (5.13) can be used to determine the radius needed for a cantilever with a certain resonant frequency f_0 and a certain amplitude a at resonance as shown in figure 5.30. The length can then be determined from equation (5.6) as shown in figure 5.31.

From figure 5.30 and figure 5.31, we find that if we want an amplitude of 100 nm (which should be measureable in an SEM) and a resonance at 1 MHz, the radius should be about 40 nm and the length should be about 4 μm.

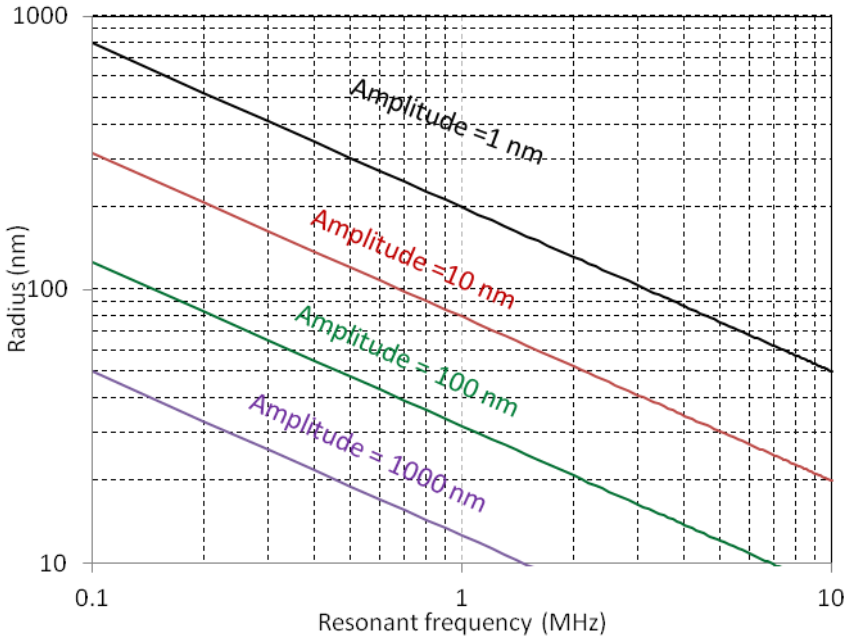

Figure 5. 30: Variation of nanorod oscillation of amplitude for different radius and resonant frequency

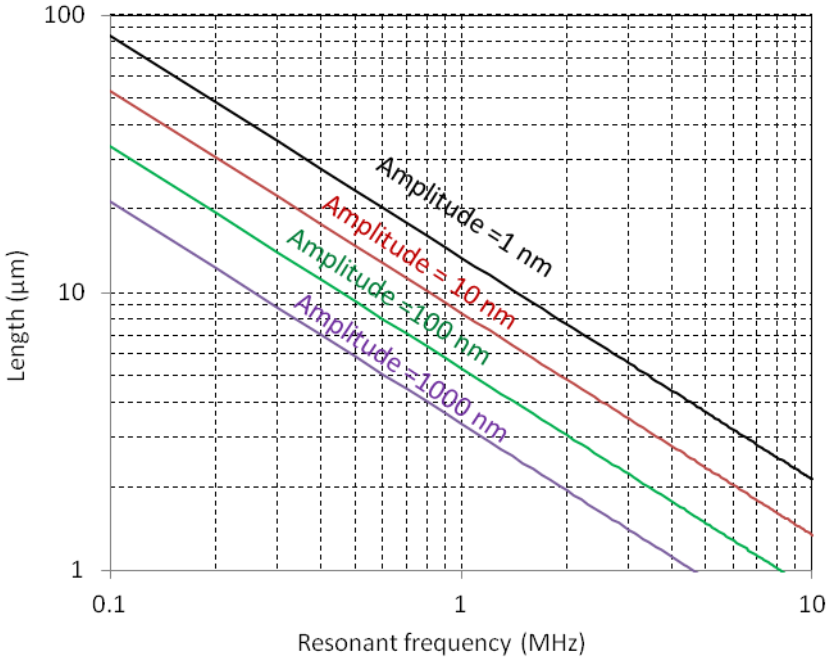

Figure 5. 31: Variation of nanorod oscillation of amplitude for different lengths and resonant frequency

5.4.4 Secondary electron responses from an oscillating cantilever

Detection of the oscillation of cantilevers was attempted in an SEM. We begin by analysing the secondary electron signal detected when the primary electron beam is scanned linearly across an oscillating cantilever of width 2*r*. The geometry is shown in figure 5.35: the cantilever is oriented in the *y*-direction and oscillates in the *x*-*y* plane. The electron beam is scanned across the cantilever in the *x*-direction at a fixed value of *y* at a fixed rate *dx*/*dt*. At this value of y the amplitude of the cantilever oscillation is *a*. The voltage generated by the secondary electron detector is sampled every τ seconds.

We define a response function g(*x*) as the secondary electron voltage when the SEM is scanned across the stationary cantilever. If the cantilever is harmonically driven at frequency *f*, the instantaneous secondary electron voltage is now g($x - a \sin\theta$), where $\theta = 2\pi ft$. The cantilever is assumed to oscillate rapidly by comparison with the e-beam scanning speed of 1.97nm·μs^{-1}; it also relates to the sampling rate of 390 kS s^{-1} so that the measured secondary electron signal is the time-averaged secondary electron voltage over all possible positions of the nanorod:

$$\left\langle V_{SE}(x)\right\rangle = \frac{1}{2\pi}\int_0^{2\pi} g\left(x - a\sin\theta\right)d\theta \qquad (5.14).$$

In principle this allows the measured signal to be calculated for any arbitrary response function g(*x*), which can be determined by measurements on the stationary cantilever. In the case where g(x) is a "top hat" function (*i.e.* where g(*x*) can take only two values: g(*x*) = V_{on} when the electron beam is incident upon the cantilever and g(x) = V_{off} when it is not), $\langle V_{SE}(x)\rangle$ can be calculated analytically as follows.

The position of the radial centre of the cantilever is given by $x_0 = a\sin\theta$, where $\theta = 2\pi ft$. The positions of the radial edges of the cantilever are given by $x_1 = a\sin\theta - r$, and $x_2 = a\sin\theta + r$.

In terms of the relationship between absolute vibration amplitude and the radius of the nanorod deposition by FIB-induced deposition, two cases will be discussed.

5.4.4.1 Small vibration amplitude (a<r)

$a<r$ ("small amplitude oscillations" as shown in figure 5.32 (a))

For $|x| < (r - a)$ the electron beam hits the cantilever for all θ, so the average secondary electron voltage is $\langle V_{SE} \rangle = V_{on}$.

For $|x| > (r + a)$ the electron beam misses the cantilever for all θ, so the average secondary electron voltage is $\langle V_{SE} \rangle = V_{off}$.

For $(r - a) < |x| < (r + a)$, (see figure 5.32 (a)) the e-beam hits the cantilever when $\theta_1 < \theta < \theta_2$ and misses the cantilever for the rest of the full-cycle. Hence

$$\langle V_{SE} \rangle = \frac{1}{2\pi}\left\{V_{on}(\theta_2 - \theta_1) + V_{off}(2\pi - (\theta_2 - \theta_1))\right\} \quad (5.15),$$

where $\theta_1 = \sin^{-1}\{(x - r)/a\}$ and $\theta_2 = \pi - \theta_1$. Hence

$$\frac{\langle V_{SE} \rangle - V_{off}}{V_{on} - V_{off}} = \frac{1}{2\pi}\left[\pi - 2\sin^{-1}\left(\frac{|x| - r}{a}\right)\right] \quad (5.16).$$

5.4.4.2 Large vibration amplitude (a>r)

$a>r$ ("large amplitude oscillations" as shown in Figure 5.32 (b))

For $|x| > (r + a)$ the electron beam misses the cantilever for all θ, so the average secondary electron voltage is $\langle V_{SE} \rangle = V_{off}$.

For $(a - r) < |x| < (a + r)$ the situation is the same as above, and equation (5.16) still holds.

For $|x| < (a - r)$, (see Figure 5.32 (b)) the e-beam hits the cantilever when $\theta_3 < \theta < \theta_4$ and misses the cantilever for the rest of the half-cycle.

Hence

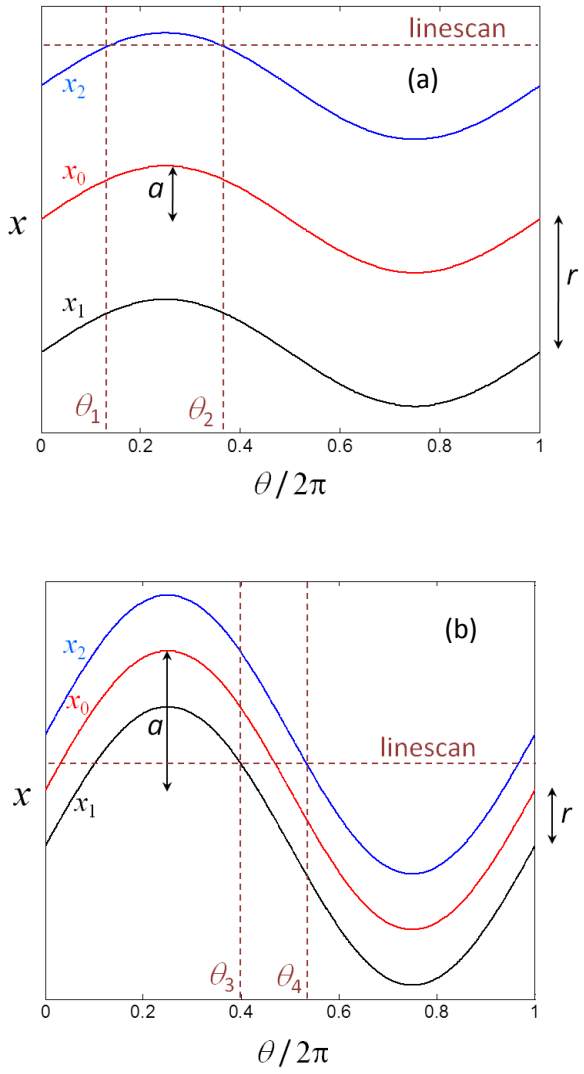

Figure 5. 32: The position of the central axis x_0 (red) and edges x_1 (black) and x_2 (blue) of a cantilever of width $2r$ as a function of $\theta = 2\pi ft$. (a) the amplitude a of the oscillation is smaller than r; the horizontal dashed line shows an illustrative electron-beam scan for the case $(r - a) < |x| < (r + a)$; (b) the amplitude a of the oscillation is larger than r; the horizontal dashed line shows an illustrative electron-beam scan for the case $|x| < (a - r)$.

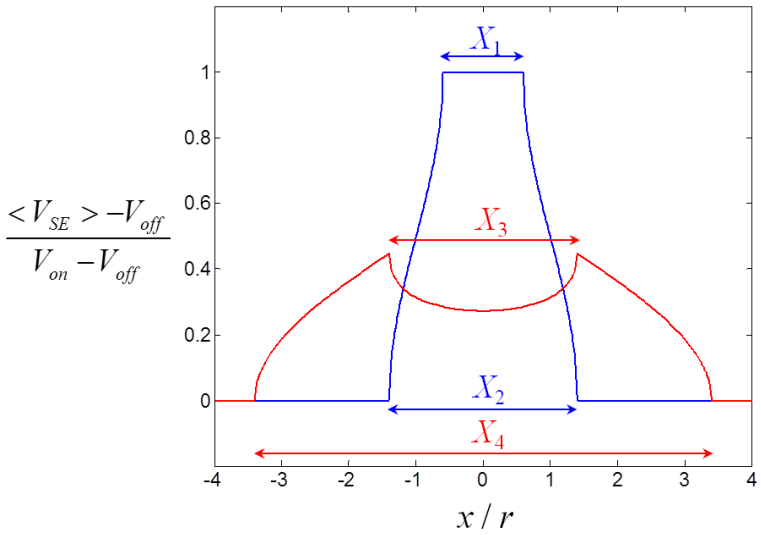

Figure 5. 33: Calculated time-averaged secondary electron voltage as the electron-beam is scanned across a cantilever of width 2r oscillating with amplitude a. Blue line: $a = 0.4r$; red line: $a = 2.4r$. The X_i are the distances between discontinuities in the voltage (see text for details)

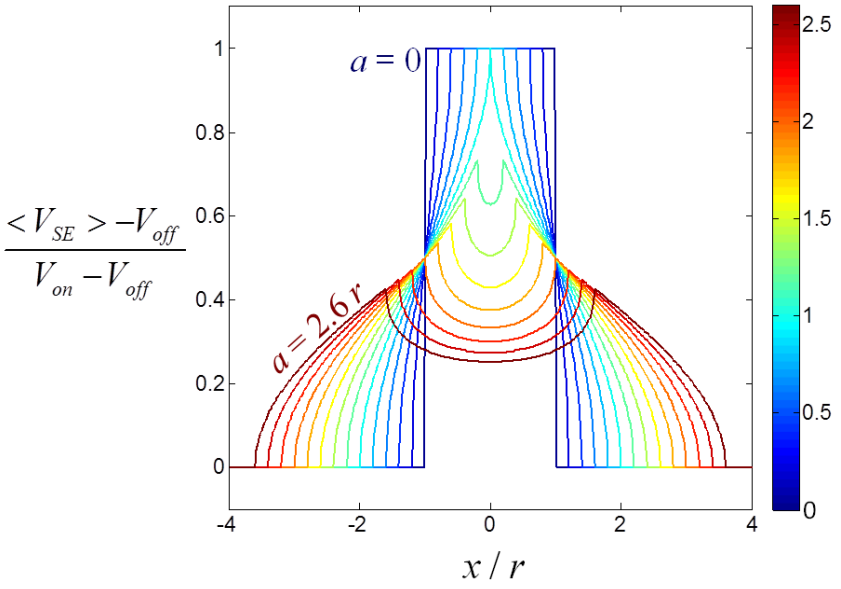

Figure 5. 34: A full set of linescans with different amplitude

Hence the inverse of the time-averaged secondary-electron signal in the limit of large amplitude oscillations is a direct measure of the oscillation amplitude, as noted by Nishio *et al*. (11) in the context of carbon nanotube mechanical resonators.

$$\langle V_{SE} \rangle = \frac{1}{\pi}\left\{V_{on}(\theta_4 - \theta_3) + V_{off}(\pi - (\theta_4 - \theta_3))\right\} \quad (5.17),$$

where $\theta_3 = \sin^{-1}\{(x - r)/a\}$ and $\theta_4 = \sin^{-1}\{(x + r)/a\}$. Hence

$$\frac{\langle V_{SE} \rangle - V_{off}}{V_{on} - V_{off}} = \frac{2}{\pi}\sin^{-1}\left(\frac{r}{a}\right) \quad (5.18).$$

In the limit $a >> r$ this approximates to

$$\frac{\langle V_{SE} \rangle - V_{off}}{V_{on} - V_{off}} = \frac{2r}{\pi a} \quad (5.19).$$

Figure 5.33 shows the calculated time-averaged secondary electron voltage as the electron beam is scanned across a cantilever of width 2*r* as the amplitude a increases from 0 to 2.8*r*, assuming a "top-hat" response function g(*x*). Note that, provided the amplitude is small enough, all the linescans pass through the points $|x| = r$, $\langle V_{SE} \rangle - V_{off} / (V_{on} + V_{off}) = 0.5$. Figure 5.34 shows the variation of the amplitude from 2.6*r* to 0.

5.5 Dynamic measurement with linescan mode

In this section, the dynamic response of vertical C-W-nanorods was measured using an SEM imaging technique. A single linescan across the vibrating nanorod was used. The linescan speed and the variations of resonant frequency and *Q* factor with the dimensions of vertical C-W-nanorods will also be discussed.

5.5.1 Effect of electron beam scan speed

A FIB-induced deposition deposited vertical C-W-nanorod with a length of 34 μm and a diameter of 126 nm was excited to vibrate by a piece of electrical piezo actuator in an SEM chamber. A linescan technique was used to scan across the vibrating nanorod. Then the vibration information (i.e. averaged secondary electron voltage) was collected through the SE-detector. The experimental configuration can be seen in figure 5.25 and detailed

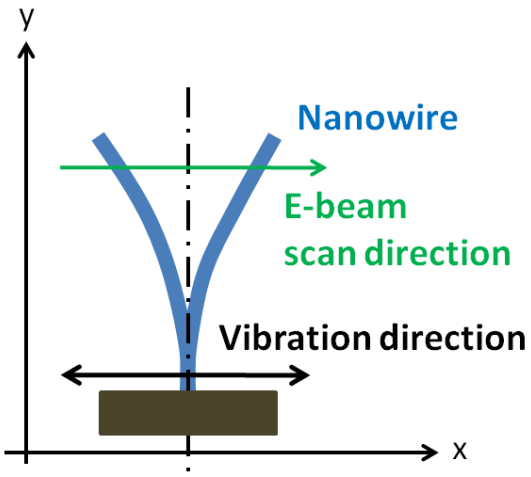

Figure 5. 35: Schematic diagram of geometry of e-beam and nanorod

measurement process was also shown in section 5.3. Linescan measurements are made with the nanorod oriented along the *y*-direction. The nanorod is excited so that it performs sinusoidal transverse oscillations in the *x*-direction. The electron-beam is scanned in the *x*-direction at some fixed value of *y*. Figure 5.35 shows the schematic diagram of the geometry of e-beam and nanorod. The scanning rate (dx/dt) of a single electron beam scanning across both the stationary and vibrating nanorod was investigated as shown in figure 5.36. First, the shape of a single linescan (i.e. the secondary average voltage as a function of *x* position) is affected by the scanning rate of the electron beam. It is clear to see that the linescan shape became asymmetric from figure 5.36 (a) to (c), as the scanning rate decreases. The reason might be that the electron beam deflects the vibrating nanorod slightly when it scans across the nanorod too slowly. Second, the scanning rate of the electron beam affects the number of data points collected. The relationship between sampling rate of the data acquisition card *S*, the period of each linescan *T* and data points collected *n* is illustrated as follows:

$$n = S \times T$$

The sampling rate of the data acquisition card we used here is 390,000 samples per second at maximum. The same length of linescan (583 nm), i.e. the distance the single electron beam scanned over, was used in all the measurements in figure 5.36. In figure 5.36 (a), the time of a single linescan is 0.25 ms, thus the number of data points collected is 97 points and the scanning rate of electron beam is 2.3 $nm \cdot \mu s^{-1}$. The time of a single linescan is 0.46 ms and 6.65 ms in figure 5.36 (b) and (c), respectively. Then the number of data points collected across the vibrating nanorod is 179 points and 2630 points, respectively. The scanning rate of electron beam is 1.28 $nm \cdot \mu s^{-1}$ and 0.22 $nm \cdot \mu s^{-1}$, respectively.

Based the scanning rate of electron beam and the sampling rate of the data acquisition card (390 kS/s), the spatial resolution is calculated to be 5.9 nm, 3.3 nm and 0.22 nm for figure 5.36 (a), (b) and (c), respectively. Therefore, the higher scanning rate of electron beam results in a loss of spatial resolution. Although the lower scanning rate of the electron beam is helpful to gain lots of data points, it increases the time that the nanorod is exposed to the electron beam. This could cause serious carbon deposition on the nanorod resulting in resonant frequency drifting of the nanorod. Therefore, by comparing these three scan speed of electron beam as plotted in figure 5.36, the scan speed of 1.28 $nm \cdot \mu s^{-1}$ as used in figure 5.36 (b) is a good compromise.

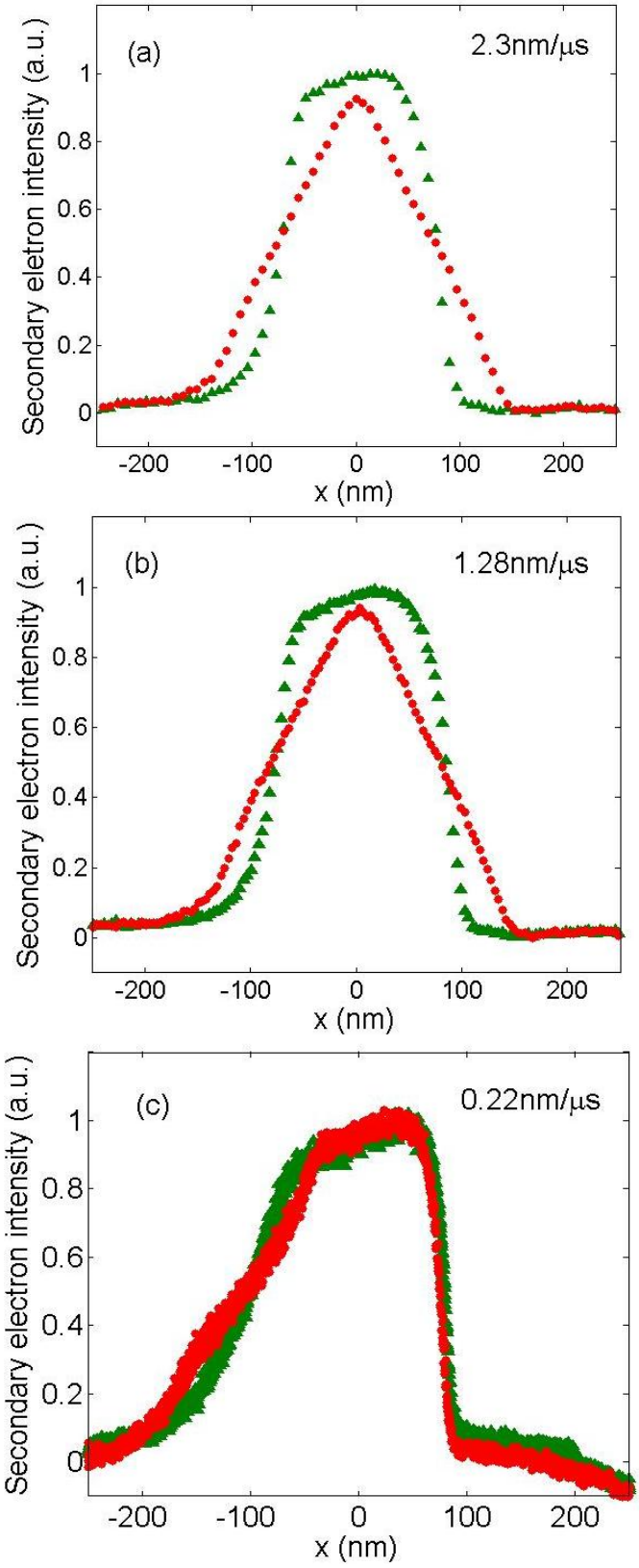

Figure 5. 36: Linescans across a vibrating nanorod with different scan speed (a) Linescan with a speed of 2.3 nm·μs^{-1}; (b) Linescan with a speed of 1.28 nm·μs^{-1}; (c) Linescan with a speed of 0.22 nm·μs^{-1} (The blue dot line is the electron beam intensity when the nanorod is nominally stationary, the red dot line is the electron beam intensity when it is vibrating)

5.5.2 Secondary electron response from an oscillating nanorod

After the nanorod with a length of 34 μm and a diameter of 120 nm was excited to vibrate, a linescan with a speed of 1.28 $nm \cdot \mu s^{-1}$ was scanned across the nanorod at each driving frequency step and the secondary electron response was detected by SE-detector. Figure 5.37 is the SEM images of a stationary and vibrating nanorod. Figure 5.38 shows that the average secondary electron voltage as a function of the electron beam position across the nanorod. In Figure 5.38 (a), the vibration amplitude (a) of the nanorod is much larger than the radius (r) of the nanorod of 60 nm.

The experimental data in figure 5.38 (a) can be divided into five areas. In area A and A', $|x| > (a+r)$, the electron beam misses the nanorod and the average secondary electron voltage $\langle V_{SE} \rangle$ is minimum. In area B and B', $(a - r) < |x| < (a + r)$, the electron beam hits the nanorod for certain positions of the nanorod, and the intensity of the secondary electrons is given by equation (5.8). In area C, $|x| < a - r$, the secondary electrons response changes according to equation (5.10). The experimental data was fitted as shown in figure 5.38 (a) according to the theory in Chapter 5.4. Through fitting, the vibration amplitude was calculated to be 170 nm at the frequency of 51.7 kHz. Figure 5.38 (b) shows the case where vibration amplitude of the nanorod is smaller than the radius of the nanorod (60 nm). In area D and D', $|x| > (a+r)$, the electron beam misses the nanorod and the average secondary electron voltage is minimum. In area E, E', $(a - r) < |x| < (a + r)$, the electron beam hits the nanorod for certain positions of the nanorod, the intensity of the secondary electrons is as shown as equation (5.18). In area F, the electron beam hit the nanorod for all position of the nanorod. The experimental data was fitted as shown in figure 5.38 (b) according to the theory in chapter 5.4. Through fitting, the vibration amplitude was calculated to be 58 nm at the frequency of 51.6 kHz. With this technique, the vibration amplitude can be extracted at each frequency step and the typical vibration amplitude as a function of driving frequency can be plotted.

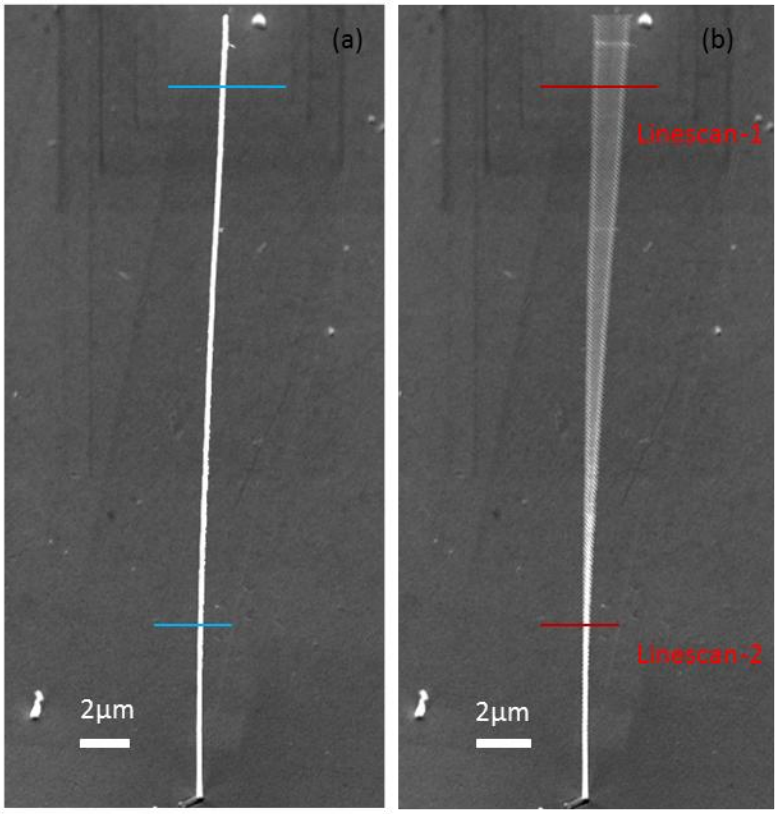

Figure 5. 37: SEM images of (a) without and (b) with vibration of the C-W-nanorod (both of the images were viewed at angle of 45^{o} to the surface normal.)

A FIB-induced deposited C-W-nanorod with a length of 34 µm and a diameter of 124 nm was swept with a driving frequency from 51.8 kHz to 51.98 kHz at 20 V_{pp} from the function generator. A full set of linescans were recorded at each frequency step as shown in figure 5.39. It can be seen that the shape of the linescan changes from broader to narrower as the driving frequency of the piezo goes away from the resonance of the nanorod. This measurement is consistent with the simulation shown in figure 5.32.

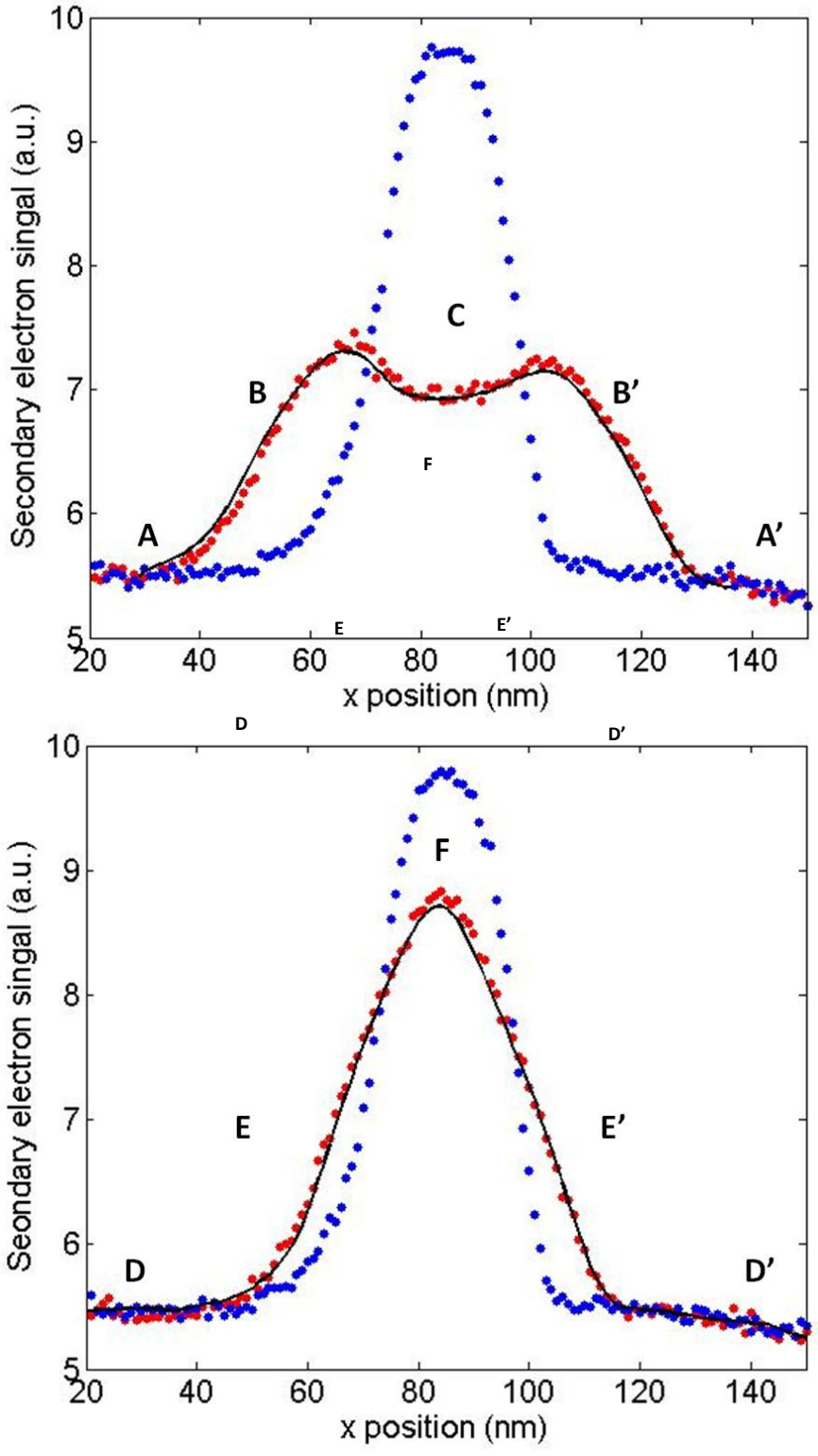

Figure 5. 38: Electron beam intensity as a function of *x* position across the vibrating nanorod. The blue dot line is the secondary electron signal across the stationary nanorod, the red dot line is the secondary electron signal of the vibrating linescan and the black line is the fitting. (a) correspond to linescan-1 in figure 5.35, where the vibration amplitude is larger than the radius of the nanorod; (b) correspond to linescan-2, where the vibration amplitude is smaller than the radius of the nanorod.

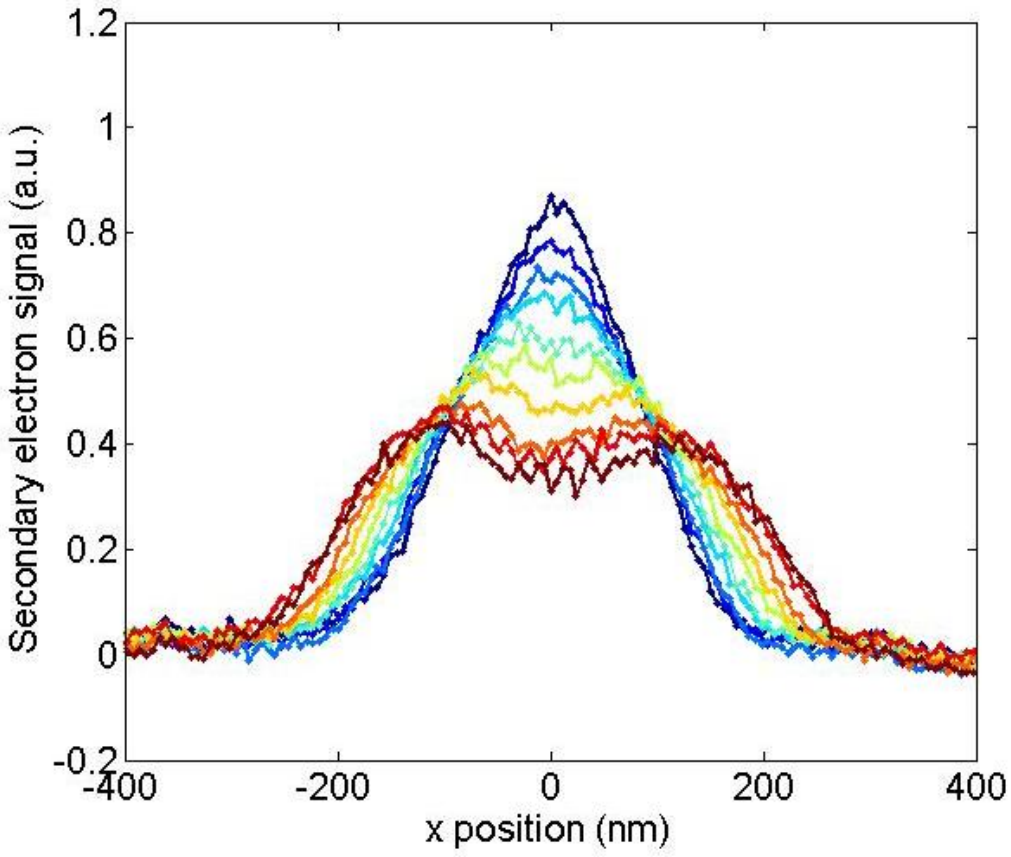

Figure 5. 39: Variation of linescans with different vibration amplitude when the driving frequency from the function generator increases 51.8 kHz to 51.98 kHz at 20 V_{pp}. (The vibration amplitude decreased from black linescan to red linescan.)

5.5.3 Q-factor of resonators

If the driving frequency is swept through a function generator and the single electron beam scans over the vibrating nanorod at each frequency step, the absolute vibration amplitude as a function of driving frequency can be obtained. A C-W-nanorod fabricated by FIB-induced deposition with a length of 20 μm and a diameter of 110 nm was swept from 60 kHz to 61.4 kHz with piezo amplitude of 20 V_{pp}. The single electron beam scanned across the vibrating nanorod and the corresponding frequency response was acquired at each step frequency. By fitting to the model in Chapter 5, the absolute vibrating amplitude at each frequency step

was obtained. Figure 5.40 shows the typical absolute vibration amplitude as a function of driving frequency.

In order to obtain the *Q*-factor of the C-W-nanorod, the vibration amplitude as a function of driving frequency was fitted in figure 5.40 by using forced Lorentz function as shown in equation (175) (5.20).

$$a = \frac{a_0}{\sqrt{\left(1-\frac{f^2}{f_0^2}\right)^2 + \frac{f^2}{Q^2 \times f_0^2}}} \qquad (5.20),$$

where a is the forced oscillation amplitude, a_0 is the forcing amplitude, f is the driving frequency and f_0 the resonant frequency. Through the fitting, the quality factor Q and resonant frequency can be extracted. In this measurement, the resonant frequency is 60.7 kHz and the Q factor is 392. The plot in figure 5.40 also shows that the measurement noise floor of vibration amplitude with this SEM imaging technique is as low as 5 nm.

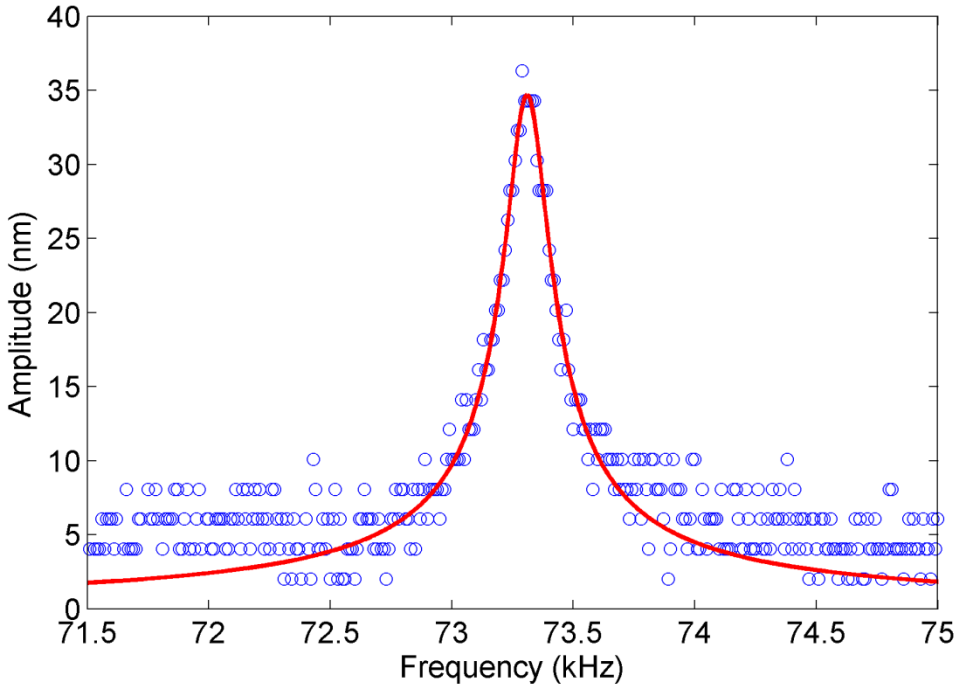

Figure 5. 40: Vibration amplitude as a function of drive frequency (The blue circles are the experimental data and the red line is the fitting)

5.5.4 Dimension dependence of resonant frequency

In order to investigate the relationship between the resonant frequency of C-W-nanorod and its dimension, free-standing C-W-nanorods with different length and diameters were fabricated by FIB-induced deposition and their resonant frequencies were detected through the SEM imaging technique with our home-made setup by sweeping the driving frequency. The dependence of resonant frequency, dimension and mechanical properties of the nanorod is shown in equation (152) (5.21):

$$f_1 = \left(\frac{1.875^2}{4\pi} \sqrt{\frac{E}{\rho}} \right) \cdot \frac{R}{l^2} \qquad (5.21),$$

where E is the Young's modulus of the nanorod, R is the radius and l is the length of the nanorod, and ρ is its density. EDS measurement shows that the FIB-induced depsotion

deposited C-W-nanorod contains 65% carbon, 25% tungsten and 10% gallium. Therefore, the density of the FIB-induced deposition deposited C-W-nanorod can be estimated from the following equation (5.22):

$$\rho = 65\%\rho_c + 25\%\rho_W + 10\%\rho_{Ga} \quad (5.22),$$

where the density of carbon $\rho_c = 2260\ kg \cdot m^{-3}$ (11,179)

the density of tungsten bulk $\rho_W = 19350\ kg \cdot m^{-3}$,

the density of gallium bulk $\rho_{Ga} = 5907\ kg \cdot m^{-3}$.

Hence, the density of FIB-induced deposition deposited tungsten can be referred to this value to conduct the following experiment work, $\rho = 7 \times 10^3 kg \cdot m^{-3}$.

Variation of the first order resonance with the dimensions of the nanorods is shown in figure 5.41. The slope of the linear fit is 942 m/s, from which the Young's modulus of the C-W-nanorod was calculated to be 79±30 GPa according to equation (5.21).

Alternatively, if the Young's modulus is known, the density of the resonator can be calculated according equation (5.21). Thus, detecting the density of the resonators can be one more application of the dynamic measurement to characterize the structure of materials.

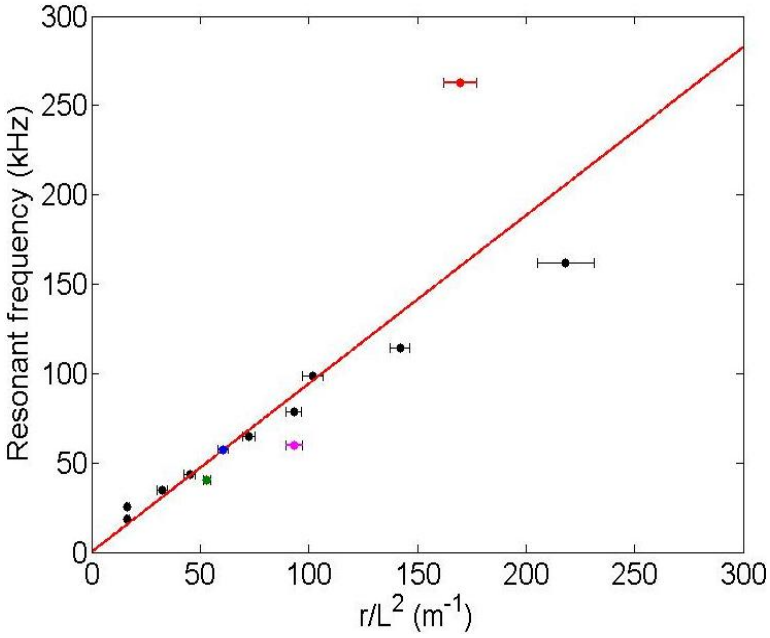

Figure 5. 41: Variation of resonant frequency with dimensions of nanorods (The dots are the experimental data and the red line is the fitting.)

5.5.5 Variation of Q factor with resonant frequency

Q-factors were also investigated as shown in figure 5.42 by measuring nanorods with different resonant frequencies. Note that the *Q* factor of the nanorod with the highest resonant frequency is slightly larger than the rest.

The reason for this is that the diameter of this nanorod was reduced by milling its sidewall with focused gallium ion beam as described in section 4.4. This process may cause gallium ion implanting into the nanorod. Since the density of the nanorod increased, the *Q*-factor might be increased as well. The other dots in figure 5.42 are the original C-W-nanorods deposited with FIB-induced deposition. The *Q*-factor of those C-W-nanorods is distributed between 300 and 600.

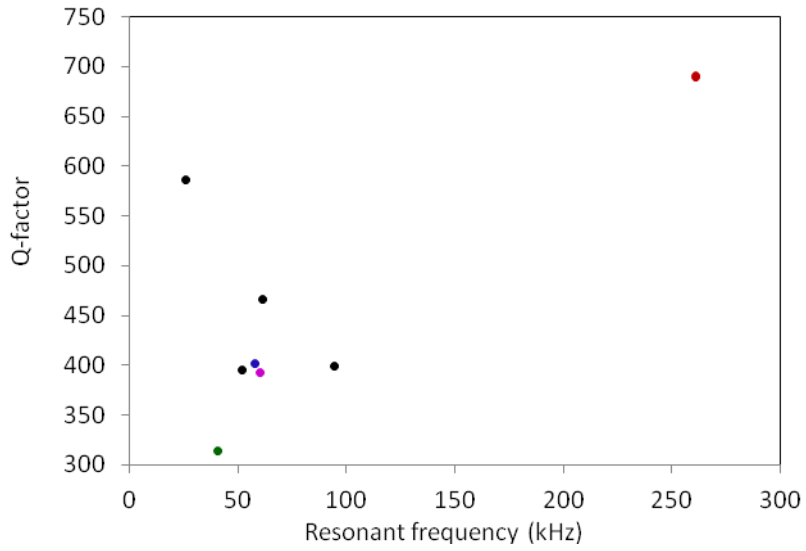

Figure 5. 42: *Q*-factor as a function of resonant frequency of different nanorods (The colored dots correspond to figure 5.39)

5.5.6 Variation of amplitude

With the resonant frequency detection method as demonstrated above, the vibration amplitude along the vertical C-W-nanorod from the free end to the clamped end was measured as shown in figure 5.43. The nanorod was fabricated by FIB-induced deposition and has a length of 34 μm and a diameter of 124 nm. The driving frequency from the function generator ranged from 51.8 kHz to 51.9 kHz and the amplitude applied on the electrical piezo actuator is 20 V_{pp}. At each position along the nanorod, a full frequency sweep was done by using the linescan technique. The vibration amplitude of the harmonic oscillation is given by the following equation according to theory (152):

$$y_1(x) = y_0\left(\left(\cos\frac{1.875}{l}x - \cosh\frac{1.875}{l}x\right) - \frac{\cos 1.875 + \cosh 1.875}{\sin 1.875 + \sinh 1.875}\left(\sin\frac{1.875}{l}x - \sinh\frac{1.875}{l}x\right)\right) \quad (5.23),$$

where 1.875 is the dimensionless eigenvalue of the first resonance mode, x is the position along the nanorod and *l* is the length of the nanorod. It can be seen that the experimental data is well fitted by the theory, confirming that the elastic properties of the nanorod are uniform along its length.

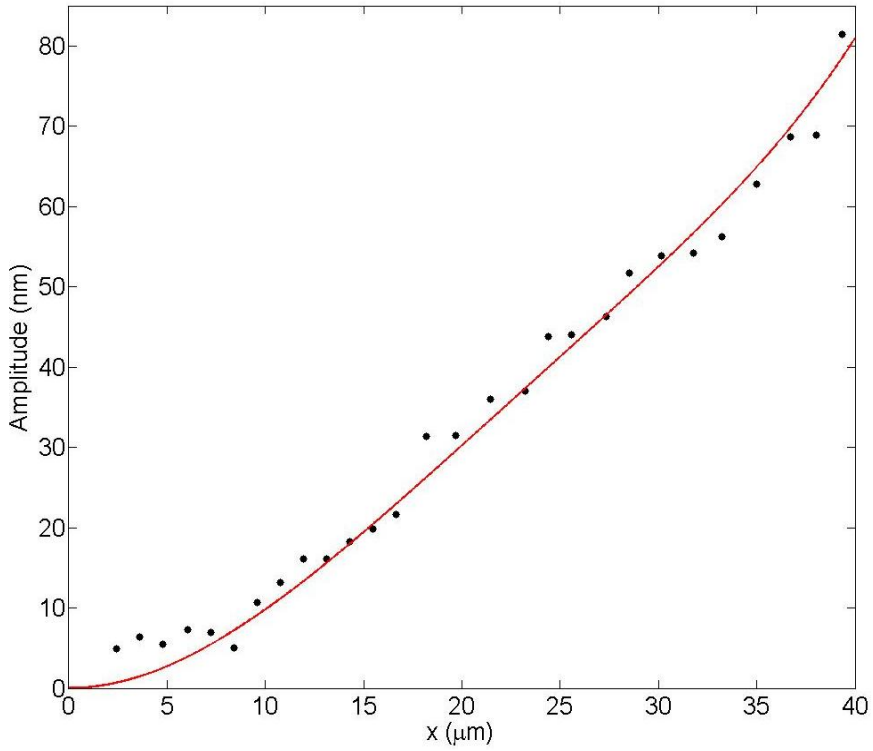

Figure 5. 43: Vibration amplitude as a function of the position along the vertical nanorod from clamped end to free end (The black dots are the experimental data and the red line is the fitting.)

5.5.7 Mass sensor

Preliminary measurement of C-W nanorods as mass sensors was conducted by depositing amorphous carbon induced by electron beam onto the tip of the nanorod. This FIB-induced deposition deposited nanorod has a length of 18 μm and a diameter of 110 nm. Its resonant frequency was detected to be 260.8 kHz in SEM chamber as shown the red line in figure 5.44. After the free end of the vertical nanorod was exposed to e-beam deposition for 3.5 hours, the resonant frequency was shifted to be 259.7 kHz as shown the black line in figure 5.44. The amplitude as a function of frequency is not fully plotted because these measurements were done manually, which took about 60 mins during the driving resonant frequency was fully swept and data was exported at each frequency step. In the process, e-beam carbon deposition continued and affected the collection of full amplitude as a function

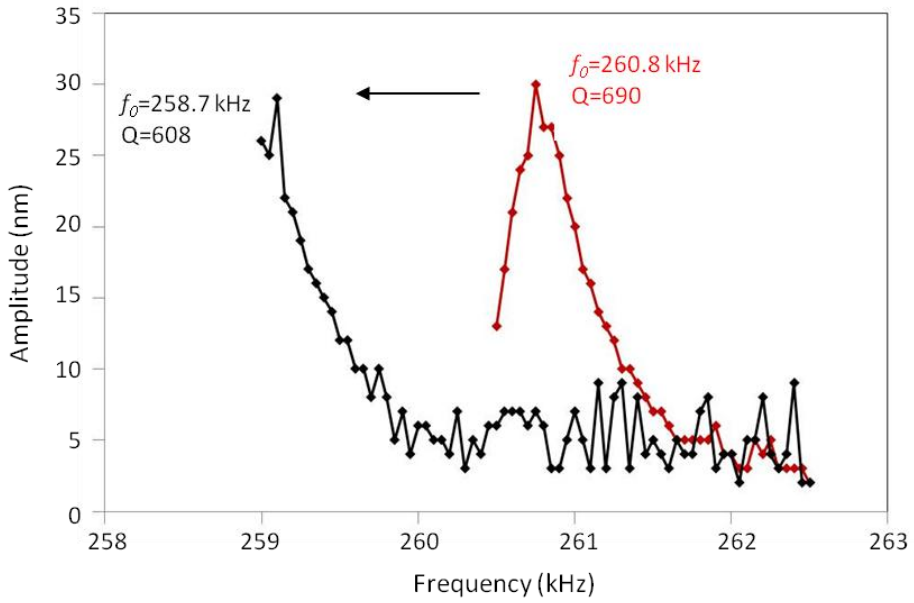

Figure 5. 44: Resonant frequency drifting due to mass attachment (The red curve is the amplitude as a function of frequency; the black curve is the amplitude as a function of frequency after e-beam carbon deposition on the top of the nanorod)

of frequency. Based on the point-mass model in chapter 3 equation (3.29), we calculated the mass from its frequency shift. It is 2.9×10^{-16} g. Due to the aim of the project, we focused on developing high frequency resonators and setup design. Therefore, the mass detection experiment was only carried out for one time, from which the mass resolution (δm) of this resonator reaches the level of $\sim10^{-16}$ g.

5.5.8 Comparison of characterization techniques

Similarly, Nishio *et al.*(11) also investigated the resonant frequency detection of nanomechanical resonators by focusing a single stationary electron beam in the vibration centre of the resonator with SEM/FIB to record the secondary voltage changes. Their detailed method can be seen in ref. (11). However, his theory and experiment only works, when the vibration amplitude of the resonantor is much larger than the diameter of the resonator.

Ivo Utke's group (87) also explored the resonant frequency and *Q*-factor of nanomechanical resonators by using a single stationary electron beam focused on the edge of the vibrating resonator in an SEM as shown in section 4.5. A group of tungsten nanomechanical resonators were tested with his setup as shown in section 5.6. However, the limitation of his research setup is that the absolute vibration amplitude is impossible to obtain. Nonaka *et al.* (174) used thermal noise to excite the resonator to oscillation and used linescan was analysed to obtain the vibration amplitude by fitting a model. With their model vibration amplitude smaller than the radius of the resonators can be detected. Their model took consideration of the cross-sectional geometry by assuming a cylindrical resonator with uniform material properties. This limited the application of their technique. The technique I have developed in this thesis enables me to overcome this issue and detect the vibration amplitude with model-independent.

5.5.9 Comparison of static and dynamic measurement of C-W nanorods

Figure 5.45 shows the relationship between the Young's modulus and the diameter of tungsten nanowires fabricated by FIB-induced deposition. The blue data are obtained by static measurements, i.e. AFM force-displacement curves. The experimental details can be seen in section 4.4. The green data are obtained by dynamic measurements, i.e. resonant frequency detection in an SEM. Since the resonant frequency is detected, the young's modulus can be calculated from the measured resonant frequency according to equation (5.21). The experimental details of dynamic measurement are described in section 5.5. We can see that the Young's modulus exhibits a size effect, although both measurement techniques overlap within the accuracy of the measurement. The Young's modulus decreases from ~110 GPa to ~20 GPa with an increasing diameter of tungsten nanowire from 110 nm to 330 nm.

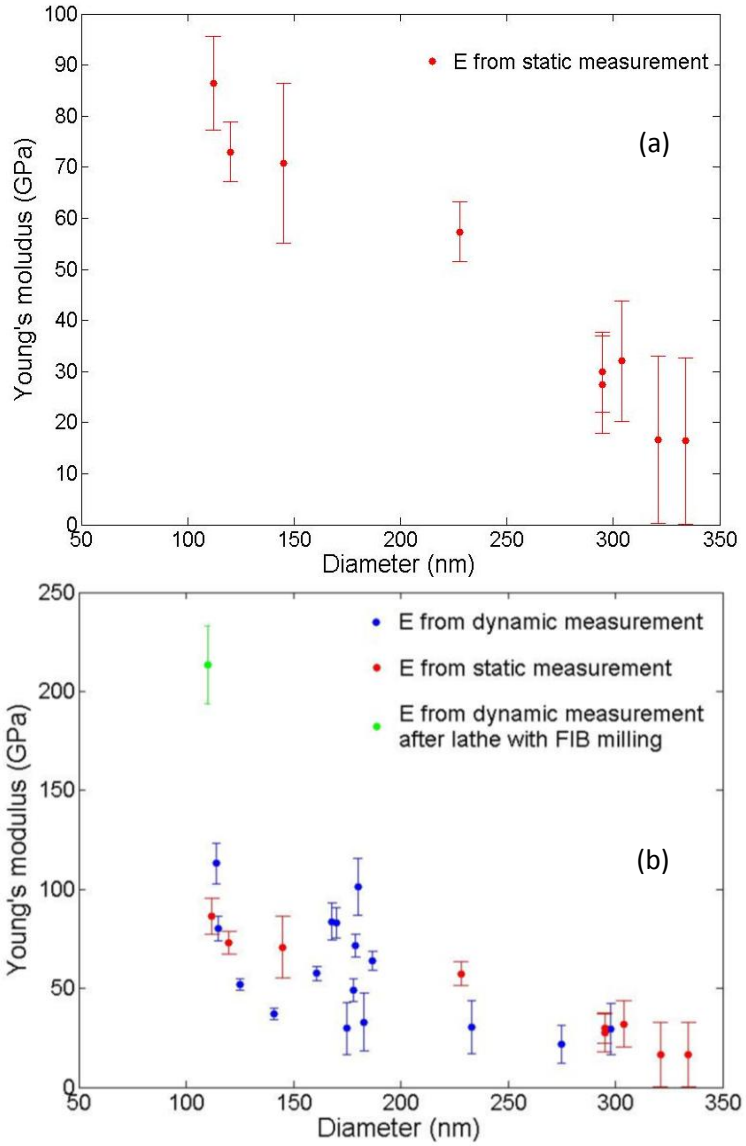

Figure 5. 45: Young's modulus as a function of the diameter of nanowires fabricated with FIB induced tungsten deposition (a) Young's modulus as a function of the diameter of nanowires, where the red dots represent the Young's modulus obtained from dynamic (Data of figure 5.20 replotted) (b) Same data as (a) replotted with Young's modulus obtained from dynamic measurement and an additional data point: the green dot here is the Young's modulus from dynamic measurement of a nanowire thinned by the FIB milling technique

This result suggests that nanowires fabricated with FIB induced deposition have radially non-uniform mechanical properties. EDS analysis of FIB-deposited carbon pillars (179) shows that the core of the nanowire is a gallium-rich region and that the carbon percentage decreases from the core to the edge of the nanowire. The edge of the pillar is a carbon rich

region and the size of the gallium rich region is limited to around 40 nm (179). Similar results also have been found in the work of Kometani *et al.* (176). In the context of our nanowires, it is reasonable to assume that when the nanowire is very thin, it contains less carbon and tungsten; hence the stiffness of the nanowire is dominated by the gallium rich region leading to a comparatively high value of the Young's modulus. Conversely when the nanowire is thicker, the carbon and tungsten in the nanowire shell result in a comparatively low value of Young's modulus.

To confirm this conjecture, we have used FIB milling to remove the outer (possibly carbon-rich) shell of the nanowire along its entire length. The detailed procedure can be seen in section 4.4. Figure 5.46 shows the SEM images of the nanowire shows before and after the thinning process. Then the dynamic measurement was conducted on this nanowire, giving a Young's modulus of 213 GPa.

The original diameter of the nanowire in figure 5.46 (a) is 180 nm and the diameter is reduced to 110 nm after being thinned by FIB milling as shown in figure 5.46 (b). The length of the nanowire is not changed. From figure 5.46 (b), we can see a layer of thickness 35 nm was removed from the surface of the nanowire. Therefore, one of the important reason for the large Young's modulus is that the thinning process removed the shell of the nanowire (probably the carbon rich region), which has a lower Young's modulus. The second possible reason is that the FIB milling caused gallium-ion implantation into the nanowire. Hence, the thinning process by FIB milling confirms the core-shell structure of the nanowire fabricated with FIB induced tungsten deposition.

In this section, dynamic measurement of tungsten nanomechanical resonator fabricated with FIB-induced deposition was carried out. The results show that the variation of resonant frequency with the dimension of nanorod is consistent with the theory. The *Q*-factor of the resonators ranges from 300 to 600. The mass sensitivity can reach to the level of 10^{-16} g. In

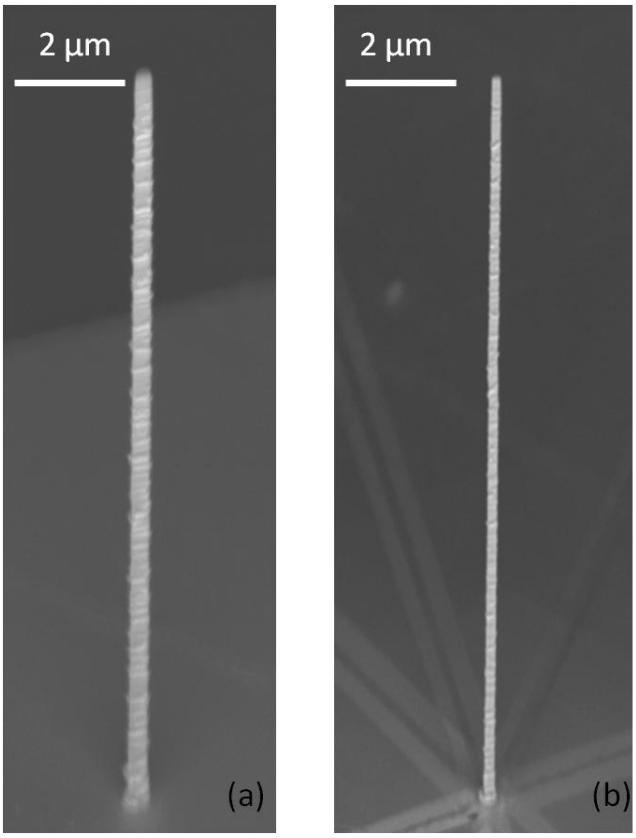

Figure 5. 46: SEM images of vertical nanowire fabricated by FIB induced tungsten deposition (a) is the original nanowire fabricated by FIB induced tungsten deposition (the length is 18 μm and the diameter is 180 nm) (b) is the same nanowire thinned from its sides wall by FIB milling (length is 18 μm and diameter is 110 nm)

addition, the measurement technique developed in this work took the advantages of SEM, which enable the noise floor of amplitude detection as low as 5 nm.

5.6 Dynamic measurement with spotmode

In this section, resonant frequencies of vertical C-W-nanorods were measured using an alternative SEM imaging technique. A single electron beam was fixed on the edge of the vibrating nanorod to detect its resonant frequency and the frequency response through

secondary electron signal was analysed. Variation of resonant frequency with dimensions of vertical C-W-nanorods and *Q* factor will also be discussed.

5.6.1 Dual mode resonant frequency

Vertical C-W-nanorods with different lengths and diameters were deposited by FIB-induced deposition on silicon substrates with both scanning mode and spot mode. The current and energy of gallium ion beam is 1 pA and 30 kV, respectively. Then the nanorod was excited to vibrate by a piezoelectric actuator in an SEM chamber (Hitachi S-3600). The amplitude-frequency curves were achieved by using secondary electron detection with a stationary beam near the sample. A peak of secondary electrons can be detected once the nanorod reaches its maximal amplitude during the vibration. The detailed experimental procedure can be seen in section 4.5 of chapter 4. When the driving frequency applied on the piezo was swept in certain range, dual resonant frequencies (i.e. orthogonal mode resonant frequencies) with their vibration planes perpendicular were observed.

Table 5.3 shows the orthogonal mode resonant frequencies of nanorods with different lengths and diameters. f_x is the resonant frequency when the vibration of the nanorod is along the *x*-axis and Q_x is the quality factor measured under this resonant frequency. f_y is the resonant frequency when the vibration of the nanorod is along the y-axis and Q_y is the quality factor measured under this resonant frequency. The reason for the orthogonal mode resonant frequencies is that the cross section of the nanorod is not circular but elliptical. The elliptical cross section of the nanorod is caused by the astigmatism of the gallium ion beam. According to the theory in section 3.5 of chapter 3, the ratio of the orthogonal mode resonant frequency of the nanorod is equal to the ratio of the radius, which means $f_x/ f_y=R_{min}/R_{max}$. It can be seen in Table 5.3 that f_x/ f_y ranges from 0.80 to 0.99, which also illustrates the focusing of the gallium ion beam changes. In addition, the variation of Q_x/ Q_y does not correlate with f_x/ f_y.

Table 5.3 Orthogonal mode resonant frequency

Sample No.	f_x**(kHz)**	Q_x	f_y**(kHz)**	Q_y	$f_x/f_y = R_{min}/R_{max}$	Q_x/Q_y
2-SpodM	179.208	439	180.937	326	0.990443	1.35
5-SpodM	642.897	386	670.157	469	0.959322	0.822
6-SpodM	484.036	629	501.049	451	0.966044	1.40
7-SpodM	453.369	476	493.392	518	0.918881	0.919
1-ScanM	88.132	432	93.316	373	0.944445	1.16
2-ScanM	134.655	404	146.433	366	0.919569	1.10
3-ScanM	176.656	353	187.859	357	0.940363	0.990
4-ScanM	228.454	377	246.172	345	0.928027	1.09
5-ScanM	314.712	393	393.427	570	0.799925	0.690
8-ScanM	786.715	315	868.796	478	0.905523	0.659
1-SpodM	209.142	356	248.356	435	0.842106	0.818
3-SpodM	266.136	413	273.852	452	0.971824	0.913

5.6.2 Effect of FIB-induced deposition mode of C-W-nanorod on its resonant frequency

To understand the resonant frequency dependence on the dimensions of the C-W-nanorods and also the relationship between mechanical properties (Young's Modulus) and the FIB-induced deposition mode, two sample sets were separately prepared. Table 5.4 shows the length and diameters of nanorods from both sample sets. In sample set No.1, vertical C-W-nanorods with various lengths and diameters were deposited by FIB-induced deposition with spot mode under a constant gallium ion beam current of 1 pA and energy of 30 kV. Then resonant frequencies were detected with the SEM spot mode technique. Figure 5.47 (a) shows the resonant frequency variation with dimension of nanorod. According to equation

(5.21), the slope from fitting in figure 5.47 (a) reveals the Young's modulus and the density of the C-W-nanorod. Similar to the analysis in section 5.5.4, the density can be assumed from EDS measurement, which is 7000 kg/m^3. Therefore, the slope of 1237 m/s gives the Young's modulus of 136±89 GPa.

In sample set No.2, vertical C-W-nanorods were fabricated by FIB-induced deposition with a scanning mode under a constant gallium ion beam current of 1 pA and energy of 30 kV. With this scanning mode, the focused Ga^+ beam repeatedly raster scanned over a defined area of 10nm×10nm. Similarly, the slope from theoretical fitting in figure 5.47 (b) is 1006 m/s, from which the Young's modulus was calculated to be 90±8.4 GPa.

By comparing with figures 5.47 (a) and (b), it can be seen that C-W-nanorod fabricated by FIB-induced deposition with scanning mode shows that the resonant frequency dependence upon the dimensions of the nanorods is consistent with the theory. It indicates that the mechanical stiffness (Young's modulus) and density of nanorods are uniform. Nanorods fabricated by FIB-induced deposition with spot mode shows that resonant frequency dependence of dimensions of nanorods scattered along the theoretical fitting. It illustrated that a larger variation of Young's modulus happens to C-W-nanorods.

Table 5.4 Dimension of C-W-nanorod fabricated with FIB-induced deposition

Sample No.		1	2	3	4	5	6	7	8
Sample Set No. 1(Spot mode)	*L* (μm)	15.69	19.74	13.97	10.93	8.638	13.07	16.56	10.35
	Da(nm)	141.18	96.26	105.23	109.90	94.42	103.06	104.87	97.98
Sample Set No. 2 (Scan mode)	*L* (μm)	22.7	19.95	17.12	16.05	12.74	11.26	9.525	8.309
	Da(nm)	94.68	107.90	105.67	117.10	110.00	105.50	105.77	102.88

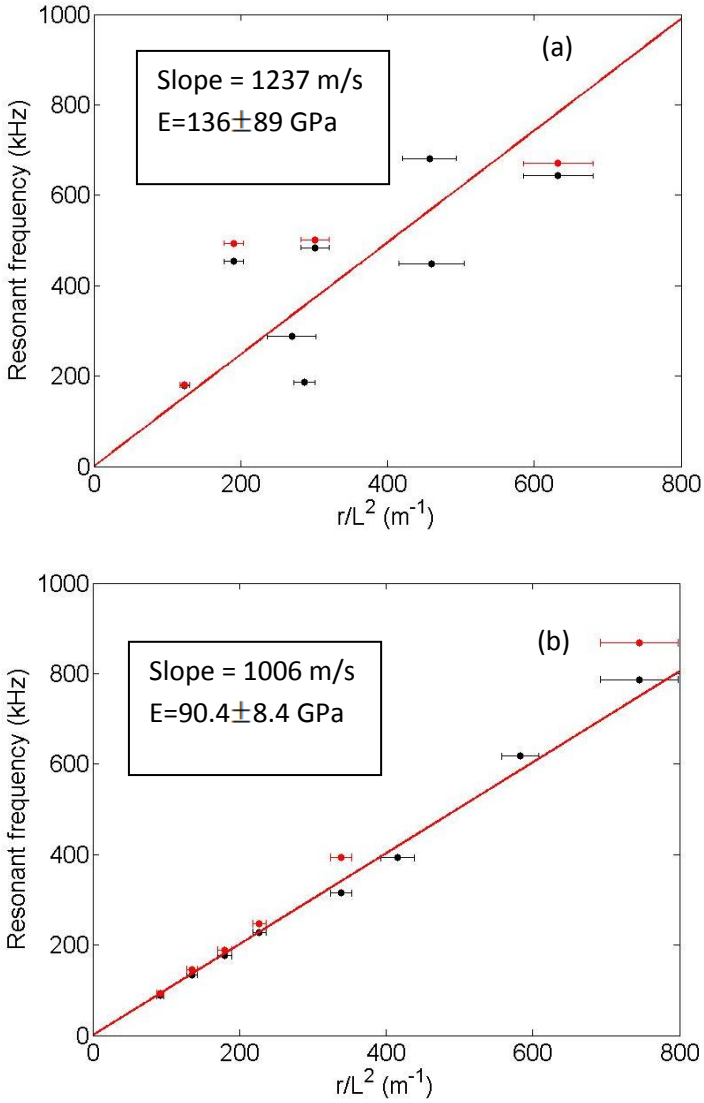

Figure 5. 47: Variation of resonant frequency with dimension of nanorod (a) variation of resonant frequency with dimension of nanorod in sample No.1 (b) variation of resonant frequency with dimension of nanorod in sample No.2

5.6.3 Q factor

From the phase response as demonstrated in section 5.5.1, the *Q*-factor was calculated for each C-W-nanorod according to the theory in section 3.2. Figure 5.48 shows variation of *Q*-factor with resonant frequency of nanorods fabricated by FIB-induced deposition with spot mode and scan mode. As seen in figure 5.48 (a), the *Q*-factor of nanorods fabricated with spot mode of FIB-induced deposition ranges from 300 to 700 for resonant frequencies in the range 100 to 700 kHz. The *Q*-factor of nanorods deposited with scan mode FIB-induced deposition scatters in a narrower range of 300 to 600 for resonant frequencies in the range

100 to 800 kHz. The *Q*-factor in both graphs is independent of resonant frequency. The effect of the deposition mode of FIB induced deposition on *Q*-factor is different from what we expected. We expected nanorods grown with spot mode deposition to exhibit a repeatable uniform material structure because the beam is fixed at a single point. The effect of the deposition mode on the material structure of nanorods is not well known yet. However, the materials structure of the nanorods has an influence on the internal energy dissipation, limiting both the resonant frequency and *Q*-factor.

The typical internal dissipation mechanisms consist of thermoelastic, phonon-electron and phonon-phonon interactions. Phonon-phonon dissipation is the dominant energy dissipation mechanism in semiconducting and insulating resonators at room temperature (177). A high phonon velocity maximises the resonant frequency for given dimensions (177). According to theoretical equation (5.21), the phonon velocity is defined by the resonant frequency and dimensions:

$$c_p = \frac{f_0 \times L^2}{r} \tag{5.24},$$

In order to investigate the relationship between the internal energy dissipation and the phonon velocity of the resonators, the *Q*-factor as a function of phonon velocity for different samples is plotted in figure 5.49. The sample-to-sample variation of phonon velocity in figure 5.49 (a) reveals a large variation of the material structure of resonators fabricated with spot mode. Hence, we can conclude that the scanning mode of the FIB deposition results in more repeatable material structures than spot mode. Comparing with other materials, SiC has a much higher phonon velocity of 11400 m/s and *Q* factor of 4000, the phonon velocity of Si ranges from 8500 to 9300 m/s and it has *Q* factor of 15000 and diamond has a phonon velocity and *Q* factor of 18000 m/s and 2500-3000, respectively (178). It is clear that the phonon velocity of tungsten nanomechanical resonator is lower than the general resonators. The low phonon velocity probably is the main reason, which limits its *Q* factor and resonant frequency.

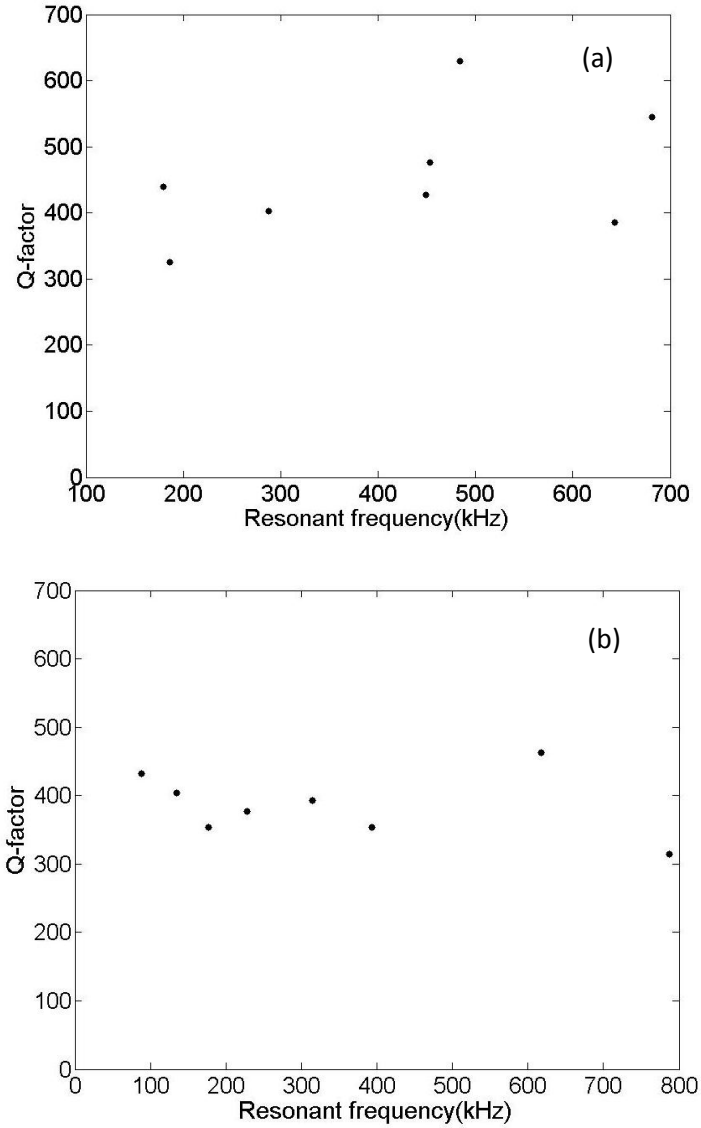

Figure 5. 48: Variation of *Q*-factor with resonant frequency of C-W nanorods (a) variation of *Q*-factor with resonant frequency of C-W nanorods in sample set No.1 (b) variation of *Q*-factor with resonant frequency of C-W nanorods in sample set No.2

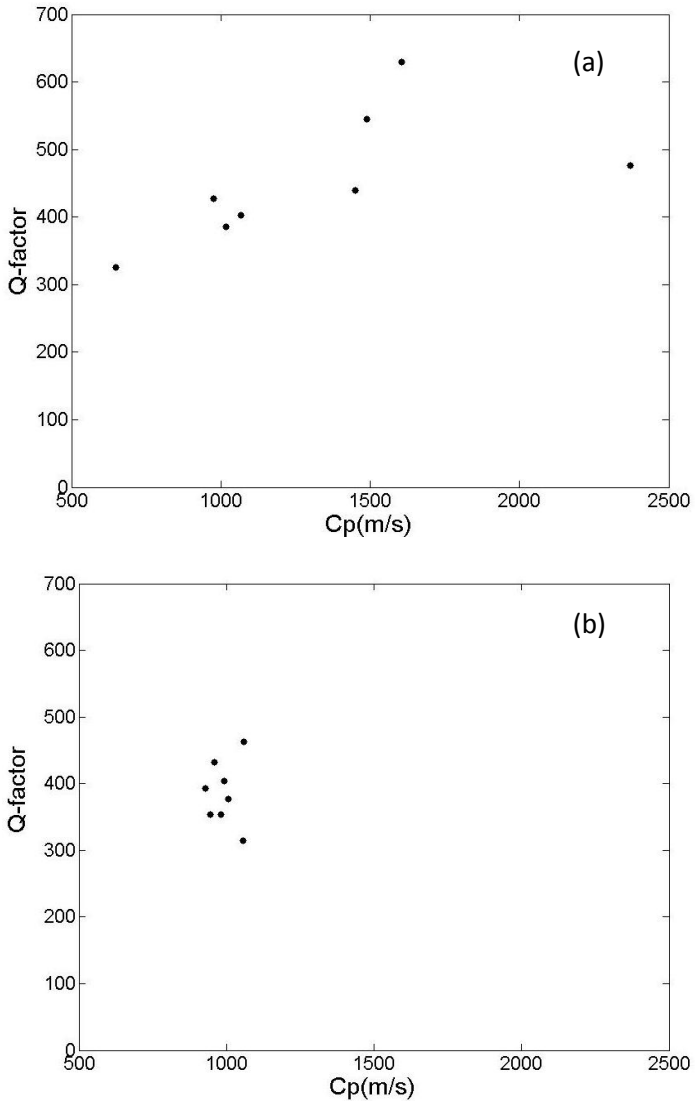

Figure 5. 49: Variation of *Q*-factor with the phonon velocity of C-W nanorods (a) variation of *Q*-factor with phonon velocity of C-W nanorods in sample set No.1 (b) variation of *Q*-factor with phonons of C-W nanorods in sample set No.2 (The phonon velocity values were obtained from equation (5.7) using values of the resonant frequency measured as described in Section 5.7.2, the length and radius were determined by SEM image)

5.6.4 Estimated mass resolution

In order to investigate the mass sensitivity of tungsten nanomechanical resonator fabricated by FIB-induced deposition, the point-mass model is employed as demonstrated in section 3 of chapter 3. Therefore, we assume a point mass is attached on the top the tungsten nanomechanical resonator. According to equation (3.39) the mass resolution of nanomechanical resonators is estimated to be

$$\delta m = \frac{2m^* \times \delta f}{f} = \frac{2m^*}{Q} \quad (5.25),$$

where m^* is the effective mass of the resonator. (The relationship between effective mass and real mass of the resonator can be seen in section 3 of chapter 3.) Q is obtained during the measurement of resonant frequency detection, which has been discussed in the previous sections. However, in reality, the ultimate mass resolutions of resonators depend on the minimum detectable frequency shift.

In figure 5.50, we show the variation of the estimated mass resolution with the resonant frequency of tungsten nanomechanical resonators. The smallest estimated mass which could be detected by the C-W-nanorod with the current setup is 0.25×10^{-15} g. The estimated mass resolution is independent of orthogonal mode resonant frequency up to 800 kHz.

Figure 5.51 shows the variation of estimated mass resolution with the effective mass of the tungsten nanomechanical resonators. Smaller effective masses result in better mass resolution according to equation 5.25. Therefore if the dimension of the tungsten nanomechanical resonator is reduced, the estimated mass resolution will increase linearly.

In this section, dynamic measurements of tungsten nanomechanical resonators fabricated with FIB-induced deposition were carried out. The results show that the variation of resonant frequency with the dimension of nanorod fabricated with scanning mode of FIB-induced deposition is consistent with the theory. The Q-factor of the resonators ranges from 300 to 600. The estimated mass resolution of tungsten nanomechanical resonators can reach the level of 10^{-15} g.

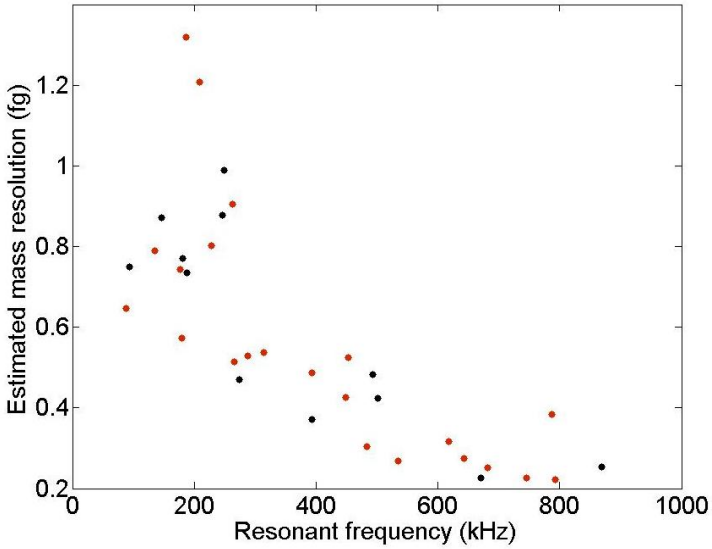

Figure 5. 50: Estimated mass resolution as a function of resonant frequency of tungsten nanomechanical resonators (Data is extracted from Figure 5.47 (a) and (b). The black dot is the resonant frequency and the red dot is the orthogonal resonant frequency. 20 red (black) dots are measurement from 20 samples)

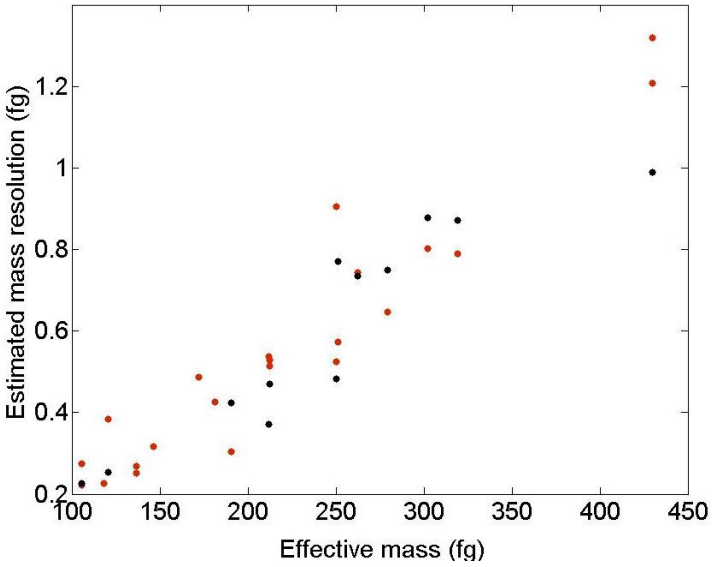

Figure 5. 51: Estimated mass resolution as a function of effective mass of tungsten nanomechanical resonators (Data is extracted from Figure 5.50). The black dot is the effective mass of the resonator at its resonant frequency and the red dot is the effective mass of the resonator at its orthogonal resonant frequency. 20 red (black) dots are measurement from 20 samples)

Chapter 6 Conclusions and Future Works

6.1 Conclusions

I have fabricated vertical C-W-nanorods with FIB induced tungsten deposition as ultrasensitive nanomechanical resonators by investigating the process parameters to grow the desired nanorods. The minimum diameter of the vertical C-W-nanorod is about 90 nm with a gallium ion beam current of 1 pA and an accelerating voltage of Ga^+ of 30 kV. A heating temperature of tungsten precursor gas is kept at 69^{o}C to make the local gas pressure is substantial for the deposition. The length of the vertical C-W-nanorod deposited by FIB-induced deposition is time dependent. This suggests nanorods with various length and diameter can be controlled individually through changing the FIB induced deposition parameters. However, it is difficult to avoid protrusions on the sidewall of the nanorod and the reason for this is still not well known.

In order to make ultrasensitive resonators, I scaled down the dimension of the induced deposition deposited vertical C-W-nanorods by thinning its thickness with FIB milling on its side wall at 50 pA, 10 kV and an ion incident angle of 63^o. The minimum diameter can reach about 60 nm without bending the vertical nanorod. This technique enables fabrication of thinner nanorods with focused gallium ion beam. This indicates nanorods with smaller dimensions can be fabricated to achieve higher resonant frequencies to make ultrasensitive sensors.

Both singly- and doubly-clamped C-W-nanorods were fabricated with FIB to study its static mechanical properties with AFM force displacement measurement. Young's modulus of both singly- and doubly-clamped nanorods was found to be size dependent, which increases from 20 GPa to 87 GPa with an decreasing diameter from 400 nm to 110 nm.

Dynamic properties characterisation of tungsten nanomechanical resonator fabricated with FIB-induced deposition was carried out with our homemade experimental setup by an SEM linescan analysing technique. Resonant frequencies of nanorods with different dimensions were measured and the variation of resonant frequency with the dimension of nanorod is consistent with the classical beam theory. The *Q*-factor of the resonators ranges from 300 to 600. The mass sensitivity can reach to the level of 10^{-15} g.

The in-situ dynamic measurement of nanomechanical resonators within an SEM indicates one of the applications of this technique can be used to study the mechanical properties of the resonators, such as Young's modulus, density, and deposition uniformity of FIB-induced deposition. Another popular application is to be used as mass sensor. However, the mass sensitivity is not very high at the moment compared with sensitivity of carbon nanotube, which has a mass sensitivity of 10^{-21}g. Therefore, the important work needs to do in the future is to increase the mass sensitivity by increasing its resonant frequency significantly.

6.2 Summary discussion of Significance of the work

In this section, I will summarise the significance results of my work and discuss its importance in the field of the nanomechanical resonators. The novelty of the work is primarily in two areas: investigating the suitability of tungsten nanomechanical resonators grown by FIB induced deposition and the design of an in situ measurement setup with its corresponding SEM linescan data analysing techniques. I will discuss each of these in turn as the following content.

First, rather than using conventional fabrication method, I used FIB to fabricate nanomechanical resonators. This reason is that the FIB has the advantages to choose variation material and grow resonators in any desired position. In order to explore the suitability of FIB induced tungsten deposition grown resonators as ultra-sensitive mass sensors, I fabricated more than 60 tungsten nanomechanical resonators. The length of these resonators ranges from 10 μm to 70 μm and the thickness ranges from 80 nm to 270 nm. Important factors to decide the final mass sensitivity of nanomechanical resonators includes young's modulus, resonant frequency, effective mass (i.e. ¼ mass) and Q-factor. Therefore, I investigated both its static mechanical properties with AFM force displacement measurement and dynamic mechanical properties with a homemade setup inside of an SEM chamber. The young's modulus of the tungsten nanomechanical resonators shows a size effect and it rangs from 20 to 80 GPa with a decreasing diameter from 400 nm to 110 nm. The young's modulus indicates the stiffness of the material, which is proportional its resonant frequency. Compared with the typical resonators including Si (170 GPa), Si_3N_4 (180 GPa) and diamond -like-carbon (187 GPa), the FIB induced tungsten deposition is slightly lower, but is much lower than carbon nanotubes (600 GPa).

The dynamic mechanical properties characterisation allows me to measure the resonant frequency of the tungsten nanomechanical resonators and *Q*-factor. The resonant frequency of these 60 resonators ranges from 20 kHz to 860 kHz. Here, the highest detectable resonant frequency is limited by the homemade setup. I also studied the relationship between dimensions of the resonators and its resonant frequencies by measuring more than 60 resonators. The results are consistence with the classic finite beam vibration theory, which also indicates the FIB induced tungsten deposition is uniform. The smaller the dimension of the resonator is, the higher the resonant frequency is, and the more sensitive the resonator will be. Also a smaller dimension results a smaller mass of the resonators. According to the mass sensitivity is proportional to $k^{-0.5}M^{1.5}$ (M is the effective mass (1/4 of its real mass of the

resonators and *k* is the stiffness of the resonator), reducing the dimension of the resonators is very important. Hence, I developed a new technique with the FIB to thin the vertical nanorod from 90 to 60 nm uniformly, which attributes to increase its resonant frequency and its mass sensitivity of the tungsten resonators eventually. This FIB lathe technique enables to fabricate thinner C-W rod, which is much lower than the limitation thickness of the FIB induced tungsten deposition, i.e. 90 nm. This thinning technique of FIB also can be applied to reduce dimensions of other type of nanorods. Compared with the annular milling of FIB, the FIB thinning technique can fabricated uniform vertical nanorods instead of needle shape like nanorods, which is not useful to fabricate ultrasensitive resonators. The characterisation also shows the *Q*-factor of the tungsten nanomechanical resonators, which is about 300 to 600. Compared with other type of resonators, the Si (10000), Si_3N_4 (4500), diamond (3000) and carbon nanotubes (1000), the *Q*-factor is lower. The possible reason the amorphous material structure causes higher internal energy dissipation to the resonators. The low *Q*-factor is also of the reasons for a lower resonant frequency of the resonators. The estimated mass resolution of the tungsten nanomechanical resonators is in the level of 10^{-15}g. It is not as sensitive as the carbon nanotube resonators, which is about 10^{-21}g. This is because the mass sensitivity is inverse proportional to the *Q*-factor. Therefore, the *Q* factor would need to be improved substantially in future in order for these resonators to be competitive.

Second, I built an electronic piezo-actuator inside a commercial SEM by using polymer piezo film. The polymer piezo film has larger range vibration frequency ranging from several Hz to 10^9 Hz, which extends the application for testing resonators with a larger range of dimensions. Due to the electron beam induced carbon contamination in the SEM chamber decrease the sensitivity of the nanomechanical resonators, I developed a real-time data acquisition system and wrote a LabVIEW code to control the whole system automatically. With this measurement system, the tungsten nanomechanical resonators only exposes to the electron beam for a few seconds, which reduced the carbon contamination on the

nanomechanical resonators significantly. I used the SEM linescan technique to characterise the dynamic properties of the tungsten nanomechanical resonator, which includes absolute vibration amplitude, resonant frequency and *Q*-factor. By fitting linescans for vibrating resonators making use of the linescan with excitation at the same position, the absolute amplitude of the vibrations can be extracted. Since the amplitude as a function of driving frequency is plotted, the Lorentzian fit shows the resonant frequency and *Q*-factor of the nanomechancial resonators. Except large vibration amplitude, the small vibration amplitude (i.e. smaller than half of the thickness of the resonator) can be detected. Then I also studied the effect of the scanning speed of electron beam across the oscillating resonator and found the optimum scanning speed of around 2 nm/μs by compromising asymmetry linescans caused by the low scanning speeds and loss of spatial resolution caused by high scanning speeds.

Using electron microscopy to characterise nanomechanical resonators have been published. In the work of Utke *et al*.(87), the nanomechanical resonator was excite to vibration and the electron beam was fixed at the position, in which the vibration amplitude of the resonator reached its maximum in a SEM chamber, then the phase and amplitude of the secondary-electron signal is measured using lock-in detection at the drive frequency. The technique allows detecting resonant frequency and the *Q*-factor of the nanomechanical resonators. In the work of Nishio *et al*. (11), the carbon nanotube resonator was excited to vibrate with a piezo actuator. The electron beam was fixed at the equilibrium position of the resonators and the induced secondary electron intensities in terms of the oscillation amplitude of the carbon nanotube resonator was used to obtain the oscillation amplitude and resonant frequency. As an alternative to this "spot-mode" method, Nonaka *et al*. (174) used thermal noise to excite the resonator to oscillation. Then the secondary-electron signal from an electron beam which is linearly scanned across the oscillating resonator was analysed to obtain the vibration

amplitude by fitting a model. This model took consideration of the cross-sectional geometry by assuming a cylindrical resonator with uniform material properties.

By comparing with my measurement technique, the technique of Utke *et al.* (87) does not permit absolute measurements of the vibration amplitude, whereas the method of Nishio *et al*. (11) is only relevant to the case, in which the vibration amplitude is much larger than the thickness of the resonators. Comparing with the work of Nonaka *et al.* (174), the analysing technique I developed does not require a model of secondary electron emission from the resonator to be specified before fitting to the data. My technique can be straightforwardly applied to resonators with arbitrary cross-sectional geometry, and to resonators whose materials properties are not radically homogeneous. Table 6.1 shows the comparison all of the three methods with my technique.

In my experiment, by using an electronic piezo-actuator, the full harmonic response may be measured; hence not only the resonant frequency but also the *Q*-factor may be determined. The combination which my technique provides of this feature with full linescan measurements (as distinct from spot-mode measurements) has not been previously reported in the literature and will be an important tool to enable complete characterisation of nanomechanical resonators. Besides, I also studied the effect of changing the electron beam scanning speeds of this technique. Its importance can be seen in the situation of a small-amplitude oscillation. In this case, a slower beam scanning speed is necessary on the condition that the sampling frequency of the DAQ card reaches its up limitation. This has been not reported in the literature.

In summary, the work presented here is novel broadly in two areas. Firstly, I investigated the suitability of FIB induced tungsten deposited nanomechanical resonators as ultrasensitive mass sensor. This is important because the Young's modulus, resonant frequency and *Q*-factor show the mass sensing possibility of the tungsten nanomechanical resonators. This contributes to the field of nanomechanical resonators. Secondly, I developed the SEM

linescan analysing technique. This is important because the technique is generically applicable and model-independent; it can therefore be straightforwardly applied to resonators with inhomogeneous materials properties and with arbitrary geometry. The accuracy with which the absolute amplitude can be measured in our approach is ultimately limited by the size of the focussed electron beam. This technique is likely to be important in the development of resonators with high stiffness (and hence high resonant frequency) for applications in high-resolution mass measurements. It is particularly suited to resonators of nanoscale cross-sectional dimensions in which the materials properties have not been well characterised in advance.

Table 6.1 Comparison of techniques for characterisation of nanomechanical resonators with SEM mode

	SEM mode	Measures absolute amplitude?	Model independent?	Measusred amplitude<radius (a<r)?
This work	Linescan	Yes	Yes	Yes
Utke *et al.*	Spot (x=a)	No	Yes	Yes
Nishio *et al.*	Spot (x=a)	Yes	Yes	No
Nonaka *et al.*	Linescan	Yes	No	Yes

Here x is the electron beam position, a is the amplitude, r is the radius of the nanowire.

6.3 Future work

High stiffness, low mass, ultrahigh resonant frequency and high *Q*-factor are the most important attributes of ultrasensitive nanomechanical resonators. At the moment, the *Q*-factor of our tungsten nanomechanical resonators ranges from 300 to 600, which is much lower by comparison with silicon based resonators (15000) and carbon nanotubes (1000). Internal energy dissipation is the main reason for the lower *Q*-factor of our resonators. The material structures of the resonators have a significant impact on the internal energy dissipation, however, the reason is not well known yet. Therefore, one important work in future is to investigate the reasons for the internal energy dissipation of our resonators and

then find out the possible solutions to maximize the *Q*-factor. This will contribute to increases in the resonant frequency and higher mass sensitivity of the resonators.

In order to fabricate an ultrasensitive mass sensor, another important work in future is to reduce the volume of the resonators by minimizing their dimensions. The mass of the nanomechanical resonators is proportional to their volume. We noticed that the geometry of the nanomechanical resonators also plays an important role on the final mass sensitivity. According to table 3.1 and the following equation, we can see the mass sensitivity is related to the effective mass and stiffness of resonators:

$$\delta M \propto \frac{M_{eff}^{5/4}}{K_{eff}^{3/4}}$$

The above equation also shows that a smaller mass of the resonator gives a better mass resolution. Therefore, it is necessary to minimise the volume of the resonator by reducing both its thickness (i.e. cross-sectional area) and its length. The dimension reducing can be realised by using FIB milling technique or other milling method or by fabricating with neon FIB or helium FIB induced deposition.

The above equation also shows that the mass sensitivity of the nanomechanical resonators is approximately inversely proportional to the stiffness of the resonators. That is to say increasing the stiffness of the resonator is one way to obtain an ultrasensitive mass sensing device. From an engineering point of view (and making use of classic beam-bending theory), if a beam with I-cross section has the same cross sectional area as a beam with a circular cross sectionthen the latter one exhibits a lower stiffness. Therefore, a nanorod with an I-cross section should be considered to improve the mass sensitivity of nanomechanical resonators.

In this case, the FIB has the advantages to fabricate a beam with an arbitrary cross section. Figure 6.1 shows an SEM image of a tungsten I-beam fabricated with FIB induced deposition at 50 pA and 30 kV. This is the only I-beam to have been grown with FIB induced deposition at the moment.

In future, reducing the cross-sectional dimensions (*a*, *b*, *c*) of the I-beam is an important work to make its effective mass as low as possible for ultra-sensitive mass sensors. The minimum cross-section of an I-beam grown by FIB induced deposition at the moment is much larger than a minimum circular cross section. It is also very challenging to trim a circular cross section into a I cross section by FIB milling. However, due to the higher stiffness of an I beam, it is still worth exploring more fabrication methods in addition to FIB to fabricate I-beams as an ultrasensitive mass sensors.

The readout system of ultrasensitive mass sensors is also a critical part of their future application. Practical application of the ultrasensitive mass sensing device will require working at ambient conditions. Therefore, the read-out system will be different from that in an SEM chamber. Nanoscale electro-mechanical systems are one option for future research. We plan to develop doubly clamped beams over a trench in a silicon substrate as the mass sensor. An ac current will pass through the mass sensor and it will be excited by a varying magnetic field. The sample will then be connected with a phase-locked loop (PLL) circuit which will be used to lock onto, and to track, the minute mechanical resonance signal.

Therefore, exploring theories about material structure and energy dissipation, new fabrication methods to make stiff nanoscale devices, designing beam with I-cross section as ultrasensitive mass sensors and building up new readout systems are the main focus of our future work.

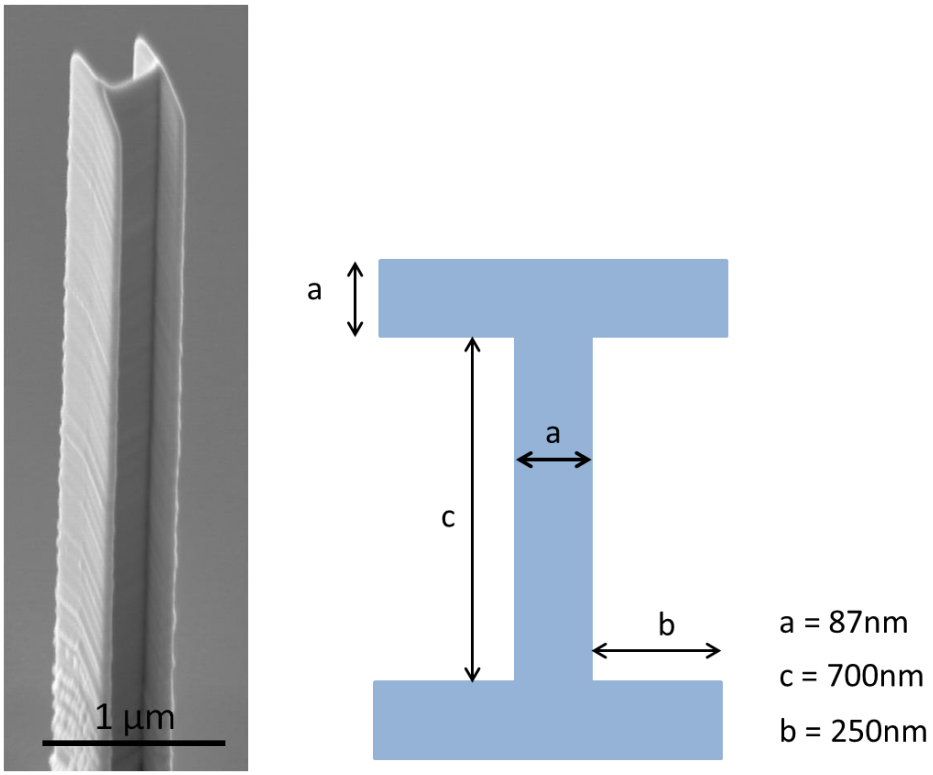

Figure 6. 1: SEM image of a tungsten I-beam fabricated with FIB induced deposition. (SEM viewing was at an angle of 36^{o}. The blue drawing shows the cross-section of the I-beam)

Reference

1. Raiteri R, Grattarola M, Butt H-J, Skládal P. (2001). Micromechanical cantilever-based biosensors. *Sensors and Actuators B: Chemical* **79**: 115-26
2. Ilic B, Czaplewski D, Zalalutdinov M, Craighead HG, Neuzil P, Campagnolo C, Batt C. (2001). Single cell detection with micromechanical oscillators. *Journal of Vacuum Science & Technology B* **19**: 2825-8
3. Gupta A, Akin D, Bashir R. (2003). Resonant mass biosensor for ultrasensitive detection of bacterial cells. *Journal of Vacuum Science & Technology B* **22**: 2785
4. Morita T, Kometani R, Watanabe K, Kanda K, Haruyama Y, Hoshino T, Kondo K, Kaito T, Ichihashi T, Fujita J-i, Ishida M, Ochiai Y, Tajima T, Matsui S. (2003). Free-space-wiring fabrication in nano-space by focused-ion-beam chemical vapor deposition. *Journal of Vacuum Science & Technology B: Microelectronics and Nanometer Structures* **21**: 2737-41
5. Craighead HG. (2000). Nanoelectromechanical Systems. *Science* **290**: 1532-5
6. Ekinci KL. (2005). Electromechanical Transducers at the Nanoscale: Actuation and Sensing of Motion in Nanoelectromechanical Systems (NEMS). *Small* **1**: 786-97
7. Eom K, Jung H, Jeong S, Kim C, Yoon D, Kwon T. (2011). Nanomechanical Motion of Microcantilevers Driven by Ion-Induced DNA Conformational Transitions. *BioNanoScience* **1**: 117-22
8. Utke I, Friedli V, Purrucker M, Michler J. (2007). Resolution in focused electron- and ion-beam induced processing. *Journal of Vacuum Science & Technology B: Microelectronics and Nanometer Structures* **25**: 2219-23
9. Lavrik NV, Datskos PG. (2003). Femtogram mass detection using photothermally actuated nanomechanical resonators. *Applied Physics Letters* **82**: 2697-9
10. Sawaya S, Akita S, Nakayama Y. (2006). In situ mass measurement of electron-beam-induced nanometer-sized W-related deposits using a carbon nanotube cantilever. *Applied Physics Letters* **89**: 193115
11. Nishio M, Sawaya S, Akita S, Nakayama Y. (2005). Carbon nanotube oscillators toward zeptogram detection. *Applied Physics Letters* **86**: 133111
12. Igaki J-y, Nakamatsu K-i, Kometani R, Kanda K, Haruyama Y, Kaito T, Matsui S. (2006). Mechanical characteristics and applications of diamondlike-carbon cantilevers fabricated by focused-ion-beam chemical vapor deposition. *Journal of Vacuum Science & Technology B: Microelectronics and Nanometer Structures* **24**: 2911-4
13. Forsen E, Abadal G, Ghatnekar-Nilsson S, Teva J, Verd J, Sandberg R, Svendsen W, Perez-Murano F, Esteve J, Figueras E, Campabadal F, Montelius L, Barniol N, Boisen A. (2005). Ultrasensitive mass sensor fully integrated with complementary metal-oxide-semiconductor circuitry. *Applied Physics Letters* **87**: 043507
14. Ekinci KL, Huang XMH, Roukes ML. (2004). Ultrasensitive nanoelectromechanical mass detection. *Applied Physics Letters* **84**: 4469-71
15. Li X, Ono T, Wang Y, Esashi M. (2003). Ultrathin single-crystalline-silicon cantilever resonators: Fabrication technology and significant specimen size effect on Young's modulus. *Applied Physics Letters* **83**: 3081-3

16. Ilic B, Craighead HG, Krylov S, Senaratne W, Ober C, Neuzil P. (2004). Attogram detection using nanoelectromechanical oscillators. *Journal of Applied Physics* **95**: 3694-703
17. Verbridge SS, Parpia JM, Reichenbach RB, Bellan LM, Craighead HG. (2006). High quality factor resonance at room temperature with nanostrings under high tensile stress. *Journal of Applied Physics* **99**: 124304
18. Sazonova V, Yaish Y, Ustunel H, Roundy D, Arias TA, McEuen PL. (2004). A tunable carbon nanotube electromechanical oscillator. *Nature* **431**: 284-7
19. Husain A, Hone J, Postma HWC, Huang XMH, Drake T, Barbic M, Scherer A, Roukes ML. (2003). Nanowire-based very-high-frequency electromechanical resonator. *Applied Physics Letters* **83**: 1240-2
20. Evoy S, Riegelman MA, Naguib N, Haihui Y, Jaroenapibal P, Luzzi DE, Gogotsi Y. (2005). Dielectrophoretic assembly of carbon nanofiber nanoelectromechanical devices. *Nanotechnology* **4**: 570-5
21. Fujita J, Ishida M, Sakamoto T, Ochiai Y, Kaito T, Matsui S. (2001). Observation and characteristics of mechanical vibration in three-dimensional nanostructures and pillars grown by focused ion beam chemical vapor deposition. *Journal of Vacuum Science & Technology B* **19**: 2834-7
22. Dohn S, Hansen O, Boisen A. (2006). Cantilever based mass sensor with hard contact readout. *Applied Physics Letters* **88**: 264104--3
23. Poncharal P, Wang ZL, Ugarte D, de Heer WA. (1999). Electrostatic Deflections and Electromechanical Resonances of Carbon Nanotubes. *Science* **283**: 1513-6
24. Joshi AY, Sharma SC, Harsha SP. (2011). Zeptogram scale mass sensing using single walled carbon nanotube based biosensors. *Sensors and Actuators A: Physical* **168**: 275-80
25. Kwon T, Eom K, Park J, Yoon DS, Lee HL, Kim TS. (2008). Micromechanical observation of the kinetics of biomolecular interactions. *Applied Physics Letters* **93**: 173901
26. Kwon T, Park J, Yang J, Yoon DS, Na S, Kim CW, Suh JS, Huh YM, Haam S, Eom K. (2009). Nanomechanical in situ monitoring of proteolysis of peptide by Cathepsin B. *PLoS ONE* **4**: e6248
27. Burg TP, Godin M, Knudsen SM, Shen W, Carlson G, Foster JS, Babcock K, Manalis SR. (2007). Weighing of biomolecules, single cells and single nanoparticles in fluid. *Nature* **446**: 1066-9
28. Campbell GA, Mutharasan R. (2006). Use of piezoelectric-excited millimeter-sized cantilever sensors to measure albumin interaction with self-assembled monolayers of alkanethiols having different functional headgroups. *Analytical Chemistry* **78**: 2328-34
29. Eom K, Yang J, Park J, Yoon G, Soo Sohn Y, Park S, Yoon DS, Na S, Kwon T. (2009). Experimental and computational characterization of biological liquid crystals: a review of single-molecule bioassays. *International Journal of Molecular Sciences* **10**: 4009-32
30. Naik AK, Hanay MS, Hiebert WK, Feng XL, Roukes ML. (2009). Towards single-molecule nanomechanical mass spectrometry. *Nature Nanotechnology* **4**: 445-50
31. Ilic B, Yang Y, Aubin K, Reichenbach R, Krylov S, Craighead HG. (2005). Enumeration of DNA Molecules Bound to a Nanomechanical Oscillator. *Nano Letters* **5**: 925-9
32. Waggoner PS, Craighead HG. 2007. Micro- and nanomechanical sensors for environmental, chemical, and biological detection. *Lab on a Chip* **7**: 1238-55
33. Binnig G, Quate CF, Gerber C. (1986). Atomic force microscope. *Physical Review Letters* **56**: 930-3

34. Albrecht TR, Akamine S, Carver TE, Quate CF. (1990). Microfabrication of cantilever styli for the atomic force microscope. *Journal of Vacuum Science & Technology A: Vacuum, Surfaces, and Films* **8**: 3386-96
35. Wolter O, Bayer T, Greschner J. (1991). Micromachined silicon sensors for scanning force microscopy. *Journal of Vacuum Science & Technology B: Microelectronics and Nanometer Structures* **9**: 1353-7
36. Thundat T, Warmack RJ, Chen GY, Allison DP. (1994). Thermal and ambient-induced deflections of scanning force microscope cantilevers. *Applied Physics Letters* **64**: 2894-6
37. Barnes JR, Stephenson RJ, Welland ME, Gerber C, Gimzewski JK. (1994). Photothermal spectroscopy with femtojoule sensitivity using a micromechanical device. *Nature* **372**: 79-81
38. Barnes JR, Stephenson RJ, Woodburn CN, Oshea SJ, Welland ME, Rayment T, Gimzewski JK, Gerber C. (1995). Erratum: A femtojoule calorimeter using micromechanical sensors. *Review of Scientific Instruments* **66**: 3083
39. Raiteri R, Butt H-J. (1995). Measuring Electrochemically Induced Surface Stress with an Atomic Force Microscope. *The Journal of Physical Chemistry* **99**: 15728-32
40. Butt H-J. (1996). A Sensitive Method to Measure Changes in the Surface Stress of Solids. *Journal of Colloid and Interface Science* **180**: 251-60
41. Berger R, Delamarche E, Lang HP, Gerber C, Gimzewski JK, Meyer E, Güntherodt H-J. (1997). Surface Stress in the Self-Assembly of Alkanethiols on Gold. *Science* **276**: 2021-4
42. Fritz J, Baller MK, Lang HP, Rothuizen H, Vettiger P, Meyer E, -J. Güntherodt H, Gerber C, Gimzewski JK. (2000). Translating Biomolecular Recognition into Nanomechanics. *Science* **288**: 316-8
43. Rugar D, Budakian R, Mamin HJ, Chui BW. (2004). Single spin detection by magnetic resonance force microscopy. *Nature* **430**: 329-32
44. Budakian R, Mamin HJ, Rugar D. (2006). Spin manipulation using fast cantilever phase reversals. *Applied Physics Letters* **89**: 113113
45. Yang YT, Callegari C, Feng XL, Ekinci KL, Roukes ML. (2006). Zeptogram-Scale Nanomechanical Mass Sensing. *Nano Letters* **6**: 583-6
46. Li M, Tang HX, Roukes ML. (2007). Ultra-sensitive NEMS-based cantilevers for sensing, scanned probe and very high-frequency applications. *Nature Nanotechnology* **2**: 114-20
47. JensenK, Kim K, ZettlA. (2008). An atomic-resolution nanomechanical mass sensor. *Nature Nanotechnology* **3**: 533-7
48. O'Connell AD, Hofheinz M, Ansmann M, Bialczak RC, Lenander M, Lucero E, Neeley M, Sank D, Wang H, Weides M, Wenner J, Martinis JM, Cleland AN. (2010). Quantum ground state and single-phonon control of a mechanical resonator. *Nature* **464**: 697-703
49. Paul MR, Clark MT, Cross MC. (2006). The stochastic dynamics of micron and nanoscale elastic cantilevers in fluid: fluctuations from dissipation. *Nanotechnology* **17**: 4502
50. Tamayo J, Calleja M, Ramos D, Mertens J. (2007). Underlying mechanisms of the self-sustained oscillation of a nanomechanical stochastic resonator in a liquid. *Physical Review B* **76**: 180201
51. Badzey RL, Mohanty P. (2005). Coherent signal amplification in bistable nanomechanical oscillators by stochastic resonance. *Nature* **437**: 995-8

52. Sato M, Hubbard BE, Sievers AJ, Ilic B, Czaplewski DA, Craighead HG. (2003). Observation of Locked Intrinsic Localized Vibrational Modes in a Micromechanical Oscillator Array. *Physical Review Letters* **90**: 044102
53. Mouaziz S, Boero G, Popovic RS, Brugger J. (2006). Polymer-based cantilevers with integrated electrodes. *Journal of Microelectromechanical Systems* **15**: 890-5
54. Peng HB, Chang CW, Aloni S, Yuzvinsky TD, Zettl A. (2006). Ultrahigh Frequency Nanotube Resonators. *Physical Review Letters* **97**: 087203
55. Greaney PA, Grossman JC. (2008). Nanomechanical Resonance Spectroscopy: A Novel Route to Ultrasensitive Label-Free Detection. *Nano Letters* **8**: 2648-52
56. Robertson J. (2002). Diamond-like amorphous carbon. *Materials Science & Engineering R-Reports* **37**: 129-281
57. Zhu R, Wang D, Xiang S, Zhou Z, Ye X. (2008). Piezoelectric characterization of a single zinc oxide nanowire using a nanoelectromechanical oscillator. *Nanotechnology* **19**: 285712
58. Anja B, Søren D, Stephan Sylvest K, Silvan S, Maria T. (2011). Cantilever-like micromechanical sensors. *Reports on Progress in Physics* **74**: 036101
59. Ramos D, Arroyo-Hernández Ma, Gil-Santos E, Duy Tong H, Van Rijn C, Calleja M, Tamayo J. (2009). Arrays of Dual Nanomechanical Resonators for Selective Biological Detection. *Analytical Chemistry* **81**: 2274-9
60. Yang J, Ono T, Esashi M. (2000). Mechanical behavior of ultrathin microcantilever. *Sensors and Actuators A: Physical* **82**: 102-7
61. Kovacs GTA, Maluf NI, Petersen KE. (1998). *Bulk micromachining of silicon*. Presented at Proceedings of the IEEE
62. Pechmann R, Kohler JM, Fritzsche W, Schaper A, Jovin TM. (1994). The Novolever: A new cantilever for scanning force microscopy microfabricated from polymeric materials. *Review of Scientific Instruments* **65**: 3702-6
63. Genolet G, Brugger J, Despont M, Drechsler U, Vettiger P, Rooij NFd, Anselmetti D. (1999). Soft, entirely photoplastic probes for scanning force microscopy. *Review of Scientific Instruments* **70**: 2398-401
64. Wang X, Ryu KS, Bullen DA, Zou J, Zhang H, Mirkin CA, Liu C. (2003). Scanning Probe Contact Printing. *Langmuir* **19**: 8951-5
65. Gaitas A, Gianchandani YB. (2006). An experimental study of the contact mode AFM scanning capability of polyimide cantilever probes. *Ultramicroscopy* **106**: 874-80
66. Andrew WM, Mark AP, Lawrence AB, Jonathan SC. (2004). Injection moulding of high aspect ratio micron-scale thickness polymeric microcantilevers. *Nanotechnology* **15**: 1628
67. McFarland AW, Poggi MA, Bottomley LA, Colton JS. (2004). Production and characterization of polymer microcantilevers. *Review of Scientific Instruments* **75**: 2756-8
68. McFarland AW, Colton JS. (2005). Chemical sensing with micromolded plastic microcantilevers. *Journal of Microelectromechanical Systems* **14**: 1375-85
69. Zhang XR, Xu X. (2004). Development of a biosensor based on laser-fabricated polymer microcantilevers. *Applied Physics Letters* **85**: 2423-5
70. Lee LP, Berger SA, Liepmann D, Pruitt L. (1998). High aspect ratio polymer microstructures and cantilevers for bioMEMS using low energy ion beam and photolithography. *Sensors and Actuators A: Physical* **71**: 144-9
71. Yao T-J, Yang X, Tai Y-C. (2002). BrF3 dry release technology for large freestanding parylene microstructures and electrostatic actuators. *Sensors and Actuators A: Physical* **97–98**: 771-5

72. Katragadda R, Wang Z, Khalid W, Li Y, Xu Y. (2007). Parylene cantilevers integrated with polycrystalline silicon piezoresistors for surface stress sensing. *Applied Physics Letters* **91**: 083505--3
73. Anders G, Stephan K, Asger LV, Anders K, David L, Kresten Y, Jørn MH, Marta C, Arunava M, Anja B. (2010). Thermoplastic microcantilevers fabricated by nanoimprint lithography. *Journal of Micromechanics and Microengineering* **20**: 015009
74. Jun Z, Xuefeng W, David B, Kee R, Chang L, Chad AM. (2004). A mould-and-transfer technology for fabricating scanning probe microscopy probes. *Journal of Micromechanics and Microengineering* **14**: 204
75. Ransley JHT, Watari M, Sukumaran D, McKendry RA, Seshia AA. (2006). SU8 bio-chemical sensor microarrays. *Microelectronic Engineering* **83**: 1621-5
76. Guo LJ. (2004). Recent progress in nanoimprint technology and its applications. *Journal of Physics D: Applied Physics* **37**: R123
77. Schift H. (2008). Nanoimprint lithography: An old story in modern times? A review. *Journal of Vacuum Science & Technology B: Microelectronics and Nanometer Structures* **26**: 458-80
78. Foulds IG, Johnstone RW, Parameswaran M. (2008). Polydimethylglutarimide (PMGI) as a sacrificial material for SU-8 surface-micromachining. *Journal of Micromechanics and Microengineering* **18**: 075011
79. Legtenberg R, Tilmans HAC, Elders J, Elwenspoek M. (1994). Stiction of surface micromachined structures after rinsing and drying: model and investigation of adhesion mechanisms. *Sensors and Actuators A: Physical* **43**: 230-8
80. Tenje M, Keller S, Dohn S, Davis ZJ, Boisen A. (2010). Drift study of SU8 cantilevers in liquid and gaseous environments. *Ultramicroscopy* **110**: 596-8
81. Martin C, Llobera A, Villanueva G, Voigt A, Gruetzner G, Brugger J, Perez-Murano F. (2009). Stress and aging minimization in photoplastic AFM probes. *Microelectronic Engineering* **86**: 1226-9
82. Stephan K, Daniel H, Anja B. (2010). Fabrication of thin SU-8 cantilevers: initial bending, release and time stability. *Journal of Micromechanics and Microengineering* **20**: 045024
83. Haefliger D, Hansen O, Boisen A. (2006). Self-Positioning of Polymer Membranes Driven by Thermomechanically Induced Plastic Deformation. *Advanced Materials* **18**: 238-41
84. Dai H, Franklin N, Han J. (1998). Exploiting the properties of carbon nanotubes for nanolithography. *Applied Physics Letters* **73**: 1508-10
85. Akita S, Nishijima H, Nakayama Y, Tokumasu F, Takeyasu K. (1999). Carbon nanotube tips for a scanning probe microscope: their fabrication and properties. *Journal of Physics D: Applied Physics* **32**: 1044
86. Utke I, Friedli V, Michler J, Bret T, Multone X, Hoffmann P. (2006). Density determination of focused-electron-beam-induced deposits with simple cantilever-based method. *Applied Physics Letters* **88**: 031906--3
87. Friedli V, Utke I, Mølhave K, Michler J. (2009). Dose and energy dependence of mechanical properties of focused electron-beam-induced pillar deposits from Cu($C_5HF_6O_2)_2$. *Nanotechnology* **20**: 385304
88. Dongfeng Z, Jean-Marc B, Reymond C, Laetitia P, Ivo U, Johann M. (2009). In situ tensile testing of individual Co nanowires inside a scanning electron microscope. *Nanotechnology* **20**: 365706
89. Sadki ES, Ooi S, Hirata K. (2004). Focused-ion-beam-induced deposition of superconducting nanowires. *Applied Physics Letters* **85**: 6206-8

90. Li W, Fenton JC, Warburton PA. (2009). Focused-Ion-Beam Direct-Writing of Ultra-Thin Superconducting Tungsten Composite Films. *Applied Superconductivity, IEEE Transactions on* **19**: 2819-22
91. Li W, Cui A, Gu C, Warburton PA. (2012). Atomic resolution top-down nanofabrication with low-current focused-ion-beam thinning. *Microelectronic Engineering* **98**: 301-4
92. Ross IM, Luxmoore IJ, Cullis AG, Orr J, Buckle PD, Jefferson JH. (2006). Characterisation of tungsten nano-wires prepared by electron and ion beam induced chemical vapour deposition. *Journal of Physics: Conference Series* **26**: 363
93. Guillamón I, Suderow H, Vieira S, Fernández-Pacheco A, Sesé J, Córdoba R, Teresa JMD, Ibarra MR. (2008). Nanoscale superconducting properties of amorphous W-based deposits grown with a focused-ion-beam. *New Journal of Physics* **10**: 093005
94. Khaderbad MA, Choi Y, Hiralal P, Aziz A, Wang N, Durkan C, Thiruvenkatanathan P, Amaratunga GAJ, Rao VR, Seshia AA. (2012). Electrical actuation and readout in a nanoelectromechanical resonator based on a laterally suspended zinc oxide nanowire. *Nanotechnology* **23**: 025501
95. Tanner SM, Gray JM, Rogers CT, Bertness KA, Sanford NA. (2007). High-Q GaN nanowire resonators and oscillators. *Applied Physics Letters* **91**: 203117-3
96. Nam C-Y, Jaroenapibal P, Tham D, Luzzi DE, Evoy S, Fischer JE. (2006). Diameter-Dependent Electromechanical Properties of GaN Nanowires. *Nano Letters* **6**: 153-8
97. Meyer G, Amer NM. (1988). Novel optical approach to atomic force microscopy. *Applied Physics Letters* **53**: 2400-2
98. Hoummady M, Farnault E, Yahiro T, Kawakatsu H. (1997). Simultaneous optical detection techniques, interferometry, and optical beam deflection for dynamic mode control of scanning force microscopy. *Journal of Vacuum Science & Technology B* **15**: 1539-42
99. Lavrik NV, Sepaniak MJ, Datskos PG. (2004). Cantilever transducers as a platform for chemical and biological sensors. *Review of Scientific Instruments* **75**: 2229-53
100. Tipple CA, Lavrik NV, Culha M, Headrick J, Datskos P, Sepaniak MJ. (2002). Nanostructured Microcantilevers with Functionalized Cyclodextrin Receptor Phases: Self-Assembled Monolayers and Vapor-Deposited Films. *Analytical Chemistry* **74**: 3118-26
101. Carr DW, Evoy S, Sekaric L, Craighead HG, Parpia JM. (2000). Parametric amplification in a torsional microresonator. *Applied Physics Letters* **77**: 1545-7
102. Mamin HJ, Rugar D. (2001). Sub-attonewton force detection at millikelvin temperatures. *Applied Physics Letters* **79**: 3358-60
103. Rugar D, Yannoni CS, Sidles JA. (1992). Mechanical detection of magnetic resonance. *Nature* **360**: 563-6
104. Senesac LR, Corbeil JL, Rajic S, Lavrik NV, Datskos PG. (2003). IR imaging using uncooled microcantilever detectors. *Ultramicroscopy* **97**: 451-8
105. Martinez NF, Kosaka PM, Tamayo J, Ramirez J, Ahumada O, Mertens J, Hien TD, Rijn CV, Calleja M. (2010). High throughput optical readout of dense arrays of nanomechanical systems for sensing applications. *Review of Scientific Instruments* **81**: 125109-9
106. Oden PI, Datskos PG, Thundat T, Warmack RJ. (1996). Uncooled thermal imaging using a piezoresistive microcantilever. *Applied Physics Letters* **69**: 3277-9
107. Abedinov N, Grabiec P, Gotszalk T, Ivanov T, Voigt J, Rangelow IW. (2001). Micromachined piezoresistive cantilever array with integrated resistive microheater for calorimetry and mass detection. *Journal of Vacuum Science & Technology A: Vacuum, Surfaces, and Films* **19**: 2884-8

108. Sung-Jin P, Doll JC, Rastegar AJ, Pruitt BL. (2010). Piezoresistive Cantilever Performance-Part II: Optimization. *Journal of Microelectromechanical Systems* **19**: 149-61
109. Zurn S, Hsieh M, Smith G, Markus D, Zang M, Hughes G, Nam Y, Arik M, Polla D. (2001). Fabrication and structural characterization of a resonant frequency PZT microcantilever. *Smart Materials and Structures* **10**: 252
110. DeVoe DL, Pisano AP. (1997). Modeling and optimal design of piezoelectric cantilever microactuators. *Microelectromechanical Systems, Journal of* **6**: 266-70
111. Khaderbad MA, Choi Y, Hiralal P, Aziz A, Wang N, Durkan C, Thiruvenkatanathan P, Amaratunga GAJ, Rao VR, Seshia AA. (2012). Electrical actuation and readout in a nanoelectromechanical resonator based on a laterally suspended zinc oxide nanowire. *Nanotechnology* **23**
112. Lee JH, Yoon KH, Kim TS. (2002). Characterization of Resonant Behavior and Sensitivity Using Micromachined PZT Cantilever. *Integrated Ferroelectrics* **50**: 43-52
113. Adams JD, Parrott G, Bauer C, Sant T, Manning L, Jones M, Rogers B, McCorkle D, Ferrell TL. (2003). Nanowatt chemical vapor detection with a self-sensing, piezoelectric microcantilever array. *Applied Physics Letters* **83**: 3428-30
114. Lee SS, White RM. (1996). Self-excited piezoelectric cantilever oscillators. *Sensors and Actuators A: Physical* **52**: 41-5
115. Britton Jr CL, Jones RL, Oden PI, Hu Z, Warmack RJ, Smith SF, Bryan WL, Rochelle JM. (2000). Multiple-input microcantilever sensors. *Ultramicroscopy* **82**: 17-21
116. Verd J, Abadal G, Teva J, Uranga A, Barniol N, Esteve J, Duch M, Perez-Murano F. (2005). *High-sensitivity capacitive readout system for resonant submicrometer-scale cantilevers based sensors*. Presented at IEEE International Symposium on Circuits and Systems
117. Erbe A, Weiss C, Zwerger W, Blick RH. (2001). Nanomechanical Resonator Shuttling Single Electrons at Radio Frequencies. *Physical Review Letters* **87**: 096106
118. Kenny TW, Kaiser WJ, Waltman SB, Reynolds JK. (1991). Novel infrared detector based on a tunneling displacement transducer. *Applied Physics Letters* **59**: 1820-2
119. DiLella D, Whitman LJ, Colton RJ, Kenny TW, Kaiser WJ, Vote EC, Podosek JA, Miller LM. (2000). A micromachined magnetic-field sensor based on an electron tunneling displacement transducer. *Sensors and Actuators A: Physical* **86**: 8-20
120. Ghatnekar-Nilsson S, Forsén E, Abadal G, Verd J, Campabadal F, Pérez-Murano F, Esteve J, Barniol N, Boisen A, Montelius L. (2005). Resonators with integrated CMOS circuitry for mass sensing applications, fabricated by electron beam lithography. *Nanotechnology* **16**: 98
121. Schmid S, Wendlandt M, Junker D, Hierold C. (2006). Nonconductive polymer microresonators actuated by the Kelvin polarization force. *Applied Physics Letters* **89**: 163506--3
122. Unterreithmeier QP, Weig EM, Kotthaus JP. (2009). Universal transduction scheme for nanomechanical systems based on dielectric forces. *Nature* **458**: 1001-4
123. Schmid S, Senn P, Hierold C. (2008). Electrostatically actuated nonconductive polymer microresonators in gaseous and aqueous environment. *Sensors and Actuators A: Physical* **145–146**: 442-8
124. Schmid S, Hierold C, Boisen A. (2010). Modeling the Kelvin polarization force actuation of micro- and nanomechanical systems. *Journal of Applied Physics* **107**: 054510--6
125. Mitra B, Gaitas A. (2009). Thermally actuated tapping mode atomic force microscopy with polymer microcantilevers. *Review of Scientific Instruments* **80**: 023703

126. Ilic B, Krylov S, Craighead HG. (2010). Theoretical and experimental investigation of optically driven nanoelectromechanical oscillators. *Journal of Applied Physics* **107**: 034311--13
127. Naik AK, Hanay MS, Hiebert WK, Feng XL, Roukes ML. (2009). Towards single-molecule nanomechanical mass spectrometry. *Nat Nano* **4**: 445-50
128. Petersen KE, Guarnieri CR. (1979). Young's modulus measurements of thin films using micromechanics. *Journal of Applied Physics* **50**: 6761-6
129. Taechung Y, Chang-Jin K. (1999). Measurement of mechanical properties for MEMS materials. *Measurement Science and Technology* **10**: 706
130. Srikar V, Spearing S. (2003). A critical review of microscale mechanical testing methods used in the design of microelectromechanical systems. *Experimental Mechanics* **43**: 238-47
131. Chen CQ, Shi Y, Zhang YS, Zhu J, Yan YJ. (2006). Size Dependence of Young's Modulus in ZnO Nanowires. *Physical Review Letters* **96**: 075505
132. Cuenot S, Frétigny C, Demoustier-Champagne S, Nysten B. (2004). Surface tension effect on the mechanical properties of nanomaterials measured by atomic force microscopy. *Physical Review B* **69**: 165410
133. Wong EW, Sheehan PE, Lieber CM. (1997). Nanobeam Mechanics: Elasticity, Strength, and Toughness of Nanorods and Nanotubes. *Science* **277**: 1971-5
134. Wu B, Heidelberg A, Boland JJ. (2005). Mechanical properties of ultrahigh-strength gold nanowires. *Nat Mater* **4**: 525-9
135. Nagy A, Strahl A, Neuhäuser H, Schrader S, Behrens I, Peiner E, Schlachetzki A. (2004). Mechanical spectroscopy of thin layers of PPV polymer on Si substrates. *Materials Science and Engineering: A* **370**: 311-5
136. Haramina T, Kirchheim R, Tibrewala A, Peiner E. (2008). Mechanical spectroscopy of thin polystyrene films. *Polymer* **49**: 2115-8
137. Xu S, Mutharasan R. (2009). Cantilever biosensors in drug discovery. *Expert Opinion on Drug Discovery* **4**: 1237-51
138. Schmid S, Hierold C. (2008). Damping mechanisms of single-clamped and prestressed double-clamped resonant polymer microbeams. *Journal of Applied Physics* **104**: 093516--12
139. Blagoi G, Keller S, Johansson A, Boisen A, Dufva M. (2008). Functionalization of SU-8 photoresist surfaces with IgG proteins. *Applied Surface Science* **255**: 2896-902
140. Ramos D, Tamayo J, Mertens J, Calleja M, Villanueva LG, Zaballos A. (2008). Detection of bacteria based on the thermomechanical noise of a nanomechanical resonator: origin of the response and detection limits. *Nanotechnology* **19**: 035503
141. Ramos D, Tamayo J, Mertens J, Calleja M, Zaballos A. (2006). Origin of the response of nanomechanical resonators to bacteria adsorption. *Journal of Applied Physics* **100**: 106105
142. Burg TP, Manalis SR. (2003). Suspended microchannel resonators for biomolecular detection. *Applied Physics Letters* **83**: 2698-700
143. Braun T, Ghatkesar MK, Backmann N, Grange W, Boulanger P, Letellier L, Lang H-P, Bietsch A, Gerber C, Hegner M. (2009). Quantitative time-resolved measurement of membrane protein-ligand interactions using microcantilever array sensors. *Nature Nanotechnology* **4**: 179-85
144. Sisquella X, de Pourcq K, Alguacil J, Robles J, Sanz F, Anselmetti D, Imperial S, Fernàndez-Busquets X. (2010). A single-molecule force spectroscopy nanosensor for the identification of new antibiotics and antimalarials. *The Journal of the Federation of American Societies for Experimental Biology* **24**: 4203-17

145. Datskos PG, Rajic S, Sepaniak MJ, Lavrik N, Tipple CA, Senesac LR, Datskou I. (2001). Chemical detection based on adsorption-induced and photoinduced stresses in microelectromechanical systems devices. *Journal of Vacuum Science & Technology B: Microelectronics and Nanometer Structures* **19**: 1173-9
146. Krause AR, Neste CV, Senesac L, Thundat T, Finot E. (2008). Trace explosive detection using photothermal deflection spectroscopy. *Journal of Applied Physics* **103**: 094906
147. Li D, Liu J, Kwok RTK, Liang Z, Tang BZ, Yu J. (2012). Supersensitive detection of explosives by recyclable AIE luminogen-functionalized mesoporous materials. *Chemical Communications* **48**: 7167-9
148. Pinnaduwage LA, Boiadjiev V, Hawk JE, Thundat T. (2003). Sensitive detection of plastic explosives with self-assembled monolayer-coated microcantilevers. *Applied Physics Letters* **83**: 1471-3
149. Finot E, Rouger V, Markey L, Seigneuric R, Nadal MH, Thundat T. (2012). Visible photothermal deflection spectroscopy using microcantilevers. *Sensors and Actuators B: Chemical* **169**: 222-8
150. Yun M, Kim S, Lee D, Jung N, Chae I, Jeon S, Thundat T. (2012). Photothermal cantilever deflection spectroscopy of a photosensitive polymer. *Applied Physics Letters* **100**: 204103-4
151. Budynas WYR. (2002). *Roak's Formulars for Stress and Strain*. New York: McGraw-Hill Professional Publication
152. Graff KF. (1991). *Wave Motion in Elastic Solids*. New York: Oxford University Press
153. Rabe U, Janser K, Arnold W. (1996). Vibrations of free and surface-coupled atomic force microscope cantilevers: Theory and experiment. *Review of Scientific Instruments* **67**: 3281-93
154. Vinzenz Friedli SH, Johann Michler, Ivo Utke. (2008). Applied Scanning Probe Methods VIII. Springer
155. Yasumura KY, Stowe TD, Chow EM, Pfafman T, Kenny TW, Stipe BC, Rugar D. (2000). Quality factors in micron- and submicron-thick cantilevers. *Microelectromechanical Systems, Journal of* **9**: 117-25
156. Yao N. 2007. *Focused Ion Beam System*. New York: Cambridge University Press
157. Gierak J. (2009). Focused ion beam technology and ultimate applications. *Semiconductor Science and Technology* **24**: 043001
158. LA Giannuzzi FS. (2005). *Introduction to Focused Ion Beam*. New York: Springer
159. Giannuzzi LA. (2005). *Introduction of Focused Ion Beam*. New York: Springer
160. Allen TE, Kunz RR, Mayer TM. 1988. Monte Carlo calculation of low-energy electron emission from surfaces. *Journal of Vacuum Science & Technology B: Microelectronics and Nanometer Structures* **6**: 2057-60
161. Dubner AD, Wagner A, Melngailis J, Thompson CV. (1991). The role of the ion-solid interaction in ion-beam-induced deposition of gold. *Journal of Applied Physics* **70**: 665-73
162. Callegari V, Nellen PM. (2007). Spontaneous growth of uniformly distributed In nanodots and InI3 nanowires on InP induced by a focused ion beam. *physica status solidi (a)* **204**: 1665-71
163. Utke I, Hoffmann P, Melngailis J. (2008). Gas-assisted focused electron beam and ion beam processing and fabrication. *Journal of Vacuum Science & Technology B: Microelectronics and Nanometer Structures* **26**: 1197-276
164. Morita T, Kometani R, Watanabe K, Kanda K, Haruyama Y, Hoshino T, Kondo K, Kaito T, Ichihashi T, Fujita J-i, Ishida M, Ochiai Y, Tajima T, Matsui S. (2003). Free-space-wiring fabrication in nano-space by focused-ion-beam chemical vapor

deposition. *Journal of Vacuum Science & Technology B: Microelectronics and Nanometer Structures* **21**: 2737-41
165. Sarvesh KT, Neeraj S, Dhamodaran S, Vishwas NK. (2008). Controlled manipulation of carbon nanopillars and cantilevers by focused ion beam. *Nanotechnology* **19**: 205302
166. Hoyle PC, Ogasawara M, Cleaver JRA, Ahmed H. (1993). Electrical resistance of electron beam induced deposits from tungsten hexacarbonyl. *Applied Physics Letters* **62**: 3043-5
167. Chiang TP, Sawin HH, Thompson CV. (1997). Surface kinetic study of ion-induced chemical vapor deposition of copper for focused ion beam applications. *Journal of Vacuum Science & Technology A: Vacuum, Surfaces, and Films* **15**: 3104-14
168. Utke I, Hoffmann P, Melngailis J. (2008). Gas-assisted focused electron beam and ion beam processing and fabrication. *Journal of Vacuum Science & Technology B: Microelectronics and Nanometer Structures* **26**: 1197-276
169. Binnig G, Rohrer H, Gerber C, Weibel E. (1982). Surface Studies by Scanning Tunneling Microscopy. *Physical Review Letters* **49**: 57-61
170. Wenger MP. (2009). *Mechanical and Structural Properties of Collagen Fibrils*. Univerisity College London
171. Butt H-J, Cappella B, Kappl M. (2005). Force measurements with the atomic force microscope: Technique, interpretation and applications. *Surface Science Reports* **59**: 1-152
172. Hutter JL, Bechhoefer J. (1993). Calibration of atomic-force microscope tips. *Review of Scientific Instruments* **64**: 1868-73
173. Tripathi SK, Shukla N, Dhamodaran S, Kulkarni VN. (2008). Controlled manipulation of carbon nanopillars and cantilevers by focused ion beam. *Nanotechnology* **19**: 205302
174. Nonaka K, Tamaru K, Nagase M, Yamaguchi H, Warisawa Si, Ishihara S. (2009). Evaluation of Thermal–Mechanical Vibration Amplitude and Mechanical Properties of Carbon Nanopillars Using Scanning Electron Microscopy. *Japanese Journal of Applied Physics* **48**: 06FG7-FG7-5
175. D.S.Jones. (1961). *Electrical and Mechanical Oscillations*. London: Routledge and Kegan Paul London
176. Reo K, Sunao I. (2009). Nanoelectromechanical device fabrications by 3-D nanotechnology using focused-ion beams. *Science and Technology of Advanced Materials* **10**: 034501
177. Tabrizian R, Rais-Zadeh M, Ayazi F. (2009). *Effect of phonon interactions on limiting the f.Q product of micromechanical resonators*. Presented at Solid-State Sensors, Actuators and Microsystems Conference, 2009. TRANSDUCERS 2009.
178. Sekaric L, Parpia JM, Craighead HG, Feygelson T, Houston BH, Butler JE. (2002). Nanomechanical resonant structures in nanocrystalline diamond. *Applied Physics Letters* **81**: 4455-7
179. Fujita J, Ishida M, Ichihashi T, Sakamoto T, Ochia Y, Kaito T and Matsui S. (2002). Structure of resonant characterisation of amorphous carbon pillars grown by focused-ion-beam chemical vapor deposition. *Japanese Journel of Applied Physics* **41**: 4423–4426

Appendix I

PUBLICATIONS

1. *Model-independent Quantitative Measurement of Nanomechanical Oscillator Vibrations using electron-microscope line-scans,* Huan Wang, J. C. Fenton, O. Chiatti and P. A. Warburton, Review of Scientific Instruments 84 (2013) 075002
2. *Felling of Individual Freestanding Nanoobjects Using Focused-Ion-Beam Milling for Investigations of Structural and Transport Properties,* Wuxia Li, J.C. Fenton, A. Cui, Huan Wang, Y. Wang, C. Gu. D.W. McComb and P.A. Warburton, Nanotechnology 23 (2012) 105301

CONFERENCE PRESENTATIONS

1. *Focused Ion Beam deposited tungsten nanomechanical resonators,* Huan Wang, O. Chiatti, J.C. Fenton and P.A. Warburton, Institute of Physics, 2011, Manchester, UK (poster presentation)
2. *Nanomechanical resonators grown by Focused Ion Beam deposition,* Huan Wang, O. Chiatti, J.C. Fenton and P.A. Warburton, Material Research Society, 2011, San Francisco, USA (oral presentation)
3. *Nanomechanical resonators grown by Focused Ion Beam deposition*, Huan Wang, O. Chiatti, J.C. Fenton and P.A. Warburton, Institute of Physics, 2010, Warwick, UK (poster presentation)
4. *Fabrication and mechanical characterization of tungsten nanorods*, Huan Wang, E. J. Romans and P. A. Warburton, UK NanoFIB Network meeting, 2009, Oxford, UK (poster presentation)
5. *CrossBeam User Meeting MPI, 2012, Stuttgart, Germany*

Appendix II

LabVIEW code

Figure 1 is the front panel of the LabVIEW code

Part-1: Command of sweep frequency and amplitude (certain ac voltage) is sent to the function generator to apply on the piezo-actuator

Part-2: Settings for the data acquisition system

Part-3: Setting for folders to save the acquired real-time data and plotting.

Original s and *Original v* shows the plotting of raw data when the nanowire is stationary and oscillating, individually; *Separate s* and *Separate v* shows the plotting of the separated raw data based on the trigger value; *Final s* and *Final v* shows the plotting of the average raw data after being separated

Figure 2 (a) is the first part of block diagram of the Lab VIEW code

Part-1: The command code to send to the function generator

Part-2: Data acquisition code

The row data was acquire from SE-detector and data acquisition parameter setting as shown in *part-2-a*, find a folder to save it and plot it as shown in *part-2-b*. *Part-2-a* includes 10 case

structures (as shown from figure 3 to figure 12), which shows how the data was acquired step by step.

Figure 2 (b) is the second part of the block diagram of the LabVIEW code

This codes shows how the acquired data is saved in a folder automatically, plotted and how the raw is being analysed by separating each row data set followed by averaging. This is shown in *part-3-a*. *Part-3-b* shows how the averaged data is fitted with the theory and the absolute vibration amplitude is extracted, then the amplitude as a function of driving frequency is plotted.

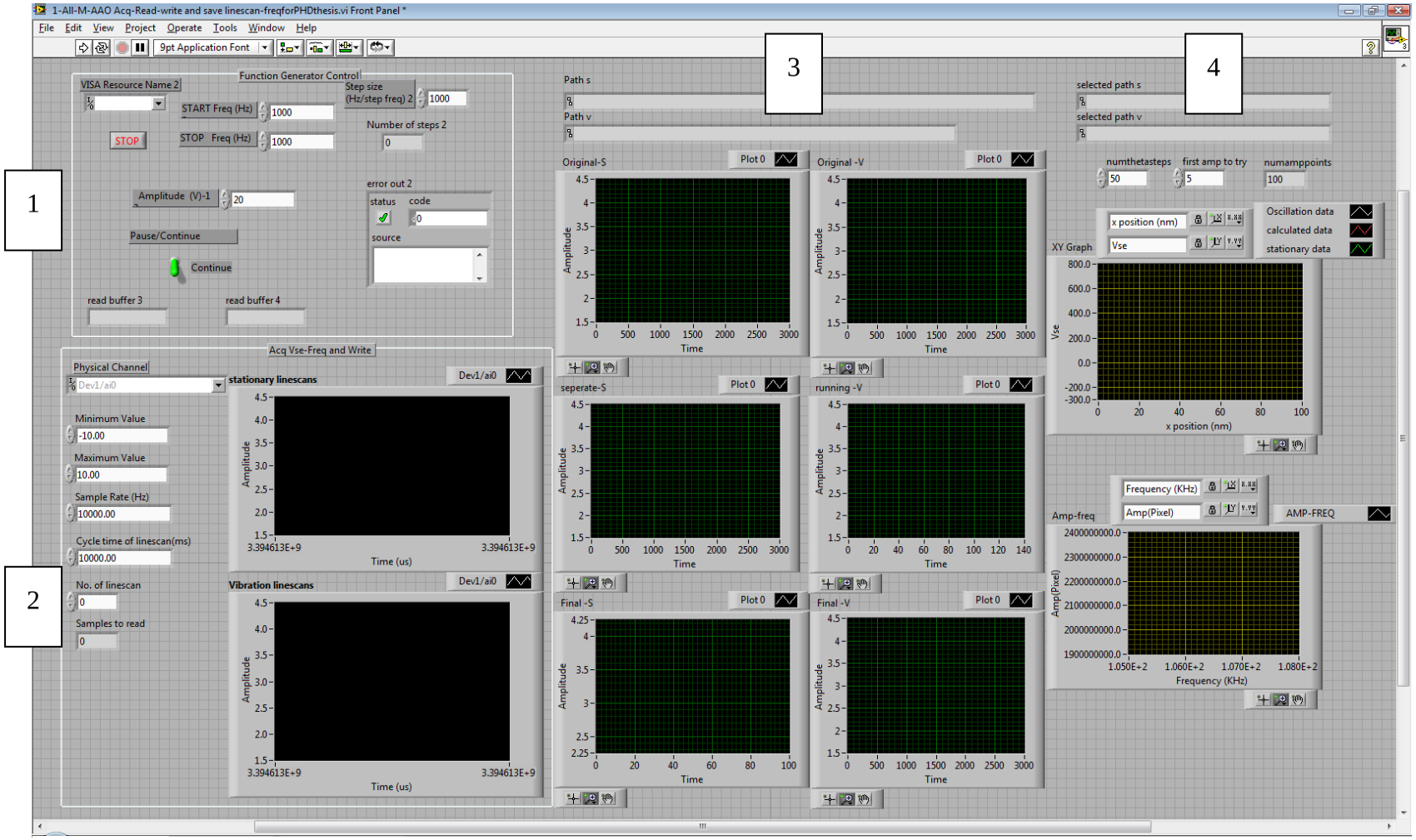

Figure 1 The front panel of the LabVIEW code for controlling the operation of the homemade measurement system, data acquisition and data analysing

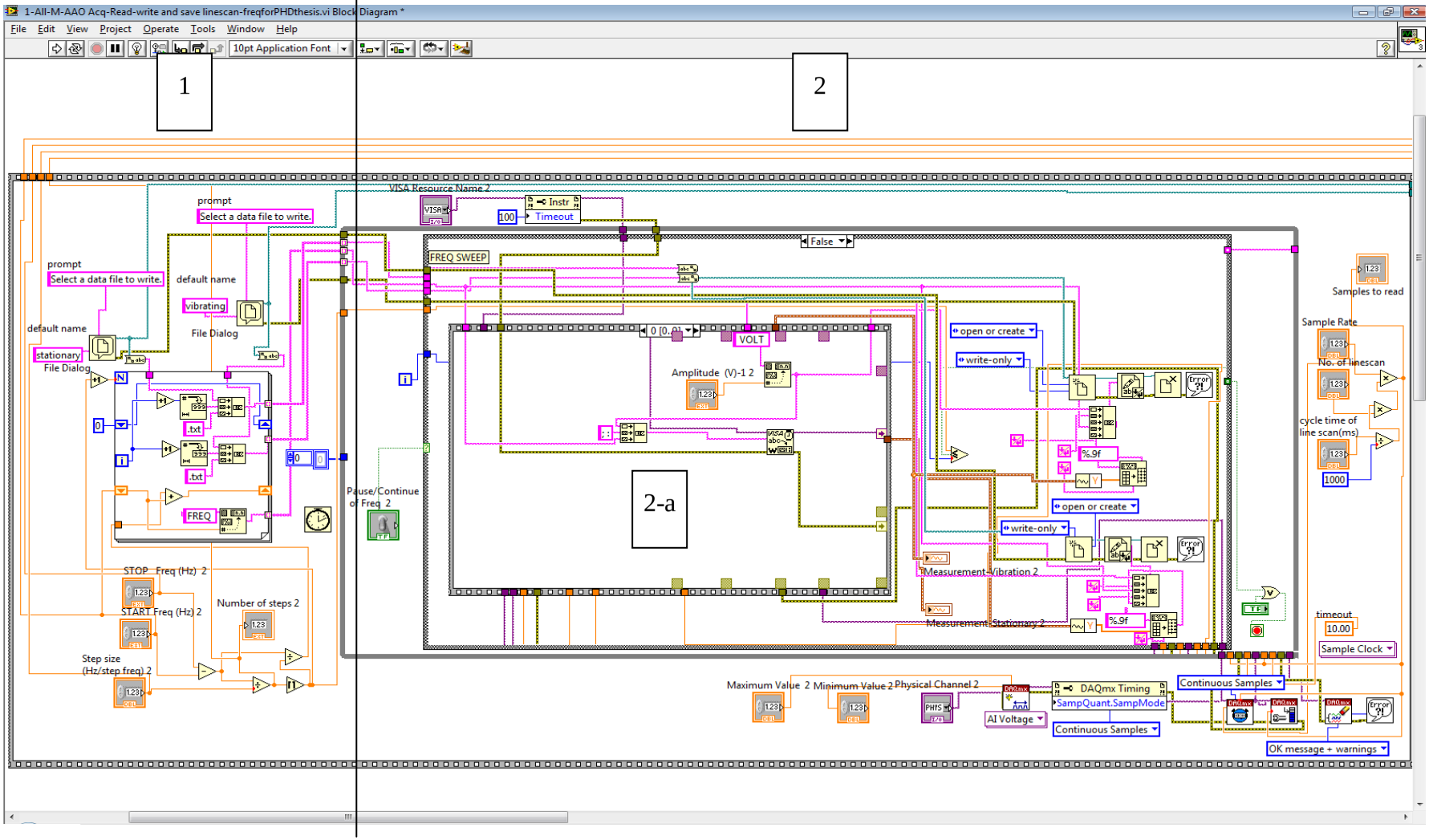

Figure 2(a) block diagran of the LabVIEW code for controlling the operation of the homemade measurement system, data acquisition and data analysing (part 1 and part 2)

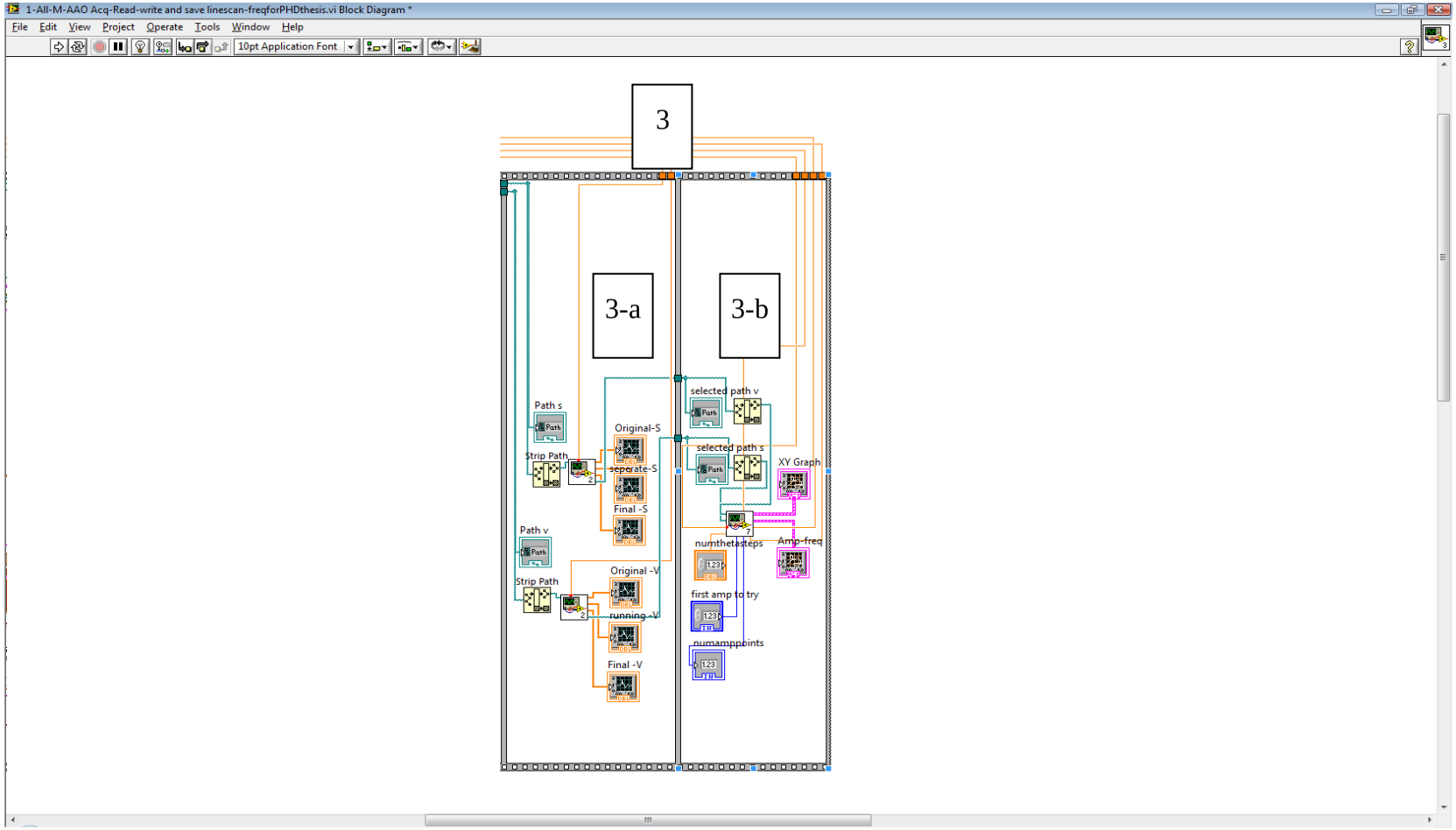

Figure 2(b) block diagran of the LabVIEW code for controlling the operation of the homemade measurement system, data acquisition and data analysing (part 3)

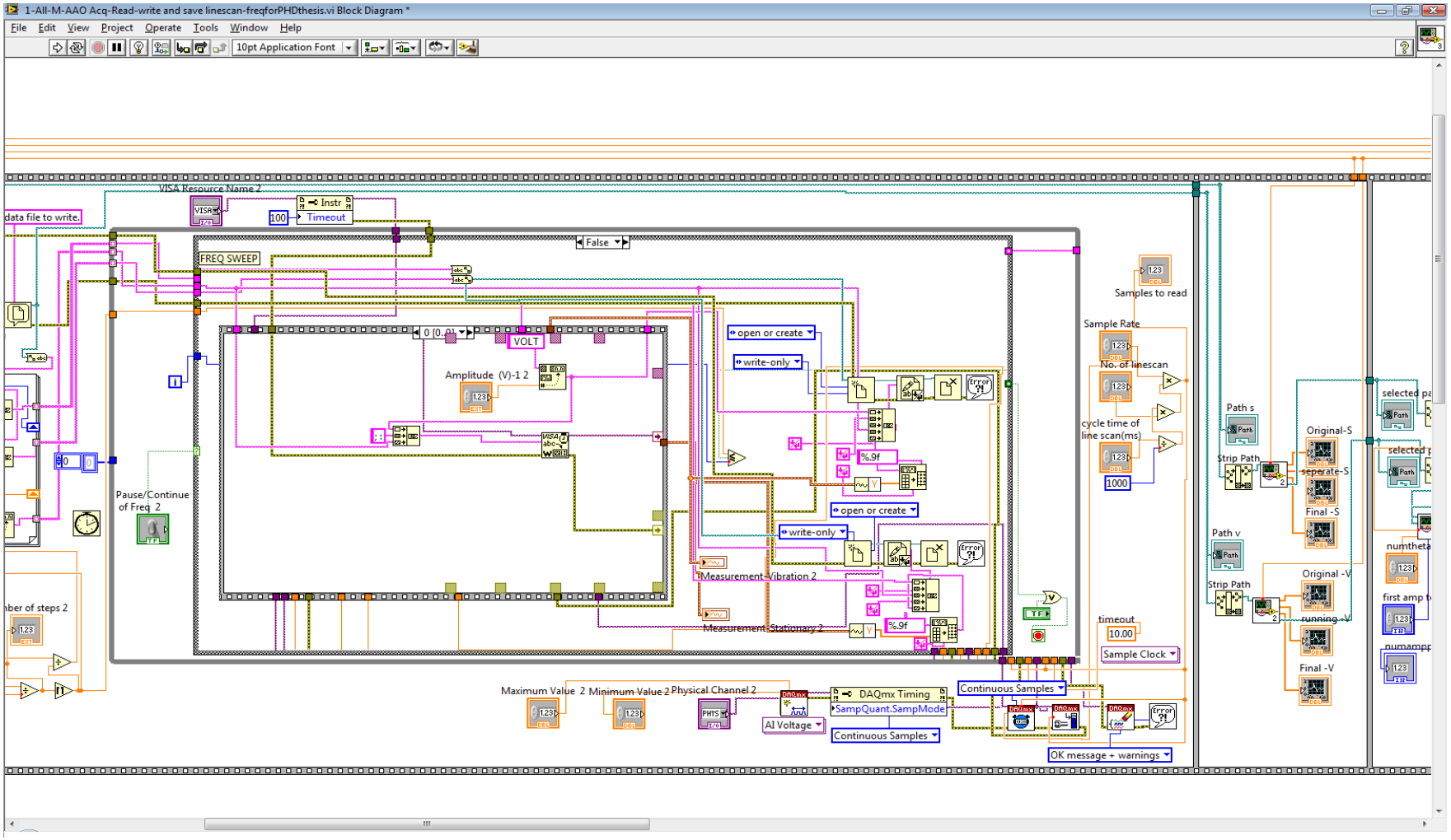

Figure 3 Case structure 1 for the data acquisition. This case structure shows command of amplitude(ac voltage) and a sweep frequency was sent to the function generator. Then, the amplitude and and frequency were exported to a file and saved

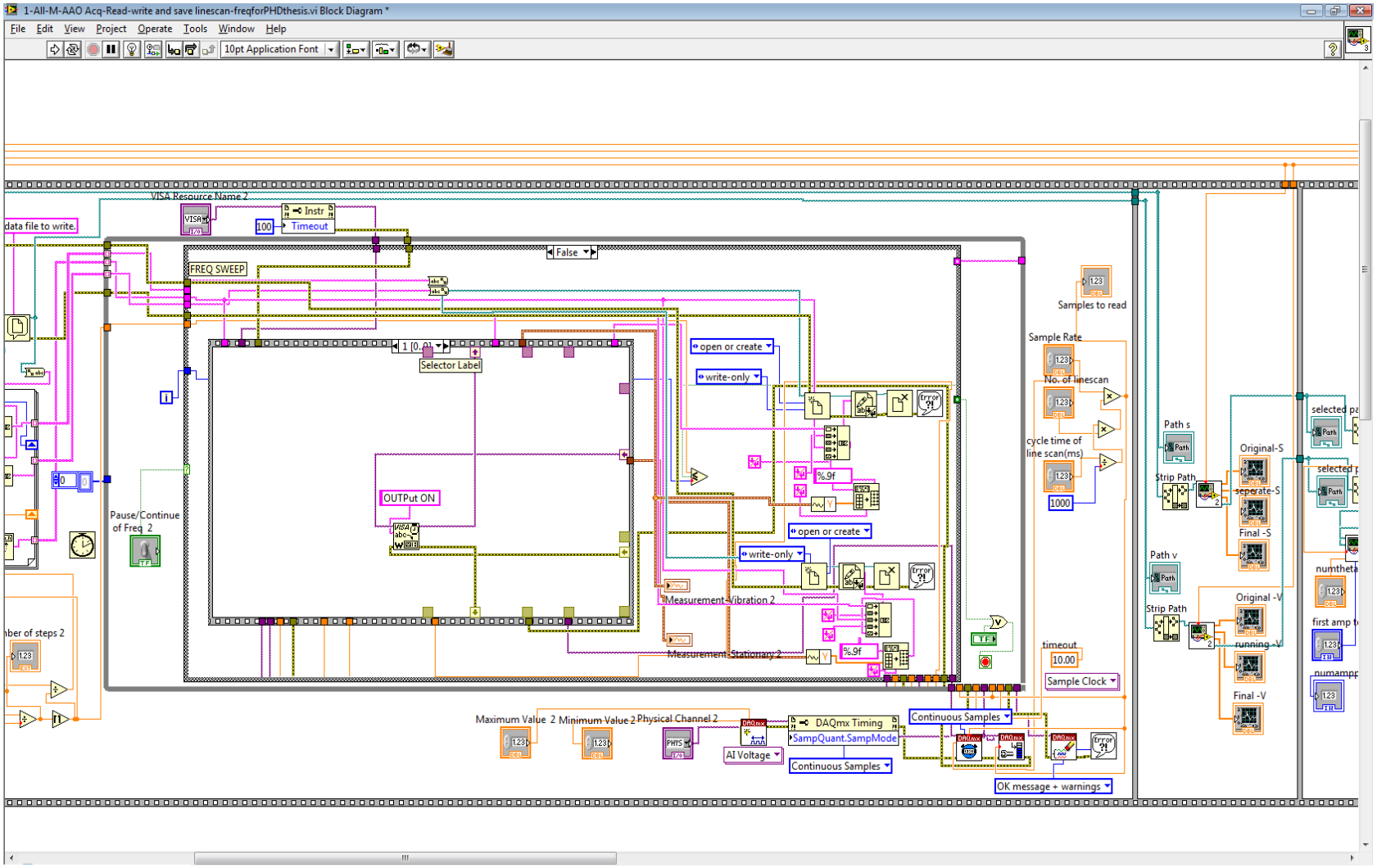

Figure 4 Case structure 2 for the data acquisition. This case structure shows command of switching on was sent to the function generator

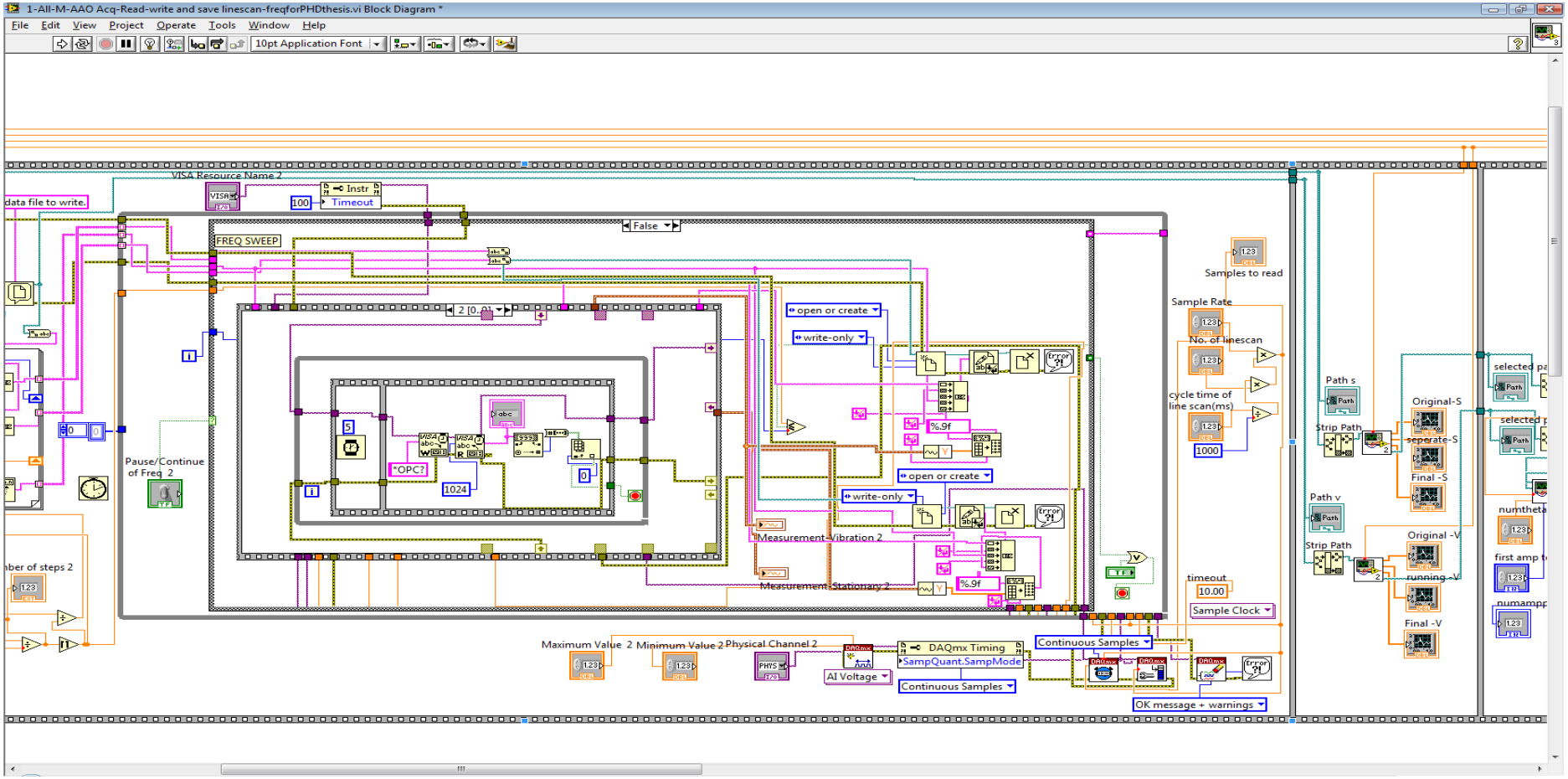

Figure 5 Case structure 3 for the data acquisition of linescans. This case structure shows the programme was forced to wait 5 ms to ensure a single linescan across a vibrating resontor is finished. The linescan data at one frequency step was exported from SE-detector. Wait for 5 ms, then linescan at next frequency step was exported. The loop of data acquisition continued until the sweep frequency stopped.

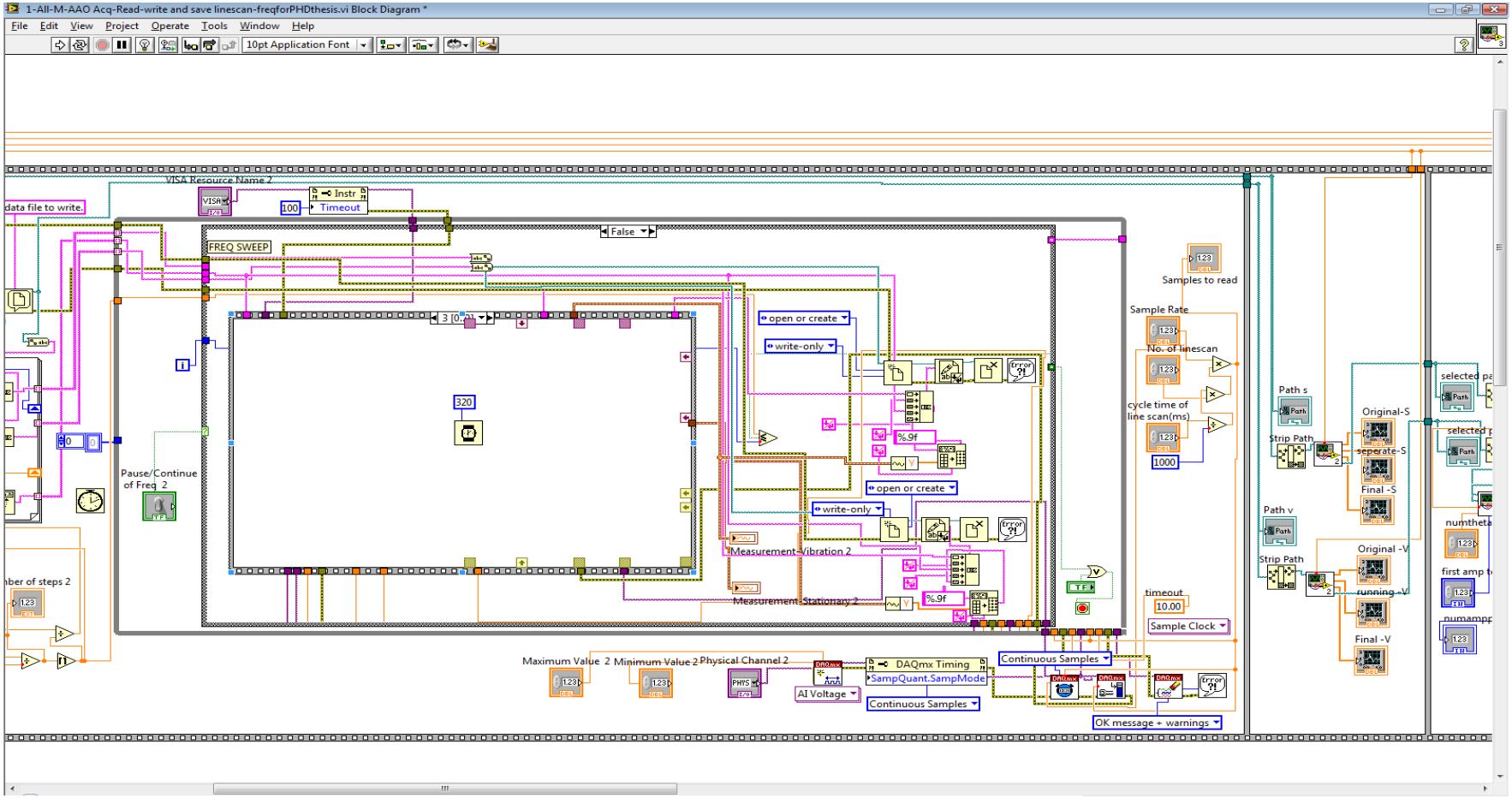

Figure 6 Case structure 4 for the data acquisition. This case structure shows the programme was forced to wait 320 ms
To ensure there is enough time for the SE-detector to collect all of the linescan data

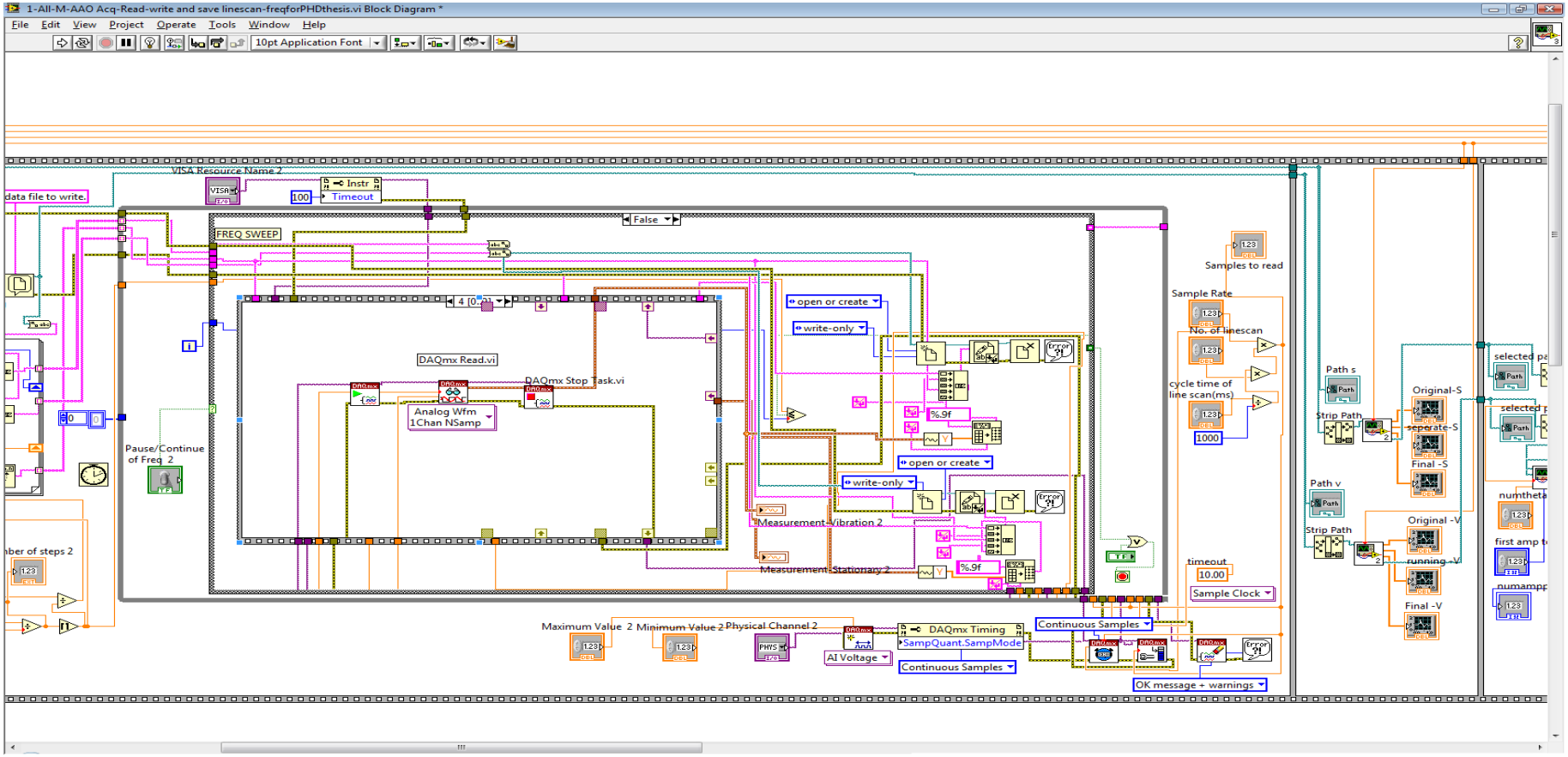

Figure 7 Case structure 5 for the data acquisition. This case structure shows the DAQ acquire the data from SE-detector and export them to different files and save them

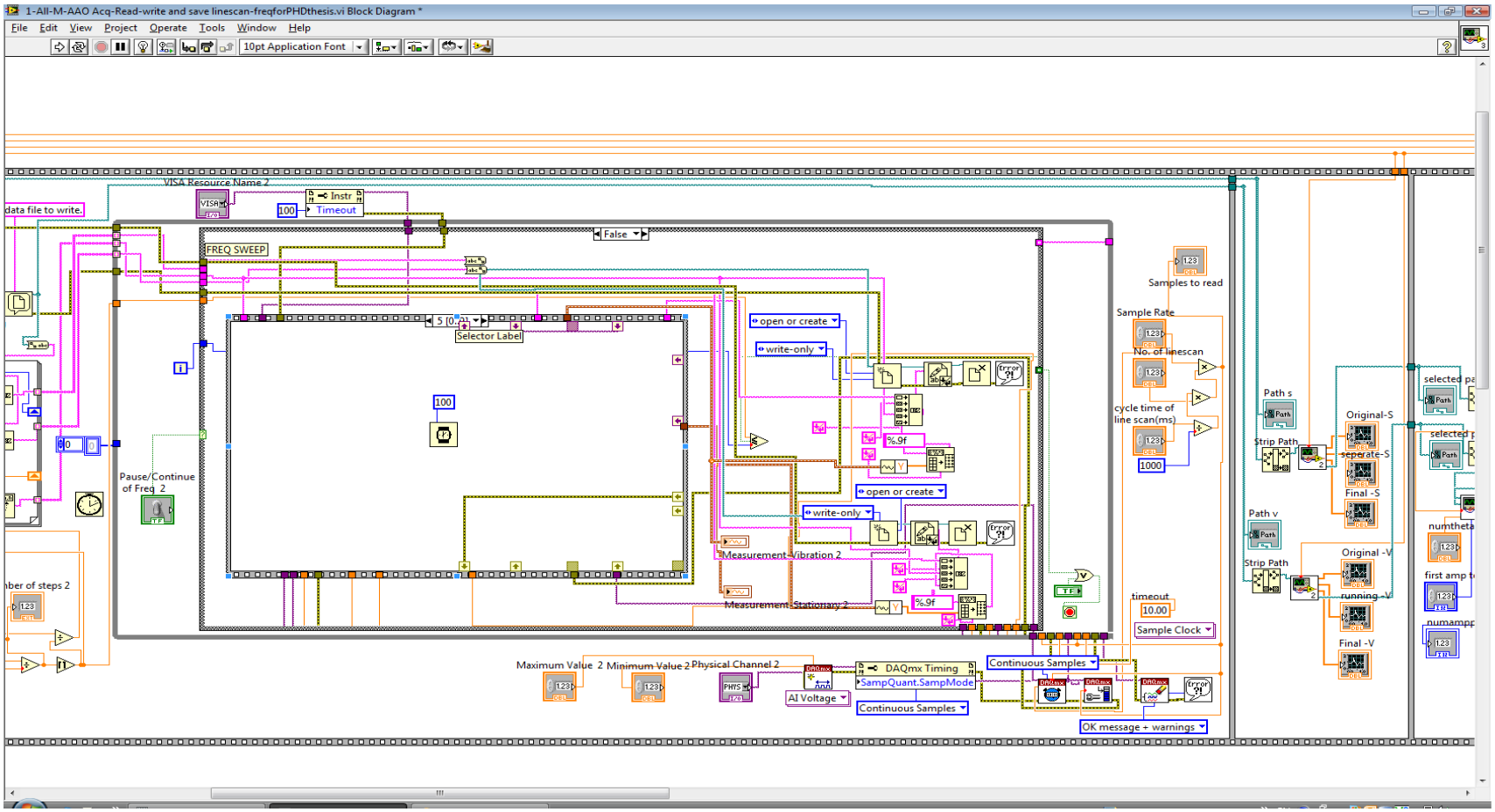

Figure 8 Case structure 6 for the data acquisition. This case structure shows the program was forced to wait 100 ms to ensure all of the data are exported and saved

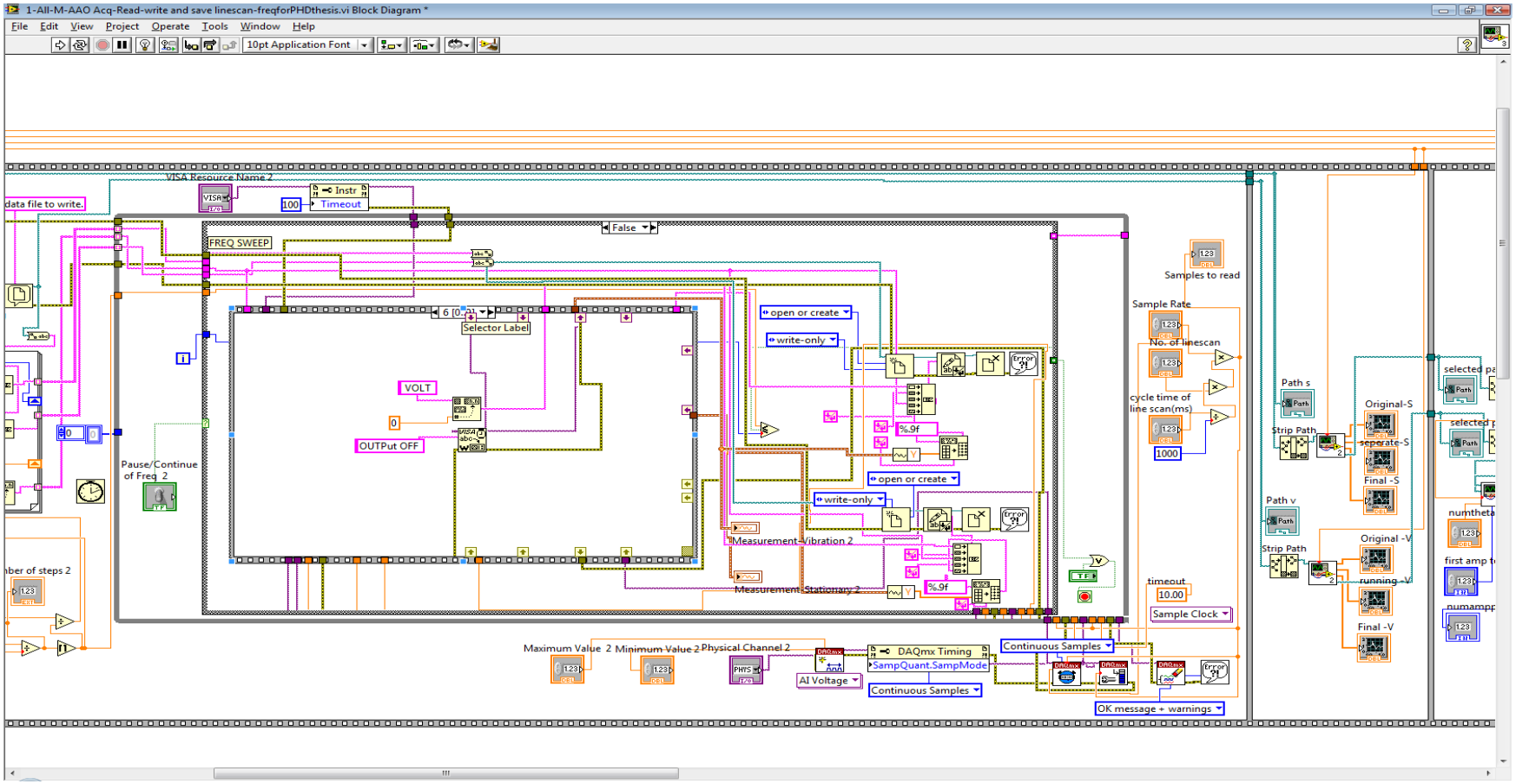

Figure 9Case structure 7 for the data acquisition. This case structure shows the program was forced to switch off the function generator

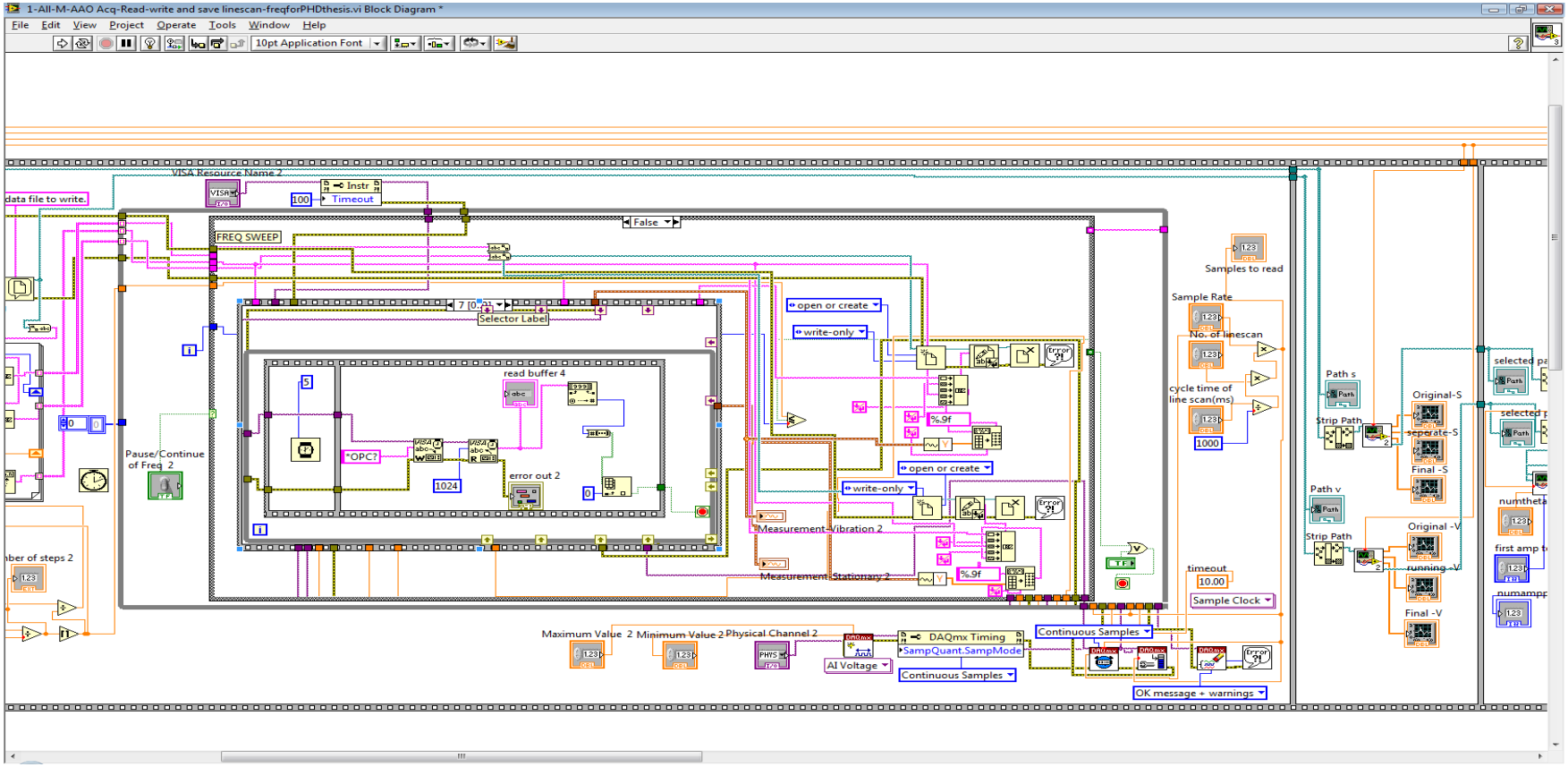

Figure 10 Case structure 8 for the data acquisition. . This case structure shows the programme was forced to wait 5 ms to ensure a single linescan across a stationary resonator is finished. The linescan data at one frequency step was exported from SE-detector. Wait for 5 ms, then linescan at next frequency step was exported. The loop of data acquisition continued until the sweep frequency stoppe

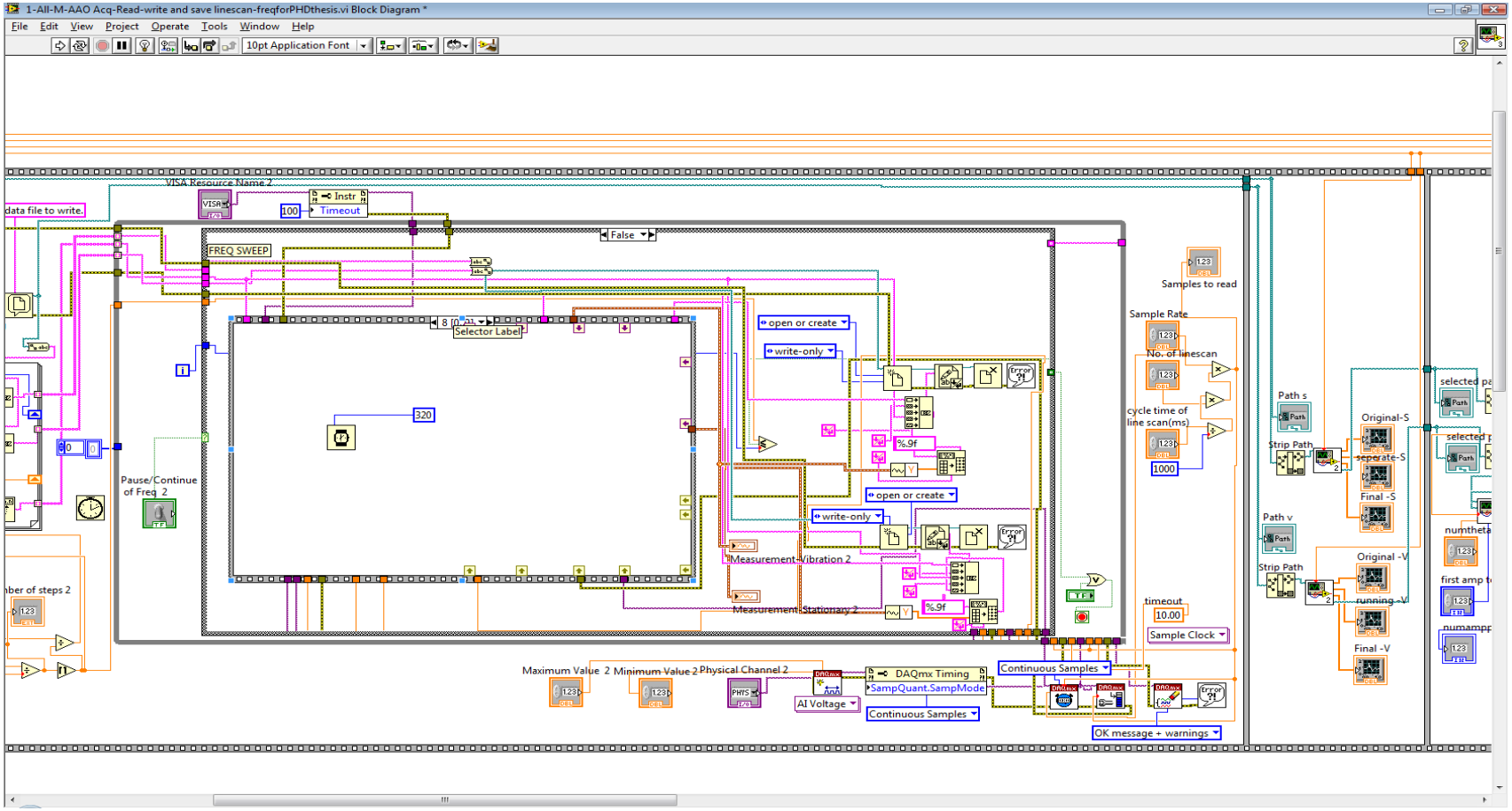

Figure 11 Case structure 9 for the data acquisition. This case structure shows the programme was forced to wait 320 ms To ensure there is enough time for the SE-detector to collect all of the linescan data

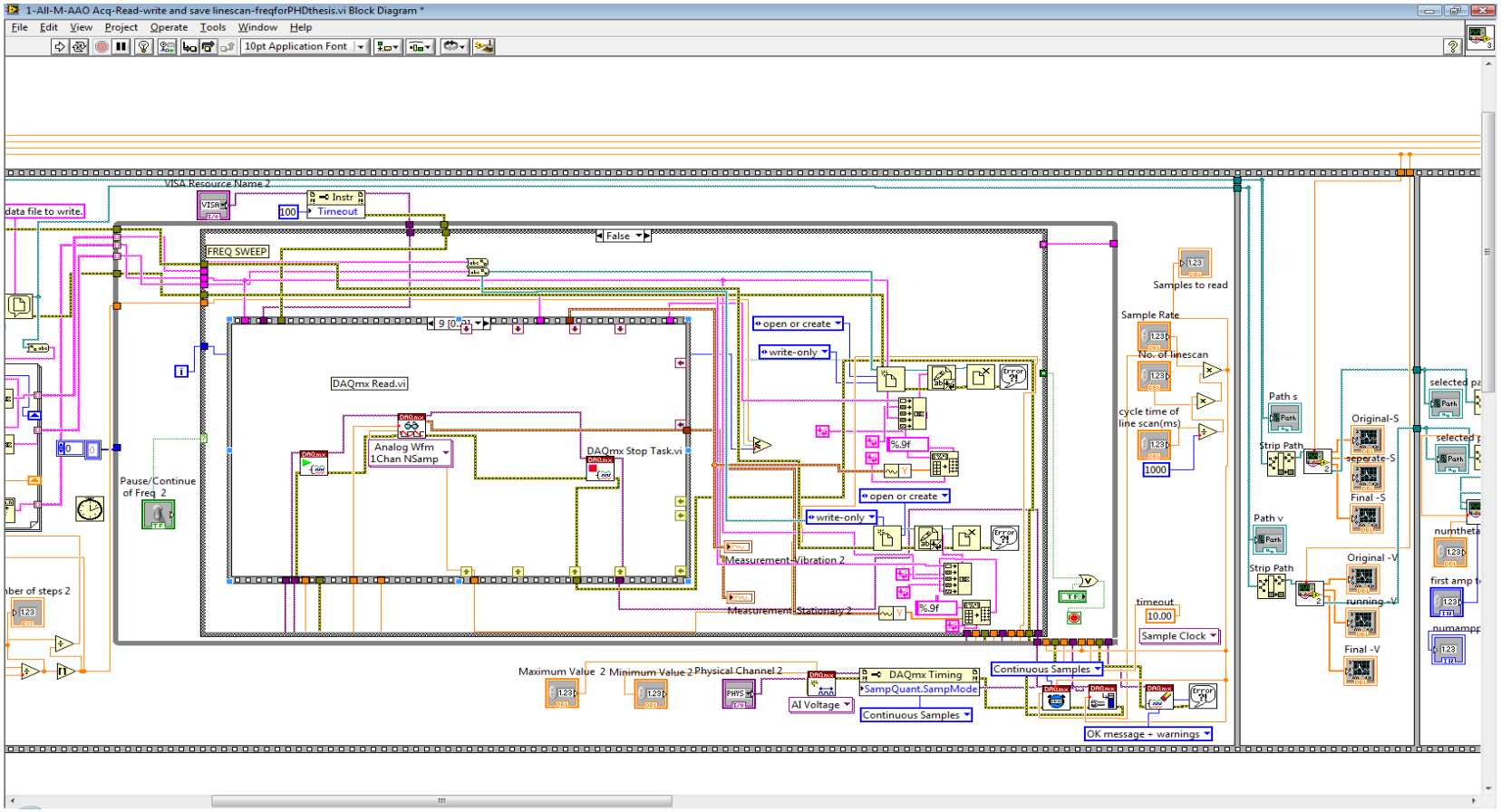

Figure 12 Case structure 10 for the data acquisition. This case structure shows the DAQ acquire the data from SE-detector and export them to different files and save them